Aix*Marseille université
Socialement engagée

NNT : 2023AIXM0001

THÈSE DE DOCTORAT

Soutenue à Aix-Marseille Université
le 7 octobre 2024 par

Martino SILVETTI

Thermodynamics and optical properties of point defects in wurtzite Boron Nitride

Discipline
Physique et sciences de la matière

Spécialité
Matière Condensée et Nanosciences

École doctorale
ED 352 Physique et Sciences de la Matière

Laboratoire/Partenaires de recherche
PIIM - Physique des interactions ioniques et moléculaires - UMR 7345

Composition du jury

Nicolas CAVASSILAS PU, IM2NP, Aix Marseille Université	Président du jury
Pina ROMANIELLO DR-CNRS, Lab. de Physique Théorique, Université Paul Sabatier, Toulouse	Rapporteuse
Xavier BLASE DR-CNRS, Institut Néel, Grenoble	Rapporteur
Michele AMATO MCF, Lab. de Physique des Solides, Université Paris-Saclay, Orsay	Examinateur
Elena CANNUCCIA MCF, PIIM, Aix-Marseille Université	Co-directrice de thèse
Cédric PARDANAUD MCF-HDR, PIIM, Aix Marseille Université	Directeur de thèse
Claudio ATTACCALITE DR-CNRS, CINaM, Aix Marseille Université	Membre invité

PIIM Physique des Interactions Ioniques et Moléculaires
anr agence nationale de la recherche
cnrs

Affidavit

I, undersigned, Martino Silvetti, hereby declare that the work presented in this manuscript is my own work, carried out under the scientific supervision of Cédric Pardanaud and the co-supervision of Elena Cannuccia, in accordance with the principles of honesty, integrity and responsibility inherent to the research mission. The research work and the writing of this manuscript have been carried out in compliance with both the French national charter for Research Integrity and the Aix-Marseille University charter on the fight against plagiarism.

This work has not been submitted previously either in this country or in another country in the same or in a similar version to any other examination body.

Marseille, 11 July 2024

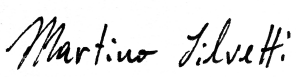



This work is licensed under Creative Commons Attribution-NonCommercial-NoDerivatives 4.0 International Public License

Liste de publications et participation aux conférences

Liste des publications et/ou brevets réalisées dans le cadre du projet de thèse :

1. Martino Silvetti, Claudio Attaccalite, and Elena Cannuccia, "Pressure dependence of electronic, vibrational and optical properties of wurtzite-boron nitride", in *Physics Review Materials 7, 055201*, Published 30 May 2023.

Participation aux conférences et écoles d'été au cours de la période de thèse :

1. "Defect in Solids for Quantum Technologies", Budapest, Hungary, June 2024 (**Poster presentation**) ;
2. "27th ETSF Workshop on Electronic Excitations", Marseille, France, June 2024 (**Oral presentation**) ;
3. "Advanced Quantum Materials 2023 - International Workshop", Marseille, France, June 2023 (**Poster presentation**) ;
4. "Inaugural Workshop on Boron Nitride - BNW2023", Montpellier, France, Mai 2023 (**Poster presentation**) ;
5. "Introductory days to Quantum Computing for Physics and Chemistry", GDR REST - GDRN BODY, Grenoble, France, Janvier 2023 ;
6. "18th ETSF Young Researchers Meeting", Marseille, France, Septembre 2022 (**Oral presentation**) ;
7. "Ab Initio Many-Body Methods and Simulations with the Yambo code (smr 3694)", ICTP, Trieste, Italy, Avril 2022 ;
8. "Introduction to ScaLAPACK and MAGMA libraries @ MdIS/Idris" Prace, en ligne, Mars 2022 ;

Abstract and keywords

Wurtzite boron nitride (wBN) is a boron nitride polytype resulting from the layered hexagonal form (hBN) undergoing a high pressure-induced phase transition. This material holds a role of intermediary in the hexagonal to cubic (cBN) phase transformation, and it has been believed for a long time to be a metastable form occurring only at very high pressure. For this reason the progress in the research on this material has fallen behind when compared to the efforts spent in studying the hBN and cBN which instead are stable at ambient pressure and easier to produce. Nonetheless, recently wBN has been stabilized at ambient conditions and macroscopic millimeter-size samples have been produced by direct transition from hBN under high pressure. These new synthesis methods pave the way to the possibility of manufacturing and utilize this material in optoelectronic applications in the UV range under harsh conditions since it is a superhard semiconductor with a wide band gap. Therefore this crystal is also interesting as a potential host for defect-induced electronic states for which applications in the field of quantum technologies can be also envisaged similarly to the defects currently studied in hBN and cBN . Moreover, small domains of wBN are always present in cBN samples along with other boron nitride polymorphs, thus affecting its optical properties. The scope of this thesis is to fill the gap in the knowledge of wBN with a particular emphasis on its potential as a defect host. Here we present a totally *ab initio* study of the electronic and optical properties of wBN based on the well-established Density Functional Theory (DFT) and Many-Body Perturbation Theory (MBPT) approaches. After having introduced the theoretical tools needed to explore the ground and excited states properties, we study the material in its pristine form and we accurately describe the electronic structure and band gap, together with the dielectric function including excitonic effects by use of the Bethe-Salpeter equation (BSE). This study is carried out in the range of pressures involved in the wBN synthesis. Then we will introduce simple defects in the structure (vacancies, antisites and carbon-related monomers and dimers) and we will use the formation energy formalism to study their thermodynamics. Finally the role of defects in determining the optical properties of the material is assessed by mean of the BSE diagonalization on top of DFT calculations, thanks to a remapping procedure for the pristine crystal static screening that has been developed and implemented in the `Yambopy` code.

Keywords: Point defects, boron nitride, luminescence, defect formation energy, Density Functional Theory, Many-Body Perturbation Theory, Bethe-Salpeter equation, screening.

Résumé et mots-clés

Le nitrure de bore en forme de wurtzite (wBN) est un polytype du nitrure de bore résultant de la forme hexagonale stratifiée (hBN) subissant une transition de phase induite par une pression élevée. Ce matériau joue un rôle d'intermédiaire dans la transformation de la phase hexagonale à la phase cubique (cBN), et on a longtemps cru qu'il s'agissait d'une forme métastable ne se produisant qu'à très haute pression. C'est pourquoi les progrès de la recherche sur ce matériau ont pris du retard par rapport aux efforts consacrés à l'étude du hBN et du cBN qui sont stables à la pression ambiante et plus faciles à produire. Néanmoins, le wBN a récemment été stabilisé dans des conditions ambiantes et des échantillons macroscopiques de taille millimétrique ont été produits par transition directe à partir du hBN sous haute pression. Ces nouvelles méthodes de synthèse ouvrent la voie à la possibilité de fabriquer et d'utiliser ce matériau dans des applications optoélectroniques dans le domaine des UV dans des conditions difficiles, puisqu'il s'agit d'un semi-conducteur super dur avec une large bande interdite. Par conséquent, ce cristal est également intéressant en tant qu'hôte potentiel d'états électroniques induits par des défauts, pour lesquels des applications dans le domaine des technologies quantiques peuvent également être envisagées, à l'instar des défauts actuellement étudiés dans hBN et cBN . En outre, de petits domaines de wBN sont toujours présents dans les échantillons de cBN avec d'autres polymorphes de nitrure de bore, ce qui affecte ses propriétés optiques. L'objectif de cette thèse est de combler les lacunes dans la connaissance de wBN en mettant particulièrement l'accent sur son potentiel en tant qu'hôte de défauts. Nous présentons ici une étude totalement *ab initio* des propriétés électroniques et optiques de wBN basée sur les approches bien établies de la Théorie du Fonctionnelle Densité (DFT) et de la Théorie des Perturbation à N-Corps (MBPT). Après avoir introduit les outils théoriques nécessaires pour explorer les propriétés des états fondamentaux et des états excités, nous étudions le matériau dans sa forme pure et primitive et nous décrivons avec précision la structure électronique et la bande interdite, ainsi que la fonction diélectrique incluant les effets excitoniques en utilisant l'équation de Bethe-Salpeter (BSE). Cette étude est réalisée dans la gamme de pressions impliquées dans la synthèse de wBN . Nous introduirons ensuite des défauts simples dans la structure (lacunes, antisites et monomères et dimères à base de carbone) et nous utiliserons le formalisme de l'énergie de formation pour étudier leur thermodynamique. Enfin, le rôle des défauts dans la détermination des propriétés optiques du matériau est évalué avec la diagonalisation de la BSE en utilisant comme base de départ les états de Kohn-Sham, grâce à une procédure de remappage de l'écrantage statique du crystal primitif qui a été développé et mis en œvre dans le code numérique `Yambopy`.

Mots-clés : défauts ponctuels, nitrure de bore, luminescence, énergie de formation

des défauts, Théorie du Fonctionnel Densité, Théorie de perturbation à N-corps, équation de Bethe-Salpeter, écrantage.

Résumé étendu

Le nitrure de bore est un composé diatomique qui peut exister sous diverses formes polymorphes, telles que les structures monoclinique (mBN), rhomboédrique (rBN), hexagonale (hBN), cubique (cBN) et de type wurtzite (wBN). Parmi celles-ci, les formes hexagonale et cubique ont été particulièrement étudiées car elles sont stables à la pression ambiante.

Récemment, l'intérêt pour hBN a considérablement augmenté en raison de ses caractéristiques uniques. Il est constitué de couches bidimensionnelles avec une hybridation sp^2 liées entre elles par de faibles forces de Van der Waals. L'écart entre les couches empêche l'écrantage des lignes de champ générées par l'attraction entre l'électron et la lacune lors de l'excitation. Bien qu'il s'agisse d'un matériau à large bande interdite indirecte, hBN présente un rendement quantique en photoluminescence exceptionnellement élevé qui s'explique par un fort couplage entre les excitons et les phonons. Cette interaction intense est due au faible écrantage qui conduit à une forte localisation des excitons. Ces caractéristiques rendent ce matériau particulièrement intéressant comme émetteur dans l'ultraviolet. Par ailleurs, la phase cubique a également suscité un grand intérêt. Le cBN est souvent qualifié de "super dur" dans la littérature, sa dureté n'étant surpassée que par celle du diamant. Comme le hBN , il fait partie des semi-conducteurs à large bande interdite (environ 6.4 eV).

De plus, le hBN et le cBN sont considérés comme des matériaux aptes à contenir des défauts ponctuels, ce qui ouvre des perspectives fascinantes pour l'étude des corrélations entre certains signaux de luminescence et des défauts spécifiques. L'intérêt pour ces matériaux, en tant qu'hôtes potentiels de niveaux de défauts, est également motivé par la possibilité d'ingénierie et d'exploitation de ces niveaux pour des applications potentielles dans les technologies quantiques. Par exemple, la vacance de bore chargée négativement dans le hBN est un défaut actuellement étudié pour la détection quantique, tandis que le complexe $O_N V_B$ dans le cBN est étudié comme potentiel centre de couleur, isoélectronique avec le complexe N_V^- dans le diamant.

En raison de l'intérêt porté à cBN et hBN , des parallèles ont souvent été établis entre ces deux semi-conducteurs et leurs équivalents à base de carbone, hBN étant défini comme l'équivalent du graphite. Alors que la recherche sur les défauts dans le nitrure de bore hexagonal et cubique a progressé, la forme wBN n'a pas été particulièrement étudiée et pour l'instant elle n'a pas été considérée comme un hôte pour des défauts ponctuels. Pourtant wBN joue un rôle intermédiaire dans la transition de phase de l'hexagonal au cubique sous haute pression. Entre 100 et 130 kBar, les couches de hBN se déforment ("buckling"), les liaisons de Van der Waals sont remplacées par des liaisons covalentes le long de la direction (0001) (axe z), et le système adopte l'hybridation sp^3 en forme wurtzite. Après la création de la wurtzite, le système évolue

facilement vers la phase cubique, rendant la production d'échantillons de *w*BN pur extrêmement difficile. Cependant, la production de *c*BN à partir de *h*BN n'est pas parfaite, et les domaines où la transition de phase se termine par des phases autres que la cubique sont toujours présents dans les échantillons de *c*BN . En conséquence, *w*BN est toujours présent dans de petites régions des échantillons de *c*BN , avec d'autres phases.

Depuis la première synthèse par Bundy et Wentorf en 1963, les échantillons de *w*BN étudiés étaient principalement des cristallites micrométriques obtenues à partir de poudres de *h*BN . Plus récemment, grâce à de nouvelles techniques, Deura et al. ont réussi à produire en 2016 des échantillons macroscopiques de *w*BN à partir de monocristaux de *h*BN . Les expériences de réflectance infrarouge menées par Segura et al. en 2019 suggèrent qu'il est possible de produire un échantillon de *w*BN à partir de *h*BN et que la phase reste stable une fois la pression relâchée. Chen et al. ont ensuite suggéré que de tels échantillons macroscopiques de *w*BN sont stabilisés par un système de défauts macroscopiques.

Le fait qu'il existe actuellement plusieurs indications suggérant que le *w*BN peut être stable à la pression ambiante et produit en quantités macroscopiques, et le fait qu'il est néanmoins présent en tant que défaut dans les échantillons de *c*BN , modifiant potentiellement leurs propriétés optiques, motive notre intérêt pour les propriétés électroniques et optiques du *w*BN .

Dans cette thèse, nous menons une étude entièrement *ab initio* des propriétés éléctroniques, vibrationnelles et optiques du *w*BN , ainsi que de son potentiel en tant qu'hôte pour les défauts ponctuels. L'objectif est d'explorer les caractéristiques qui pourraient être intéressantes à l'avenir pour une éventuelle utilisation et mise en œuvre du *w*BN dans l'industrie des semi-conducteurs pour l'optoélectronique et potentiellement comme plate-forme pour les technologies quantiques.

Le travail a été devéloppé en deux phases. Dans la première phase, nous avons étudié le *w*BN dans sa structure pure d'origine, c'est-à-dire sans défauts. Une fois les propriétés de la forme pure établies, nous avons ensuite considéré un modèle constitué de l'hôte et d'un ensemble de défauts, et exploré ses propriétés thermodynamiques, électroniques et optiques. Les défauts étudiés incluent les lacunes, les antisites, les substituants du carbone et le dimère de carbone. En général, l'effet des défauts dans un matériau est de faire apparaître des niveaux plats et sans dispersion dans la structure de la bande électronique, éventuellement dans la bande interdite. Nous expliquons maintenant plus en détail le contenu des différents chapitres qui composent cette thèse.

Après une brève introduction, le chapitre 1 présente les outils théoriques utilisés pour explorer les propriétés de l'état fondamental du *w*BN , sujet de notre recherche. Nous commencerons par définir le problème à N-électrons, l'interaction électron-électron et les difficultés associées à ce terme d'interaction non locale dans la résolution de l'Hamiltonien. La méthode utilisée dans cette thèse pour résoudre l'hamiltonien électronique est la Théorie de la Fonctionnelle de la Densité (DFT) selon l'approche de Kohn et Sham. Cette méthode est désormais la référence pour décrire

de manière satisfaisante les propriétés structurelles et électroniques des matériaux.

La DFT repose sur un changement de paradigme. Au lieu de résoudre l'hamiltonien pour obtenir ses fonctions d'onde, la DFT utilise la fonction de densité électronique comme variable centrale d'une fonctionnelle d'énergie. Ce traitement découle des deux théorèmes de Hohenberg et Kohn, qui stipulent essentiellement que non seulement un hamiltonien à N électrons a un certain ensemble d'états propres déterminant la densité électronique, y compris un état particulier qui est l'état fondamental, mais qu'inversement, sauf dégénérescence, une densité électronique donnée correspondra à la densité électronique de l'état fondamental d'un unique hamiltonien à N électrons. Ainsi, étant donné une densité électronique d'état fondamental, celle-ci détermine le potentiel et donc tous les états du système. Pour rendre la DFT opérationnelle et utilisable, l'approche de Kohn et Sham consiste à simplifier le système d'électrons en interaction en un système auxiliaire de "pseudo-électrons de Kohn-Sham" sans interaction, qui est plus facile à résoudre. Ce système auxiliaire est trouvé approximativement en définissant un potentiel d'échange-corrélation dans l'hamiltonien auxiliaire. Cette approximation conduit à l'ensemble des équations de Kohn-Sham, qui sont résolues de manière auto-cohérente pour obtenir les propriétés électroniques du système. Dans ce travail, la résolution des équations de Kohn-Sham est effectuée par le programme `PWSCF`, contenu dans le paquet Quantum Espresso, le code que nous avons utilisé. Le schéma auto-cohérent utilisé par `PWSCF` est illustré dans la Fig. 0.1. L'hamiltonien auxiliaire est résolu en une série de cycles auto-cohérents (SCF)

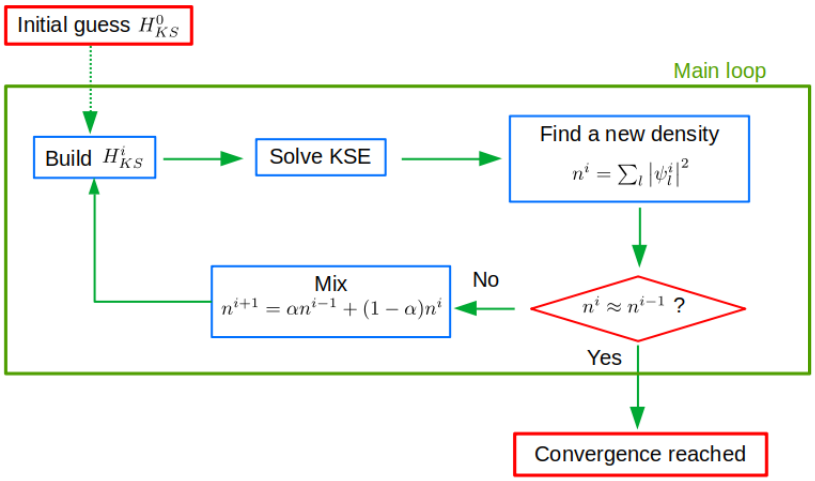

Figure 0.1. – Schéma de résolution auto-cohérente de l'hamiltonien auxiliaire de Kohn-Sham, tel qu'il est utilisé dans le code numérique Quantum Espresso.

jusqu'à atteindre la convergence de l'énergie. Quantum Espresso travaille dans l'espace réciproque du cristal en utilisant une base d'ondes planes pour les états de Bloch, ce qui fait que les niveaux d'énergie et les états dépendent fortement du nombre de vecteurs $\boldsymbol{G}$ de l'espace réciproque utilisés dans l'expansion et du nombre de points $\boldsymbol{k}$ de la zone de Brillouin où les énergies sont échantillonnées. Par conséquent, dans le cadre de notre méthodologie, il est crucial de prêter attention à la convergence des

quantités que nous souhaitons calculer en fonction de ces paramètres.

Une fois les équations résolues, il est possible d'utiliser les états trouvés comme approximations des états mono-électroniques du système, permettant ainsi d'obtenir la structure de bande du système. De plus, la DFT permet de calculer les forces agissant sur les atomes et d'effectuer une série de cycles SCF pour obtenir des structures cristallines optimisées. Enfin, il est également possible d'étendre la DFT pour traiter les phonons, grâce à la Théorie Perturbative de la Fonctionnelle Densité, à laquelle nous consacrerons une petite section dans ce chapitre.

La DFT sera utilisée à la fois pour étudier la phase pure du *w*BN et le système avec les défauts mentionnés précédemment. Lorsque nous parlons de thermodynamique des défauts, nous faisons essentiellement référence à leur énergie de formation, qui détermine la facilité avec laquelle ces défauts peuvent se former dans le cristal. Elle se compose des termes suivants :

— la différence entre l'énergie du système avec le défaut et celle du système primitif ;
— les potentiels chimiques des espèces à enlever et à ajouter pour créer le défaut ;
— le potentiel chimique électronique (énergie de Fermi) nécessaire pour charger le défaut ;
— une correction de la "limite diluée" pour les défauts chargés.

La DFT sera utilisée pour évaluer les trois premiers termes de l'énergie de formation mentionnés, en utilisant l'approche dite de supercellule. D'un point de vue numérique, l'introduction d'un défaut dans le matériau pose des défis, car elle brise la symétrie de translation du système simulé, qui impose naturellement des conditions périodiques et donc une symétrie de translation. Cela oblige à utiliser de grandes supercellules pour simuler un système avec le défaut. Une supercellule plus grande permet de simuler une densité plus faible d'un certain type de défaut dans le système. Dans notre étude, nous avons utilisé des supercellules contenant 576 atomes et nous avons constaté qu'un plus grand nombre d'atomes dépasserait les capacités de calcul des superordinateurs disponibles.

La correction de limite diluée mentionnée a pour but de neutraliser l'interaction fallacieuse entre un défaut chargé et ses images périodiques. Cette correction ne peut être calculée qu'approximativement. Dans cette thèse, nous adopterons le schéma de Freysoldt, Neugebauer et Van de Walle (FNV) pour cette correction.

Un des inconvénients majeurs de la DFT est qu'elle est essentiellement une théorie d'état fondamental, ce qui la rend insuffisante pour décrire avec précision les propriétés des états excités, telles que les propriétés électroniques et optiques. Un exemple frappant de cette limitation est le cas du germanium, pour lequel la DFT prédit une bande interdite nulle, alors qu'en réalité, il s'agit d'un semi-conducteur. En général, la DFT tend à sous-estimer la largeur des bandes interdites électroniques, car elle ne prend pas correctement en compte les effets de l'écrantage et ne décrit pas bien les interactions entre électrons et lacunes.

Pour obtenir une description plus précise des propriétés électroniques et optiques des matériaux, nous devons recourir à des outils plus avancés, comme ceux présentés au chapitre 2. Lors d'une excitation optique, un électron est promu à un nouvel état,

laissant derrière lui une lacune considérée comme une charge positive. Les autres électrons réagissent à la présence de cette lacune en réarrangeant leurs états. Dans la théorie perturbative à N-corps (MBPT), on remplace les électrons par des quasi-électrons, qui représentent à la fois l'électron et le nuage de polarisation généré par les autres électrons, permettant d'écranter l'interaction électronique. En utilisant la fonction de Green G comme quantité centrale et en intégrant l'interaction écrantée W due à la polarisation, nous pouvons dévéloper G autour de la fonction de Green G_0 des états non-interageants (en pratique calculée à partir des états de Kohn-Sham). Dans ce chapitre, nous dériverons un ensemble de quantités étroitement liées à la fonction de Green du système, couplées dans un système d'équations intégro-différentielles connues sous le nom d'équations de Hedin. En théorie, ces équations devraient être résolues de manière auto-cohérente. Cependant, en pratique, leur résolution exacte est impossible, et nous devons utiliser un schéma d'approximation. L'approximation que nous adopterons est appelée approximation GW. Dans ce cadre, l'une des quantités de l'ensemble des équations de Hedin, la self-énergie Σ_{xc}, est approximée par la convolution de G avec le potentiel écranté W.

Une fois la self-énergie déterminée, elle peut être utilisée pour corriger la structure de bande électronique calculée par la DFT. La structure de bande corrigée $E^{(qp)}_{i\boldsymbol{k}}$ est obtenue à partir de la structure calculée par la DFT $E^{(ks)}_{i\boldsymbol{k}}$, en appliquant une correction

$$E^{(qp)}_{i\boldsymbol{k}} = E^{(ks)}_{i\boldsymbol{k}} + Z_{i\boldsymbol{k}} \langle \psi^{ks}_{i,\boldsymbol{k}} | \Sigma_{xc\,i\boldsymbol{k}}(E^{(ks)}_{i\boldsymbol{k}}) - V^{(ks)}_{xc} | \psi^{ks}_{i,\boldsymbol{k}} \rangle \tag{0.1}$$

où $\psi^{ks}_{i,\boldsymbol{k}}$ sont les états de Kohn-Sham, $V^{(ks)}_{xc}$ est le potentiel d'échange-corrélation utilisé dans la DFT et $Z_{i\boldsymbol{k}}$ est un facteur de renormalisation. Cette technique permet d'obtenir des bandes interdites comparables à celles obtenues expérimentalement dans les expériences ARPES et ARPES inverse. Pour obtenir des propriétés optiques précises, des techniques encore plus avancées sont nécessaires.

La photo-excitation d'un électron entraîne la création d'une lacune et la réorganisation de tous les autres électrons, qui sont alors soumis à des effets de polarisation. L'électron excité et la lacune interagiront également à travers un potentiel écranté, formant un système analogue à un atome d'hydrogène, appelé exciton. L'exciton peut être simulé en résolvant l'équation de Bethe-Salpeter (BSE), laquelle peut être réécrite sous une forme pseudo-hamiltonienne. Les énergies propres et les états propres de cette forme correspondent aux niveaux et états excitoniques. Les vecteurs propres excitoniques permettent de calculer les éléments de matrice des dipôles électriques, qui déterminent la fonction diélectrique. En résolvant la BSE, on peut alors obtenir des propriétés optiques telles que l'absorption (proportionnelle à la partie imaginaire de la fonction diélectrique).

Les techniques discutées jusqu'à présent peuvent être appliquées aux matériaux dans leur forme primitive à l'aide du code `yambo`. Cependant, l'introduction de défauts et l'utilisation de l'approche de supercellule compliquent considérablement l'application de la méthode GW. Une alternative viable est de résoudre directement la BSE en utilisant les fonctions d'onde de Kohn-Sham comme données d'entrée,

sans calculer les corrections des quasiparticules dans l'approximation GW . Pour obtenir de bonnes approximations tout en évitant le calcul de GW , on peut utiliser des fonctionnels hybrides en DFT qui incluent une composante d'échange dans le potentiel d'échange-corrélation. Ces fonctionnels hybrides permettent d'obtenir des bandes interdites proches de celles calculées avec GW .

Un autre problème lié à l'utilisation de la supercellule est le calcul de l'écrantage statique dans le cadre de l'approximation de la phase aléatoire (RPA), qui est nécessaire pour résoudre la BSE. Pour alléger les calculs, nous avons développé une méthode de remappage de l'écrantage statique de la cellule primitive du wBN sur la supercellule. Cette méthode permet de résoudre la BSE pour la supercellule en utilisant les états obtenus par la DFT hybride et l'écrantage statique de la cellule primitive pure. L'avantage de cette approche est que l'écrantage statique de la cellule primitive est beaucoup plus facile à calculer. La procédure de remappage de l'écrantage de l'espace réciproque de la cellule primitive à l'espace réciproque de la supercellule a été mise en œuvre à l'aide d'un programme développé par l'auteur de cette thèse en collaboration avec le Dr. Fulvio Paleari, durant trois semaines au détachement S3 de l'Institut des Nanosciences du Conseil National de la Recherche Italien à Modène. Ce logiciel sera intégré dans la bibliothèque logiciel Yambopy pour le post-traitement du code `yambo` .

Cette méthode a ensuite été combinée avec les approches les plus couramment utilisées dans la littérature pour étudier l'émission des états défectueux. Ces méthodes adaptent la théorie de Franck-Condon aux systèmes de défauts et se basent sur la construction d'un diagramme de configuration de coordonnées (CCD). Les types d'excitations considérés peuvent inclure des transitions internes (entre états défectueux) ou des transitions de capture radiative (entre états défectueux et bande de conduction). La méthode de calcul utilisée pour traiter ces transitions est souvent la méthode DFT à occupations contraintes, appelée ΔSCF. Cependant, cette méthode présente plusieurs problèmes de convergence et essaie de décrire les excitations tout en restant dans le cadre de la DFT, qui est essentiellement une théorie de l'état fondamental, inadaptée au traitement des états excités. De plus, nous nous sommes aperçus que il n'est pas clair comment la méthode ΔSCF peut prendre en compte les effets de Jahn-Teller dans les systèmes étudiés.

Dans le chapitre 3, nous presenterons nos resultats pour le wBN pur dans le cadre de la DFT et de la MBPT. En partant des positions atomiques trouvées dans la littérature pour le wBN , nous avons mené les études de convergence sur le nombre de points $\boldsymbol{k}$ et l'énergie de coupure. Nous avons ensuite obtenu, pour des pressions comprises entre 0 et 200 kBar (à des intervalles de 50 kBar), les structures optimisées grâce à l'optimisation de géométrie effectué dans le cadre de la DFT. Pour chacune des géométries obtenues aux différentes pressions, nous avons dérivé la structure de bande du matériau en utilisant l'approche GW et nous l'avons comparée à celle obtenue par DFT (le cas de 0 kBar est illustré dans le panneau a) de la Fig.0.2). Comme prévu, la bande interdite s'est élargie avec la correction des quasiparticules par rapport à celle obtenue avec la DFT. Cependant, nous avons remarqué que, tandis que la bande interdite directe (la transition directe se produisant au point X_{GW} situé sur la direction Γ-M de l'espace réciproque) augmentait avec la pression, la bande interdite indirecte

(la transition indirecte se situant entre les points Γ et K) diminuait (Fig.0.2 panneau b). Ce comportement inverse peut s'expliquer par les contributions différentes des états $2s$ et $2p$ du bore et des états $2s$ et $2p$ de l'azote à la structure de bande aux points $\boldsymbol{k}$ impliqués dans les transitions directe et indirecte.

De même, le DFPT nous a permis d'étudier les modes de phonons le long d'un chemin de points à haute symétrie dans la zone de Brillouin (Fig. 0.2 panneau c). Nous avons également remarqué que, lorsque les pressions augmentent, les énergies des modes de phonon aux points Γ et K augmentent en fonction de la réduction de la distance entre les atomes.

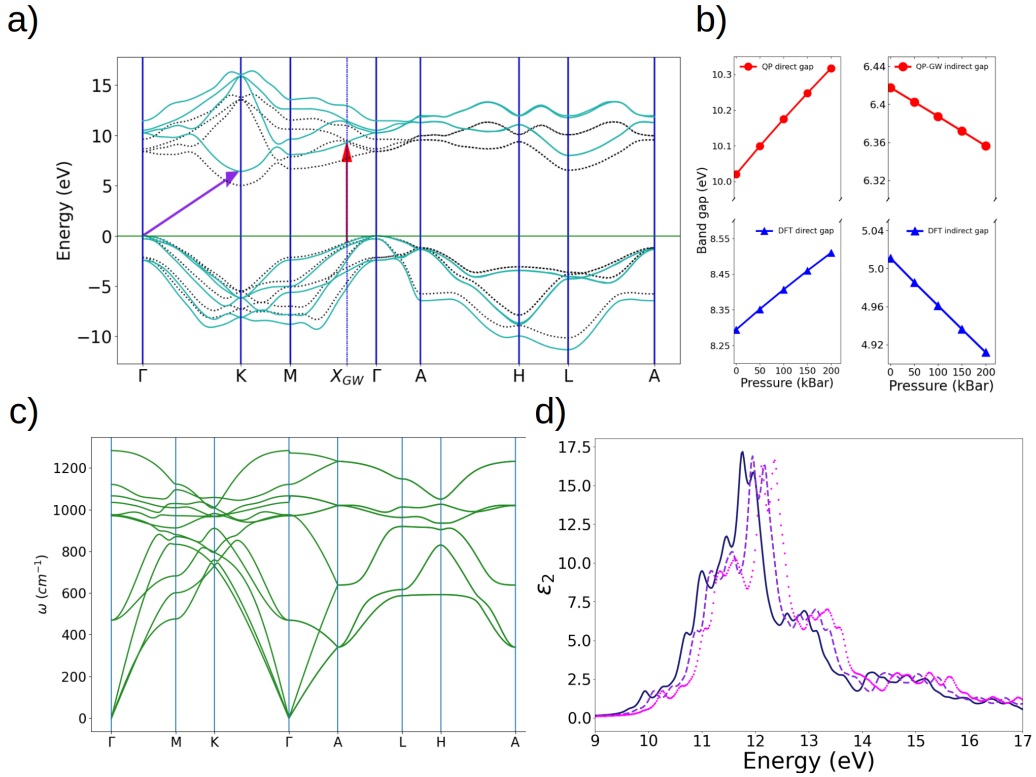

Figure 0.2. – Panneau a) : structure à bande éléctronique à 0 kbar obtenue dans la DFT (ligne pointillée noire) et avec la correction de quasiparticule (ligne pleine verte). La flèche rouge représente la transition directe, la flèche violette est la transition indirecte ; panneau b) évolution de la bande interdite directe et indirecte en fonction de la pression au niveau de la DFT (bleu) et avec la correction de quasisparticule (rouge) ; panneau d) : dispersion phononique à 0 kBar ; panneau d) : spectre de d'absorption obtenue avec la BSE à 0 (linge bleue continue), 100 (ligne violette discontinue)et 200 (ligne fuchsia pointillée) kBar.

Dans le panneau d) de la Fig. 0.2, nous présentons le spectre d'absorption, calculé à l'aide de l'équation de Bethe-Salpeter (BSE) pour trois des pressions examinées. Le décalage vers des énergies plus élevées avec l'augmentation de la pression peut être attribué à la croissance de la bande interdite directe qui élève les énergies des excitons.

De plus, en étant un système à bande interdite indirecte, nous avons étudié la luminescence assistée par les phonons. La transition qui nous intéresse est la transition indirecte Γ →K. Avec 12 modes de phonon dans le wBN , nous avons construit 12 supercellules, chacune étant configurée pour que le point K soit remappé en Γ. Chaque supercellule est associée à un mode de phonon spécifique, et les atomes y ont été déplacés selon le mode phonon correspondant. Pour chaque mode, l'Hamiltonien de la BSE a été diagonalisé en utilisant l'écrantage statique à l'équilibre. Afin d'éviter la nécessité d'appliquer la méthode *GW* à chaque supercellule, nous avons opté pour une correction "à ciseaux" afin de reproduire la position de l'exciton au point K, avec un décalage rigide de la structure de bande obtenue par DFT. Cette approche nous a permis de calculer les éléments de la matrice de dipôle, dont la dérivée seconde est utilisée dans la formule de Roosbroeck-Shockley pour la luminescence avec couplage exciton-phonon.

Pour finir dans le chapitre 4, nous appliquons la théorie des défauts pour établir les diagrammes des énergies de formation des différents défauts examinés. Chaque défaut a été introduit dans une supercellule de dimensions $6 \times 6 \times 4$, avec un total de 576 atomes (575 dans le cas des lacunes). Nous avons ensuite réalisé une optimisation structurelle de ces supercellules contenant les défauts, en utilisant une fonctionnelle semi-local (non hybride) et en imposant divers états de charge. Pour chaque configuration, nous avons vérifié la présence éventuelle de niveaux dégénérés avec occupation fractionnelle, ce qui indique la manifestation de l'effet Jahn-Teller. Lorsque l'effet Jahn-Teller était détecté, nous avons procédé à une nouvelle optimisation de la structure en ajustant légèrement la position du défaut, permettant à la structure de relaxer vers un nouveau minimum de la surface d'énergie potentielle et d'éliminer la dégénérescence.

Une fois la dégénérescence éliminée, nous avons utilisé la structure optimisée pour calculer l'énergie totale au point Γ en employant la fonctionnelle hybride Gau-PBE, qui fournit une estimation du gap comparable à celle obtenue avec la méthode *GW* sur la cellule primitive. Les potentiels chimiques de l'azote, du bore, et du carbone (dans le cas des substituants) ont été déterminés en considérant leurs phases pures respectives. Étant donné la diversité des formes polymorphes disponibles pour ces éléments, nous avons choisi d'utiliser le bore α-rhomboédrique, l'azote gazeux et le diamant comme réservoirs chimiques pour nos calculs. Pour chaque espèce chimique, nous avons réalisé des tests de convergence sur l'énergie de coupure et le nombre de points $\boldsymbol{k}$, suivi de relaxations structurelles et du calcul de l'énergie totale en utilisant la fonctionnelle hybride.

Enfin, les corrections pour les défauts chargés, présentées au chapitre 1, ont été calculées en utilisant le schéma de Freysoldt, Neugebauer et Van de Walle avec le programme `sxdefectalign`. Les énergies totales des supercellules, les potentiels chimiques, et les corrections pour les limites diluées ont été intégrés dans les calculs des énergies de formation pour élaborer les diagrammes en fonction du potentiel chimique électronique. Ces diagrammes couvrent les conditions de richesse en bore (pauvre en azote) et de richesse en azote (pauvre en bore). Les résultats sont illustrés dans la Fig. 0.3.

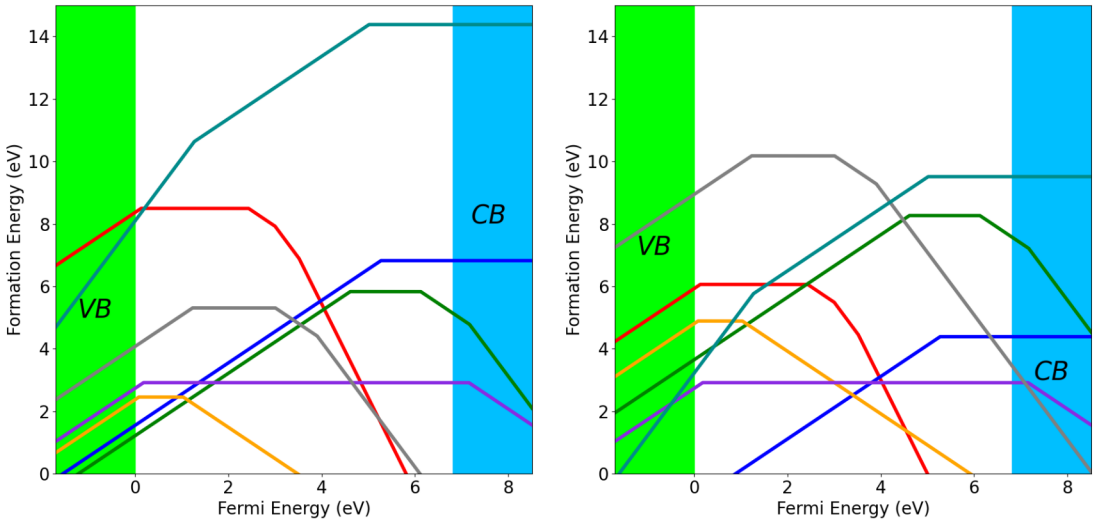

Figure 0.3. – Énergies de formation dans le limite riche en Bore (gauche) et riche en Azote (droite) obtenue avec la fonctionnelle hybride. Rouge : V_B, vert : V_N, bleu : C_B, jaune : C_N, violet : C_2, gris : B_N, cyan : N_B.

En plus des énergies de formation, nous avons pu dériver les niveaux de transition de charge (CTL) en utilisant à la fois la fonctionnelle semi-local et la fonctionnelle hybride, puis comparer les résultats en les rapportant à une échelle énergétique absolue, où le zéro a été défini comme l'énergie du vide.

Pour chaque défaut, l'analyse des niveaux monoélectroniques a permis de déterminer leur localisation ou leur hybridation avec les états du matériau massif, ainsi que les symétries et déformations induites dans la structure cristalline. En ce qui concerne les lacunes, l'aimantation du spin et le remplissage des niveaux ont été interprétés à l'aide d'un modèle basé sur les liaisons brisées « pendantes ». Pour les substituants et les antisites, nous avons construit et rempli les orbitales hybridées sp^3. Nous avons ensuite analysé l'ordre de remplissage des niveaux, leur évolution en fonction de la charge du défaut, ainsi que leur dégénérescence. Enfin, les isosurfaces des $|\psi|^2$ ont été visualisées dans l'espace réel.

Les transitions analysées à l'aide de la méthode ΔSCF ont été examinées pour certains niveaux spécifiques. Nous avons étudié les transitions entre les états défectueux et les états situés au fond de la bande de conduction pour les défauts C_B^0, C_N^- ainsi que pour le dimère $(C_N C_B)^0$. Pour chacune de ces transitions, des diagrammes de Franck-Condon ont été construits, permettant d'identifier les décalages Stokes et Antistokes.

Cette approche a été comparée à une analyse alternative basée sur la méthode de Bethe-Salpeter Equation (BSE). En partant des états de Kohn-Sham obtenus par DFT avec une fonctionnelle hybride et en utilisant le programme de remappage précédemment mentionné, il a été possible de résoudre la BSE pour les supercellules avec défauts, en contournant donc le calcul *GW* et le calcul de l'écrantage statique

sur la supercellule.

Les résultats montrent que, pour le dimère, les états excitoniques associés aux états de défaut ne contribuent pas de manière significative au spectre d'absorption par rapport aux états dans le bulk. En revanche, ces états de défaut deviennent plus prononcés dans le cas du défaut C_N^-.

En conclusion, nous avons utilisé la Théorie Perturbative à N-corps pour obtenir des propriétés optiques précises pour le nitrure de bore wurtzite, en utilisant la DFT comme point de départ et en incluant les effets excitoniques.

Par la suite, nous avons réalisé une étude exploratoire pour évaluer le potentiel du wBN en tant qu'hôte de défauts, en examinant sa déformation structurelle et l'évolution de ses propriétés optiques à l'aide de différentes méthodes. Ces résultats offrent non seulement une meilleure compréhension du rôle des inclusions de wurtzite dans les spectres expérimentaux de cBN , mais ouvrent également la voie à des applications potentielles du wBN dans les domaines de l'optoélectronique et des technologies quantiques.

Remerciements

Writing this thesis would not have been possible without the people who supported me during these three years of PhD programme. Of course, this journey would not have even started if Elena had not believed in me in the first place, choosing me for this job and introducing me in the vast and multifaceted world of theoretical spectroscopy and *ab initio* methods. Thank you for everything you have taught to me, for your guidance and support as a thesis director and, more importantly, for the patience whenever I got stuck during the research process. I thank Cédric for the nice discussions at work concerning physics, teaching and bureaucracy and for his invaluable advices whenever I had to prepare a presentation. I also want to thank the rest of the H2M team Stéphane, Céline, Pascale, Jennifer, Jordan and Dmytro, together with all the members of the administration and technical staff of the PIIM laboratory for creating a very friendly working environment such that I have been happy to come to my office every morning. I am very thankful to Claudio Attaccalite for his priceless help on some aspects of exciton physics and the `yambo` code, to Fulvio Paleari for the time he dedicated to my training on the Yambopy Python classes, the technicalities of the remapping procedure and for the nice discussions on Many-Body Perturbation theory during my stay in Modena, and to all the members of the jury of my PhD defence. I want to express my most heartfelt thanks to all my colleagues and friends, wherever they are now, either here in France or around the world. My colleagues in Marseille with whom I embarked on this journey, Mattia (who introduced me to the lost cause and yet still alive world of film photography and is a stakeholder of the Coffee Machine Investment Fund), Federica, Anass, Surabhi, Daniele, Paco, Alodie (who is also a stakeholder of the Coffee Machine Investment Fund), the three "M" Matheus, Matthieu and Matisse, Ana, Akbar, Julien, Madhu, Yosvany, Aleksandr, Jay, Mun, Céline, Daniel, José, Silvia, Simone Grillo and Pierre Lechifflart. I am glad that I had the honour to have lunch and chat with you and drink beer together in CoursJu. My PhD would not have been such a positive and cool experience without you; Federica, who taught me how to survive in a quirky and yet wonderful city like Marseille, thanks for the visits at the museums, the bicycle trips and the hikes on the Calanques; all my friends who have always been there for me during and before my PhD programme, Scar, Giulio, Nicholas, Harisa, Matteo, Fabiola, Accia and Elena, Riccardo "the Pichua", Tax, "Unfortunately" Fra', Giacomo, Simone, Diego, Francesco, Cristina, Betta, Gigio, Maria, Mattia "the Menk", Lucrezia, Bożena, Kaizad, Rosa, Anna, Luigi, Danny, Lappo and Migliozzi. Finally I would like to show my gratitude to all my family, my parents and my brother for being always there for me and for always endorsing my curiosity and thirst for knowledge.

I acknowledge the French National Agency of Research (ANR) for funding this project (ANR-20-CE47-0009). The Centre de Calcul Intensif d'Aix-Marseille (Mésocentre d'Aix-Marseille Université) and the TGCC are acknowledged for granting access to their high performance computing resources. I acknowledge A. Saúl and K. Boukari for the management of the computer cluster Rosa at the Centre Interdisciplinaire de Nanoscience à Marseille (CINaM). I am also grateful to Ádám Gali, Gergő Thiering and Anton Pershin for fruitful discussions on defect physics.

Table des matières

Affidavit 2

Liste de publications et participation aux conférences 3

Abstract and keywords 4

Résumé et mots-clés 5

Résumé étendu 7

Remerciements 17

Table des matières 19

Table des figures 21

Liste des tableaux 28

Introduction 30

1. Ground state properties and methodologies 34
- 1.1. The Many-Body problem . . . 34
  - 1.1.1. Adiabatic approximation . . . 35
  - 1.1.2. Hartree - Fock method and symmetry properties . . . 36
- 1.2. Density Functional Theory . . . 37
- 1.3. Kohn-Sham DFT in practice . . . 41
- 1.4. Density Functional Perturbation Theory . . . 46
- 1.5. Point defects and supercell approach . . . 48
  - 1.5.1. Formation energy and charge transition levels . . . 50
- 1.6. Conclusions . . . 58

2. Excited states properties 59
- 2.1. Many Body Perturbation Theory and the *GW* approximation . . . 59
  - 2.1.1. Green's function formalism . . . 61
  - 2.1.2. The GW approximation . . . 71
- 2.2. The Bethe-Salpeter equation . . . 73
- 2.3. Optics in practice . . . 74
- 2.4. Defect optical properties and the Franck-Condon model . . . 78
- 2.5. Supercell remapping of the screening . . . 83
- 2.6. Conclusions . . . 86

3. Study of pristine *w*BN **87**
3.1. A review of wurtzite Boron Nitride . . . 87
3.2. Preliminary study and convergence tests . . . 90
3.3. Optimization of the geometry . . . 91
3.4. Vibrational properties . . . 92
3.5. Electronic properties . . . 97
3.6. Optical properties . . . 100
3.7. Phonon-assisted luminescence . . . 104
3.8. Conclusions . . . 106

4. Thermodynamics and optical properties of defects in *w*BN **109**
4.1. Computation of the formation energies . . . 109
4.1.1. Structural relaxation and total energy . . . 109
4.1.2. Chemical potential . . . 112
4.1.3. Dilute limit corrections . . . 115
4.2. Results and discussion . . . 118
4.2.1. Vacancies . . . 120
4.2.2. Carbon substitutionals . . . 126
4.2.3. Carbon dimer . . . 128
4.2.4. Antisites . . . 130
4.3. Optical properties of defects . . . 134
4.3.1. Optical properties using the ΔSCF approach. . . . 134
4.3.2. Remapped screening BSE approach . . . 137
4.4. Conclusions . . . 142

Conclusion **146**

A. Calculation of the vacuum level **148**

Table des figures

0.1. Schéma de résolution auto-cohérente de l'hamiltonien auxiliaire de Kohn-Sham, tel qu'il est utilisé dans le code numérique Quantum Espresso. 9

0.2. Panneau a) : structure à bande éléctronique à 0 kbar obtenue dans la DFT (ligne pointillée noire) et avec la correction de quasiparticule (ligne pleine verte). La flèche rouge représente la transition directe, la flèche violette est la transition indirecte; panneau b) évolution de la bande interdite directe et indirecte en fonction de la pression au niveau de la DFT (bleu) et avec la correction de quasisparticule (rouge); panneau d) : dispersion phononique à 0 kBar; panneau d) : spectre de d'absorption obtenue avec la BSE à 0 (linge bleue continue), 100 (ligne violette discontinue)et 200 (ligne fuchsia pointillée) kBar. 13

0.3. Énergies de formation dans le limite riche en Bore (gauche) et riche en Azote (droite) obtenue avec la fonctionnelle hybride. Rouge : V_B, vert : V_N, bleu : C_B, jaune : C_N, violet : C_2, gris : B_N, cyan : N_B. 15

1.1. Scheme of the SCF iterative algorithm used by standard DFT codes such as Quantum Espresso to solve the Kohn-Sham equations. Index i denotes the ith iteration. 42

1.2. Reciprocal lattice for a generic hexagonal crystal with a dense $\boldsymbol{k}$-grid in the 1BZ. The vector $\boldsymbol{G}$ connects a periodic image BZ with the 1BZ in the center. The $\boldsymbol{G}_{max}$ vector lenght determines the E_{cut} corresponding to the blue circle and the last $\boldsymbol{G}$ components included in the sum Eq. 1.33. All the $\boldsymbol{G}$ outside of the blue circle are not included in the calculations. 44

1.3. Pseudopotential and s wavefunctions computed for Mo, adapted from [45]. 45

1.4. 2D projected schematic depiction for several types of defects and their notation in a bi-atomic crystal lattice like BN. Red atoms correspond to boron, blue atoms represent nitrogen, black dots stand for carbon atoms, white atomic sites depict vacancies. Interstitial and defects more complex than the trimers are not showed. 49

1.5. Illustrative example of a formation energy diagram for a defect that can be in charge state $q = -1, 0, 1$. Each dashed line corresponds to a charge state q. The dashed lines become solid black as they enter in the stability band gap range and they are the lowest. The CTLs $\epsilon(+/0)$ and $\epsilon(0/-)$ are also reported. 51

2.1. Excitation process of an electron in ARPES (panel a)) and Inverse ARPES (panel b)). If the electron is not excited into a free state one has absorption and the electron e^- and the positive hole h^+ can form a bound exciton (panel c). Panel d) is a pictorial representation of an electron and a quasielectron. 60
2.2. Evolution of the poles of the spectral function when we pass form the non interacting system (left) to an interacting system (right), also satellites due to plasmons and other excitations appear. 65
2.3. Easy-to-remember representation of Hedin's equations. 71
2.4. Feynamn diagrams of the BSE. 74
2.5. GW method workflow as implemented by the `yambo` code. 76
2.6. Pictorial band structure at DFT level (a), with quasiparticle correction (b) and excitonic level after solution of the BSE (c). The E_b is the binding energy of the electron and hole in the exciton. Note how the quasiparticle band gap E_{gap}^{qp} is larger than the original DFT band gap E_{gap}^{DFT}. The excitonic level E_{exc} is obtained as eigenenergy from diagonalization of the BSE in Hamiltonian form Eq. 2.78. 77
2.7. BSE workflow. Note that in principle it would be possible to calculate the BSE Hamiltonian and kernel by using a static screening ϵ in GW-RPA approximation rather than just RPA. It would be also possible to calculate the kernel without including the W. 77
2.8. Panel a) : level scheme obtained via hybrid-DFT for C_B^0 in wBN; panel b) : $|\psi|^2$ isosurface of a defect state; panel c) : same isosurface of panel b) from a different angle; panel d) : isosurface of a bulk state. 79
2.9. Franck-Condon model for a generic system with its connection with the absorption and emission spectra. 80
2.10. Relation between the primitive (red) and supercell (green) reciprocal lattice vectors and momenta. Panel a) : illustrative examples of a $\boldsymbol{G}$ and a $\boldsymbol{g}$ vector in a 2D case and a 2×2 supercell; panel b) : relation between the $\boldsymbol{Q}$, $\boldsymbol{q}$, $\boldsymbol{g}$, $\boldsymbol{G}$ and $\boldsymbol{g}_{\boldsymbol{Q}}$ vectors. 84
2.11. Absorbance spectrum obtained using BSE on top of DFT using the remapped static screening (blue solid line) and the screening computed directly on the supercell (orange solid line). Also the independent particle spectra for the two cases are reported (dashed lines). 85

3.1. Prospects of wurzite primitive cell in three different orientations : the reader's eye sight line is perpendicular to the x-axis (left panel), the y-axis (central panel) and parallel to the z-axis (right panel). Blue atoms represent nitrogen while brown atoms represent boron. The red arrows are the crystal primitive lattice vectors $\boldsymbol{a}_1$, $\boldsymbol{a}_2$ and $\boldsymbol{c}$. 88
3.2. Vectors used in the Miller-Bravais 4-indices notation for hexagonal cells. The $(10\bar{1}0)$ is the blue arrow in the left panel. 89

3.3. Convergence of the total energy per electron with respect to the cut-off energy (left) and the $\boldsymbol{k}$-point grid used (right). The 0 is set to the minimum value in order to highlight the energy differences between the calculations 91
3.4. Cell parameters as functions of pressures. a (red circles) is the basal plane lattice parameter of the hexagonal primitive cell, while c (blue triangles) is the lattice parameter in the (0001) direction. Our theoretical values are compared with the experimental a (orange circles) and c (deepskyblue triangles) parameters taken from Ref. [92]. 92
3.5. The nine optical phonon modes for the C_{6v} point group. Note that E modes are doubly degenerate. 94
3.6. Left panel : path covering the high symmetry points in the 1BZ; right panel : computed phonon dispersion at 0 kBar, note the three acoustic modes with 0 frequency at Γ. The highest level is made of two almost degenerate bands obtained by applying the LO-TO splitting. 95
3.7. Left panel : energies and identification of the optical phonon modes at Γ as a function of pressure; right panel : phonon density of state computed at 0 kBar (green solid line), 200 kBar (yellow dashed line). The computed phonon DOS is compareed with the experimental one (blue dotted line) taken from Ref. [108]. 96
3.8. Top left panel : band structure for 0 kBar pressure at DFT (black dotted) and quasiparticle level (light green solid line). The indirect (purple) and direct (red) transition are highlighted with two arrows; top right panel : evolution of the direct and indirect gap at different pressures at both DFT and quasiparticle level; bottom panel : a comparison of the quasiparticle band structure computed at 0 (blue) and 200 (red) kBar. 98
3.9. DFT band structure at 0 kBar with wavefunctions projected on the atomic orbitals of B and N. A colormap associates each color to different weights of contribution from one atom and the other. 99
3.10. BSE spectra obtained for different numbers of polarisation bands and $\boldsymbol{k}$-grids. Top panels : imaginary (left) and real (right) part of the dielectric functions obtained with 100 polarization bands using a $9 \times 9 \times 6$ (light green), a $12 \times 12 \times 8$ (coral orange) and a $15 \times 15 \times 10$ (dark khaki) $\boldsymbol{k}$-grid; bottom panels : imaginary (left) and real (right) parts of the BSE dielectric functions obtained with a $12 \times 12 \times 8$ $\boldsymbol{k}$-grid using 50 (blue violet) and 100 (goldenrod) polarization bands. 101
3.11. Different BSE spectra at 0 kBar obtained considering different intervals of valence and conduction bands in the computation. Indigo : four valence bands and 2 conduction bands; blueviolet : three valence bands and 4 conduction bands; mediumslateblue : 3 valence bands and three conduction bands; fuchsia : two valence bands and two conduction bands. For all the calculations 50 polarization bands with a $12 \times 12 \times 8$ $\boldsymbol{k}$-grid have been used. 102

3.12. Real (left panel) and imaginary (right panel) parts of the dielectric spectra obtained using the BSE at 0 (solid navy blue), 100 (dashed purple) and 200 kBar (dotted fuchsia). 102
3.13. Imaginary part of the dielectric function computed at 0 kBar using the BSE (black solid line), in RPA independent particle approximation (yellow dashed dotted line) and in independent GW quasiparticle approximation (red dotted line). The blue dashed line is the measured dielectric function presented in Ref. [102]. 103
3.14. Excitonic wavefunction for the first five excitons at 0 kBar. Top left panel : first non degenerate dark state ; top right panel : second and third degenerate dark excitons ; bottom center : fourth and fifth degenerate bright excitons. Since the exciton is rather delocalised it has been represented on an expanded $7 \times 7 \times 3$ supercell. The reader's eyesight is parallel to the (0001) direction of the crystal. 105
3.15. Phonon energies at K point as functions of the pressure. 106
3.16. wBN supercell used to refold the K point into Γ to study he phonon-assisted luminescence. 107
3.17. Luminescence spectra obtained by use of the Roosbroeck-Shockley formula. Panel a) : average over the three directions ; panel b) : contributions with xy polarisation ; panel c) : contributions with z polarisation . . . 108

4.1. Depiction of the static Jahn-Teller distortion for the first neighbours of the vacancy V_B^- on the (0001) bilayer (panel a)) and from a random point of view (panel b)). The atomic displacement from the unstable high symmetry configuration are depicted as blue arrows. 112
4.2. Workflow followed to compute the relaxed structures and the total energies. 113
4.3. Pristine phases for the atoms involved in the formation of the defect studied. Panel a) : α-rhombohedral boron ; panel b) : nitrogen molecule N_2 ; panel c) : diamond. 114
4.4. Alignment for the potentials computed by `sxdefectalign` in the three directions for the B_N^{2-}. The green line is the defective supercell potential referenced to the potential of the bulk $V_{def} - V_{bulk}$. The blue line is the long range potential computed using the model charge presented in Eq. 1.85. The yellow line is the difference between the two, determining the alignment (black dashed line) where it reaches a plateau far from the defect. 116
4.5. Formation energy diagrams at PBE level (top row) and Gau-PBE level (bottom row) in the Boron (left column) and N-rich limit (right column). Red : V_B ; green : V_N ; blue : C_B ; yellow : C_N ; purple : CC ; grey : B_N, dark cyan : N_B. The green and blue bands on the sides correspond to the valence and the conduction band, respectively, of the bulk pristine. . . 119

4.6. CTLs at PBE (on the left of each plot) and Gau-PBE level (on the right of each plot). The blue area is the conduction band and the yellow area is the valence band of the bulk. 120
4.7. Interatomic distances between the first neighbours of the generic vacancy V forming a tetrahedron around the defect with edges lying on the (0001) plane (panel a)) and out of the (0001) plane (panel b)). 121
4.8. V_B orbitals filling scheme to predicts the magnetisation m for the different charge states in Bohr magneton units. 122
4.9. V_B one-electron levels at Gau-PBE level at different charge states. A black dot represents an occupied state while a blank dot represents an empty state. 123
4.10. z-axis prospect of the a state in charge states $q = -3$, $q = -2$ and $q = -1$ of V_B, the asymmetry of the isosurface can be clearly noticed (circled in red). 124
4.11. Left panel : $|\psi|^2$ of the state with spin up occupied by one of the excess electrons in V_B^0. The other two states present the same degree of delocalization ; right panel : spin polarization for the charge states $q = 0$. 124
4.12. V_N filled dangling bond orbitals and their respective magnetisation m, for the different charge states, in Bohr magneton units 125
4.13. V_N one-electron level scheme obtained from hybrid functional theory. Yellow and blue areas are the valence and the conduction bands respectively. Red and blue lines correspond to the spin up and spin down channels respectively. Black dots are the occupied states. Empty dots are the empty states. 125
4.14. $|\psi|^2$ of the in-gap states for V_N^0, projected on the xy plane (top row) and on the plane perpendicular to the $\boldsymbol{a}_1$ direction (bottom row). Left column shows refers to the singly-degenerate state, center and right columns to the e_x and e_y states. The overall shapes do not change significantly in other negative charge states. 126
4.15. First neighbours tetrahedral cage around a carbon substitutional (brown). The distances used in Tab. 4.6 are also defined. 127
4.16. Filling scheme for the sp^3 hybridized orbital for C_B (left) and C_N (right). 128
4.17. Kohn-Sham one-electron levels for the C_B defect. 129
4.18. Kohn-Sham one-electron levels for the C_N defect. 129
4.19. Definitions for the interatomic distances in the C_BC_N. 130
4.20. One-electron level scheme for the carbon dimer obtained via DFT with the Gau-PBE functional. Since for different charge states only minor readjustements occur and there is no structure deep in the gap, only 4 states in proximity of the VBM and the CBM are considered. 131
4.21. Carbon dimer charge distribution. 131
4.22. B_N hybridization and filling scheme. 132
4.23. One-electron levels obtained for the B_N defect with the Gau-PBE functional. The green arrow denotes a transition which might be useful in quantum technologies. 133

4.24. $|\psi|^2$ for the one-electron states in the gap of B_N. Panel a), b) and c) : states at charge state B_N^0. We chose to show the isosurfaces at $q = 0$ by way of illustration, since the same shape is retained for charge states $q = -2$ and $q = 1$; panel d), e) and f) : one-electron states in the gap for $q = -1$. 134
4.25. Orbital filling scheme and level structure for the N_B defect. 135
4.26. Level schemes for the transitions considered for the ΔSCF approach to luminescence. The green arrows highlight the states where we constrain the occupation. 136
4.27. Comparison between the absorbance spectra obtained via BSE on a primitive cell using one conduction and one valence band (orange), on a primitive cell using one conduction and two valence band (navy blue) and on a supercell using a remapped screening using 144 valence and 144 conduction bands (clear blue). 138
4.28. Migration process of bands during refolding. On the left the bands included in BSE in the primitive cell and on the right the corresponding folded levels in the supercell. In both panels the colours are used to distinguish the bands and the corresponding levels from which they have origin. Solid and dashed lines denote bands and levels included and not included in the BSE, respectively. 139
4.29. Absorption spectra for the C_2^0 defect using 100 bands for BSE diagonalization. The static screening used has been remapped (orange) and calculated directly on the supercell using 1585 polarisation bands (clear blue). Dashed lines are the independent particle spectra obtained from BSE without including the screening (colours are overlapped). 140
4.30. C_2^0 absorption spectra using different number of bands in the BSE hamiltonian. Solid lines report the spectra obtained using 100 (clear blue), 110 (orange), 120 (dark blue). Exciton positions were obtained using the SLEPC algorithm (spectrum in dashed lines) and are represented as red vertical lines. 141
4.31. C_2^0 absorption spectra obtained using in the BSE 100 (clear blue), 110 (solid orange), 120 (solid dark blue) and 288 bands (solid blue). Intensities for 100, 110 and 120 bands have been enhanced by 50 times. Also a comparison with the pristine material absorption computed using the remapped screening (dashed red) is reported. 142
4.32. Panel a) : band structure of the dimer (dashed line) and the pristine crystal (solid lines), computed at PBE level. Red flat lines correspond to defect states involved in the transitions discussed; panel b) : $|\psi|^2$ of the state #1155. 144
4.33. Optical spectra obtained using the remapped static screening and different ranges of bands for the C_N^{-1} defect. By increasing the number of bands the intensity of the structures at lower energies are enhanced. In the inset the same behaviour is showed in detail for the low energy excitons. 145

4.34. $|\psi|^2$ of the states involved in the excitons listed in Tab. 4.11 with the reader's eye sight line parallel to the (0001) direction. 145

A.1. The $(10\bar{1}0)$ direction (blue arrow) in the wurtzite structure. The reader's sightline is along the (0001) direction. 148
A.2. Series of transformations made to correctly arrange the wurtzite atoms in the orthohrombic primitive cell. a. b and c cell parameters are also visualized. 149
A.3. Three-steps procedure (from top to bottom) to build the supercell by adding the vacuum and reconstructing the non-polar surfaces. For reasons of space and clarity only 40 atoms are represented instead of 64. 150
A.4. Convergence of total energy per atom in the orthorhombic supercell with respect to the number of atoms. Vacuum distance is kept constant at 40 bohr. 152
A.5. Plot of the potential $V_{bulk}(z)$ at PBE (top panel) and Gau-PBE level for the bulk wBN supercell used as reference for the formation energies. . 153
A.6. Plot of the potential $V_{orth}(z)$ at PBE (top panel) and Gau-PBE level for the orthorhombic supercell. The dashed lines indicate $\overline{V}_{vac}$ (brown and navy blue) and $\overline{V}_{slab}$ (red and blue-violet) 154

Liste des tableaux

3.1. Atomic positions for the Wurtzite structure in crystal coordinates. . . . 88
3.2. Character table for C_{6v} symmetry group 93
3.3. Phonon modes at Γ and comparison with data from the literature. IR and Raman activity is also given. 95
3.4. LO-TO splittings computed in our phonon calculations. 96
3.5. Born effective charges and their resulting macroscopic dielectric tensors in their diagonal form. ϵ_∞ is defined as the average of the diagonal elements of the dielectric tensor Eq. 3.5 while $\Delta\epsilon_\infty$ is defined as $(\epsilon_\infty^{\parallel} - \epsilon_\infty^{\perp})/\epsilon_\infty$. Z^B is the average on the diagonal of the Born effective charges tensor and $Z^\star$ is the screened effective charge. 97
3.6. Difference between the band gaps computed with and without the quasiparticle correction. 97
3.7. Band gaps at 0 kBar obtained for different $\boldsymbol{k}$-grids and number of polarization bands. 100
3.8. Energies of the first bright excitons at different pressures and their binding energy. The values are also reported in the figure in the right panel where we report direct gap (star points), the exciton energies (triangles) and their difference, i.e. the binding energy (circles) 104

4.1. Reference chemical potentials and enthalpies for the pure phases considered in formation energy calculation at both PBE and Gau-PBE level (eV). 115
4.2. Limiting values for the chemical potentials at Both PBE and Gau-PBE level (eV). 115
4.3. Dilute limit correction computed at PBE level. The second, third and fourth columns report the plateaus manually detected in the three directions. The fifth column is the average. Last column reports the computed correction. Corrections for charge states $q = 0$ are identically 0 and do not appear in the table. 117
4.4. Dilute limit correction computed at Gau-PBE level. The meaning of each column is the same as Tab. 4.3. 118
4.5. Structural data for the boron and nitrogen vacancies after relaxation, in Å . The interatomic distances are defined in Fig. 4.7. When the Jahn-Teller distortion is present, we report also the same quantities after the degeneracy removal (with the superscript JT). 122

4.6. Structural data in Å for the carbon substitutionals, where the distances are defined in Fig. 4.15. Again, the distances distorted due to the Jahn-Teller effect are denoted by the JT superscript. 127
4.7. Interatomic distances for the carbon dimer. 130
4.8. Antisite-nearest neighbours interatomic distances in Å. 132
4.9. Results for the transitions studied using the ΔSCF approach. HO and LU labels denote the highest and the lowest unoccupied levels, respectively. 137
4.10. C_2^0 exciton analysis with numerical identifier of the one-particle states defining the corresponding electron-hole pairs. 143
4.11. C_N^{-1} exciton data and their composition in electron-hole pairs. 143

A.1. Convergence test with respect to the number of atoms and the thickness of the vacuum region. The last column reports the difference between the total energy per atom and the same quantity in the previous row, for a constant number of atoms. 151
A.2. Convergence data for the Gau-PBE calculation on the orthorhombic supercell. 153
A.3. Energies in eV (with both functionals) for the averaged potentials $\overline{V}_{bulk}$, $\overline{V}_{slab}$ and $\overline{V}_{vac}$, the HOMO and LUMO E_{VBM} and E_{CBM} and their absolute values E_{VBM}^{abs} and E_{CBM}^{abs} 153

Introduction

The economical, social, demographic and environmental challenges that mankind is facing can be tackled only if the great transformations that we are observing are accompanied by a great technological development. Semiconductor microelectronics plays an important role in this dynamics. We can safely state that today there is almost no device more complex than a lightbulb that does not include a chip as a component. Smartphones, photovoltaic panels, computers, LEDs, sensors etc. are all devices that rely on semiconductors.

The urge for smaller semiconductor devices which are more and more efficient steers a large part of today's research efforts in both the public and the private sector. The endeavour to which the microprocessor industry is committed is reducing the dimensions of the transistors in order to increase their density in integrated circuits, allowing at the same time a reduction of power consumption and a larger number of operation executed per second. This evolution towards smaller scales of the dimensions of the transistors follows the Moore's law which also implies that we are reaching a saturation limit in this miniaturization process.

The LED lightning technology is directly affected by the research on semiconductors. New materials with a band gap wider than more conventional platforms like Si and Ge are currently investigated as they enable the production of emitters and optoelectronic devices in the UV and deep-UV energy range [1].

At the moment we are assisting to a call for novel materials with new properties that can be tailored for a particular technological use. These requirements can now be fulfilled by engineering and conceiving new structures like for example 2D materials and heterostructures [2].

Among the possible ways of engineering a material, point defects in semiconductors constitutes a flourishing line of research. Defects are always present to some extent in a real crystal and they can not be avoided completely during the synthesis and the growth of a sample of any material [3]. It is commonly known that the presence of defects heavily affects the properties of the host material. Their presence can be both detrimental or advantageous for the human activity. They are responsible for the degradation of the performance and efficiency of a device because they can act as recombination centres (Shockley-Read-Hall recombination) that hinder for example the desired radiative emission in favour of heath dissipation [4, 5]. On the other hand, the presence of impurities is necessary for doping and tuning of the p and n conductivity in a semiconductor, which is the basis of the diode and transistor technology. Understanding the thermodynamics and the abundances of defects in a given material means understanding their possible manipulations.

Recently, point defects have also attracted interest as potential platforms for quan-

tum technologies (quantum information, computation and sensing). What makes defects appealing as potential qubits or single photon emitters (hereinafter "SPE") is their ability to introduce localized electronic states in the bulk electronic structure of the crystal host, with energy levels possibly in the band gap. From this point of view a defect resembles a sort of "trapped atom-like" system embedded in the host [6]. Ideally, these features should fulfil pivotal necessities of these technologies which are 1) storing quantum information in a defect for a time as long as possible and then 2) retrieve it thorough a spin-optical interface [6, 7]. Moreover a potential platforms should fulfil several criteria like, for example, a small coupling with the spin bath and being a paramagnetic state [8, 9, 10] . Several candidates have been studied using SiC [11, 12, 13], cubic boron nitride ("*c*BN ") [14, 15] and AlN [16] as host but unfortunately a defect with perfect qualities as qubit or quantum sensing platform has not been found yet. Even the best candidate (the negatively charged nitrogen-vacancy complex in diamond NV^- [17, 18]) is far from ideal and the quest for new defective systems is still going on.

In this context a major role is played by first principle *ab initio* calculations[19] which are methods capable of simulating the structural, vibrational, electronic and optical properties of materials without any external or experimental input except for the masses and the positions of the atoms. These methods on one hand can help in designing new material thanks to their predictive power, on the other hand they are capable of providing a *a posteriori* theoretical interpretation to the experimental data. *ab initio* calculations have a long history of success in studying defects hosted by several materials, like GaSe and GaS [20], ZnO [21, 22], TMDs like MoS_2 [23], hexagonal boron nitride ("*h*BN ") [24], defects in SiC and the NV^- colour centre in diamond. In particular, we mention the case of GaN [25, 26], which as been successfully used to produce blue LEDs and was worth the Nobel prize [27].

The present work is a totally *ab initio* study of boron nitride ("BN") in its wurtzite polymorph ("*w*BN ") and it aims at unveiling the electronic and optical properties of this material in its ideal pristine phase as well as a potential host for defects. The interest towards *w*BN stems from the remarkable properties that have been already investigated in other BN polymorphs, which are all wide band gap semiconductors. As already mentioned the cubic form *c*BN has been taken into consideration as a potential defect host for qubits, since the V_BO_N electronic level structure resembles that one of the NV^- in diamond. Moreover it is a superhard material, with hardness second only to diamond [28]. More importantly, *h*BN has been studied for its remarkable optical properties. It is a layered material where the layers are bonded by Van der Waals bonds. Its photoluminescence quantum yield is comparable to that one of ZnO (50%) [29] and for this reason it has been mistaken for a direct gap material [30]. Nonetheless, it has been proved to be an indirect gap material [31] and its high quantum yield has been explained with an exciton-phonon coupling mechanism [32]. Its bright emission in the UV range has been proved useful for example for disinfection purposes. Closely related to these materials is *w*BN that has been produced in macroscopic samples only recently [33] and is believed to have a hardness comparable to that one of *c*BN. For this material we can therefore envisage implementations in optoelectronic devices

in harsh conditions. Moreover, its wide band gap makes this material interesting as a defect host, and its point symmetry different from that one of *c*BN offers new opportunities for defect-induced level structures. Lastly, even though not many experimental studies have been already conducted on single *w*BN crystals, it is commonly found as small domains in *c*BN samples, thus potentially altering its electronic properties. Therefore an *ab initio* study of *w*BN may indirectly help in interpreting the experimental data concerning *c*BN [34].

Structure of the thesis

This thesis is structured as follows. In Chaps. 1 and 2 we outline the theoretical and mathematical methodologies that we are going to use to study the material with and without defects.

In particular, Chap. 1 is devoted to the ground state properties. We define the many-body problem in solid state physics and provide a non-exhaustive introduction to the Density Functional Theory ("DFT") approach. We will take the point of view of a DFT code user, and discuss some subtilities of the implementation of this theory. We will also briefly review Density Functional Perturbation Theory ("DFPT") in order to treat the lattice dynamics and compute the vibrational properties of a crystal. Finally we outline the formation energy formalism and the supercell approach to defective materials.

In Chap. 2 we move our focus to the optical properties, which by definition deal with excited states. Since the electronic excitations are not well described within DFT we introduce the Many-Body Perturbation Theory ("MBPT") along with the Green's function formalism and the concept of quasiparticle. The particular flavour of MBPT which we will discuss is the *GW* approximation and we will see that this technique is capable of giving accurate electronic band structures. The *GW* technique also serves as a good starting point to study the optical properties by solving the Bethe-Salpeter equation ("BSE") which allows to include the excitonic effects. The coupling mechanism between excitons and phonons is then briefly illustrated. Finally we discuss the theory of the radiative transitions in the presence of defects using the Franck-Condon configuration coordinate ("CCD") formalism and introduce an alternative technique based on the remapping of the screening from a primitive cell to a supercell.

The second part of the thesis is made by Chaps. 3 and 4 where we apply the techniques introduced so far and discuss the results.

Chap. 3 is devoted to the vibrational, electronic and optical properties of *w*BN in its pristine form. We explore the phonon modes, the quasiparticle corrected electronic band structure and we show that this material is an indirect wide band gap semiconductor. The excitons and the dielectric functions are also studied by mean of the BSE. A particular emphasis is put on the behaviour of the studied quantities on the pressure, since *w*BN is the result of a high pressure-induced phase transition. Finally we calculate the phonon-assisted luminescence spectrum.

Chap. 4 instead is concerned by our study of the defective systems. For each defect studied we explore the formation energy, the Charge Transition Levels ("CTL"), the electronic properties and the defect-induced structural deformation on the host. The optical properties of some selected defects are studied by using the ΔSCF approach in the CCD formalism. The difficulties encountered are partially overcome by solving the BSE using the remapped screening from the primitive cell which allows to find in good approximation the absorbance spectrum of the defective systems. In the conclusions we summarize the results obtained and provide some perspective for further developments.

1. Ground state properties and methodologies

In this chapter we introduce the theoretical framework that we will use to study the ground state properties of *w*BN and the thermodynamics of point defects. In Sec. 1.1 we define the problem that we are tackling in the study of a general crystal structure, which is a many-body system, and explain the adiabatic approximation. In Sec. 1.2 we provide the theoretical foundations of the Density Functional Theory ("DFT"), which is the cornerstone of many *ab initio* methods that have become the standard methodologies in physics, material science, chemistry etc. and has a history of success, as well as some shortcomings. Sec. 1.3 explains how DFT is generally implemented in codes like Quantum Espresso [35, 36] to simulate a crystal electronic structure. Few words are spent in Sec. 1.4 to show, without going into details, some generalities of Density Functional Perturbation Theory (DFPT) and its use to study the vibrational properties of materials in the context of DFT. In Sec. 1.5 we will finally introduce the physics of defects and explain how one can use the mathematical tools developed in the previous sections to conduct a study on a defective system.

1.1. The Many-Body problem

The solid state problem is a many body problem, meaning that in principle, for N electrons of indices $i = 1, ..., N$ and K nuclei of indices $I = 1, ...K$, we have to diagonalize the Hamiltonian

$$\hat{H}_{tot} = \hat{T}_e + \hat{T}_n + \hat{V}_{en} + \hat{V}_{nn} + \hat{V}_{ee} \tag{1.1}$$

which can be explicited as

$$\hat{H}_{tot} = -\hbar^2 \sum_i \frac{\nabla_i^2}{2m} - \hbar^2 \sum_I \frac{\nabla_I^2}{2M_I} - \sum_{i,I} \frac{Z_I e^2}{|\boldsymbol{r}_i - \boldsymbol{R}_I|} + \frac{1}{2} \sum_{I \neq J} \frac{Z_I Z_J e^2}{|\boldsymbol{R}_I - \boldsymbol{R}_J|} + \frac{1}{2} \sum_{i \neq j} \frac{e^2}{|\boldsymbol{r}_i - \boldsymbol{r}_j|} \tag{1.2}$$

where m and $\boldsymbol{r}_i$ are the masses and positions of the electrons, Z_I, M_I and $\boldsymbol{R}_I$ are the atomic number, mass and position of the nuclei, respectively. e is the elementary electric charge and $\hbar$ is the Planck constant. The Laplacians ∇_i^2 and ∇_I^2 are understood to be with respect to the electron and nuclei positions. The terms $\hat{T}_e$ and $\hat{T}_n$ of Eq. 1.1 are the kinetic energy of electrons and nuclei, $\hat{V}_{en}$ is the electron-nucleus attraction and the last two terms $\hat{V}_{nn}$ and $\hat{V}_{ee}$ are the electron-electron and nucleus-nucleus repulsions, respectively, where the $\frac{1}{2}$ avoids double counting of the same pair of particles. Unfortunately the Hamiltonian Eq. 1.1 is practically impossible to diagonalize for the

many-body eigenstates $\Psi_{tot}(\boldsymbol{r}_1,...,\boldsymbol{r}_N;\boldsymbol{R}_1,...,\boldsymbol{R}_K)$ therefore a series of approximations are needed.

1.1.1. Adiabatic approximation

From this moment on we use the global coordinate $\boldsymbol{r}$ to indicate the electronic coordinates $\{\boldsymbol{r}_i\}$ and $\boldsymbol{R}$ to indicate the nuclear coordinates $\{\boldsymbol{R}_I\}$. We notice that the electron mass is thousands times smaller than the nuclear masses. We can thus make an expansion of the Hamiltonian Eq. 1.1 considering the small term $\hat{T}_n$ as a perturbation. This means that the electrons follow the displacement of the nuclei instantaneously and that their motions are decoupled. We factorize the wavefunction n of the system as

$$\Psi_n(\boldsymbol{r},\boldsymbol{R}) = \sum_j \chi_{nj}(\boldsymbol{R})\,\psi_j(\boldsymbol{r};\boldsymbol{R}) \tag{1.3}$$

where $\chi_{nj}(\boldsymbol{R})$ is the nuclear part and $\psi_j(\boldsymbol{r};\boldsymbol{R})$ is the electronic part. The sum is over the electronic states j at fixed nuclear coordinates. By applying Hamiltonian Eq. 1.1 on the factorized wavefunction Eq. 1.3 and multiplying on the left by an electronic state $\psi_{j'}$, after an integration we obtain an equation for the lattice dynamics [37, 38]

$$\left[-\hbar^2\sum_I \frac{\nabla_I^2}{2M_I} + E_j(\boldsymbol{R})\right]\chi_{nj}(\boldsymbol{R}) = \mathscr{E}_{nj}\chi_{nj}(\boldsymbol{R}) \tag{1.4}$$

where $\mathscr{E}_{nj}$ is the energy of the system in nuclear state n and electronic state j and E_j is the Born-Oppenheimer Potential Energy Surface (PES) obtained from solving $\hat{H}_{BO}$ for the electronic hamiltonian at "frozen" configuration $\boldsymbol{R}$

$$\hat{H}_{BO} = \hat{T}_e + \hat{V}_{ext} + \hat{V}_{ee} + E_{nn} \tag{1.5}$$

In deriving Eq. 1.4 we neglected the off-diagonal matrix elements that arise from the interaction terms of the Hamiltonian Eq. 1.1 when multiplied on the left and on the right by the electronic wavefunctions in state j and j'. Together with the factorization Eq. 1.3 this is called the adiabatic Born-Oppenheimer approximation. Since in the Hamiltonian Eq. 1.5 we treated the coordinates $\boldsymbol{R}$ as parameters and $\boldsymbol{r}$ as dynamical variables, the original nucleus-nucleus interaction term $\hat{V}_{nn}$ becomes the constant term E_{nn} (since it is slowly varying with respect to space and time) which can be reabsorbed in the eigenvalues of $\hat{H}_{BO}$, so that from now on we can simply work with the electronic Hamiltonian

$$\hat{H} = \hat{T}_e + \hat{V}_{ext} + \hat{V}_{ee} \tag{1.6}$$

In writing the electronic Hamiltonian Eq. 1.6 we introduced the term $\hat{V}_{ext}$ which in principle may include the term $\hat{V}_{en}$ and any other external potential applied to the electrons like an external electric field, but in our applications we can assume it as

equal to $\hat{V}_{en}$ [1]. Solving the electronic Hamiltonian

$$\hat{H}(\boldsymbol{R})\psi_j(\boldsymbol{r};\boldsymbol{R}) = E_j(\boldsymbol{R})\psi_j(\boldsymbol{r};\boldsymbol{R}) \tag{1.7}$$

for different nuclear configurations $\boldsymbol{R}$ means exploring the Potential Energy Surface (PES) of the system. In the Born-Oppenheimer approximation we thus decouple the electronic eigenvalue problem Eq. 1.7 from the lattice problem Eq. 1.4, by neglecting the terms describing the electronic transition induced by the nuclear motion.

1.1.2. Hartree - Fock method and symmetry properties

A first attempt to solve the Hamiltonian Eq. 1.7 is the Hartree-Fock method [39] ("HF"). Since in the present thesis we do not use the HF method we do not describe it in detail, nonetheless, some concepts linked to this methodology must be given as they will be useful later for introducing the DFT and the MBPT techniques. In the HF method one defines an energy functional of the electronic wavefunction $E[\psi_{el}]$.

$$E[\psi_{el}] = \frac{\langle\psi_{el}|\hat{H}|\psi_{el}\rangle}{\langle\psi_{el}|\psi_{el}\rangle} \tag{1.8}$$

The many-electron eigenfunction of the Hamiltonian Eq. 1.7 is assumed to be approximated by a single antisymmetric product of one-electron wavefunctions $\phi_i(\boldsymbol{r}_j,\sigma_j)$, called Slater determinant

$$\psi_{el}(\boldsymbol{r}) = \frac{1}{\sqrt{N!}}\begin{vmatrix} \phi_1(\boldsymbol{r}_1,\sigma_1) & \phi_1(\boldsymbol{r}_2,\sigma_2) & \cdots & \phi_1(\boldsymbol{r}_N,\sigma_N) \\ \phi_2(\boldsymbol{r}_1,\sigma_1) & \phi_2(\boldsymbol{r}_2,\sigma_2) & \cdots & \phi_2(\boldsymbol{r}_N,\sigma_N) \\ \vdots & \vdots & \ddots & \vdots \\ \phi_N(\boldsymbol{r}_1,\sigma_1) & \phi_N(\boldsymbol{r}_2,\sigma_2) & \cdots & \phi_N(\boldsymbol{r}_N,s_N) \end{vmatrix} \tag{1.9}$$

with σ_i spin coordinate. This wavefunction fulfils the antisymmetry condition for the electrons (which are Fermions), i.e.

$$\psi_{el}(...,\boldsymbol{r}_i\sigma_i,...,\boldsymbol{r}_j\sigma_j,...) = -\psi_{el}(...,\boldsymbol{r}_j\sigma_j,...,\boldsymbol{r}_i\sigma_i,...) \tag{1.10}$$

Nonetheless, it is worth mentioning that density is not affected by the exchange of two electrons

$$\left|\psi_{el}(...,\boldsymbol{r}_i\sigma_i,...,\boldsymbol{r}_j\sigma_j,...)\right|^2 = \left|\psi_{el}(...,\boldsymbol{r}_j\sigma_j,...,\boldsymbol{r}_i\sigma_i,...)\right|^2 \tag{1.11}$$

Minimization of the functional Eq. 1.8 in the Lagrange multipliers ϵ_μ reads the Hartree-Fock equations [39]

$$-\hbar^2\frac{\nabla_i^2}{2m} - \hbar^2\frac{Ze^2}{|\boldsymbol{R}_I-\boldsymbol{r}_i|} + \sum_\mu\left(\hat{J}_\mu - \hat{K}_\mu\right)\phi_\mu(\boldsymbol{r}_i) = \epsilon_\mu\phi_\mu(\boldsymbol{r}_i) \tag{1.12}$$

1. This $\hat{V}_{ext}$ is not the one that we will introduce in Sec. 2.1 to derive the dielectric function.

The eigenvalues ϵ_μ play the role of Lagrange multipliers and their physical interpretation is given by the Koopmans' theorem. The operator $\hat{J}_\mu$ corresponds to the Hartree electrostatic interaction between each pair of electrons, while $\hat{K}_\mu$ is the Fock exchange term due to the antisymmetry of the trial wavefunction used. It is important to remark that the operators $\hat{J}_\mu$ and $\hat{K}_\mu$ contain the one-electron wavefuntions. In practice since the left side of Eq. 1.12 also includes the wavefunctions, the Hartree-Fock equations must be solved self-consistently. An initial guess for the Slater determinant is given, the left-side operator in Eq. 1.12 is computed and then diagonalized. The resulting wavefunctions are then used to construct a new operator and the cycle is repeated until the convergence is reached. The concept of self-consistent solution is important for the other method discussed in the present thesis, i.e. DFT.

Another important concept that will be useful later on is the Slater determinant Eq. 1.9. The exact many-electron wavefunction can be expressed only by an expansion in an infinite set of Slater determinants including also empty states. Post-Hartree-Fock methods make use of such expansion. Here we are only considering one Slater determinant. The physics that is not captured in this single-determinant picture is usually referred to as correlation effects. The methods we are going to discuss try somehow to include this correlation.

Such calculations are impractical for solid state systems, therefore a different approach is needed and we will see in Secs. 1.2 and 2.1 the methodologies adopted in this work to avoid this impediment. Nonetheless, these alternative techniques are affected by a problem that is not present in the HF method. The Hartree and the Fock terms include by construction a spurious self-interaction term each. Those terms cancel out. This is not the case in Density Functional Theory where the self-interaction term is partially cancelled but not in an exact way as in the HF method.

1.2. Density Functional Theory

In order to avoid the problems encountered in the Hartree-Fock method a change of paradigma of the viable approaches is to be considered. The HF approach is pretty standard in the sense that it does not depart from using the usual quantum mechanics methodology and the wavefunction is still the main tool used. Of course, HF method is complicated by the fact that the HF equations are not simple eigenvalue problems and they need to be solved self-consistently. The two Hohenberg and Kohn's theorems (hereinafter "HK") [40, 41] formulated in the '60s suggested that one may rewrite the minimization problem working with the electronic density rather than the wavefunctions. We state here the two theorems valid for a system with Hamiltonian of the kind Eq. 1.6 :

First Hohenberg and Kohn's theorem
The potential $\hat{V}_{ext}$ in a system of interacting electrons is determined by the ground state density $n_{gs}(\boldsymbol{r})$.

This means that not only if $\hat{V}_{ext}$ is known then the ground state is uniquely determined (that is the usual approach in quantum mechanics) but also that if a density $n(\boldsymbol{r})$ is given then there is only one $\hat{V}_{ext}$ such that $n(\boldsymbol{r})$ is the ground state density of the system, i.e. $n(\boldsymbol{r}) = n_{gs}(\boldsymbol{r})$. Moreover since $n(\boldsymbol{r})$ determines $\hat{V}_{ext}$, all the states of the system are also determined by $n(\boldsymbol{r})$.

Second Hohenberg and Kohn's theorem
There exists an energy functional of the density, $E[n(\boldsymbol{r})]$ universally valid for every $\hat{V}_{ext}$. Given a particular $\hat{V}_{ext}$, the functional is minimized by the ground state density $n_{gs}(\boldsymbol{r})$ and its minimum corresponds to the ground state energy.

Therefore one can use the variational principle to find the ground state energy, given $E[n(\boldsymbol{r})]$.

The methodologies that are based on the two HK theorems constitute the Density Functional Theory. The proofs of the HK theorems are quite simple and can be found in any DFT textbook [41]. The problem with the two HK theorems is that they only ensure the existence of the functional, which remains unknown. The two theorems became finally operative thanks to the approach to DFT developed by Kohn and Sham [42, 41]. The idea of the Kohn-Sham (KS) approach is to find an auxiliary non-interacting "pseudoelectron" system with the same ground state density $n_{gs}(\boldsymbol{r})$ as the interacting one. For this auxiliary system, the two HK theorems are valid and therefore

— the first HK theorem ensures that $n_{gs}(\boldsymbol{r})$ uniquely determines a new external Kohn-Sham potential $\hat{V}_{KS}$;
— the second HK theorem ensures the existence of an energy functional $E'[n_{aux}(\boldsymbol{r})]$ of the auxiliary pseudoelectron density, $n_{aux}(\boldsymbol{r})$ that is minimized by the same $n_{gs}(\boldsymbol{r})$ that minimizes the energy of original interacting system.

We usually refer to these pseudoelectrons as "Kohn-Sham" electrons and to their states as "Kohn-Sham states". For the auxiliary system we may write the energy functional as the sum of the kinetic energy of the KS electrons and the external Kohn-Sham potential V_{KS}

$$E'[n_{aux}(\boldsymbol{r})] = T_{KS}[n_{aux}(\boldsymbol{r})] + \int \mathrm{d}\boldsymbol{r}\, n_{aux}(\boldsymbol{r}) V_{KS}(\boldsymbol{r}) \tag{1.13}$$

From Eq. 1.13 one of the advantages of using a non-interacting auxiliary system is clear. In fact the complicated kinetic energy term $\hat{T}_e$ of the interacting system Eq. 1.6 is now just a sum over the kinetic energies of each single pseudoelectron and we can work with the one-particle KS wavefunctions ϕ_i^{KS}

$$T_{KS}[n_{aux}(\boldsymbol{r})] = -\frac{\hbar^2}{2m}\sum_i \int \mathrm{d}\boldsymbol{r}\phi_i^*(\boldsymbol{r})\nabla_i^2\phi_i(\boldsymbol{r}) = -\frac{\hbar^2}{2m}\sum_i \int \mathrm{d}\boldsymbol{r}\left|\nabla\phi_i^{KS}(\boldsymbol{r})\right|^2 \tag{1.14}$$

We now consider the energy functional of the interacting system

$$E[n(\boldsymbol{r})] = T_e[n(\boldsymbol{r})] + E_{ee}[n(\boldsymbol{r})] + \int \mathrm{d}\boldsymbol{r}\, V_{ext}(\boldsymbol{r}) n(\boldsymbol{r}) \tag{1.15}$$

where we introduced the complicated term $E_{ee}[n(\boldsymbol{r})]$ that contains the information on the many-electron interaction. We may rewrite Eq. 1.15 as

$$\begin{aligned} E[n(\boldsymbol{r})] = T_e[n(\boldsymbol{r})] + T_{KS}[n(\boldsymbol{r})] - T_{KS}[n(\boldsymbol{r})] + E_H[n(\boldsymbol{r})] - E_H[n(\boldsymbol{r})] \\ + E_{ee}[n(\boldsymbol{r})] + \int \mathrm{d}\boldsymbol{r}\, V_{ext}(\boldsymbol{r}) n(\boldsymbol{r}) \end{aligned} \tag{1.16}$$

where we added and subtracted T_{KS} and the Hartree term E_H

$$E_H[n(\boldsymbol{r})] = \frac{e^2}{2} \int \mathrm{d}\boldsymbol{r}' \mathrm{d}\boldsymbol{r} \frac{n(\boldsymbol{r}) n(\boldsymbol{r}')}{|\boldsymbol{r} - \boldsymbol{r}'|} \tag{1.17}$$

It is important to bear in mind that this Hartree term includes a self-interaction between an electron and itself, introducing an error that is not present in the HF method. We reorganize Eqs. 1.15 and 1.16 by defining the exchange-correlation potential

$$V_{xc}(\boldsymbol{r}) = \frac{\delta E_{xc}[n(\boldsymbol{r})]}{\delta n(\boldsymbol{r})} \tag{1.18}$$

with

$$E_{xc}[n(\boldsymbol{r})] = T_e[n(\boldsymbol{r})] - T_{KS}[n(\boldsymbol{r})] + E_{ee}[n(\boldsymbol{r})] - E_H[n(\boldsymbol{r})] \tag{1.19}$$

Then the energy functional becomes

$$E[n(\boldsymbol{r})] = T_{KS}[n(\boldsymbol{r})] + E_H[n(\boldsymbol{r})] + \int \mathrm{d}\boldsymbol{r}\, V_{ext}(\boldsymbol{r}) n(\boldsymbol{r}) + E_{xc}[n(\boldsymbol{r})] \tag{1.20}$$

With Eq. 1.20 we just rephrased the problem without adding anything new, but in this shape we have recast the energy functional so that three terms, easy to calculate - T_{KS}, E_H and the integral of V_{ext} - are isolated from the rest. The remaining term, difficult to compute - V_{xc} - needs to be approximated in some way. V_{xc} contains the correlation effects missing in T_{KS}, and the exchange-correlation effects missing in E_{ee}. From Eq. 1.20 we can obtain an operative equation. We make the functional derivative with respect to the Kohn-Sham pseudoelectron wavefunction of index l

$$\begin{aligned} \frac{\delta E[n(\boldsymbol{r})]}{\delta \phi_l^{KS*}(\boldsymbol{r})} = \frac{\delta T_{KS}[n(\boldsymbol{r})]}{\delta \phi_l^{KS*}(\boldsymbol{r})} + \frac{e^2}{2} \frac{\delta}{\delta \phi_l^{KS*}(\boldsymbol{r})} \int \mathrm{d}\boldsymbol{r} \mathrm{d}\boldsymbol{r}' \frac{n(\boldsymbol{r}) n(\boldsymbol{r}')}{|\boldsymbol{r}' - \boldsymbol{r}|} + \\ + \frac{\delta}{\delta \phi_l^{KS*}(\boldsymbol{r})} \int \mathrm{d}\boldsymbol{r}\, V_{ext}(\boldsymbol{r}) n(\boldsymbol{r}) + \frac{\delta E_{xc}[n(\boldsymbol{r})]}{\delta \phi_l^{KS*}(\boldsymbol{r})} \end{aligned} \tag{1.21}$$

a change of variable reads

$$\begin{aligned}\frac{\delta E[n(\boldsymbol{r})]}{\delta\phi_l^{KS*}(\boldsymbol{r})} =& \frac{\delta T_{KS}[n(\boldsymbol{r})]}{\delta\phi_l^{KS*}(\boldsymbol{r})} + \frac{e^2}{2}\frac{\delta}{\delta n(\boldsymbol{r})}\int \mathrm{d}\boldsymbol{r}\mathrm{d}\boldsymbol{r}'\frac{n(\boldsymbol{r})n(\boldsymbol{r}')}{|\boldsymbol{r}'-\boldsymbol{r}|}\frac{\delta n(\boldsymbol{r})}{\delta\phi_l^{KS*}(\boldsymbol{r})} + \\ &+ \frac{\delta}{\delta n(\boldsymbol{r})}\int \mathrm{d}\boldsymbol{r} V_{ext}(\boldsymbol{r})n(\boldsymbol{r})\frac{\delta n(\boldsymbol{r})}{\delta\phi_l^{KS*}(\boldsymbol{r})} + \frac{\delta E_{xc}[n(\boldsymbol{r})]}{\delta n(\boldsymbol{r})}\frac{\delta n(\boldsymbol{r})}{\delta\phi_l^{KS*}(\boldsymbol{r})}\end{aligned} \tag{1.22}$$

but $\frac{\delta n}{\delta\phi_l^{KS*}} = \phi_l^{KS}$ then Eq. 1.22 reads

$$\begin{aligned}\frac{\delta E[n(\boldsymbol{r})]}{\delta\phi_l^{KS*}(\boldsymbol{r})} =& \frac{\delta T_{KS}[n(\boldsymbol{r})]}{\delta\phi_i^{KS*}(\boldsymbol{r})} + \frac{e^2}{2}\frac{\delta}{\delta n(\boldsymbol{r})}\left(\int \mathrm{d}\boldsymbol{r}\mathrm{d}\boldsymbol{r}'\frac{n(\boldsymbol{r})n(\boldsymbol{r}')}{|\boldsymbol{r}'-\boldsymbol{r}|}\right)\phi_l^{KS}(\boldsymbol{r}) + \\ &+ \frac{\delta}{\delta n(\boldsymbol{r})}\left(\int \mathrm{d}\boldsymbol{r} V_{ext}(\boldsymbol{r})n(\boldsymbol{r})\right)\phi_l^{KS}(\boldsymbol{r}) + \left(\frac{\delta E_{xc}[n(\boldsymbol{r})]}{\delta n(\boldsymbol{r})}\right)\phi_l^{KS}(\boldsymbol{r})\end{aligned} \tag{1.23}$$

Then

$$\frac{\delta E[n(\boldsymbol{r})]}{\delta\phi_l^{KS*}(\boldsymbol{r})} = -\frac{\hbar^2}{2m}\nabla^2\phi_l^{KS}(\boldsymbol{r}) + \frac{\delta E_H[n(\boldsymbol{r})]}{\delta n(\boldsymbol{r})}\phi_l^{KS}(\boldsymbol{r}) + \frac{\delta E_{ext}[n(\boldsymbol{r})]}{\delta n(\boldsymbol{r})}\phi_l^{KS}(\boldsymbol{r}) + \frac{\delta E_{xc}[n(\boldsymbol{r})]}{\delta n(\boldsymbol{r})}\phi_l^{KS}(\boldsymbol{r}) \tag{1.24}$$

In Eq. 1.24 we defined E_{ext} as

$$E_{ext}[n(\boldsymbol{r})] = \int \mathrm{d}\boldsymbol{r} V_{ext}(\boldsymbol{r})n(\boldsymbol{r}) \tag{1.25}$$

We now apply the variational principle

$$\int \mathrm{d}\boldsymbol{r}\left(\frac{\delta E[n(\boldsymbol{r})]}{\delta\phi_l^{KS*}(\boldsymbol{r})} - E_{KS}\frac{\delta n(\boldsymbol{r})}{\delta\phi_l^{KS*}(\boldsymbol{r})}\right)\delta\phi_l^{KS*}(\boldsymbol{r}) = 0 \tag{1.26}$$

where the factors E_{KS} are the Lagrange multipliers.[2] By using Eq. 1.24 in Eq. 1.26 we have

$$\int \mathrm{d}\boldsymbol{r}\left(-\frac{\hbar^2}{2m}\nabla^2\phi_l^{KS}(\boldsymbol{r}) + V_{KS}(\boldsymbol{r})\phi_l^{KS}(\boldsymbol{r}) - E_{KS}\phi_l^{KS}(\boldsymbol{r})\right)\delta\phi_l^{KS*}(\boldsymbol{r}) = 0 \tag{1.27}$$

i.e.

$$\left(-\frac{\hbar^2}{2m}\nabla^2 + V_{KS}(\boldsymbol{r})\right)\phi_l^{KS}(\boldsymbol{r}) = E_{KS}\phi_l^{KS}(\boldsymbol{r}) \tag{1.28}$$

2. At variance with the HF method where the Koopmans' theorem holds, for these Lagrange multipliers the interpretation as energies does not have a formal justification and they are instead understood by the Janak's theorem as derivative of the total energy with respect to an infinitesimal variation of the number of electrons [43].

where we defined the V_{KS} as

$$V_{KS}(\boldsymbol{r}) = \frac{\delta E_H[n(\boldsymbol{r})]}{\delta n(\boldsymbol{r})} + \frac{\delta E_{ext}[n(\boldsymbol{r})]}{\delta n(\boldsymbol{r})} + \frac{\delta E_{xc}[n(\boldsymbol{r})]}{\delta n(\boldsymbol{r})} \tag{1.29}$$

which is exactly the Kohn-Sham external potential we were looking for in Eq. 1.13 for the non-interacting system. Equations of the type Eq. 1.28 are called Kohn-Sham equation (KSE) and the operator on the left side is the Kohn-Sham Hamiltonian

$$\hat{H}_{KS}(\boldsymbol{r}) = -\frac{\hbar^2}{2m}\nabla^2 + V_{KS}(\boldsymbol{r}) \tag{1.30}$$

The set of Kohn-Sham equations must be solved to get the ground state energy and density. Note that Eq. 1.28 is not an eigenvalue equation since the wavefunction enters the operator on the left side through the Kohn-Sham potential V_{KS} which depends on the density. Therefore the Kohn-Sham equations have to be solved self-iteratively in a self-consistent field cycle ("SCF"). In Sec. 1.3 we describe in detail the scheme used to perform the SCF loop.

1.3. Kohn-Sham DFT in practice

The iterative solution of Eq. 1.28 implies the diagonalization of the Kohn-Sham Hamiltonian Eq. 1.30, construction of the density out of the eigenfunction, and then reconstruction of a new Kohn-Sham Hamiltonian for the next iteration. The process is repeated until convergence is reached. This task is performed by several codes like for example the Quantum Espresso package [36, 35]. The entire SCF cycle to solve the Kohn-Sham equations is ilustrated in Fig. 1.1. We describe the procedure in detail. Let us consider the ith iteration of the loop. We suppose that from the previous iterations we could build the Kohn-Sham Hamiltonian $H_{KS}^{(i)}$. $H_{KS}^{(i)}$ is thus diagonalized and one then finds the ith KS wavefunctions $\phi_{KS}^{(i)}$ and thus the ith density $n^{(i)}(\boldsymbol{r})$. At this point the algorithm check for convergence and compares $n^{(i)}$ with $n^{(i-1)}$, that is, a suitable norm is evaluated which must be below a tolerance threshold. If the norm is below the threshold then the convergence has been reached and the code exits from the SCF cycle. If the value is above the threshold then the code builds a new density $n^{(i+1)}$ by mixing the densities $n^{(i)}$ and $n^{(i-1)}$ and a new KS Hamiltonian H_{KS}^{i+1} is calculated to start a new iteration. The initial anzatz for the density used to construct the 0th iteration Hamiltonian $H_{KS}^{(0)}$ is obtained from a random superposition of atomic wavefunctions.

The Kohn-Sham approach to DFT can be applied to many kinds of systems but one should always choose carefully the basis set of the wavefunctions used and the best choice is problem-dependent. Quantum Espresso is specifically tailored for solid state physics and assumes the validity of the Bloch's theorem due to translational symmetry of the lattice. The Kohn-Sham states that we are looking for will be therefore Bloch's

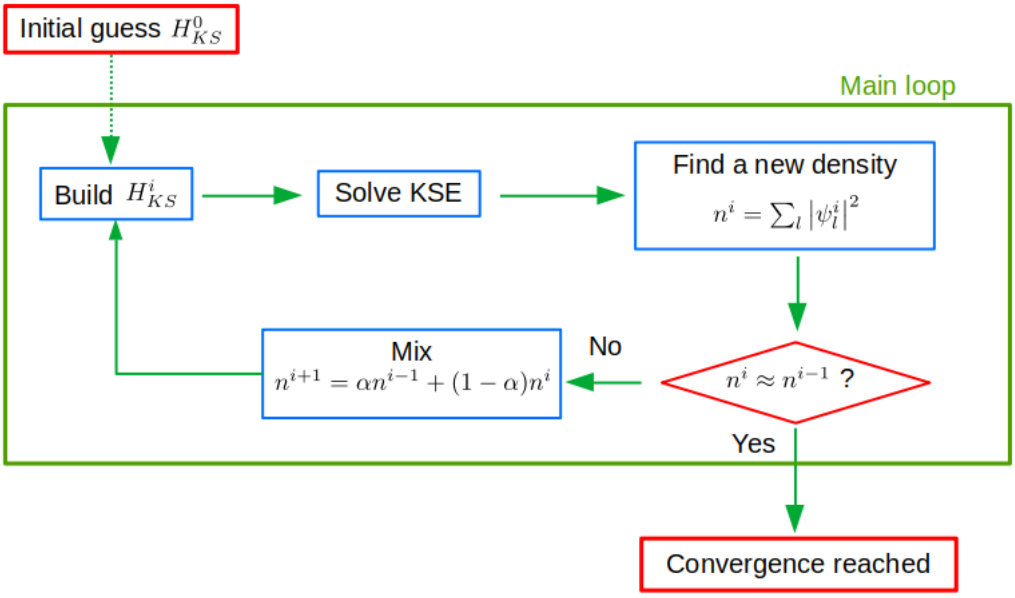

Figure 1.1. – Scheme of the SCF iterative algorithm used by standard DFT codes such as Quantum Espresso to solve the Kohn-Sham equations. Index i denotes the ith iteration.

states of the type

$$\phi_{n\boldsymbol{k}}(\boldsymbol{r}) = \mathrm{e}^{i\boldsymbol{k}\cdot\boldsymbol{r}} u_{n\boldsymbol{k}}(\boldsymbol{r}) \tag{1.31}$$

where the indices n and $\boldsymbol{k}$ refer to the band and the first Brillouin Zone (1BZ) $\boldsymbol{k}$-grid, respectively. The function $u_{n\boldsymbol{k}}(\boldsymbol{r})$ has the same periodicity of the crystal lattice, i.e if $\boldsymbol{R}$ is a lattice vector then $u_{n\boldsymbol{k}}(\boldsymbol{R}+\boldsymbol{r}) = u_{n\boldsymbol{k}}(\boldsymbol{r})$. The periodicity of the $u_{n\boldsymbol{k}}$ suggests that for a crystal they can be expanded in a plane waves $\mathrm{e}^{i\boldsymbol{G}\cdot\boldsymbol{r}}$ basis set, so that the Bloch's states are

$$\phi_{n\boldsymbol{k}}(\boldsymbol{r}) = \sum_{\boldsymbol{G}} \mathrm{e}^{i\boldsymbol{k}\cdot\boldsymbol{r}} C_{n\boldsymbol{k}}(\boldsymbol{G}) \mathrm{e}^{i\boldsymbol{G}\cdot\boldsymbol{r}} \tag{1.32}$$

where $\boldsymbol{G}$ are the reciprocal lattice vectors and $C_{n\boldsymbol{k}}$ are the coefficient of the expansion of $u_{n\boldsymbol{k}}$. In practice, since our goal is to numerically simulate $\phi_{n\boldsymbol{k}}$, we cut the infinite sum over $\boldsymbol{G}$ at a given $\boldsymbol{G}_{max}$ of maximal lenght $G_{max} = |\boldsymbol{G}_{max}|$ so that the Kohn-Sham Bloch's function computed will have the form

$$\phi_{n\boldsymbol{k}}(\boldsymbol{r}) = \sum_{\boldsymbol{G}}^{\boldsymbol{G}_{max}} C_{n\boldsymbol{k}}(\boldsymbol{G}) \mathrm{e}^{i(\boldsymbol{k}+\boldsymbol{G})\cdot\boldsymbol{r}} \tag{1.33}$$

The G_{max} is usually expressed in terms of a cut-off energy E_{cut}

$$E_{cut} = \frac{G^2_{max}}{2m} \tag{1.34}$$

The meaning of the $\boldsymbol{G}$ and $\boldsymbol{G}_{max}$ in the reciprocal lattice is illustrated in Fig. 1.2.

Since we are forced to cut our expansion at a certain $\boldsymbol{G}_{max}$, when we use an *ab initio* code like Quantum Espresso it is always good practice to ensure that we are using a sufficiently large E_{cut} such that the expansion Eq. 1.32 is well approximated by the cut expansion Eq. 1.33. Therefore, when approaching a new material one usually checks the convergence of the total energy, E_{tot}, for different values of E_{cut}. Throughout this work we will consider the total energy converged for the cut-off energy E^i_{cut} when the condition

$$\left|E_{tot}\left(E^i_{cut}\right) - E_{tot}\left(E^{i+1}_{cut}\right)\right| < 4\frac{\text{meV}}{\#\text{ of valence electrons}} \tag{1.35}$$

is fulfilled.

One should also consider the density of the $\boldsymbol{k}$-grid on which the 1BZ is sampled and the number of $\boldsymbol{k}$-points in the 1BZ must be sufficiently large to reach a certain accuracy for the Kohn-Sham wavefunctions. Therefore we have to carry out for the $\boldsymbol{k}$-grid a convergence test similar to the one described above for the cut-off energy E_{cut}. We thus study the behaviour of the total energy for different $\boldsymbol{k}$-grids. Let us define a $\boldsymbol{k}$-grid $K_i = \left(N^{(i)}_{k_x}, N^{(i)}_{k_y}, N^{(i)}_{k_z}\right)$ as the uniform set of $\boldsymbol{k}$-points such that they are in total $N^{(i)}_{k_x} \times N^{(i)}_{k_y} \times N^{(i)}_{k_z}$ in the 1BZ. We run a series of SCF calculations at fixed E_{cut} for a set of grids $\{K_i\}$ (ordered in such way that K_{i+1} is denser than K_i) and check the convergence of the total energy. Again, in this work we considered the grid K_i sufficiently dense if

$$|E_{tot}(K_i) - E_{tot}(K_{i+1})| < 4\frac{\text{meV}}{\#\text{ of valence electrons}} \tag{1.36}$$

It is worth mentioning that nowadays the error made by different codes with different approaches due to incompleteness of the $\boldsymbol{G}$ vector set or the $\boldsymbol{k}$-sampling is the same[44], meaning that it is completely governed by the convergence parameters.

A methodology often used and implemented in codes like Quantum Espresso is neglecting the dynamics of the core electrons since usually one is interested in the describing only the valence electrons which participate to the bondings between the atoms. The numerical difficulties of computing both the valence and the core electrons reside in the divergence of the atomic potential at $\boldsymbol{r} \to 0$ and the rapid oscillations of the electron wavefunctions near the nucleus which would require a large plane wave basis set. In order to avoid such obstacle, one can use pseudopotentials instead of the "real" atomic potential and sacrifice the description of the core for an accurate and fast computation of the valence electrons. The pseudopotential is built in such a way that for a $r < r_{core}$ (with r_{core} radius of the core) it is smoothly behaving. The Kohn-Sham wavefunctions found using the pseudopotential ϕ^{KS}_{ps} must mimic, for $r > r_{core}$, the Kohn-Sham states ϕ^{KS}_{ae} that one would obtain from an all-electron calculation (i.e. with the atomic potential instead of the pseudopotential). The pseudopotentials used in this work are called *norm-conserving*, meaning that the norm of ϕ^{KS}_{ps} must be equal to the norm of ϕ^{KS}_{ae} in the core region, i.e.

$$\int_0^{r_{core}} \mathrm{d}r\, r^2 \left|\phi^{KS}_{ps}(\boldsymbol{r})\right|^2 = \int_0^{r_{core}} \mathrm{d}r\, r^2 \left|\phi^{KS}_{ae}(\boldsymbol{r})\right|^2 \tag{1.37}$$

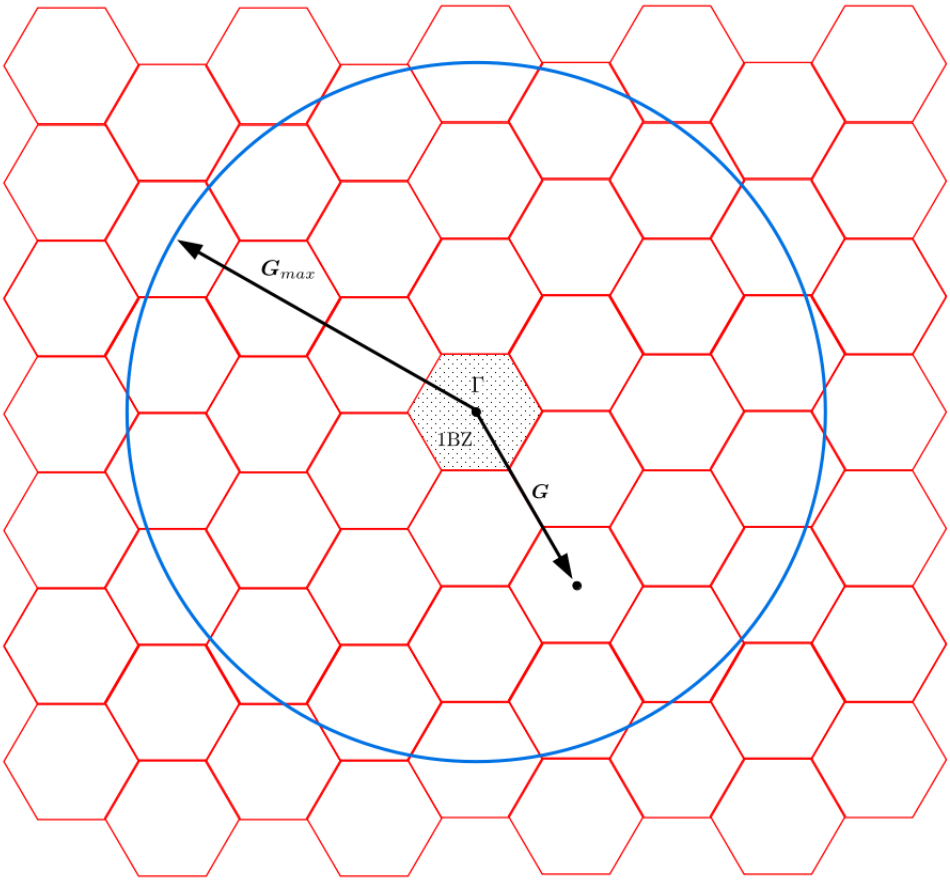

Figure 1.2. – Reciprocal lattice for a generic hexagonal crystal with a dense $\boldsymbol{k}$-grid in the 1BZ. The vector $\boldsymbol{G}$ connects a periodic image BZ with the 1BZ in the center. The $\boldsymbol{G}_{max}$ vector lenght determines the E_{cut} corresponding to the blue circle and the last $\boldsymbol{G}$ components included in the sum Eq. 1.33. All the $\boldsymbol{G}$ outside of the blue circle are not included in the calculations.

The condition Eq. 1.37 ensures that both $\phi^{KS}_{ps}(\boldsymbol{r})$ and $\phi^{KS}_{ae}(\boldsymbol{r})$ predict the same charge for the core. Moreover we impose the normalization $\langle\phi^{KS}_{ps}|\phi^{KS}_{ps}\rangle = 1$. Additional conditions on the derivatives of ϕ^{KS}_{ps} ensure a smooth behaviour and portability of the same pseudopotential in different problems. As an illustrative example, Fig. 1.3 reports a pseudopotential calculated for Mo at different angular momenta and a comparison between the ϕ^{KS}_{ae} and ϕ^{KS}_{ps} for a s-state for Mo (adapted from [45]).

Lastly, we focus on the problem of the exchange-correlation term in V_{KS} defined in Eq. 1.18. As shown in Sec. 1.2 the Kohn-Sham approach to DFT is based on having an energy functional $E[n(\boldsymbol{r})]$ from which one extracts some contributions that can be computed easily, leaving all the rest in the complicated term $V_{xc}(\boldsymbol{r})$. Then the problem of how to approximate $V_{xc}(\boldsymbol{r})$ remains. Historically, many exchange-correlation functionals have been conceived. The first and most simple example, already suggested in the original Kohn and Sham article introducing the pseudoelectron method [42],

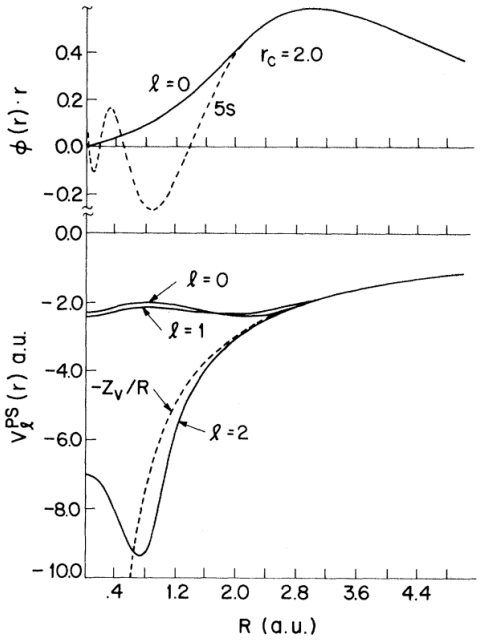

Figure 1.3. – Pseudopotential and s wavefunctions computed for Mo, adapted from [45].

was the local density approximation (LDA) and its spin-polarized version, the local spin density approximation (LSDA). In LSDA the exchange-correlation functional $E_{xc}^{LSDA}[n(\boldsymbol{r})]$ is approximated to the one of an homogeneous electron gas (HEG)

$$E_{xc}^{LSDA}[n_\uparrow(\boldsymbol{r}), n_\downarrow(\boldsymbol{r})] = \int \mathrm{d}\boldsymbol{r} E_{xc}^{HEG}(n_\uparrow(\boldsymbol{r}), n_\downarrow(\boldsymbol{r}))n(\boldsymbol{r}) \tag{1.38}$$

where the $n_\uparrow$ and $n_\downarrow$ are the spin densities for spin up and spin down states, respecitvely. The advantage of this approximation lies on the fact that for a HEG E_{xc}^{HEG} can be easily calculated (the exchange term is analytical) and it is local. The drawback is that even though LDA works well for systems where the electrons behave like a HEG (metals) it fails to deliver an accurate band gap for semiconductors where the electrons are less delocalized. The most (in)famous example is perhaps Ge, which is predicted to be a metal by LDA. A better approximation for the exchange-correlation is the generalized gradient approximation (GGA)

$$E_{xc}^{GGA}[n_\uparrow(\boldsymbol{r}), n_\downarrow(\boldsymbol{r})] = \int \mathrm{d}\boldsymbol{r} E_{xc}^{HEG}(n(\boldsymbol{r}))n(\boldsymbol{r})F\left[n_\uparrow(\boldsymbol{r}), n_\downarrow(\boldsymbol{r}), \left|\nabla n_\uparrow(\boldsymbol{r})\right|, \left|\nabla n_\downarrow(\boldsymbol{r})\right|\right] \tag{1.39}$$

where $E_{xc}^{GGA}[n(\boldsymbol{r})]$ is modulated by a functional F of both n and its gradient $\nabla n(\boldsymbol{r})$. There are many flavours of GGA exchange-correlation functionals, each one corresponding to a different way of computing F (see for example Ref. [46]). Both LDA and GGA tend to predict an underestimated band-gap for semiconductors [47].

Today's standards require the use of more refined exchange-correlation functionals (also non-local) capable of predicting the band gap more accurately than GGA.

For point defect calculations, the so-called hybrid functionals are often used. These functionals are called hybrid because they mix contributions from a local exchange-correlation functional of the density and from the Hartree-Fock exchange term which depends on the single-particle states. Compared with GGA and LDA, hybrid functionals require longer computational times since the Fock term is non-local, on the other hand they partially correct the self-interaction error. When using an hybrid functional Quantum Espresso departs from the usual SCF scheme showed in Fig. 1.1. For each SCF cycle the program considers the usual $\boldsymbol{k}$-grid and a second $\boldsymbol{q}$-grid so that a set of $\boldsymbol{k}'$ points in the 1BZ can be defined as $\boldsymbol{k}' = \boldsymbol{k} - \boldsymbol{q}$. On this $\boldsymbol{q}$ grid Quantum Espresso iteratively updates the exchange potential at the jth iteration

$$V_x \phi^{KS(j)}_{i\boldsymbol{k}}(\boldsymbol{r}) = V_x^{(j-1)} \phi^{KS(j-1)}_{i\boldsymbol{k}}(\boldsymbol{r}) + \phi^{KS(j)}_{i'\boldsymbol{k}-\boldsymbol{q}}(\boldsymbol{r}) V^{(j)}_{\boldsymbol{q}}(\boldsymbol{r}) \tag{1.40}$$

where the potential $V_{\boldsymbol{q}}(\boldsymbol{r})$ is calculated from finite $\boldsymbol{q}$ "densities" of the type $\phi^{KS*}_{i,\boldsymbol{k}-\boldsymbol{q}} \phi^{KS}_{i',\boldsymbol{k}}$. The explicit dependence of the exchange potential on the densities changes depending on which hybrid functional we are using. A very popular choice in defect calculations is the Heyd-Scuseria-Ernzerhof functional (see for example Refs. [26],[20] and [48]). The HSE hybrid functional has the inconvenient of making the calculations extremely costly. In this work we used a different hybrid functional, the Gaussian Attenuation Perdew-Burke-Ernzerhof scheme (Gau-PBE) which, like HSE, predicts a band gap close to that one obtained with more advanced methods (Many-Body perturbation theory) but with less computational intricacies. Details on this functional are provided in Refs. [49] and [50].

1.4. Density Functional Perturbation Theory

DFT can be extended to treat also the vibrational properties of the material and study the phonons. Using the Born-Oppenheimer approximation, so far we were interested only in the electronic Hamiltonian. If we want to take into account also the lattice dynamics instead, we have to move along the PES and solve Eq. 1.5 for different nuclear configurations so that E_{nn} depends explicitly from the atomic positions. Here we follow the procedure presented in Ref. [37]. The vibrational frequencies ω of the nuclei in the structure can be found by solving the eigenvalue problem

$$\det \left| \frac{1}{\sqrt{M_I M_J}} \sum_{\boldsymbol{R}_J \boldsymbol{R}_J} \frac{\partial^2 E}{\partial \boldsymbol{R}_J \partial \boldsymbol{R}_J} - \omega^2 \right| = 0 \tag{1.41}$$

with E energy of the PES . The second derivative (Hessian) in Eq. 1.41 is simplified by the Hellmann-Feynman theorem, it states that for a Hamiltonian H_λ dependent on a parameter λ, with an eigenvalue E_λ of eigenfunction $|\psi_\lambda\rangle$, the first derivative of E_λ with respect to λ is

$$E'_\lambda = \left\langle \psi_\lambda \left| \frac{\partial \hat{H}_\lambda}{\partial \lambda} \right| \psi_\lambda \right\rangle \tag{1.42}$$

In our case we take λ as the global nuclear configuration $\boldsymbol{R}$ and we focus on the Born-Oppenheimer Hamiltonian H_{BO} with eigenvalues E and eigenstates $\psi_{el}(\boldsymbol{R})$. The Hellmann-Feynman theorem allows the calculation of the forces acting on the Ith nucleus

$$\boldsymbol{F}_I(\boldsymbol{R}) = -\frac{\partial E}{\partial \boldsymbol{R}_I} = \left\langle \psi_{el}(\boldsymbol{R}) \left| \frac{\partial \hat{H}_{BO}}{\partial \boldsymbol{R}_I} \right| \psi_{el}(\boldsymbol{R}) \right\rangle \tag{1.43}$$

Explicit calculation of the forces reads

$$\boldsymbol{F}_I(\boldsymbol{R}) = -\int \mathrm{d}\boldsymbol{r}\, n(\boldsymbol{r};\boldsymbol{R}) \frac{\partial V_{ext}(\boldsymbol{r};\boldsymbol{R})}{\partial \boldsymbol{R}_I} - \frac{\partial E_{nn}(\boldsymbol{R})}{\partial \boldsymbol{R}_I} \tag{1.44}$$

and for the second derivative

$$\begin{aligned} -\frac{\partial \boldsymbol{F}_I}{\partial \boldsymbol{R}_J} = \frac{\partial^2 E(\boldsymbol{R})}{\partial \boldsymbol{R}_I \partial \boldsymbol{R}_J} = \int \mathrm{d}\boldsymbol{r} \frac{\partial n(\boldsymbol{r};\boldsymbol{R})}{\partial \boldsymbol{R}_J} \frac{\partial V_{ext}(\boldsymbol{r};\boldsymbol{R})}{\partial \boldsymbol{R}_I} + \\ \int \mathrm{d}\boldsymbol{r}\, n(\boldsymbol{r};\boldsymbol{R}) \frac{\partial^2 V_{ext}(\boldsymbol{r};\boldsymbol{R})}{\partial \boldsymbol{R}_I \partial \boldsymbol{R}_J} + \frac{\partial^2 E_{nn}(\boldsymbol{R})}{\partial \boldsymbol{R}_I \partial \boldsymbol{R}_J} \end{aligned} \tag{1.45}$$

Eq. 1.45 show that in order to calculate the vibrational frequencies using Eq. 1.41 we need to know the electronic densities at configuration $\boldsymbol{R}$, $n(\boldsymbol{r};\boldsymbol{R})$. The quantities in Eq. 1.45 can be computed within DFT. The idea is to compute the variation of n with respect to $\boldsymbol{R}$. Given a generic Hamiltonian $\hat{H}$ dependent on a parameter λ with eigenfunctions ψ the perturbation theory with respect to λ reads

$$\left(\hat{H}_0 + \lambda \hat{H}_1 + ...\right)\left(|\psi_0\rangle + \lambda |\psi_1\rangle + ...\right) = \left(E_0 + \lambda E_1 + ...\right)\left(|\psi_0\rangle + \lambda |\psi_1\rangle + ...\right) \tag{1.46}$$

with the subscripts $0, 1, ...$ denoting the order in the perturbation. To the first order Eq. 1.46 reduces to

$$\hat{H}_0 |\psi_1\rangle + \hat{H}_1 |\psi_0\rangle = E_0 |\psi_1\rangle + E_1 |\psi_0\rangle \tag{1.47}$$

Using the Kohn-Sham Hamiltonian Eq. 1.30 in the first order perturbation theory Eq. 1.47 we get the Density Functional Perturbation Theory (DFPT) equations

$$\left(\hat{H}_{KS} - E_n^{KS}\right)|\Delta\phi_n^{KS}\rangle = -\left(\Delta \hat{V}_{KS} - \Delta E_n^{KS}\right)|\phi_n^{KS}\rangle \tag{1.48}$$

where the letter Δ denotes the finite difference variation with respect to $\boldsymbol{R}$. Eq. 1.48 can be used to find the variation $\Delta\phi_n^{KS}$. The variation of the density (linear response) is linked to $\Delta\phi_n^{KS}$ by

$$\Delta n(\boldsymbol{r}) = 4\Re \sum_{n=1}^{n/2} \phi_n^{KS*}(\boldsymbol{r}) \Delta\phi_n^{KS}(\boldsymbol{r}) \tag{1.49}$$

In this way the second derivatives in Eq. 1.41 can be found. These second derivatives are linked to the interatomic force constants (IFC)

$$C_{s,l,t,m}^{\alpha\beta} = \frac{\partial^2 E}{\partial u_{s,l}^{\alpha} \partial u_{t,m}^{\beta}} \tag{1.50}$$

for the atomic displacement u of atoms s, t in the unit cells l, m along the direction $\alpha, \beta = x, y, z$. In practice one prefers to work in the reciprocal space and then Eq. 1.41 becomes

$$\det \left| \frac{1}{\sqrt{M_I M_J}} \tilde{C}^{\alpha\beta}_{s,l,t,m}(\boldsymbol{q}) - \omega^2(\boldsymbol{q}) \right| = 0 \tag{1.51}$$

The IFC in Eq. 1.51 determine the phonon dispersion for a crystal in the reciprocal space. For polar materials the vibrations at $\boldsymbol{q} = 0$ determine a macroscopic electric field which couple with the longitudinal phonons. This gives origin to the LO-TO splitting of the phonon dispersion which can be found by calculating a non-analytical contribution in $\tilde{C}^{\alpha\beta}_{s,l,t,m}(\boldsymbol{q})$ which depends on the Born effective charges $Z^\star$ [51].

1.5. Point defects and supercell approach

For a given material all the information about the crystal lattice and its space symmetry is contained in the primitive cell and its repetition in the three-dimensional space recreates the whole crystal (of infinite dimensions). A possible definition of a point defect is a microscopical breaking of such symmetry (involving few atoms). If the material does not have any defect then it is defined "pristine" or "bulk", i.e. it retains the original space group determined by its primitive cell. If a defect is present then one says that the material is defective and that it is a "host" for the defect. Indeed, in the real world there is no material without defects and the pristine material should always be intended as an approximation or an ideal model[3]. The physics of point defects is a rich and large field of study. Here we focus only on two aspects for each defect studied :

- their thermodynamics, which controls the concentration of a particular type of defect in the host;
- their optical properties, which are important for possible technological implementations.

Let us consider a simple bi-atomic compound like BN and a third type of atoms, for example carbon C. The simplest point defects we can consider involves only one atomic site and we can classify them as follows

1. simple substitutional : C replaces the B or N of the pristine material, denoted respectively as C_B and C_N
2. simple antisites : B replaces a N atom or N replaces a B atom, denoted respectively as B_N and N_B
3. single vacancies : a B or N atom is missing, denoted respectively as V_B and V_N
4. interstitial : the defect atom is out of any lattice site.

These defects can be combined together to form complexes that are more extended than one lattice point. For example

3. In the struggle to obtain samples which have less and less defects, the pristine material can also be thought as a limit in the mathematical sense.

1. divacancies are two vacancies adjacent one to the other
2. di-substitutional dimers, for example C_BC_N
3. a vacancy next to a substitutional
4. an antisite next to a substitutional or a vacancy
5. trimers : three substitutionals next to each others like C_2C_B or C_2C_N
6. tetramers, hexamers etc.

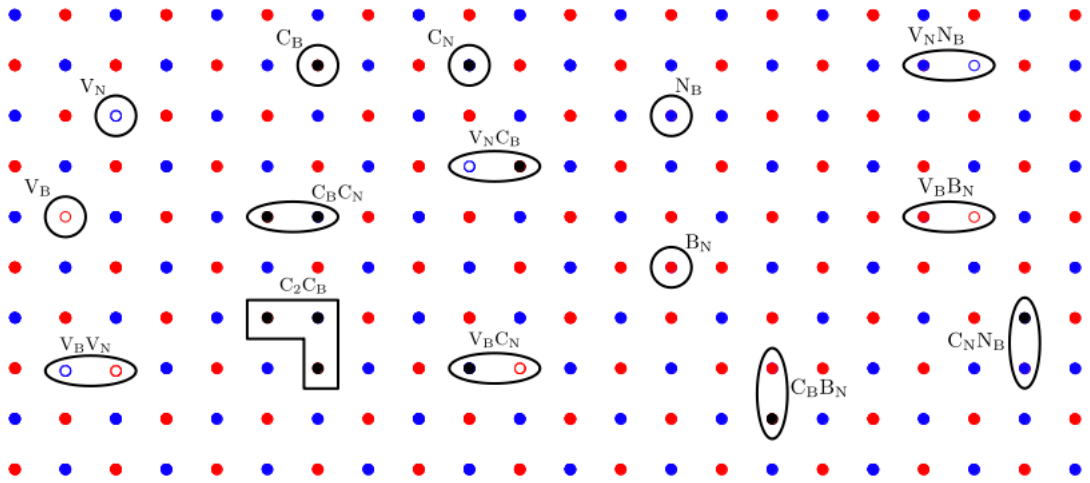

Figure 1.4. – 2D projected schematic depiction for several types of defects and their notation in a bi-atomic crystal lattice like BN. Red atoms correspond to boron, blue atoms represent nitrogen, black dots stand for carbon atoms, white atomic sites depict vacancies. Interstitial and defects more complex than the trimers are not showed.

Fig. 1.4 depicts simple point defects as well as their complexes. The presence of defects heavily affect the properties of the host material, as already mentioned in the introduction. From the point of view of the electronic properties, the insertion of a defect results in new defect-induced level, possibly in the band gap. Defect-induced levels can be poorly hybridized with the bulk states and they may be localized in a limited region around the defect. As a consequence they appear as flat bands, at odds with the rest of the band structure of the host. In the following subsections we outline the methodologies used in this work to study the formation of defects in the host material and their electronic properties.

By use of the plane waves in a DFT calculation the periodic boundary conditions and the validity of the Bloch's theorem are automatically and naturally enforced. This seems to be at variance with the definition of a defect that we gave in this section, that is the breaking of the symmetry of the host. The use of boundary conditions with a defective system will results in simulating a crystal with a concentration of defects higher than that of the real material. This problem can be partially circumvented by use of the supercell approach. Instead of carrying out the DFT calculation with only one primitive cell, in the supercell approach one inserts a defect in a unit cell made of

many primitive cells repeated. The larger the dimension of the supercell, the better the simulated crystal reproduces the dilute limit, i.e. a density of defects in the host (and therefore an average distance between the defect sites) closer to the real one. On the contrary, a small supercell results in a small average distance between the defects and consequent spurious interactions between the defect states. Those interactions will be discussed later. In practice the supercell with a size corresponding to the dilute limit would be beyond the computational capabilities of any supercomputer, the supercell sizes found in the literature are usually from few tens to few hundred of atoms (in some cases few thousands) [26, 52].

1.5.1. Formation energy and charge transition levels

In a real crystal at equilibrium, electrons are exchanged between defects and they can acquire a non-zero charge. At a computational level one considers only one defect in the supercell and assumes that the electrons in excess or missing are taken to or given by an electron reservoir with chemical potential E_F, the Fermi energy [53]. The concentration $n[X^q](T)$ of a defect X in the charge state q at temperature T in a supercell of N_{sites} available sites is [48]

$$n[X^q](T) = N_{sites} \mathrm{e}^{-\frac{G_f[X^q]}{k_B T}} \tag{1.52}$$

G_f is the Gibbs formation energy [52]

$$G_f\left[X^q\right](E_F) = F_{tot}[X^q] - F_{tot}^{bulk} + pV_f - \sum_i n_i \mu_i + E_{dil}^q + q(E_F + E_{VB}) \tag{1.53}$$

where F_{tot} and F_{tot}^{bulk} are the Helmotz free energies of the supercell with and without the defect, respectively, p is the pressure, V_f is the formation volume, μ_i is the chemical potential necessary to add or remove n_i atoms of the type i to form the defect, E_{dil}^q is the dilute limit correction to take into account the spurious interaction between the defect and its periodic image, E_{VB} is the host valence band edge used as reference for the energy scale. The Gibbs free energy 1.53 is expressed as a function of the Fermi energy E_F since a priori we do not know the chemical potential of the electron reservoir. In fact the E_F is fixed once one solves the set of equations of the type Eq. 1.52 for all the defects considered in a model and imposes the charge neutrality [48]. Further explanations on the meaning and the way to compute each single term in Eq. 1.53 will be given in the following paragraphs in this subsection. The Helmotz free energies F in Eq. 1.53 are

$$F_{tot} = F_{el} + F_{qh} + F_{ah} \tag{1.54}$$

which are the sum of an electron contribution F_{el} and the quasi-harmonic and anharmonic terms $F_{qh} + F_{ah}$ which take into account phonons. Following Refs. [20, 23] we assume that when carrying out the difference $F_{tot}[X^q] - F_{tot}^{bulk}$ in Eq. 1.53 the respective terms $F_{qh} + F_{ah}$ cancel out and only the difference $F_{el}[X^q] - F_{el}^{bulk}$ is retained. In a thermodynamic system the internal energy E, the Gibbs free energy G and the Hel-

motz free energy F are related by the Legendre transforms $G = F + pV = E - TS + pV$ with S entropy. If we neglect the formation volume V_f and we study the $T \to 0$ limit for the energy we can safely work with total energies instead of G. With these assumptions, instead of using the Gibbs free energy we can work with the quantity [52, 54, 55]

$$E_f\left[X^q\right](E_F) = E_{tot}[X^q] - E_{tot}^{bulk} - \sum_i n_i\mu_i + E_{dil}^q + q(E_F + E_{VB}) \tag{1.55}$$

which is the formation energy for the defect X in charge state q. Eq. 1.55 is the expression used in this work to study the thermodynamics of the defects (Chap. 4). DFT will be used to calculate the total energy terms, $E_{tot}[X^q]$ and E_{tot}^{bulk}, and the chemical potential. Normally the formation energy function of a defect is pictured in a formation energy diagram, like the one in Fig. 1.5. In such diagrams the plots of

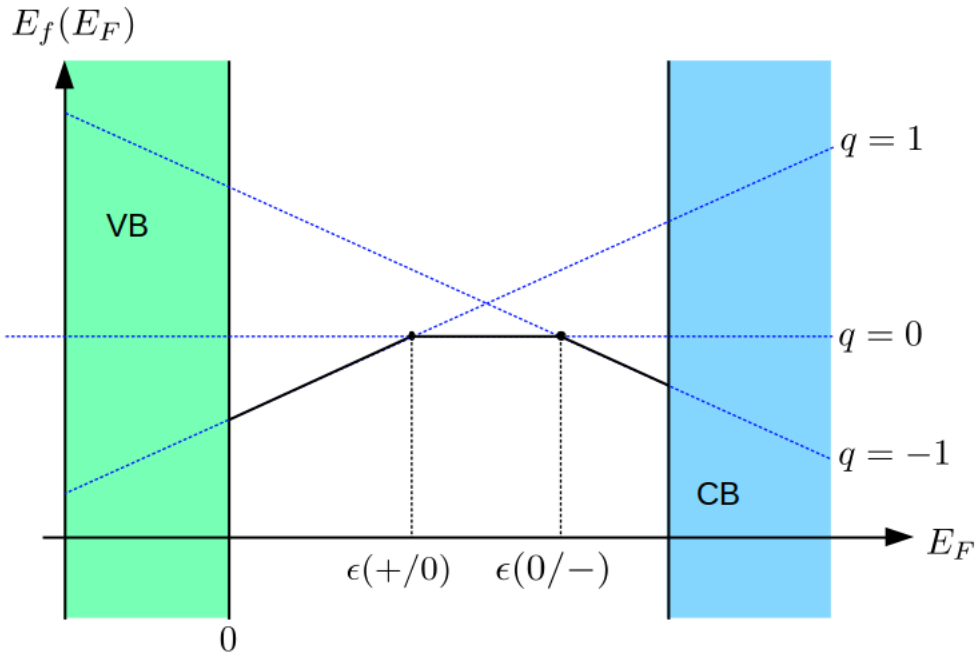

Figure 1.5. – Illustrative example of a formation energy diagram for a defect that can be in charge state $q = -1, 0, 1$. Each dashed line corresponds to a charge state q. The dashed lines become solid black as they enter in the stability band gap range and they are the lowest. The CTLs $\epsilon(+/0)$ and $\epsilon(0/-)$ are also reported.

$E_f\left[X^q\right](E_F)$ are reported for each q and they are linear functions of E_F (dashed blue lines in Fig. 1.5) where E_F is set to 0 at the valence band maximum. The defect X^q is stable if $E_f\left[X^q\right](E_F) > 0$ in a range of $E_{VBM} < E_F < E_{CBM}$ where E_{VBM} and E_{CBM} are the valence and conduction band edges, respectively, and will assume the charge state for which the formation energy is the lowest (solid lines in Fig. 1.5). The Fermi energies where a transition between two charge states q and q' occurs (which are the

intersection between the lines in Fig. 1.5) are called charge transition levels (CTL).

$$\epsilon(q/q') = \frac{E_f\left[X^q\right](E_F=0) - E_f\left[X^{q'}\right](E_F=0)}{q'-q} \tag{1.56}$$

Since normally the diagrams like Fig. 1.5 report the formation energies for several defects at the same time, the CTLs are usually depicted separately. A CTL corresponds to the point of coexistence of two charge states for a given defect and it gives the thermodynamic ionization energy. CTLs can be classified as acceptors ($\epsilon(0/-)$, one electron accepted from the reservoir) and donor levels ($\epsilon(+/0)$, electron donated to the reservoir). Their distance from the band edges determines whether the defect is likely to be thermally ionized at room temperature. On the basis of this distance a CTL can be classified as deep or shallow levels. A donor level will be shallow if it is close to the CBM and a deep level otherwise, while an acceptor level is shallow if it is close to the VBM. We now give more details about the chemical potential and the dilute limit correction.

Chemical potential In order to create the defect the host material has to exchange one or more atoms with a thermodynamic reservoir (something different from the electron reservoir mentioned in this subsection). For each atom of type i, n_i is the number of atoms added ($n_i > 0$) or removed ($n_i < 0$), while μ_i is the chemical potential of the corresponding type of atom. Consider for example a boron vacancy in wBN, V_B, in this case $n_B = -1$ while for a substitutional carbon dimer C_BC_N one has $n_B = -1$, $n_N = -1$ and $n_C = +2$. Usually the chemical potential μ_i is referenced with respect to the value μ_i^{ref} which is its limiting value, i.e. if $\mu_i > \mu_i^{ref}$ then the species i precipitates in its pristine form reservoir. The calculation of μ_i^{ref} for the reservoir i is not trivial and should consider the conditions (pressure and temperature) under which the crystal with the defects is formed. Given the conditions of creation of wBN illustrated in Sec. 3.1, we can consider as reservoirs the gas phase for nitrogen and the solid phase for boron. In the same way we used the diamond phase for carbon. For each of these phases the reference chemical potential μ_i^{ref} in general depends on temperature and pressure but it can be well approximated to the total energy per elementary unit. Thus for the atom of type i one chooses the relevant phase and calculate its total energy $E_{tot}^{(i)}$ with a DFT calculation on its unit cell made of N_i atoms while for a compound like BN one should consider the number of BN pairs in the supercell. The resulting chemical potential will be just

$$\mu_i^{ref} = \frac{E_{tot}^{(i)}}{N_i} \tag{1.57}$$

For example for carbon there are 2 atoms in the unit cell and the total energy should be divided by 2. If for BN we have a supercell of 576 atoms we have to divide the total energy by $576/2 = 288$ because there are 288 B-N pairs in a supercell. As Boron and Nitrogen must be exchanged between their reservoirs and the crystal with the defect, the chemical potential μ_i is in general different from the limiting value μ_i^{ref}. The

chemical equilibrium is given by the condition on the chemical potentials of wBN, B and N where the compound co-exists with the singular components

$$\mu_{\mathrm{BN}} = \mu_{\mathrm{B}} + \mu_{\mathrm{N}} \tag{1.58}$$

μ_{BN} is referenced to the pure bulk phases of the constituents by mean of the formation enthalpy ΔH

$$\mu_{\mathrm{BN}} = \mu_{\mathrm{B}}^{ref} + \mu_{\mathrm{N}}^{ref} + \Delta H \tag{1.59}$$

Therefore

$$\Delta H = \left(\mu_{\mathrm{B}} - \mu_{\mathrm{B}}^{ref}\right) + \left(\mu_{\mathrm{N}} - \mu_{\mathrm{N}}^{ref}\right) \tag{1.60}$$

In the boron-rich limit the B atoms will precipitate to its reference phase. This condition is avoided if

$$\mu_{\mathrm{B}} < \mu_{\mathrm{B}}^{ref} \tag{1.61}$$

From the point of view of the Nitrogen atoms the condition Eq. 1.61 is equivalent to

$$\Delta H - \left(\mu_{\mathrm{N}} - \mu_{\mathrm{N}}^{ref}\right) = \mu_{\mathrm{B}} - \mu_{\mathrm{B}}^{ref} < 0 \tag{1.62}$$

where we used Eq. 1.60. In the same way, The N atoms will not return to its pristine form for

$$\mu_{\mathrm{N}} < \mu_{\mathrm{N}}^{ref} \tag{1.63}$$

From the point of view of Boron atoms the condition Eq. 1.63 is equivalent to

$$\Delta H - \left(\mu_{\mathrm{B}} - \mu_{\mathrm{B}}^{ref}\right) = \mu_{\mathrm{N}} - \mu_{\mathrm{N}}^{ref} < 0 \tag{1.64}$$

Eqs. 1.61, 1.62, 1.63 and 1.64 give the limiting values for the chemical potentials :

$$\mu_{\mathrm{BN}} - \mu_{\mathrm{N}}^{ref} = \mu_{\mathrm{B}}^{ref} + \Delta H < \mu_{\mathrm{B}} < \mu_{\mathrm{B}}^{ref} \tag{1.65a}$$

$$\mu_{\mathrm{BN}} - \mu_{\mathrm{B}}^{ref} = \mu_{\mathrm{N}}^{ref} + \Delta H < \mu_{\mathrm{N}} < \mu_{\mathrm{N}}^{ref} \tag{1.65b}$$

where we used Eq. 1.60 to have the last identities on the right. In Eq. 1.65a the right limit corresponds to the B-rich (N-poor) condition, while the left limit corresponds to the N-rich (B-poor) condition. Conversely, in Eq. 1.65b the right limit corresponds to the N-rich (B-poor) condition and the left limit to the B-rich (N-poor) condition. In practice one usually calculates the formation energy Eq. 1.55 in the two limiting values, since one does not know *a priori* the real value of μ. One should also mention the fact that choosing the right reference phase for a given element can be quite tricky. In our case we chose the biatomic pure phase N_2 and diamond for nitrogen and carbon respectively. For boron one the choice is more difficult since there are many options. In this work we chose the α-rhombohedral polymorph as B reference phase, since it is the most stable. Another option could have been the β-rhombohedral polymorph which is almost stable as the α-rhombohedral. One can also use more complex compounds, the choice can be dictated by growth conditions. In Ref. [48] for

a defect where oxygen is involved a compound B_2O_3 is chosen as O reference phase. Finally we should mention that it is possible in principle to add the temperature and pressure dependence in computing the reference chemical potentials μ_i^{ref} as it is done in Ref. [20].

Dilute limit correction Due to the limited size of the supercells that can be feasibly computed in modern HPCs for a DFT calculation, the simulated crystal will present a density of the defect much higher than in the real crystal. As a consequence a fictitious interaction between the defect and its periodic images is introduced since the lattice parameter is smaller than the average distance between the impurities in a real material. These spurious interactions that we want to eliminate from a formation energy calculation have three causes [56] :

- a spurious overlap of the defect-induced wavefunctions;
- spurious strains at the boundaries of the supercell;
- for charged defect, a spurious electrostatic interaction.

We will neglect the first two sources of error in the calculation of the formation energy since it is the third one to dominate in most cases [56]. We thus focus in this paragraph on how to calculate the dilute limit correction term E_{dil}^q to take into account this fictitious electrostatic interaction. There are several schemes to calculate the correction approximately. Leslie and Gillan [57] considered an array of charged point defects interacting with a neutralizing background charge distribution which in the supercell approach is necessary to avoid the divergence of the electrostatic energy. They gave an expression, later corrected by Makov and Payne [58] by adding a quadrupole correction :

$$E_{dil}^q = -\frac{\alpha q^2}{2\epsilon L} - \frac{2\pi qQ}{3L^3} + o(L^{-5}) \tag{1.66}$$

where α is the Madelung constant which depends on the lattice, q is the charge of the defect, Q is the quadrupole moment, ϵ is the macroscopic dielectric constant of the host and L the lattice parameter. The correction Eq. 1.66 is not reliable [59] and another proposed method to calculate E_{dil}^q was to fit a function of the type $AL^{-1} + BL^{-n}$ in a series of formation energy calculations with increasing L to find the convergence value (limit for $L \to \infty$) [4] [59]. In this work we use the dilute correction scheme introduced by Freysoldt, Neugebauer and Van de Walle (FNV) [60, 56] which we now outline.

Let us consider, for the generic defect X^q with defect wavefunction ψ_{def}, the formation energy $E_f^{DFT}[X^q]$ computed via DFT in a supercell, where the defect interacts with its periodic images, and $E_f^{isol}[X^q]$ the "real" formation energy of the system where the defect density is low (in DFT that would correspond to a very large supercell where the periodic images are far away from the defect). We reference these formation energies to the corresponding systems where the defect is neutral, i.e. we evaluate the quantities

$$\Delta E_f^{DFT} = E_f^{DFT}[X^q] - E_f^{DFT}[X^0] \tag{1.67a}$$

4. A value $n = 3$ is found for neutral defects [59].

$$\Delta E_f^{isol} = E_f^{isol}[X^q] - E_f^{isol}[X^0] \tag{1.67b}$$

The correction is given by their difference, i.e. the quantity

$$E_{dil}^q = \Delta E_f^{DFT} - \Delta E_f^{isol} \tag{1.68}$$

In the FNV scheme one splits the dilute correction E_{dil}^q into a long range (denoted by the subscript lr) and a short range contribution (denoted by the subscript sr)

$$E_{dil}^q = E_{lr}^q + E_{sr}^q \tag{1.69}$$

We want to write the terms E_{lr}^q and E_{sr}^q explicitly.

We start by defining the potential created by the single defect in the supercell, V^q, as the quantity

$$V^q = V_{def}^q - V_{def}^0 - V_{bulk} \tag{1.70}$$

where V_{def}^q, V_{def}^0 and V_{bulk} are the sum of the Hartree and the ionic potential for the defective system in the charge states q, the defective system in the charge state 0 and the pristine crystal, respectively. The term V_{bulk} has been subtracted to use the pristine system as reference value. The potential $\overline{V}^q$ due to all the periodic images of coordinate $\boldsymbol{R}$ is a linear combination of the $V^q(\boldsymbol{r}+\boldsymbol{R})$

$$\overline{V}^q(\boldsymbol{r}) = \frac{1}{\Omega_{sc}} \sum_{\boldsymbol{G}} V^q(\boldsymbol{G}) \mathrm{e}^{\mathrm{i}\boldsymbol{G}\cdot\boldsymbol{r}} \tag{1.71}$$

with Ω_{sc} volume of the supercell and $V^q(\boldsymbol{G})$ Fourier transform of the single defect potential $V^q(\boldsymbol{r})$

$$V^q(\boldsymbol{G}) = \int_{\Omega_{cr}} \mathrm{d}\boldsymbol{r}' V^q(\boldsymbol{r}) \mathrm{e}^{-\mathrm{i}\boldsymbol{G}\cdot\boldsymbol{r}'} \tag{1.72}$$

The integral in Eq. 1.72 is over the whole crystal volume Ω_{cr} and diverges for $\boldsymbol{G}=0$. Instead of the sum Eq. 1.71 we need to use a modified sum

$$\tilde{V}^q(\boldsymbol{r}) = \frac{1}{\Omega_{sc}} \sum_{\boldsymbol{G}\neq 0} V^q(\boldsymbol{G}) \mathrm{e}^{\mathrm{i}\boldsymbol{G}\cdot\boldsymbol{r}} \tag{1.73}$$

Not including the term $\boldsymbol{G}=0$ in $\tilde{V}^q$ means that we are applying a neutralizing background charge distribution $n_q = -\frac{q}{\Omega_{sc}}$ that avoids the divergence. The quantity $\tilde{V}^q(\boldsymbol{r}) - V^q(\boldsymbol{r})$ is the excess potential with which the defect charge density $q_{def}(\boldsymbol{r}) = q\left|\psi_{def}(\boldsymbol{r})\right|^2$ and the neutralizing charge distribution n_q interact. They give origin to the energy contribution

$$E_{int} = \frac{1}{2}\int_{\Omega_{sc}} \mathrm{d}\boldsymbol{r} \left(q_{def}(\boldsymbol{r}) + n_q\right)\left(\tilde{V}^q(\boldsymbol{r}) - V^q(\boldsymbol{r})\right) \tag{1.74}$$

where the factor $\frac{1}{2}$ avoids the double counting. Nonetheless, the neutralizing background n_q also interacts with the isolated defect potential $V^q(\boldsymbol{r})$ and gives one more

energy term

$$E_{neu} = \int_{\Omega_{sc}} \mathrm{d}\boldsymbol{r}\, n_q V^q(\boldsymbol{r}) \tag{1.75}$$

The energy correction that we want to include in the formation energy calculation is $E^q_{dil} = E_{int} + E_{neu}$. By adding Eq. 1.74 to Eq. 1.75 we get

$$E^q_{dil} = \int_{\Omega_{sc}} \mathrm{d}\boldsymbol{r} \left[\frac{1}{2} \left(q_{def}(\boldsymbol{r}) + n_q \right) \left(\tilde{V}^q(\boldsymbol{r}) - V^q(\boldsymbol{r}) \right) + n_q V^q(\boldsymbol{r}) \right] \tag{1.76}$$

E^q_{dil} is not useful in the form of Eq. 1.76.

The trick of the FNV scheme is to split the potentials V^q and $\tilde{V}^q$ in a long range and a short range component

$$V^q = V^q_{lr} + V^q_{sr} \implies V^q_{sr} = V^q - V^q_{lr} \tag{1.77a}$$

$$\tilde{V}^q = \tilde{V}^q_{lr} + \tilde{V}^q_{sr} \implies \tilde{V}^q_{sr} = \tilde{V}^q - \tilde{V}^q_{lr} \tag{1.77b}$$

and introduce a model charge distribution $q_{mod}(\boldsymbol{r})$ for the long range part only. The idea is to evaluate the quantity $E_{int} + E_{neut}$ as a long range term plus a correction that contains all the information on the short range behaviour of the defect potential, with the imposition that the short range potential goes to 0 at the edge of the supercell. By analogy to Eq. 1.76 we impose that the long range interaction energy E^q_{lr} is

$$E^q_{lr} = \int_{\Omega_{sc}} \mathrm{d}\boldsymbol{r} \left[\frac{1}{2} \left(q_{mod}(\boldsymbol{r}) + n_q \right) \left(\tilde{V}^q_{lr}(\boldsymbol{r}) - V^q_{lr}(\boldsymbol{r}) \right) + n_q V^q_{lr}(\boldsymbol{r}) \right] \tag{1.78}$$

Therefore Eq. 1.69 becomes

$$\begin{aligned} E^q_{sr} = &\int_{\Omega_{sc}} \mathrm{d}\boldsymbol{r} \left[\frac{1}{2} \left(q_{mod}(\boldsymbol{r}) + n_q \right) \left(\tilde{V}^q(\boldsymbol{r}) - V^q(\boldsymbol{r}) \right) + n_q V^q(\boldsymbol{r}) \right] - \\ &\int_{\Omega_{sc}} \mathrm{d}\boldsymbol{r} \left[\frac{1}{2} \left(q_{mod}(\boldsymbol{r}) + n_q \right) \left(\tilde{V}^q_{lr}(\boldsymbol{r}) - V^q_{lr}(\boldsymbol{r}) \right) + n_q V^q_{lr}(\boldsymbol{r}) \right] \end{aligned} \tag{1.79}$$

Once we choose a $q_{mod}(\boldsymbol{r})$ the long range potential is known

$$V^q_{lr}(\boldsymbol{r}) = \frac{1}{\epsilon} \int_{\Omega_{cr}} \mathrm{d}\boldsymbol{r}' \frac{q_{mod}(\boldsymbol{r}')}{|\boldsymbol{r} - \boldsymbol{r}'|} \tag{1.80}$$

where the dielectric constant ϵ takes into account the screening of the model charge distribution $q_{mod}(\boldsymbol{r})$. The periodic long range potential $\tilde{V}^q_{lr}(\boldsymbol{r})$ can be obtained from $V^q_{lr}(\boldsymbol{r})$ in an analogous way as we already did in Eq. 1.73 by building its Fourier series. Eq. 1.77b then allows to determine $\tilde{V}^q_{sr}$. The short range periodic part of the potential $\tilde{V}^q_{sr}$ can be seen, up to a constant C, as the superposition (over all periodic supercells of the crystal at position $\boldsymbol{R}$) of the isolated defect short range interaction evaluated in

the coordinate $\boldsymbol{r}+\boldsymbol{R}$, $V_{sr}^{q}(\boldsymbol{r}+\boldsymbol{R})$.

$$\tilde{V}_{sr}^{q}(\boldsymbol{r}) = \sum_{\boldsymbol{R}} V_{sr}^{q}(\boldsymbol{r}+\boldsymbol{R}) + C \tag{1.81}$$

Since by definition we imposed that the short range potential should be 0 at the edge of the supercell we make the approximation for Eq. 1.81

$$\tilde{V}_{sr}^{q}(\boldsymbol{r}) \approxeq V_{sr}^{q}(\boldsymbol{r}) + C \tag{1.82}$$

Therefore Eq. 1.82 with Eq. 1.77b gives

$$V_{sr}^{q}(\boldsymbol{r}) \approxeq \tilde{V}^{q}(\boldsymbol{r}) - \tilde{V}_{lr}^{q}(\boldsymbol{r}) - C \tag{1.83}$$

The short range contribution to the dilute correction E_{sr}^{q} is parametrized as $E_{sr}^{q} = -q\Delta$ with

$$\Delta = \frac{1}{\Omega_{sc}} \int_{\Omega_{sc}} \mathrm{d}\boldsymbol{r}\, V_{sr}^{q}(\boldsymbol{r}) \tag{1.84}$$

Eqs. 1.84, 1.83 and 1.80 give all the quantities needed to calculate the right side of Eq. 1.79 and obtain E_{dil}^{q}. The choice one makes for the q_{mod} is crucial. In [56] and [60] a model is proposed for the charged carbon vacancy in diamond $\mathrm{V_C^{2+}}$ for which the original Gaussian model for q_{mod} could not give good results.

$$q_{mod}(r) = qxN_{\alpha}\mathrm{e}^{-\frac{r}{\alpha}} + q(1-x)N_{\beta}\mathrm{e}^{-\frac{x^2}{\beta^2}} \tag{1.85}$$

with $N_{\alpha} = \frac{1}{8\pi\alpha^3}$ and $N_{\beta} = \frac{1}{\pi^{3/2}\beta^3}$. The second term of Eq. 1.85 is the localized part of the charge and β is not important as long as this term stays localized. Terms x and α are obtained by fitting the wavefunction on the supercell.

The FNV scheme is practically implemented by the `sxdefectalign` code[61]. The needed Hartree and ionic potentials are readily available from standard Quantum Espresso post-processing. V_{lr}^{q} (Eq. 1.80) and thus $\tilde{V}_{lr}^{q}$ are calculated using the model charge Eq.1.85 and the dielectric constant ϵ. A first run of the program gives the difference $\tilde{V}_{sr}^{q} = \tilde{V}^{q} - \tilde{V}_{lr}^{q}$ which must reach a plateau C at the supercell edge (see Eq. 1.83). This C is then used in a second run of the program to adjust the alignment so that V_{sr}^{q} is 0 far from the defect. The second run finally gives the value of E_{dil}^{q}. It is now worth briefly mentioning several problems that affect the FNV scheme.

1. It is not clear which should be the choice of the dielectric constant used in Eq. 1.80. Following the arguments of Kumagai and Oba [62] we concluded that the ϵ_{stat} static dielectric constant should be used in case the defective structure is relaxed and ϵ_{∞} in case the atomic positions are fixed. We opted for the former option and we used the experimental value found by Segura *et al.* [63] without the uncertainty, $\epsilon_{stat} = 6.65$;
2. in the first run the plateau C is found in a way that is not strictly rigorous. One looks at the plot of the quantity $\tilde{V}^{q} - \tilde{V}_{lr}^{q}$ and loosely finds the plateau C in the area where the oscillations are dumped far from the defect;

3. The quantity $\tilde{V}^q - \tilde{V}^q_{lr}$ is plotted in the three directions separately and one can find a different C_α plateau for each coordinate $\alpha = x, y, z$. This fact makes difficult to find the dilute correction for anisotropic materials such as wBN. In this work we used an average $\langle C \rangle$ over the three directions

$$\langle C \rangle = \frac{\sum_\alpha C_\alpha}{3}. \tag{1.86}$$

1.6. Conclusions

In this Chapter we outlined the state-of-the-art techniques that we are going to use to explore the ground state properties of wBN as a pure intrinsic material as well as a defect host. We stated the problem of solid state physics by defining a Many-Body Hamiltonian for both the atoms and the electrons in a material in the most general possible way. Then we established a set of approximations in order to diagonalize it. We separated the electron from the lattice problem using the Born-Oppenheimer approximation so that we can then focus on the electronic problem using the Density Functional Theory (DFT). In this theory one replaces the complicated interacting many-electron problem with an equivalent pseudoelectron problem where the particles are easily treated as they are non-interacting. By minimizing the energy for this equivalent system one obtains the Kohn-Sham equations which are practically solved in a self-consistent loop by a DFT code like Quantum Espresso. The quality of a self-consistent calculation is subjected to a careful choice of the convergence parameters concerning the number of reciprocal lattice vectors used to calculate the Kohn-Sham states and the number of sampling $\boldsymbol{k}$ points considered in the Brillouin zone. The DFT formalism can also be extended to compute the vibrational properties of a material (the Density Functional Perturbation Theory). Finally we provided a scheme to treat a material in presence of defects using DFT. We introduced the formation energy of a defect which is the main quantity that governs its concentration. The formation energy is computed using a supercell approach. Each one of the terms in the formation energy expression have been discussed in relation to the way to calculate them in a DFT context. Firstly, one has to consider the ability of a defect to exchange electrons with the environment (i.e. other defects in the crystal). Secondly, the fact that in order for a defect to form, the pristine material needs to exchange atoms with the defect reservoir. Lastly, one needs to take into account the electrostatic spurious interactions arising from the limitations in computing large supercells.

2. Excited states properties

In this chapter we depart from the theory outlined in Chap. 1 which has been mainly conceived to study the ground state properties of materials. Although those methodologies are particularly useful especially in providing the total energies and the relaxed atomic positions, a more refined theory is needed to study electronic excitations. A good option is the many-body perturbation theory ("MBPT") which is the one applied in this work to explore the excited states of wBN.

In Sec. 2.1 after presenting the quasiparticle concept and an example of experiments that are not well explained in the context of DFT, we introduce the main ingredient of MBPT, that is the Green's function. We present the way to take into account the many-body and screening effects when computing the electronic band structure with reasonable approximations. In Sec. 2.2 we will present the Bethe-Salpeter equation (BSE) which delivers information about the neutral excitations of the crystal while in Sec. 2.3 we will see how the BSE can be used in practice to link the excited state properties to the optics of the material under study. Finally in Secs. 2.4 and 2.5 we will present two different methodologies to study the optical properties of defects.

2.1. Many Body Perturbation Theory and the *GW* approximation

Although DFT has been rather successful in providing a good description of geometries and electronic densities for solids in their ground state, it is not appropriate to study excited states. In general in spectroscopy experiments one excites the system by perturbing it and measuring its response to such perturbation. We briefly present here three prototypical experiments that can be used to show that a ground state theory such as DFT can not satisfactorily describe an excited system, i.e. angle-resolved photo-emission spectroscopy ("ARPES") (Fig. 2.1, panel a), Inverse ARPES (Fig. 2.1, panel b) and absorption (Fig. 2.1, panel c).

In ARPES experiments a photon excites an electron which is ejected from the sample, leaving behind a positively charged hole h^+ in the valence band. Therefore ARPES allows us to measure the density and energy of occupied states. Conversely, in inverse ARPES a free electron is injected into the sample and decays to the conduction band minimum by emitting a photon, allowing to study the unoccupied states. Both experiments are not well described by a one-particle ground state theory like DFT since it does not take into account the reaction and relaxation of all the other electrons in the sample after one electron is added or removed (polarization and screening effects). A way to include such effects while retaining the one-particle picture is by introducing

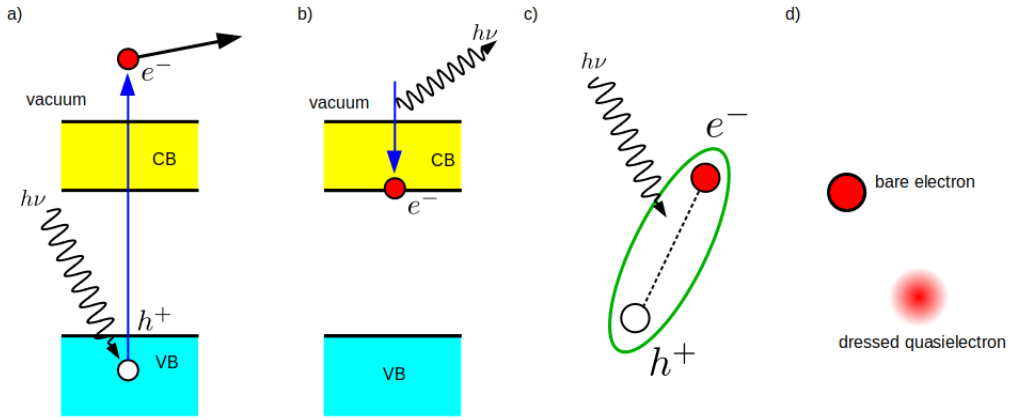

Figure 2.1. – Excitation process of an electron in ARPES (panel a)) and Inverse ARPES (panel b)). If the electron is not excited into a free state one has absorption and the electron e^- and the positive hole h^+ can form a bound exciton (panel c). Panel d) is a pictorial representation of an electron and a quasielectron.

the concept of quasiparticle (quasielectrons or quasiholes). A quasielectron can be understood as an electron "dressed" by a cloud of other electrons surrounding it, which renormalizes its excitation energy (see Fig. 2.1, panel d).

Unlike ARPES and inverse ARPES, in absorption experiments a neutral excitation occurs. The electron is not ejected from the system and it is just excited to another state, creating an electron-hole pair. The electron-hole pair can eventually form a hydrogen like-bound state (Fig. 2.1 panel c) called exciton. The exciton is a two-particle excitation which is not described by the one-quasiparticle picture (although involving dressed particles) and therefore a more complex theory is needed. This mathematical tool is the Bethe-Salpeter equation (BSE).

Other notable experiments that we can mention in relation to neutral excitations such as absorption are the electron energy loss spectroscopy (EELS) and photoluminescence (PL). In EELS an incoming probe electron transfers its energy either to an electron of the system which is then excited and can form an exciton or to a collective excitation of the electrons (plasmons). In PL one has the recombination of an electron-hole pair, emitting a photon. [1]

In the next sections, we introduce the *ab initio* scheme that has been followed in the present thesis to provide the following quantities :

1. the quasiparticle correction to the band structure computed with DFT, ΔE^{qp}, so that the quasiparticle-corrected band structure is $E^{qp} = E^{DFT} + \Delta E^{qp}$. This correction to DFT results, with few exceptions, in a widening of the band gap computed with DFT;

1. It might be tempting to think PL as simply the inverse of absorption. An important difference is the fact that PL is a spontaneous emission prompted by an interaction with the vacuum, while absorption is mainly caused by the interaction with an external electromagnetic field and the spectra will be in general different.

2. the optics of the material, i.e. its polarizability χ or equivalently its dielectric function ϵ, which are linked to the key quantities of the experiments described above. For example the macroscopic dielectric function determines the absorption spectrum by mean of its imaginary part $\epsilon_2(\omega) = \Im(\epsilon_M(\omega))$. Similarly, the loss function in EELS experiments is given by $-\Im\left(\frac{1}{\epsilon_M(\omega)}\right)$.

2.1.1. Green's function formalism

In the following we introduce a quantity which contains the spectroscopic information that we want, the Green's function G for the interacting many-electron system. The strategy is to write this G as a perturbation expansion starting from the simpler non-interacting system Green's function G_0, where the electron-electron interaction is switched off. This is called Many-Body Perturbation Theory ("MBPT"). Usually there are two ways to write this perturbation theory.

One - the diagrammatic approach - is based on Wick's theorem [64] and it makes use of rules to derive the Feynman diagrams corresponding to each order of expansion. The other method - the Schwinger's functional derivative approach [65, 66] - uses the functional derivative. The latter approach allows to recast the problem in a set of integro-differential equations to be solved in order to find the expansion [67, 68, 65, 66]. In the following paragraphs we sketch the main steps of this scheme.

Note on the notation in use : In what follows we adopt a short notation for convolutions. We denote the set of space, time and spin coordinates of indices α,β and γ with their index itself, i.e. $\alpha = (\boldsymbol{r}_\alpha, t_\alpha, \sigma_\alpha)$, $\beta = (\boldsymbol{r}_\beta, t_\beta, \sigma_\beta)$ and $\gamma = (\boldsymbol{r}_\gamma, t_\gamma, \sigma_\gamma)$. For two quantities A and B we adopt the notation

$$A(\alpha, \overline{\beta})B(\overline{\beta}, \gamma) := \int \mathrm{d}\beta A(\alpha, \beta)B(\beta, \gamma) \tag{2.1}$$

where

$$\int \mathrm{d}\beta := \sum_{\sigma_\beta} \int_\Omega \mathrm{d}\boldsymbol{r}_\beta \int_{-\infty}^{\infty} \mathrm{d}t_\beta \tag{2.2}$$

The integral in space coordinates in Eq. 2.2 is over the whole crystal volume Ω and the sum over the spin coordinate $\sum_\sigma$ will be neglected in the further derivations (the definition remains nonetheless valid in the case we want to explicitly include spin in our theory). We will adopt a similar notation in the case the time variable is not taken into account : for the partial coordinate $x_\alpha := (\boldsymbol{r}_\alpha, \sigma_\alpha)$ the integration is

$$\int \mathrm{d}x_\alpha := \sum_{\sigma_\alpha} \int_\Omega \mathrm{d}\boldsymbol{r}_\alpha \tag{2.3}$$

For a function f of a complete variable 1 and a partial coordinate x_2 it is possible to use a δ to reconstruct the function of the complete variable, e.g.

$$f(1, x_2)\delta(t_1, t_2) = f(1, 2) \qquad f(1, x_2) = f(1, x_2, \overline{t_2})\delta(\overline{t_2}, t_1) \tag{2.4}$$

The same rule applies if we have a function v local in its complete variable and we want to link it with its non-local counterpart :

$$v(1)\delta(1,2) = v(1,2) \qquad v(1) = v(1\overline{2})\delta(\overline{2},1) \tag{2.5}$$

If f is a function of two variables 1 and 2, we imply the limit with the notation

$$f(1,1^+) = \mathrm{tr}_\sigma \lim_{\boldsymbol{r}_2 \to \boldsymbol{r}_1} \lim_{t_2 \to t_1} f(1,2) \tag{2.6}$$

Given a function f with inverse f^{-1} and two functions v and w, the following "chain rules" apply

$$\frac{\delta f(1)}{\delta v(2)} = \frac{\delta f(1)}{\delta w(\overline{3})} \frac{\delta w(\overline{3})}{\delta v(2)} \tag{2.7a}$$

$$\frac{\delta f(u(1),2,3)}{\delta u(4)} = -f(u(1),2,\overline{2'}) \frac{\delta f^{-1}(u(1),\overline{2'},\overline{3'})}{\delta u(4)} f(u(1),\overline{3'},3) \tag{2.7b}$$

where $1'$ and $2'$ are understood to be new variables unrelated to 1 and 2. Throughout this chapter, we will often introduce new indices or change their names in a consistent way. Lastly, given a function f, its inverse is the function f^{-1} such that

$$f(1,\overline{3}) f^{-1}(\overline{3},2) = \delta(1,2) \tag{2.8}$$

Hamiltonian Since we are interested in simulating experiments where the number of particles may vary it is convenient to work in the second quantization formalism. The many-body Hamiltonian in second quantization reads

$$\hat{H} = \int \mathrm{d}x \hat{\psi}^\dagger(x) \hat{h}_0(\boldsymbol{r}) \hat{\psi}(x) + \int \mathrm{d}x \mathrm{d}x' \hat{\psi}^\dagger(x) \hat{\psi}^\dagger(x') v(\boldsymbol{r},\boldsymbol{r}') \hat{\psi}(x') \hat{\psi}(x) \tag{2.9}$$

where $\hat{h}_0$ includes the kinetic energy and the ionic local potential while the interaction term v is the Coulomb repulsion between two electrons $v(\boldsymbol{r},\boldsymbol{r}') = e^2/\left|\boldsymbol{r}-\boldsymbol{r}'\right|$. We now perturb the system with an external potential V_{ext} and derive the linear response of the system to such field. V_{ext} is just a mathematical trick to introduce, in the problem, the perturbation which the system undergoes during an experiment. We require V_{ext} to be scalar, Hermitian and non-local in space but local in time. After we have derived the quantities that we want, we will make the limit for $V_{ext} \to 0$ and eliminate it from the equations. The interaction Hamiltonian corresponding to V_{ext} is

$$\hat{H}' = \int \mathrm{d}x \mathrm{d}x' \hat{\psi}^\dagger(x) V_{ext}(x,x',t) \hat{\psi}^\dagger(x') \tag{2.10}$$

and the total Hamiltonian becomes $\hat{H}_{tot} = \hat{H} + \hat{H}'$. We may exploit the fact that we have a total Hamiltonian $\hat{H}_{tot}$ split into an original Hamiltonian $\hat{H}$ and a new interacting Hamiltonian $\hat{H}'$ to go from the Schrödinger picture to Dirac's interaction picture. The

field operators $\hat{\psi}$ become

$$\hat{\psi}(1) = \mathrm{e}^{\frac{i}{\hbar}\hat{H}t_1}\hat{\psi}(x_1)\mathrm{e}^{-\frac{i}{\hbar}\hat{H}t_1} \tag{2.11a}$$

$$\hat{\psi}^\dagger(1) = \mathrm{e}^{\frac{i}{\hbar}\hat{H}t_1}\hat{\psi}^\dagger(x_1)\mathrm{e}^{-\frac{i}{\hbar}\hat{H}t_1} \tag{2.11b}$$

Note that $\hat{\psi}^\dagger(1)$ is defined by making the h.c. first and then going from the Schrödinger picture to Dirac's picture. The interaction Hamiltonian becomes

$$\hat{H}'_I = \mathrm{e}^{\frac{i}{\hbar}\hat{H}t_1}\hat{H}'\mathrm{e}^{-\frac{i}{\hbar}\hat{H}t_1} \tag{2.12}$$

Dirac's interaction picture is similar to the Heisenberg's picture, with the difference that here the operators evolve only with $\hat{H}$ and not with the total Hamiltonian. The time evolution operator $\hat{S}(t_1,t_2)$ from t_1 to t_2 is

$$\hat{S}(t_1,t_2) := \mathrm{e}^{-\frac{i}{\hbar}\int_{t_1}^{t_2}\mathrm{d}t\hat{H}'_I(t)} \tag{2.13}$$

from which the limit $t_a \to -\infty$ and $t_b \to \infty$ gives

$$\hat{S} := \mathrm{e}^{-\frac{i}{\hbar}\int_{-\infty}^{\infty}\mathrm{d}t\hat{H}'_I(t)} \tag{2.14}$$

These definitions will be used for what comes next.

Green's function We now introduce the crucial quantity in MBPT which allows us to go from the Kohn-Sham non-interacting particle picture to a quasiparticle formalism.

For a system of N particles the one-particle Green's function is defined as the time ordered expectation value for the field operators $\hat{\psi}$ and $\hat{\psi}^\dagger$ in Heisenberg's picture [64]

$$i\hbar G(1,2) = \frac{\langle N\left|T\left[\hat{\psi}(1)\hat{\psi}^\dagger(2)\right]\right|N\rangle}{\langle N|N\rangle} = \frac{1}{\langle N|N\rangle}\begin{cases}\langle N|\hat{\psi}(1)\hat{\psi}^\dagger(2)|N\rangle & \text{for } t_1 > t_2\\ -\langle N|\hat{\psi}^\dagger(2)\hat{\psi}(1)|N\rangle & \text{for } t_2 > t_1\end{cases} \tag{2.15}$$

where $|N\rangle$ is the ground state of the N-electron system. The minus sign in the second line of the Eq. 2.15 accounts for the anticommutation rules for Fermions [2]. The first line of Eq. 2.15 gives the probability amplitude for an electron to propagate from position $\boldsymbol{r}_2$ at time t_2 to position $\boldsymbol{r}_1$ at time t_1. The second line gives the probability amplitude for a hole to propagate from position $\boldsymbol{r}_1$ at time t_1 to a position $\boldsymbol{r}_2$ at time t_2. From Eq. 2.15 we see the advantages of using the Green's function. Indeed, by construction it forces us to work with electrons and holes on the same footing, so that there is no propagation of electrons without propagation of a hole. Another advantage is the fact that the Green's function contains information on observables,

2. It should be kept in mind that the time ordering operator T is not an operator in the mathematical sense. It is a symbol that indicate in which order we should let several operators act on a state depending on time. This is the reason why exchanging the order of two fermionic operators the anticommutation rules must be fulfilled.

without the necessity of knowing the entire complicated N-particle wavefunction. For example, G contains the information on the ground state energy of the system through the Galitskii-Migdal formula [69] or the expectation value of a generic one-particle observable $\hat{O}$ [64]. In particular the Green's function is related to the expectation value of the electron density

$$\langle\hat{\rho}(1)\rangle = -i\hbar G(1,1^+) = \mathrm{tr}_\sigma \lim_{\boldsymbol{r}_2\to\boldsymbol{r}_1}\lim_{t_2\to t_1} G(\boldsymbol{r}_1,t_1,\boldsymbol{r}_2,t_2) \tag{2.16}$$

The Green's function is particularly useful in treating the removal or addition of an electron to the system. By performing a Fourier transform on G into the $\boldsymbol{k},\omega$-space and using the completeness relations for the sth eigenstate $|N+1,s\rangle$ ($|N-1,s\rangle$) of the $N+1$ ($N-1$) interacting system, we have the Lehmann's representation of G [70, 71]

$$G(x_1,x_2,\omega) = \sum_s \frac{f_s(x_1)f_s^*(x_2)}{\omega - E_s + i\eta\cdot\mathrm{sgn}(\mu - E_s)} \tag{2.17}$$

where the small convergence term η has been added and we took into account that the chemical potential is the minimal (maximal) energy for addition (removal). f_s are the Dyson's orbitals

$$f_s(x) = \begin{cases} \langle N|\psi(x)|N+1,s\rangle & \text{with } E_s = E_{N+1,s} - E_N \quad \text{if } E_s \geq \mu \\ \langle N-1,s|\psi(x)|N\rangle & \text{with } E_s = E_N - E_{N-1,s} \quad \text{if } E_s < \mu \end{cases} \tag{2.18}$$

From the Lehmann's representation it is possible to write G as [71]

$$G(x_1,x_2,\omega) = \int_{-\infty}^{\infty} \mathrm{d}E \frac{A(x_1,x_2,E)}{\omega - E} \tag{2.19}$$

which defines the spectral function A

$$A(x_1,x_2,\omega) = \sum_s f_s(x_1)f_s^*(x_2)\delta(\omega - E_s) \tag{2.20}$$

normalized as $\int_{-\infty}^{\infty}\mathrm{d}\omega A(x_1,x_2,\omega) = \delta(x_1,x_2)$. The spectral function is closely related to the ARPES spectra. A particular feature of the spectral function is that

$$A(x_1,x_2,\omega) = \frac{1}{\pi}|\Im(G(x_1,x_2,\omega))| \tag{2.21}$$

Eq. 2.20 gives a formal justification to the concept of quasiparticle introduced in Sec. 2.1. In the case of non-interacting electrons the Dyson's amplitudes are all 0 unless $|N-1\rangle$ ($|N+1\rangle$) differs from $|N\rangle$ by only one orbital. If this is the case then the peaks of A are just Dirac's deltas corresponding to E_s. In case of interacting particles those peaks will assume a Lorentzian profile. Moreover the removal (addition) of an electron may also induce other excitations which appear in the (inverse) ARPES spectra as "satellites". An example are collective excitations called plasmons (see Fig. 2.2).

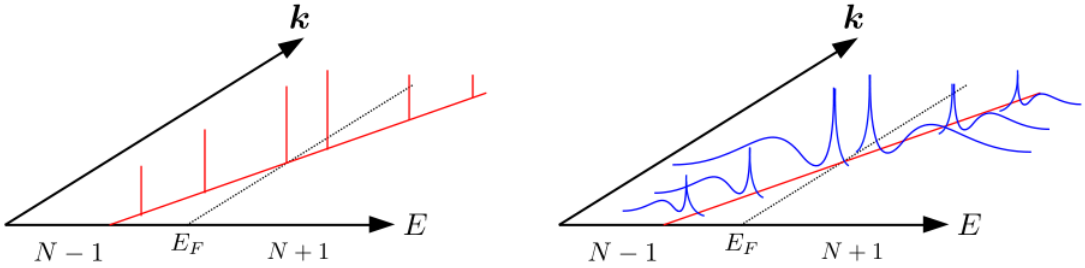

Figure 2.2. – Evolution of the poles of the spectral function when we pass form the non interacting system (left) to an interacting system (right), also satellites due to plasmons and other excitations appear.

In interaction picture the Green's function is rewritten as

$$i\hbar G(1,2) = \frac{\langle N|T[\hat{S}\hat{\psi}(1)\hat{\psi}^\dagger(2)]|N\rangle}{\langle N|\hat{S}|N\rangle} \tag{2.22}$$

In order to pursue the goal of expanding the Green's function we need to introduce the second order Green's function

$$-\hbar^2 G_2(1,2,3,4) = \frac{\langle N|T[\hat{S}\hat{\psi}(1)\hat{\psi}(2)\hat{\psi}^\dagger(4)\hat{\psi}^\dagger(3)]|N\rangle}{\langle N|\hat{S}|N\rangle} \tag{2.23}$$

One could analogously define a G_3, G_4 etc. as long the number of field operators in the numerator is even and the number of $\hat{\psi}$ is equal to the number of $\hat{\psi}^\dagger$ otherwise one would have a product between states of different number of particles. In contrast with this notation, the symbol G_0 indicates a one-particle Green's function for the non-interacting system, i.e. the system where we "switched off" the electron electron interaction[3].

Expansion of G and Dyson's equation In order to employ the Green's function instead of the wavefunction we need to write an equation of motion for it. We enforce the validity of Schrödinger equation by using the Hamiltonian operator

$$i\hbar\frac{\partial}{\partial t_1} = \hat{H}(t_1) \tag{2.24}$$

which by use of the second quantization form of $\hat{H}$ in Eq. 2.9 reads

$$i\hbar\,\hat{\psi}^\dagger(\bar{1})\frac{\partial}{\partial t_1}\hat{\psi}(\bar{1}) = \hat{\psi}^\dagger(\bar{1})\hat{h}_0(\bar{1})\hat{\psi}(\bar{1}) + \hat{\psi}^\dagger(\bar{1})\hat{\psi}^\dagger(\bar{2})\,v(\bar{1},\bar{2})\hat{\psi}(\bar{2})\hat{\psi}(\bar{1}) \tag{2.25}$$

3. G_0 should not be mistaken for a "0-particle" Green's function.

where we could use the complete set of coordinates 1 and 2 by using a Dirac's delta where needed as prescribed in Eq. 2.4. Further manipulations lead to

$$\left(i\hbar\frac{\partial}{\partial t_1}-\hat{h}_0(1)\right)G(1,2)-V_{ext}(1,\overline{3})G(\overline{3},2)+i\hbar v(1,\overline{3})G_2(1,\overline{3}^+,2,\overline{3})=\delta(1,2) \tag{2.26}$$

where we made use of the definition of the two-particle Green's function G_2. A similar equation can be derived for $\hat{\psi}^\dagger(1)$. G_2 has the property

$$G_2(1,3,2,3^+)=G(1,2)G(3,3^+)-\frac{\delta G(1,2)}{\delta V_{ext}(3)} \tag{2.27}$$

which is valid once we built the local $V_{ext}(3)=V_{ext}(3,\overline{4})\delta(3,\overline{4})$. Eq. 2.27 can be used in Eq. 2.26 giving

$$\left(i\hbar\frac{\partial}{\partial t_1}-\hat{h}_0(1)\right)G(1,2)-V_{ext}(1)G(1,2)+i\hbar v(1,\overline{3})\left(G(1,2)G(\overline{3},\overline{3}^+)-\frac{\delta G(1,2)}{\delta V_{ext}(\overline{3})}\right)=\delta(1,2) \tag{2.28}$$

The last term in the left side of Eq. 2.28 implicitly defines a Hartree term $i\hbar v(1,\overline{3})G(1,2)G(\overline{3},\overline{3}^+)$ and an exchange-correlation term $-i\hbar v(1,\overline{3})\frac{\delta G(1,2)}{\delta V_{ext}(\overline{3})}$. We can arrange those terms in a clearer and more compact fashion. We define the Hartree potential and the exchange correlation self-energy as

$$v_H(1,4)=-i\hbar\delta(1,4)v(1,\overline{3})G(\overline{3},\overline{3}^+) \tag{2.29}$$

$$\Sigma_{xc}(1,3)=i\hbar v(1,\overline{3'})\frac{\delta G(1^-,\overline{2})}{\delta V_{ext}(\overline{3'^+})}G^{-1}(\overline{2},3) \tag{2.30}$$

which defines the irreducible self-energy Σ as

$$\Sigma=v_H+\Sigma_{xc} \tag{2.31}$$

so that Eq. 2.26 becomes

$$\left(i\hbar\frac{\partial}{\partial t_1}-\hat{h}_0(1)-V_{ext}(1)\right)G(1,2)-\Sigma(1,\overline{3})G(\overline{3},2)=\delta(1,2) \tag{2.32}$$

Eq. 2.32 is Dyson's equation in differential form. By using the definitions of G_0 and its inverse G_0^{-1} given in Eq. 2.8 and multiplying them in a suitable way from the left and the right in Eq. 2.32 we obtain the integral form of Dyson's equation

$$G(1,2)=G_0(1,2)+G_0(1,\overline{3})V_{ext}(\overline{3})\delta(\overline{3},\overline{4})G(\overline{4},2)+G_0(1,\overline{3})\Sigma(\overline{3},\overline{4})G(\overline{4},2) \tag{2.33}$$

Polarizability and screening Now that we have an equation for the Green's function we focus on the quantities related to the optical properties and we will then connect them with what has been said so far.

In a generic quantum system with unperturbed time-independent Hamiltonian H,

let us suppose that an external field $V_{ext}(2)$ couples at t_2 with the observable $\hat{B}(x_2)$, giving rise to a perturbation $\int \mathrm{d}x_2 V_{ext}(2)\hat{B}(x_2)$ so that the perturbed Hamiltonian is $H + \int \mathrm{d}x_2 V_{ext}(2)\hat{B}(x_2)$. This perturbation will result in a response of the system which is expressed as a change of the expectation value of the observable $\hat{A}_I(1)$ at later time $t_1 > t_2$ (the subscript I denotes the interaction picture). To the lowest order this response is [65]

$$\delta\left\langle \hat{A}_I(1)\right\rangle = -\int \mathrm{d}2 i\theta(t_1 - t_2)\left\langle\left[\hat{A}_I(1), \hat{B}_I(2)\right]\right\rangle V_{ext}(2) \tag{2.34}$$

This allows to define the linear response function

$$\chi_{AB}(1,2) = -i\theta(t_1 - t_2)\left\langle\left[\hat{A}_I(1), \hat{B}_I(2)\right]\right\rangle \tag{2.35}$$

In our specific case we have an external field V_{ext} perturbing the electronic density $\rho(2)$ at time t_2 and we are interested on what is the variation of $\rho(1)$ at later time t_1 due to this perturbed $\rho(2)$. Therefore the correlation function that we are looking for is

$$\chi_{\rho\rho}(1,2) = \chi(1,2) = -i\theta(t_1 - t_2)\left\langle\left[\hat{\rho}(1), \hat{\rho}(2)\right]\right\rangle \tag{2.36}$$

and the variation is, according to Eq. 2.34

$$\delta\langle\rho(1)\rangle = \int \mathrm{d}2\chi(1,2)V_{ext}(2) \tag{2.37}$$

This brings us to redefining the reducible polarisability as

$$\chi(1,2) = \frac{\delta\langle\hat{\rho}(1)\rangle}{\delta V_{ext}(2)} = -i\hbar\frac{\delta G(1,1^+)}{\delta V_{ext}(2)} \tag{2.38}$$

Now we define the total potential as

$$V_{tot}(1) = V_{ext}(1) + v_H(1), \tag{2.39}$$

the dielectric function ϵ defined by

$$\epsilon^{-1}(1,2) = \frac{\delta V_{tot}(1)}{\delta V_{ext}(2)} \tag{2.40}$$

which encodes the response of the total potential of the system to the external field V_{ext} and contains information on the screening. We remark again that at the end of the derivation we will make the limit $V_{ext} \to 0$, and this is in accordance with the fact that the Eq. 2.40 is a functional derivative and should be always intended as a limit.

Using Eq. 2.38 in Eq. 2.40 we have

$$\begin{aligned}\epsilon^{-1}(1,2) &= \frac{\delta}{\delta V_{ext}(2)}(V_{ext}(1)+v_H(1)) \\ &= \frac{\delta V_{ext}(1)}{\delta V_{ext}(2)} - \frac{\delta}{\delta V_{ext}(2)}\left(-i\hbar\delta(1,\overline{4})v(1,\overline{3})G(\overline{3},\overline{3}^+)\delta(\overline{4},1)\right) \\ &= \frac{\delta V_{ext}(1)}{\delta V_{ext}(2)} - \frac{\delta}{\delta V_{ext}(2)}\left(-i\hbar v(1,\overline{3})G(\overline{3},\overline{3}^+)\right) \\ &= \delta(1,2) + v(1,\overline{3})\chi(\overline{3},2)\end{aligned} \tag{2.41}$$

The Eq. 2.38 also suggests to us to define the irreducible polarizability

$$\tilde{\chi}(1,2) = \frac{\delta\langle\rho(\hat{1})\rangle}{\delta V_{tot}(2)} = -i\hbar\frac{\delta G(1,1^+)}{\delta V_{tot}(2)} \tag{2.42}$$

By combining Eqs. 2.41 with Eq. 2.38 and using the chain rule 2.7a

$$\begin{aligned}\chi(1,2) &= -i\hbar\frac{\delta G(1,1^+)}{\delta V_{ext}(2)} = -i\hbar\frac{\delta G(1,1^+)}{\delta V_{tot}(\overline{3})}\frac{\delta V_{tot}(\overline{3})}{\delta V_{ext}(2)} = \tilde{\chi}(1,\overline{3})\epsilon^{-1}(\overline{3},2) \\ &= \tilde{\chi}(1,\overline{3})\left(\delta(\overline{3},2) + v(\overline{3},\overline{4})\chi(\overline{4},2)\right) \\ &= \tilde{\chi}(1,2) + \tilde{\chi}(1,\overline{3})v(\overline{3},\overline{4})\chi(\overline{4},2).\end{aligned} \tag{2.43}$$

Since ϵ, χ and $\tilde{\chi}$ contain information on the screening, it is possible to look at how such screening modifies the bare Coulomb potential, by defining the screened potential W

$$W(1,2) = \epsilon^{-1}(1,\overline{3})v(\overline{3},2) \tag{2.44}$$

By using again the expression for ϵ^{-1} given in the last line of Eq. 2.41 we can connect W and χ

$$\begin{aligned}W(1,2) = \epsilon^{-1}(1,\overline{3})v(\overline{3},2) &= \left(\delta(1,\overline{3}) + v(1,\overline{4})\chi(\overline{4},\overline{3})\right)v(\overline{3},2) \\ &= v(1,2) + v(1,\overline{4})\chi(\overline{4},\overline{3})v(\overline{3},2)\end{aligned} \tag{2.45}$$

Eq. 2.45 is not useful in practice to find W since all the information on the screening is in the reducible polarizability that we do not know *a priori*. It is more convenient to rewrite it in a self-consistent form by using the chain rule 2.7a

$$\begin{aligned}W(1,2) &= v(1,2) + v(1,\overline{4})\chi(\overline{4},\overline{3})v(\overline{3},2) \\ &= v(1,2) + v(1,\overline{4})\frac{\delta\langle\hat{\rho}(\overline{4})\rangle}{\delta V_{tot}(\overline{5})}\frac{\delta V_{tot}(\overline{5})}{\delta V_{ext}(\overline{3})}v(\overline{3},2) \\ &= v(1,2) + v(1,\overline{4})\tilde{\chi}(\overline{4},\overline{5})\epsilon^{-1}(\overline{5},\overline{3})v(\overline{3},2) \\ &= v(1,2) + v(1,\overline{4})\tilde{\chi}(\overline{4},\overline{5})W(\overline{5},2)\end{aligned} \tag{2.46}$$

which is the expression for the screening potential that we will use later.

Vertex function The exchange correlation self-energy Eq. 2.30 can be rewritten by use of the chain rules Eq. 2.7a and Eq. 2.7b applied to the Green's function and its inverse :

$$\begin{aligned}\Sigma_{xc}(1,3) &= i\hbar v(1,\overline{3'})\frac{\delta G(1^-,\overline{2})}{\delta V_{ext}(\overline{3'})}G^{-1}(\overline{2},3)\\ &= i\hbar v(1,\overline{3'})\frac{\delta G(1,\overline{2})}{\delta V_{tot}(\overline{5})}\frac{\delta V_{tot}(\overline{5})}{\delta V_{ext}(\overline{3'})}G^{-1}(\overline{2},3)\\ &= -i\hbar v(1,\overline{3'})\left(G(1^-,\overline{1'})\frac{\delta G^{-1}(\overline{1'},\overline{2'})}{\delta V_{tot}(\overline{5})}G(\overline{2'},\overline{2})\right)\frac{\delta V_{tot}(\overline{5})}{\delta V_{ext}(\overline{3'})}G^{-1}(\overline{2},3)\end{aligned} \tag{2.47}$$

which, after contraction of $G(2',\overline{2})G^{-1}(\overline{2},3)$ in a $\delta(2',3)$, reads

$$\Sigma_{xc}(1,3) = -i\hbar v(1,\overline{3'})G(1^-,\overline{1'})\frac{\delta G^{-1}(\overline{1'},3)}{\delta V_{tot}(\overline{5})}\frac{\delta V_{tot}(\overline{5})}{\delta V_{ext}(\overline{3'})} \tag{2.48}$$

Therefore we need to evaluate $\frac{\delta G^{-1}(\overline{1'},3)}{\delta V_{tot}(\overline{5})}$ in Eq. 2.48. This can be achieved by looking at the Dyson's equation in integral form. By multypling and integrating on the right by $G^{-1}(\overline{2},3')$ and on the left by $G_0^{-1}(1',\overline{1})$ we rewrite Eq. 2.33 as

$$G^{-1}(1',3') = G_0^{-1}(1',3') - V_{ext}(1')\delta(1',3') - \Sigma(1',3') \tag{2.49}$$

which can be derived

$$\frac{\delta G^{-1}(1',3')}{\delta V_{tot}(5)} = \frac{\delta}{\delta V_{tot}(5)}\left(G_0^{-1}(1',3') - V_{ext}(1')\delta(1',3') - \Sigma(1',3')\right) \tag{2.50}$$

We have thus three terms

1. the first one
$$\frac{\delta G_0^{-1}(1',3')}{\delta V_{tot}(5)} = 0 \tag{2.51}$$
because G_0^{-1} does not depend on the potential since it is the inverse of the Green's function for the non interacting system;
2. the second term
$$\begin{aligned}\frac{\delta}{\delta V_{tot}(5)}\left(-V_{ext}(1')\delta(1',3')\right) &= -\frac{\delta}{\delta V_{tot}(5)}\left(V_{tot}(1') - v_H(1')\right)\delta(1',3')\\ &= -\frac{\delta V_{tot}(1')}{\delta V_{tot}(5)}\delta(1',3') + \frac{\delta v_H(3')}{\delta V_{tot}(5)}\\ &= -\delta(1',5)\delta(1',3') + \frac{\delta v_H(3')}{\delta V_{tot}(5)}\end{aligned} \tag{2.52}$$

3. The third term

$$\begin{aligned}\frac{\delta}{\delta V_{tot}(5)}\left(-\Sigma(1',3')\right) &= \frac{\delta}{\delta V_{tot}(5)}\left(-v_H(1')\delta(1'3') - \Sigma_{xc}(1',3')\right)\\ &= -\frac{\delta v_H(3')}{\delta V_{tot}(5)} - \frac{\delta \Sigma_{xc}(1',3')}{\delta V_{tot}(5)}\end{aligned} \tag{2.53}$$

By putting together Eqs. 2.51, 2.52 and 2.53 back in Eq. 2.50 we get

$$\frac{\delta G^{-1}(1',3')}{\delta V_{tot}(5)} = -\delta(1',5)\delta(1',3') - \frac{\delta \Sigma_{xc}(1',3')}{\delta V_{tot}(5)} \tag{2.54}$$

We call the same quantity but with the minus sign the irreducible vertex function [4]

$$\tilde{\Gamma}(1,2,3) = -\frac{\delta G^{-1}(1,2)}{\delta V_{tot}(3)} = \delta(1,2)\delta(1,3) + \frac{\delta \Sigma_{xc}(1,2)}{\delta V_{tot}(3)} \tag{2.55}$$

By using again the two chain rules 2.7a and 2.7b it is possible to derive a self-consistent equation for $\tilde{\Gamma}$

$$\begin{aligned}\tilde{\Gamma}(1,2,3) &= \delta(1,2)\delta(1,3) + \frac{\delta \Sigma_{xc}(1,2)}{\delta V_{tot}(3)}\\ &= \delta(1,2)\delta(1,3) + \frac{\delta \Sigma_{xc}(1,2)}{\delta G(\overline{4},\overline{5})}\frac{\delta G(\overline{4},\overline{5})}{\delta V_{tot}(3)}\\ &= \delta(1,2)\delta(1,3) + \frac{\delta \Sigma_{xc}(1,2)}{\delta G(\overline{4},\overline{5})}\left(-G(\overline{4},\overline{4'})\frac{\delta G^{-1}(\overline{4'},\overline{5'})}{\delta V_{tot}(3)}G(\overline{5'},\overline{5})\right)\\ &= \delta(1,2)\delta(1,3) + \frac{\delta \Sigma_{xc}(1,2)}{\delta G(\overline{4},\overline{5})}G(\overline{4},\overline{4'})\tilde{\Gamma}(\overline{4'},\overline{5'},3)G(\overline{5'},\overline{5})\end{aligned} \tag{2.56}$$

By renaming $4'$ as 6 and $5'$ as 7, the last line of Eq .2.56 becomes

$$\tilde{\Gamma}(1,2,3) = \delta(1,2)\delta(1,3) + \frac{\delta \Sigma_{xc}(1,2)}{\delta G(\overline{4},\overline{5})}G(\overline{4},\overline{6})\tilde{\Gamma}(\overline{6},\overline{7},3)G(\overline{7},\overline{5}) \tag{2.57}$$

With the definition of the irreducible vertex function $\tilde{\Gamma}$ one can rewrite an equation for the irreducible polarizability using again the chain rule 2.7b :

$$\begin{aligned}\tilde{\chi}(1,2) = \frac{\delta\langle\rho(\hat{1})\rangle}{\delta V_{tot}(2)} = -i\hbar\frac{\delta G(1,1^+)}{\delta V_{tot}(2)} &= i\hbar G(1,\overline{3})\frac{\delta G^{-1}(\overline{3},\overline{3'})}{\delta V_{tot}(2)}G(\overline{3'},1^+)\\ &= -i\hbar G(1,\overline{3})\tilde{\Gamma}(\overline{3},\overline{3'},2)G(\overline{3'},1^+)\end{aligned} \tag{2.58}$$

4. It is possible also to define a reducible vertex function Γ with the same definition as Eq. 2.55 but using Σ in place of Σ_{xc}.

Finally, from Eq. 2.48 we can use $\tilde{\Gamma}$ and the definitions of screened potential to express Σ_{xc} as

$$\begin{aligned}\Sigma_{xc}(1,3) &= -i\hbar v(1,\overline{3'})G(1^-,\overline{1'})\frac{\delta G^{-1}(\overline{1'},3)}{\delta V_{tot}(\overline{5})}\frac{\delta V_{tot}(\overline{5})}{\delta V_{ext}(\overline{3'})} \\ &= -i\hbar v(1,\overline{3'})G(1^-,\overline{1'})\left(-\tilde{\Gamma}(\overline{1'},3,\overline{5})\right)\epsilon^{-1}(\overline{5},\overline{3'}) \\ &= i\hbar G(1^-,\overline{1'})\tilde{\Gamma}(\overline{1'},3,\overline{5})W(1,\overline{5})\end{aligned} \tag{2.59}$$

We put together Eqs. 2.59, 2.58, 2.46, 2.33 and 2.56 :

$$\begin{aligned}\Sigma_{xc}(1,2) &= i\hbar G(1^-,\overline{4})W(1,\overline{3})\tilde{\Gamma}(\overline{4},2,\overline{3}) \\ \tilde{\chi}(1,2) &= -i\hbar G(1,\overline{3})G(\overline{4},1^+)\tilde{\Gamma}(\overline{3},\overline{4},2) \\ W(1,2) &= v(1,2)+v(1,\overline{3})\tilde{\chi}(\overline{3},\overline{4})W(\overline{4},2) \\ \tilde{\Gamma}(1,2,3) &= \delta(1,2)\delta(2,3)+\frac{\delta\Sigma_{xc}(1,2)}{\delta G(\overline{4},\overline{5})}G(\overline{4},\overline{6})G(\overline{7},\overline{5})\tilde{\Gamma}(\overline{6},\overline{7},3) \\ G(1,2) &= G_0(1,2)+G_0(1,\overline{3})\Sigma(\overline{3},\overline{4})G(\overline{4},2)\end{aligned} \tag{2.60}$$

Note that the last of Eqs. 2.60 is the Dyson's equation 2.33 after we made the limit $V_{ext}\to 0$. The integro-differential Eqs. 2.60 are called Hedin's equations [72] and in principle they should be solved self-consistently in order to obtain the quasiparticle energies. Hedin's equations and this self-consistent procedure are often depicted as the pentagon in Fig. 2.3

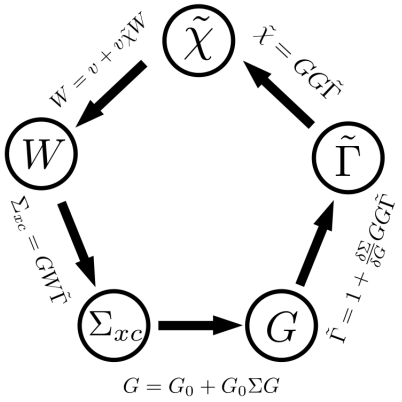

Figure 2.3. – Easy-to-remember representation of Hedin's equations.

2.1.2. The GW approximation

In practice solving exactly the Hedin's equations is impossible since convergence is not guaranteed if the initial ansatz is not properly set. Two very popular approximations that have delivered very good results for many materials are the Random Phase Approximation (RPA) and the *GW* approximation. They are often implemented

together and one thus refers to this method as the GW method. The GW approximation consists in neglecting the second term of the vertex function while retaining only the Dirac's δ, i.e. $\tilde{\Gamma}(1,2,3) \approxeq \delta(1,2)\delta(1,3)$. Therefore the self-energy is approximated to $\Sigma_{xc} \approxeq GW$, hence the name GW approximation. In the RPA approximation we approximate the polarizibility to the convolution of independent particle Green's functions and together with the GW approximation the irreducible polarizability becomes

$$\tilde{\chi}(1,2) \approxeq \tilde{\chi}_0(1,2) = -i\hbar G_0(1,2^+)G_0(2,1^+) \tag{2.61}$$

with the approximation 2.61, the last line of Eq. 2.43 allows to find the RPA for the reducible χ

$$\chi_{rpa}(1,2) = \tilde{\chi_0}(1,2) + \tilde{\chi}_0(1,\overline{3})v(\overline{3},\overline{4})\chi_{rpa}(\overline{4},2) \tag{2.62}$$

χ_{rpa} can be used in the last line of Eq. 2.41 to find the RPA approximation to ϵ^{-1}, ϵ^{-1}_{rpa}. Using Eq. 2.44 the RPA approximation to W is

$$W_{rpa}(1,2) = \epsilon^{-1}_{rpa}(1,\overline{3})v(\overline{3},2) \tag{2.63}$$

Using W_{rpa} in the expression for Σ_{xc} would result in an approximated $\Sigma_{xc} \approxeq GW_{rpa}$. Since we do not know the G *a priori* and it is one of the quantities that we may want to find we again approximate the G to the independent particle G_0 so that

$$\Sigma_{xc}(1,2) \approxeq \Sigma^{rpa}_{xc}(1,2) = iG_0(1,\overline{2})W_{rpa}(\overline{2},1) \tag{2.64}$$

Finally the newly approximated Σ_{xc} can be used to build the total approximated Σ and compute the interacting quasiparticle Green's function G with the Dyson's equation. In the GW approximation then Hedin's equations 2.60 are

$$\begin{aligned}
&\tilde{\Gamma}(1,2,3) \approxeq \delta(1,2)\delta(1,3)\\
&\tilde{\chi}_0(1,2) = -i\hbar G_0(1,2)G_0(2,1)\\
&W_{rpa}(1,2) = \epsilon^{-1}_{rpa}(1,\overline{3})v(\overline{3},2)\\
&\Sigma_{xc}(1,2) \approxeq \Sigma^{rpa}_{xc}(1,2) = iG_0(1,\overline{2})W_{rpa}(\overline{2},1)\\
&G_{rpa}(1,2) = G_0(1,2) + G_0(1,\overline{3})\Sigma^{rpa}_{xc}(\overline{3},\overline{4})G_{rpa}(\overline{4},2)
\end{aligned} \tag{2.65}$$

In practice we stop after only one iteration so we do not use the last of Eqs. 2.65. In this case the method is referred to as the GW method. It is also possible to go over the first iteration, compute $\tilde{\Gamma}$ and include it for a second iteration. The main advantage of the GW scheme is the fact that if G_0 is known then one can compute all the other quantities. Of course it is impractical to have the exact G_0 of the non-interacting quasiparticles. A good ansatz for G_0 is the one computed from the Kohn-Sham wavefunctions previously calculated with DFT. Moreover it is possible to show that the self-energy Σ_{xc} can be split into two terms, a correlation part Σ_c and a exchange part Σ_x.

2.2. The Bethe-Salpeter equation

The RPA for the polarizability often fails in providing a good spectrum for the $\epsilon_1 = \Re(\epsilon M)$ and $\epsilon_2 = \Im(\epsilon_M)$ since it stems from calculating the polarizability from two decoupled Green's functions, whereas in the original set they are coupled by the vertex function. The vertex function neglected in RPA contains the information about the exchange-correlation between an electron and the other electrons in its quasiparticle cloud and the electron-hole attraction [73]. Therefore what we need is an equation of motion for the 2-particle Green's function G_2. In particular one refers to the electron-hole coupling as excitonic effects. When we take into account not only the exchange-correlation in the electron-hole pair but also their attraction then the electron and the hole can form an exciton (Fig. 2.6, panel c). Excitonic effects can be determining for the absorption spectra and they can be included by mean of the Bethe-Salpeter equation (BSE) [73, 68, 65] which is exactly the equation of motion for G_2 that we are looking for. We start by defining the quantity L

$$L(1,1',2,2') := \frac{\delta G(1,2)}{\delta V_{ext}(2',1')} \tag{2.66}$$

By using Eq. 2.27 we can then write

$$L(1,1',2,2') = G(1,2)G(1',2') - G_2(1,1',2,2') \tag{2.67}$$

By using the chain rule 2.7b and the expression for G^{-1} Eq. 2.49 the functional derivative 2.66 can be rewritten as

$$\begin{aligned} L(1,1',2,2') = & \\ \frac{\delta G(1,2)}{\delta V_{ext}(2',1')} &= -G(1,\bar{3})\frac{\delta G^{-1}(\bar{3},\bar{4})}{\delta V_{ext}(2',1')}G(\bar{4},2) \\ &= -G(1,\bar{3})\frac{\delta}{\delta V_{ext}(2',1')}\left(G_0^{-1}(\bar{3},\bar{4}) - V_{ext}(\bar{3})\delta(\bar{3},\bar{4}) - \Sigma(\bar{3},\bar{4})\right)G(\bar{4},2) \\ &= G(1,\bar{3})\left(0 + \delta(\bar{3},2')\delta(\bar{4},1') + \frac{\delta\Sigma(\bar{3},\bar{4})}{\delta V_{ext}(2',1')}\right)G(\bar{4},2) \\ &= G(1,2')G(1',2) + G(1,\bar{3})G(\bar{4},2)\frac{\delta\Sigma(\bar{3},\bar{4})}{\delta V_{ext}(2',1')} \end{aligned} \tag{2.68}$$

The last term in the last line of Eq. 2.68 can be transformed thanks to the chain rule 2.7a and the definition for L, Eq. 2.66

$$\frac{\delta\Sigma(\bar{3},\bar{4})}{\delta V_{ext}(2',1')} = \frac{\delta\Sigma(\bar{3},\bar{4})}{\delta G(\bar{5},\bar{6})}\frac{\delta G(\bar{5},\bar{6})}{\delta V_{ext}(2',1')} = \frac{\delta\Sigma(\bar{3},\bar{4})}{\delta G(\bar{5},\bar{6})}L(\bar{5},1',\bar{6},2') \tag{2.69}$$

Therefore Eq. 2.68 becomes

$$L(1,1',2,2') = G(1,2')G(1',2) + G(1,\bar{3})G(\bar{4},2)\frac{\delta\Sigma(\bar{3},\bar{4})}{\delta G(\bar{5},\bar{6})}L(\bar{5},1',\bar{6},2') \tag{2.70}$$

By readjusting the indices, defining $L_0(1,2,3,4) = G(1,4)G(2,3)$ and the quantity $\frac{\delta\Sigma(3,4)}{G(5,6)} = K(3,6,4,5)$ we can rewrite Eq. 2.70 as

$$L(1,2,3,4) = L_0(1,2,3,4) + L_0(1,\bar{7},3,\bar{5})K(\bar{5},\bar{6},\bar{7},\bar{8})L(\bar{8},2,\bar{6},4) \tag{2.71}$$

which is the Bethe-Salpeter equation. K is called kernel while L_0 is the independent electron-hole propagator and it has a role with respect to L similar to G_0 with respect to G. The BSE can be used to find the quantity χ and since the function L is related to the polarizability

$$\chi(1,2) = -i\hbar L(1,2,1^+,2^+) \tag{2.72}$$

the optical properties are directly accessible from the reducible polarizability χ. The Bethe-Salpeter equation is depicted in the form of Feynman diagrams in Fig. 2.4.

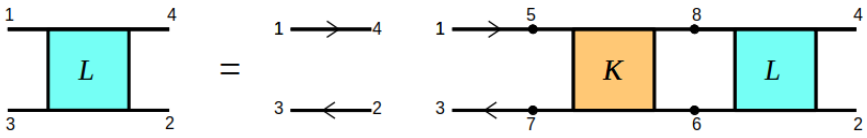

Figure 2.4. – Feynamn diagrams of the BSE.

2.3. Optics in practice

Now that we have derived a method to account for quasiparticle effects in the electronic properties of materials and an equation to include the electron-hole coupling we show how all these ingredients can be used in practice. In this section we sketch the workflow that we followed to study the optical properties of wBN using the MBPT. The procedure consists of three main steps : a DFT cycle followed by a MBPT calculation with the GW method and finally solution of the BSE. The code that we have used throughout this thesis is `yambo` [74, 75].

DFT level The SCF calculation in DFT with Quantum Espresso provides a set of Kohn-Sham states $\phi_{i\boldsymbol{k}}$. These KS states are then transferred to the `yambo` code which uses them to build the non-interacting G_0 (assuming that they are a good approximation for the Dyson's orbitals in Eq. 2.17). At this stage a very dense $\boldsymbol{k}$-grid beyond convergence should be used because we need to take into account as many vertical transition in the BZ as possible.

GW calculation At this stage we want to use the GW method to obtain the quasiparticle energies. Once the G_0 has been constructed we can make use of the Hedin's

equations in *GW* approximation Eqs. 2.65. We proceed in order :

1. from G_0 it is possible to write $\tilde{\chi_0} = G_0 G_0$. Normally one works in reciprocal space and therefore the polarizability is expressed as function of the momentum $\boldsymbol{q}+\boldsymbol{G}$ so that we can write it in a matrix form $\tilde{\chi}_{0\boldsymbol{G},\boldsymbol{G}'}(\boldsymbol{q},\omega) = \tilde{\chi}_0(\boldsymbol{q}+\boldsymbol{G},\boldsymbol{q}+\boldsymbol{G}',\omega)$. In RPA approximation Eq. 2.62 gives then $\chi^{rpa}_{\boldsymbol{G}\boldsymbol{G}'}(\boldsymbol{q},\omega)$;
2. we should use $\chi^{rpa}_{\boldsymbol{G}\boldsymbol{G}'}(\boldsymbol{q},\omega)$ to compute W_{rpa}. This implies the inversion of Eq. 2.62 for each ω which would be time costly. The plasmon-pole approximation (PPA),[76, 68] allows to carry out the inversion only at $\omega = 0$ and at $\omega = E_{pl}$ plasmon energy which is user-defined and reconstruct approximately the rest of the function $\chi^{rpa} \approx \chi^{ppa}$;
3. χ^{ppa} is used to write the PPA-approximated screened interaction W_{ppa} necessary to compute the self-energy. At this stage we dropped the $\boldsymbol{G}\boldsymbol{G}'$ subscript because from now on one works in the Kohn-Sham state basis. It is possible to show that in the exchange-correlation self-energy Σ_{xc} one can isolate a non-local exchange component Σ_x and a "correlation" non-local potential Σ_c induced by propagation of the particle added/removed

$$\Sigma_{xc} = \Sigma_x + \Sigma_c \tag{2.73}$$

   While Σ_x can be calculated quite rapidly, Σ_c requires more effort. The formulas for Σ_c and Σ_x are reported elsewhere (See Ref. [74]) ;
4. Finally the complete Σ can be reconstructed. The quasiparticle energies are given by

$$E^{QP}_{i\boldsymbol{k}} = E^{KS}_{i\boldsymbol{k}} + \left(\Sigma_{xc\,i\boldsymbol{k}}\left(E^{QP}_{\imath\boldsymbol{k}}\right) - \langle i\boldsymbol{k}|V_{xc}|i\boldsymbol{k}\rangle\right) \tag{2.74}$$

   where $E^{KS}_{i\boldsymbol{k}}$ are the kohn-Sham energies. We subtracted the used DFT exchange-correlation potential V_{xc} to account for the fact that the KS wavefunction $|i\boldsymbol{k}\rangle$ that we used as initial guess to run the *GW* calculation are the result of a DFT Hamiltonian that included already an exchange-correlation contribution.

Since the Eq. 2.74 is self-consistent in $E^{qp}_{i\boldsymbol{k}}$, the `yambo` code makes an expansion of $\Sigma_{xc\,i\boldsymbol{k}}(E^{qp})$ around $E^{KS}_{i\boldsymbol{k}}$. By re-iterating the same expansion one finds a series that is equal to

$$Z_{i\boldsymbol{k}} = \left(1 - \left.\frac{\partial\Sigma_{xc}}{\partial\omega}\right|_{\omega=E^{KS}_{i\boldsymbol{k}}}\right)^{-1} \tag{2.75}$$

So that the quasiparticle-corrected band is

$$E^{QP}_{i\boldsymbol{k}} = E^{KS}_{i,\boldsymbol{k}} + Z_{i\boldsymbol{k}}\left(\Sigma_{xc\,i\boldsymbol{k}}\left(E^{KS}_{\imath\boldsymbol{k}}\right) - \langle i\boldsymbol{k}|V_{xc}|i\boldsymbol{k}\rangle\right) \tag{2.76}$$

To sum up, Fig. 2.5 reports in a schematic way the whole workflow described above for the *GW* method to obtain the quasiparticle corrected band structure :

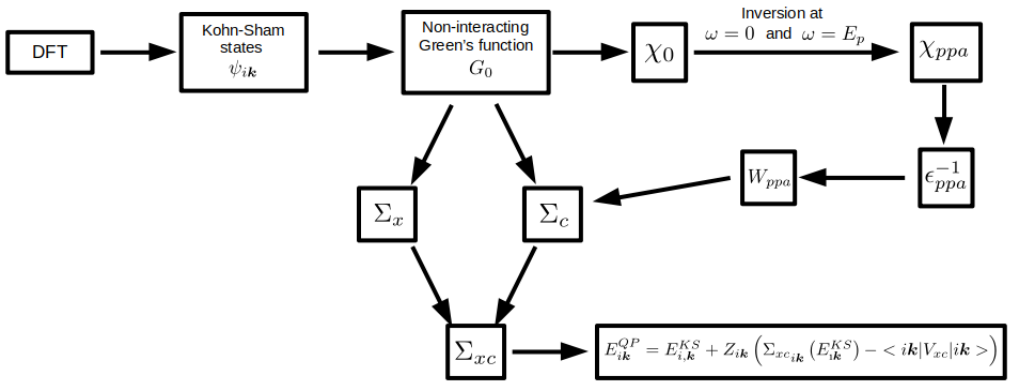

Figure 2.5. – GW method workflow as implemented by the `yambo` code.

BSE It is possible to recast the BSE Eq. 2.71 as a (pseudo)-Hamiltonian form called BSE Hamiltonian. In a basis of transitions between conduction (c) and valence (v) bands we have to solve the eigenvalue problem [73]

$$\sum_{c'v'} H^{BSE}_{(cv),(c'v')} A^{\lambda}_{c'v'} = E_\lambda A^{\lambda}_{cv} \tag{2.77}$$

with

$$H^{BSE}_{(cv),(c'v')} = (E_c - E_v)\delta_{vv'}\delta_{cc'} + (f_v - f_c)\left(\overline{v}_{(cv),(c'v')} - W_{(cv),(c'v')}\right) \tag{2.78}$$

where f_i are the occupations and E_i are the energies already corrected with the previous GW calculation, for the bands i. The eigenvalues and eigenvectors E_λ and A^{λ}_{cv} are the energies and the eigenstate of the λth exciton. W is the screened interaction between the electron-hole pair and $\overline{v}$ is the exchange potential between the electron and the hole. In principle the screened potential W has already been calculated in the previous GW step. In solving the BSE one usually makes the RPA static limit approximation so that we only need to invert the quantity $\chi^{rpa}_{\boldsymbol{GG'}}(\boldsymbol{q},\omega = 0)$. The exciton eigenstate can be used to write the macroscopic dielectric function [73]

$$\epsilon_M(\omega) = 1 - \lim_{\boldsymbol{q}\to 0} v_{\boldsymbol{G}=0}(\boldsymbol{q}) \sum_\lambda \frac{\left|\sum_{cv} \langle c|e^{-i\boldsymbol{q}\cdot\boldsymbol{r}}|v\rangle A^{\lambda}_{cv}\right|^2}{\omega - E_\lambda + i\eta} \tag{2.79}$$

Then the absorption is given by the imaginary part of ϵ_M. In the BSE Hamiltonian Eq. 2.78 we used the modified potential $\overline{v}$ defined as

$$\overline{v}_{\boldsymbol{G}}(\boldsymbol{q}) = \begin{cases} \dfrac{4\pi}{|\boldsymbol{q}+\boldsymbol{G}|} & \text{if } \boldsymbol{G} \neq 0 \\ 0 & \text{if } \boldsymbol{G} = 0 \end{cases} \tag{2.80}$$

This modified potential avoids the divergence for $\boldsymbol{q}$ and $\boldsymbol{G}$ of the usual potential v in reciprocal space $v_{\boldsymbol{G}}(\boldsymbol{q}) = \frac{4\pi}{|\boldsymbol{q}+\boldsymbol{G}|}$. The energy E_λ of the exciton can be lower than the

band gap. In that case one talks about the optical gap and the difference between the exciton energy and the band gap is the binding energy. This fact is depicted in Fig. 2.6.

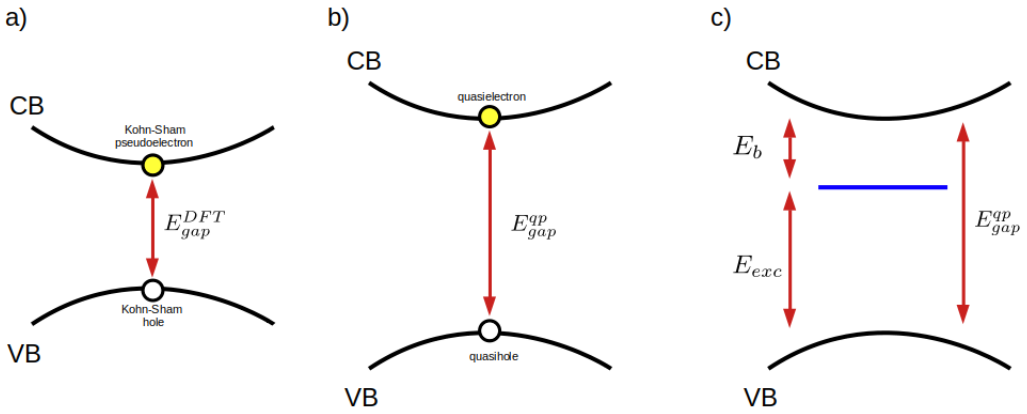

Figure 2.6. – Pictorial band structure at DFT level (a), with quasiparticle correction (b) and excitonic level after solution of the BSE (c). The E_b is the binding energy of the electron and hole in the exciton. Note how the quasiparticle band gap E_{gap}^{qp} is larger than the original DFT band gap E_{gap}^{DFT}. The excitonic level E_{exc} is obtained as eigenenergy from diagonalization of the BSE in Hamiltonian form Eq. 2.78.

The workflow of the BSE solution is schematically reported in Fig. 2.7

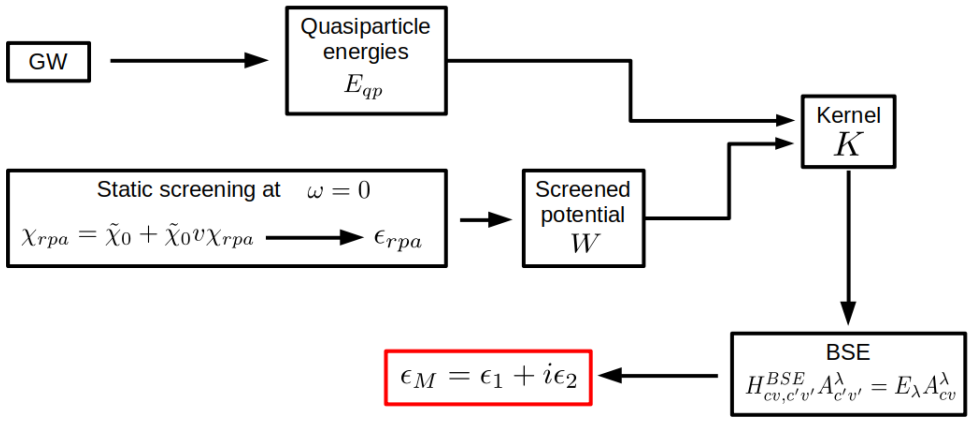

Figure 2.7. – BSE workflow. Note that in principle it would be possible to calculate the BSE Hamiltonian and kernel by using a static screening ϵ in GW-RPA approximation rather than just RPA. It would be also possible to calculate the kernel without including the W.

The excitons are composed by cv transitions. If the transition is vertical then the exciton is called direct. If instead the transition is not vertical in the 1BZ the exciton is indirect and there is a difference in momentum $\boldsymbol{q}$ between the excited quasielectron and the quasihole. The recombination of an electron-hole pair with an emission of a

photon is the cause of the luminescence. This phenomenon is highly efficient if the exciton is direct, typically in a direct gap material like ZnO. If the excitons are mostly indirect then the photoluminescence yield is inefficient, like in diamond because the recombination of the indirect exciton needs the difference in momentum $\boldsymbol{q}$. In the phonon-assisted luminescence this $\boldsymbol{q}$ can be given by a phonon, in this case we talk about "phonon-assisted" luminescence. If this process mediated by a phonon is efficient then an indirect material can also have a high quantum yield, like in the case of hBN . In this case the luminescence recombination rate can be calculated with the Roosbroeck-Shockley formula [77] generalized to the exciton case [78].

$$R(\omega) = \sum_{\nu \boldsymbol{q}} \frac{\omega(\omega + 2\Omega^2_{\nu\boldsymbol{q}})}{\pi^2 \hbar c^3} n_r(\omega) \sum_{\lambda} \frac{\partial^2 |T_\lambda|^2}{\partial R^2_{\nu\boldsymbol{q}}} \Im \left\{ \frac{1}{\hbar\omega - (E_\lambda - \Omega_{\nu\boldsymbol{q}}) + i\eta} \right\} B(E_\lambda, T_{exc}) \quad (2.81)$$

with $n_r(\omega)$ refractive index, $\Omega_{\nu\boldsymbol{q}}$ frequencies for the phonon of indices ν and $\boldsymbol{q}$, $B(E_\lambda, T_{exc})$ occupation function of the lowest excitons in Boltzmann statistics. T_λ is the dipole element present also in the numerator of Eq. 2.79 and it is derived with respect to the displacement due to the phonon.

2.4. Defect optical properties and the Franck-Condon model

We can study the optics of defects without departing from the DFT context. The method that we are going to illustrate will be then applied later in Chap. 4.

The presence of a defect in a semiconductor or an insulator introduces new electronic levels, possibly (but not necessarily) in the band gap of the host and they can be more or less localized. These levels are those generally found with a DFT calculation and they imply a single-electron picture of the problem [5] [6]. The fact that a defect level in the gap is localized makes the defect appear as some some sort of "trapped atom" even though, unlike a true atom in vacuum, it interacts with the atoms of the host, forcing us to study this localized system using the methodologies typical of solid state physics [80]. To have an idea of how a defect level looks like, in Fig. 2.8 we show as an example the $|\psi|^2$ of a localized defect level (panel b) and c)) and a delocalized bulk state (panel d)) of the C_B^0 in wBN . The localized and delocalized example states correspond to the levels marked as "defect" and "bulk" in the level scheme in panel a) of Fig. 2.8.

5. These levels must not be confused with the CTL.

6. Alternatively it is possible to construct the multielectronic state of system by considering its overall electronic configuration. This is done for example in Ref. [79].

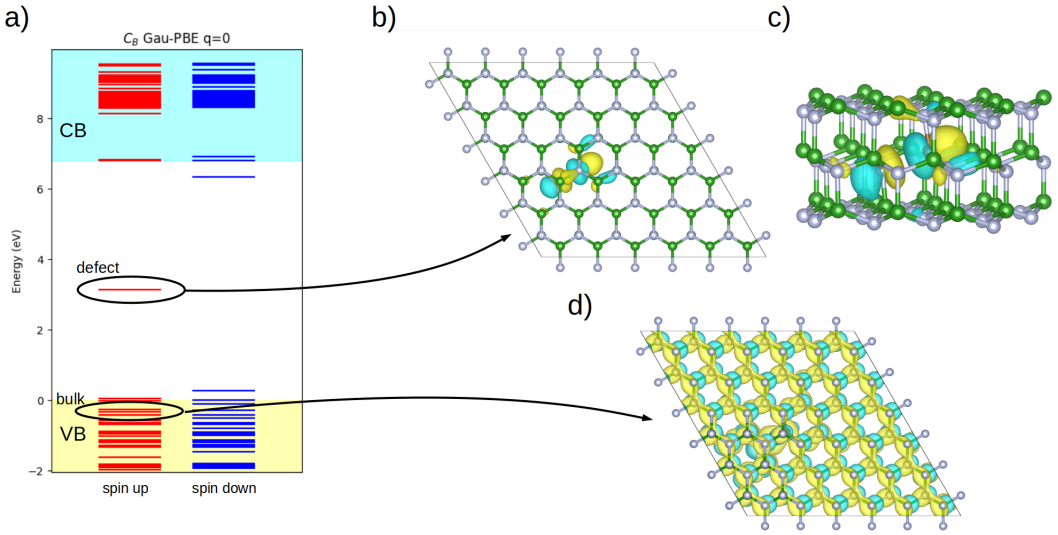

Figure 2.8. – Panel a) : level scheme obtained via hybrid-DFT for C_B^0 in wBN; panel b) : $|\psi|^2$ isosurface of a defect state; panel c) : same isosurface of panel b) from a different angle; panel d) : isosurface of a bulk state.

The optical properties of the defect inevitably involves a transition between states. The transitions studied in this work can be classified into two types :

— transitions involving a defect level and a bulk level;

— transitions between two defect levels inside the gap (internal transitions);

Although the physics involved in the two cases can be rather different, in principle they can be both studied by applying similar methods and formalisms that we are now going to illustrate to different levels of approximations, without loss of generality.

We start by noting that in general if we excite an electron from one state (the ground state) to another (the excited state) in the defective solid, the entire structure will rearrange its nuclear configuration to a new one that will minimize the total energy. Such transition and consequent nuclear relaxation can be thought in terms of a Franck-Condon configuration coordinate diagram (CCD)[3] where one associates to each of the two states a 1D potential energy surface in a harmonic approximation.

Let us consider a supercell of N nuclei where each nucleus of index $I = 1...N$ and mass M_I has coordinates $R^{gr}_{I,\alpha}$ and $R^{exc}_{I,\alpha}$ in the ground and excited state respectively, where $\alpha = x, y, z$ is the index for the cartesian coordinates. After the electronic transition each nucleus is displaced by a quantity $\Delta R_{I,\alpha} = R^{exc}_{I,\alpha} - R^{gr}_{I,\alpha}$. We can then define a configuration coordinate deformation ΔQ such that

$$\Delta Q^2 = \sum_I \sum_\alpha M_I (\Delta R_{I,\alpha})^2 \tag{2.82}$$

Similarly, we can define a Q_g and a Q_e corresponding, respectively to the relaxed structure of the ground and excited state, respectively. With these definitions it is clear that $\Delta Q = Q_e - Q_g$. From ΔQ it is also possible to define the auxiliary quantities $\Delta Q = \sqrt{M_{mod}}\Delta R$ with M_{mod} modal mass and ΔR calculated as $\Delta R = \sum_{I,\alpha} \Delta R^2_{I,\alpha}$. The

ΔQ coordinate is a practical 1D quantity that sums up the information on the overall deformation and displacements of the atomic sites in the supercell (which instead consists of $3N$ coordinates). Thanks to the definition Eq. 2.82, the potential energy surface (which is the total energy of the system as a function of the atomic configuration) for the ground state will be a just a function of Q and in the Franck-Condon model it is assumed to be a parabola with a minimum at $Q = Q_g$. We denote its minimum value with $E_{gr}^{(rel)}$. In the same way a parabola can be derived for the excited state, which will have a minimum energy $E_{exc}^{(rel)}$ for $Q = Q_e = Q_g + \Delta Q$. These parabolas can be in principle associated with two harmonic oscillators with oscillation frequencies ω_g and ω_e that depend on the system and need to be determined. This is the classical Franck-Condon model used to study the luminescence lineshape of a defect emission including the deformation of the atomic configuration due to the excitation. In general the deformation will eventually couple with phonons.

In principle each phonon mode *independently* couples with the defect excitation. By *independently* we mean that each phonon has its own oscillation frequency, will induce a different deformation and will separately introduce some peaks in the PL lineshape. Therefore we would have a different 1D CCD for each of the phonon mode considered and the problem would be computationally costly to solve. At variance, if the electron-phonon coupling is strong and the deformation ΔQ is large we can assume that all the phonon normal modes that contribute to the lineshape of the absoprtion/emission spectrum can be replaced by only one effective phonon mode. Thus we only have to consider one phonon and only one effective 1D Franck-Condon CCD.

By looking at panel a) of Fig. 2.9 we can understand how from a Franck-Condon CCD it is already possible to obtain important information on the transition without adding more complexity. First the system is in the fully relaxed configuration (point A) of the

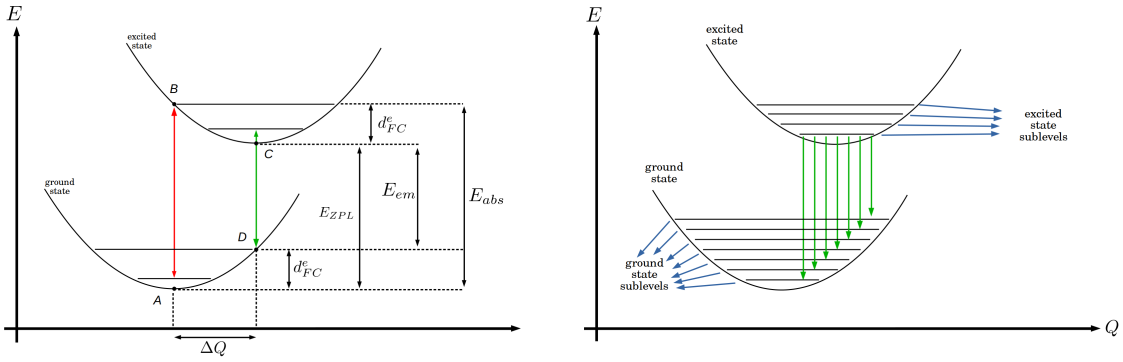

Figure 2.9. – Franck-Condon model for a generic system with its connection with the absorption and emission spectra.

ground state with total energy $E_A = E_{gr}^{(rel)}$ (the superscript "rel" stands for relaxed). An incoming photon of energy $\hbar\omega_{abs}$ engenders an absorption transition (red arrow) from the ground to the excited state (point B) where the total energy is $E_B = E_{exc}^{(unr)}$ (the

superscript "unr" stands for unrelaxed). The Franck-Condon hypothesis is that such transition is vertical, i.e. at fixed configuration, which means that we are implying that the electronic transition times are shorter than the nuclear relaxation times ($\approxeq 10^{-12}$ s [81]). This is the reason why in point B the structure is at an energy $E_{exc}^{(unr)}$ higher than that of the fully relaxed structure. Then the system relaxes to a new configuration (point C) with energy $E_C = E_{exc}^{(rel)}$. With this mechanism the system looses an amount of energy d_e. The configuration in C is different from the configuration in A and B by an amount ΔQ. At this point the system can undergo another vertical transition (the green arrow) at constant Q by emitting a photon with energy $\hbar\omega_{em} < \hbar\omega_{abs}$, ending up in point D with energy $E_D = E_{gr}^{unr}$. Finally the system relaxes back to point A by loosing an energy d_g. This very simple description based on the A→B→C→D cycle is already capable of capturing some optical features. The quantities d_e and d_g are called Stokes and Antistokes shifts respectively[15][18] and they quantify the absorbed energy dissipated through phonons :[7].

$$\hbar\omega_{abs} - \hbar\omega_{em} = d_e + d_g \tag{2.83}$$

with

$$d_e = E_B - E_C + \frac{\hbar\omega_e}{2} \tag{2.84a}$$

$$d_g = E_D - E_A + \frac{\hbar\omega_g}{2} \tag{2.84b}$$

$$E_{abs} = \hbar\omega_{abs} = E_B - E_A + \frac{\hbar\omega_g}{2} \tag{2.84c}$$

$$E_{em} = \hbar\omega_{em} = E_C - E_D + \frac{\hbar\omega_e}{2} \tag{2.84d}$$

Another important quantity is the Zero-Phonon line

$$E_{ZPL} = \left(E_C + \frac{\hbar\omega_e}{2}\right) - \left(E_A + \frac{\hbar\omega_g}{2}\right) \tag{2.85}$$

where ω_g and ω_e are the oscillating frequencies of the two harmonic oscillators associated with the ground and the excited state respectively. These frequencies allow us to introduce the so called Huang-Rhys factor for the ground/excited state

$$S_{g/e} = \frac{d_{g/e}}{\hbar\omega_{g/e}} \tag{2.86}$$

The Huang-Rhys factor tells us how many photons are emitted on average in an absorption or emission [3, 82]. Another commonly applied approximation is that in both states the defect and the lattice interact in the same way, i.e. the two parabolas have same curvature (HR theory) [18, 83] and same oscillation frequencies, thus

7. A discrepancy is found in the literature for the definition of Stokes shifts. In Ref. [3] the Stokes shift is simply $\hbar\omega_{abs} - \hbar\omega_{em} = d_e + d_g$ and d_g and d_e are referred to as the Franck-Condon shifts

$\omega_g = \omega_e = \omega_0$. This definition would allow us to find one unique Huang-Rhys factor $S = S_g = S_e$.

Finally we give more details about higher levels of complexity that can be applied for this model and we did not use in this work. Firstly, we could have considered not only transition at constant deformation but genuinely quantum transitions between the different vibrionic levels of the associated excited and ground state harmonic oscillators (See panel b) of Fig. 2.9). We denote the generic n^{th} sublevel of the ground state with $|\psi_{g,n}\rangle$ and the mth excited state sublevel with $|\psi_{e,m}\rangle$. A common approximation is to consider only the lowest vibrionic level as the initial state [84, 3], so that in emission (absorption) one has the transitions $|\psi_{e,0}\rangle \rightarrow |\psi_{g,n}\rangle$ ($|\psi_{g,0}\rangle \rightarrow |\psi_{e,m}\rangle$). This would allows to calculate the luminescence lineshape as

$$L(\omega) = \sum_n \left|\langle\psi_{g,n}|\psi_{e,0}\rangle\right|^2 \delta\left(E_{ZPL} - n\hbar\omega_0 - \hbar\omega_{em}\right) \tag{2.87}$$

At this level of complexity the ZPL is the particular transition $|\psi_{e,0}\rangle \rightarrow |\psi_{g,0}\rangle$ where the phonon is at its zero-point energy (ZPE) and the Huang-Rhys factor would be linked to the transition matrix element in Eq. 2.87 by

$$\left|\langle\psi_{g,n}|\psi_{e,0}\rangle\right|^2 = \mathrm{e}^{-S}\frac{S^n}{n!} \tag{2.88}$$

By adding another level of complexity we could finally apply the 1D model for a set of phonons separately, like it has already been done for the NV colour centre in diamond [80, 83, 82]. In this context it is possible to obtain all the features of the luminescence lineshape due to the phonon coupling which are in good agreement with the experiment. This model is particularly useful in the case where the phonon coupling is weak. Then the Huang Rhys factor is around 1 and a large part of the emission is concentrated on the ZPL and is not "dirtied" by phonon replica. In this case the emitted light can be useful for quantum technologies.

The Franck-Condon model presented has been used to study both internal transitions between defect levels and band-to-defect (defect-to-band) optical transitions. In this work we focused more on the second case since it may be useful to identify emissions due to impurities in a sample. In this case one is simulating the radiative emission due to the charge transition by promoting an electron from a defect level to the CBM. For example let us consider an acceptor defect in a crystal with a CTL $0/-$. We denote the ground state of this defect with A^- in the $q = -1$ charge state. Such defect might undergo a charge transition by giving the electron in excess to an unoccupied bulk level (most probabily the CBM), ending in the state $A^0 + e^-$ where the 0 superscripts denote the neutrality of the acceptor and the e^- is the electron in the bulk. In the same way the electron in the CBM can be recaptured back to the acceptor, reemitting a photon

$$A^0 + e^- \rightarrow A^- + \hbar\omega \tag{2.89}$$

This process is called radiative capture [81] and it is useful to study for example, the degradation of a device.

2.5. Supercell remapping of the screening

In this section we present an alternative way to treat the optical properties of defects.

Fig. 2.7 clearly shows that we need to calculate the screening in RPA in the static limit, $\epsilon_{rpa}(\omega = 0)$, which is then used to build the kernel K contained in the BSE Hamiltonian to diagonalize, Eq. 2.78. Usually, the conduction and valence energies, E_c and E_v, computed in Eq. 2.78 are the quasiparticle energies obtained from a GW calculation beforehand. This is the standard procedure that can be applied in a relatively easy way to simple crystals, like pristine wBN.

Unfortunately, when we are dealing with defects we are forced to use supercells of many atoms, making the calculation of the static screening and the quasiparticle correction quite challenging. Here we propose a methodology that allows us to circumvent this problem and then compute the optics using the BSE :

— we skip the calculation of the GW quasiparticle corrections. This can be done by using the Kohn-Sham states from a hybrid functional DFT calculation. The hybrid DFT predicts a band gap in agreement with the GW ;

— instead of using the static screening calculated on the defective system supercell we use the one computed for the pristine material primitive cell, which does not require much computational effort.

While the first point is quite straightforward, using the primitive cell static screening on the supercell is not a trivial task. The problem is that the static screening is expressed as a matrix where each entry has the $\boldsymbol{G}$-vectors as indices and they are expressed as function of the momentum. These indices as well as the momentum are not the same for the primitive cell and the supercell. We indicate with uppercase letters $\boldsymbol{G}$ and $\boldsymbol{Q}$ the reciprocal lattice and the momentum vectors for the primitive cell and with lowercase letters $\boldsymbol{g}$ and $\boldsymbol{q}$ the reciprocal lattice and momentum vectors for the supercell. When we enlarge a primitive cell to a supercell in the real space the corresponding reciprocal Brillouin zone shrinks accordingly. As a consequence, the corresponding band structure "folds" on itself. This is the reason why when carrying out a supercell calculation it is common practice to compute the energies on a $\boldsymbol{k}$-grid with less sampling points. In Chap. 4 we will see that when we will extensively apply the supercell approach to defects we will compute the electronic properties by sampling only the Γ point. On the other hand, the folding of the band structure in a smaller Brillouin zone results in many more levels at Γ point in a given range of energies. Therefore working on a supercell instead of a primitive cell means dealing with less $\boldsymbol{k}$-points at the price of using more bands to obtain the same physics.

Then starting from the primitive cell $\epsilon_{\boldsymbol{GG'}}(\boldsymbol{Q})$ we find a correspondence between the $(\boldsymbol{G},\boldsymbol{Q})$ vectors and the $(\boldsymbol{g},\boldsymbol{q})$ vectors. This correspondence is unique and is given by imposing the identity [85]

$$\chi_{\boldsymbol{G},\boldsymbol{G'}}(\boldsymbol{Q}) = \chi_{\boldsymbol{G},\boldsymbol{G'}}(\boldsymbol{q}+\boldsymbol{g_Q}) = \chi_{\boldsymbol{G}+\boldsymbol{g_Q},\boldsymbol{G'}+\boldsymbol{g_Q}}(\boldsymbol{q}) = \chi_{\boldsymbol{g},\boldsymbol{g'}}(\boldsymbol{q}) \tag{2.90}$$

This correspondence is subjected to several constraints as $\boldsymbol{g_Q}$ is a particular vector in the set of the $\boldsymbol{g}$ such that $\boldsymbol{Q} = \boldsymbol{q} + \boldsymbol{g_Q}$ and $\boldsymbol{g} = \boldsymbol{g_Q} + \boldsymbol{G}$, i.e. $\boldsymbol{Q} - \boldsymbol{q} = \boldsymbol{g} - \boldsymbol{G}$. Once this

correspondence is found we can remap the quantity $\chi_{\boldsymbol{G},\boldsymbol{G}'}(\boldsymbol{Q})$ into the corresponding $\chi_{\boldsymbol{g},\boldsymbol{g}'}(\boldsymbol{q})$.

A fundamental condition that must be fulfilled for the $\boldsymbol{g}_{\boldsymbol{Q}}$ to exist is that the two (unit cell and supercell) reciprocal lattices are commensurate. Let us suppose that we use a $\boldsymbol{k}$-grid sampling $N_{k_x} \times N_{k_y} \times N_{k_z}$ in the primitive cell and that we want to remap the screening on a supercell made of $N_x \times N_y \times N_z$ repetitions of the primitive cell. A correct remapping is possible if we choose $\frac{N_{k_x}}{N_x} \times \frac{N_{k_y}}{N_y} \times \frac{N_{k_z}}{N_z}$ as supercell sampling $\boldsymbol{k}$-grid. At the same time the number of bands in the supercell calculation will be $N^{sc}_{bnd} = (N_x \times N_y \times N_z) \cdot N^{uc}_{bnd}$ where N^{uc}_{bnd} is the number of bands used in the primitive cell calculation.

For example the screening remapping of a primitive cell on a $6 \times 6 \times 4$ supercell at Γ point, would be possible only if the screening on the unit cell has been computed using a $6 \times 6 \times 4$ $\boldsymbol{k}$-grid. The relation between the vectors in the reciprocal space is pictured in Fig. 2.10. In panel a) we have constructed a 2×2 supercell from a 2D hexagonal primitive cell. The first Brillouin zones (green for the supercell, red for the primitive cell) are the hexagons at the centre, surrounded by their periodic repetitions. The length of the supercell green hexagon sides is half the length of the red hexagons sides. The figure also shows examples of a $\boldsymbol{G}$ and a $\boldsymbol{g}$ vector. In panel b) of Fig. 2.10 we show on the left the primitive and the supercell 1BZs and on the right some other primitive and supercell Brillouin zone repetitions located at $\boldsymbol{G}$ and $\boldsymbol{g}$ respectively. We observe that the same point P is identified by the sums $\boldsymbol{g} + \boldsymbol{q} = \boldsymbol{G} + \boldsymbol{Q}$.

The remapping procedure has been implemented by the author of the present thesis in the form of a Python class interfaced with the `yambo` code databases during a three-week long visiting period at the S3 Nanoscience Centre of the italian National Council of Researches in Modena, Italy, under the supervision of Dr. Fulvio Paleari who is also the author of Ref. [85]. This class will be soon integrated in the Yambopy toolkit which is a python library for `yambo` post-processing.

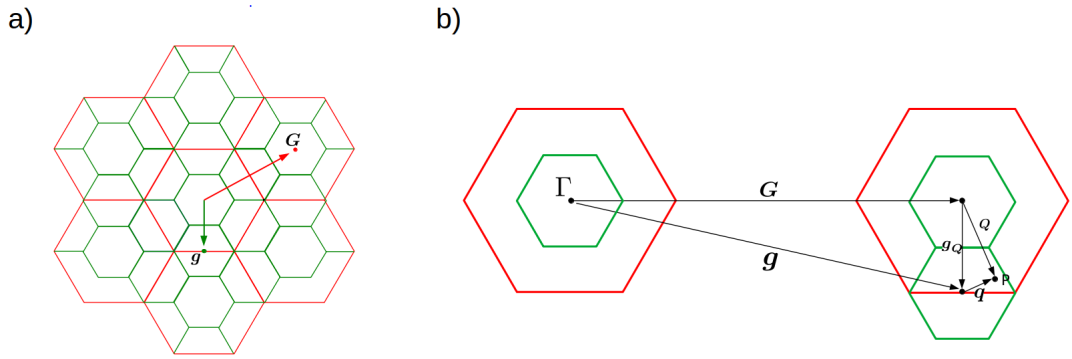

Figure 2.10. – Relation between the primitive (red) and supercell (green) reciprocal lattice vectors and momenta. Panel a) : illustrative examples of a $\boldsymbol{G}$ and a $\boldsymbol{g}$ vector in a 2D case and a 2×2 supercell; panel b) : relation between the $\boldsymbol{Q}$, $\boldsymbol{q}$, $\boldsymbol{g}$, $\boldsymbol{G}$ and $\boldsymbol{g}_{\boldsymbol{Q}}$ vectors.

Here we list the operations run by the program :

— Start with the set of all the $\boldsymbol{Q}_i$ and $\boldsymbol{q}_j$. Calculate the quantities $\hat{\boldsymbol{g}}_{ij} = \boldsymbol{Q}_i - \boldsymbol{q}_j \ \forall \ i, j$;
— among all the $\boldsymbol{g}$ find the $\boldsymbol{g}_k$ such that $\boldsymbol{g}_k = \hat{\boldsymbol{g}}_{ij}$;
— compute the vectors $\tilde{\boldsymbol{g}}_{\rho k} = \boldsymbol{G}_\rho + \boldsymbol{g}_k$;
— among the $\boldsymbol{g}$ vectors find the vector $\boldsymbol{g}_\sigma = \tilde{\boldsymbol{g}}_{\rho k}$;
— use the mapping given by the set of tuples (i, j, k, ρ, σ) to copy the right $\chi_{\boldsymbol{G},\boldsymbol{G}'}(\boldsymbol{Q})$ entry in the right $\chi_{\boldsymbol{g},\boldsymbol{g}'}(\boldsymbol{q})$

Then the static screening can be readily obtained from the polarizability χ.

The effectiveness of this procedure has been tested for wBN by first comparing the spectra obtained by remapping the screening on a supercell of the pure material. In Fig. 2.11 we used BSE on top of DFT using the screening remapped from a primitive cell sampled on a $4\times4\times4$ $\boldsymbol{k}$-grid into a $4\times4\times4$ supercell sampled at Γ. This spectrum is then compared with the one obtained by solving the BSE but using the static screening computed directly from the supercell. The two BSE spectra almost coincide.

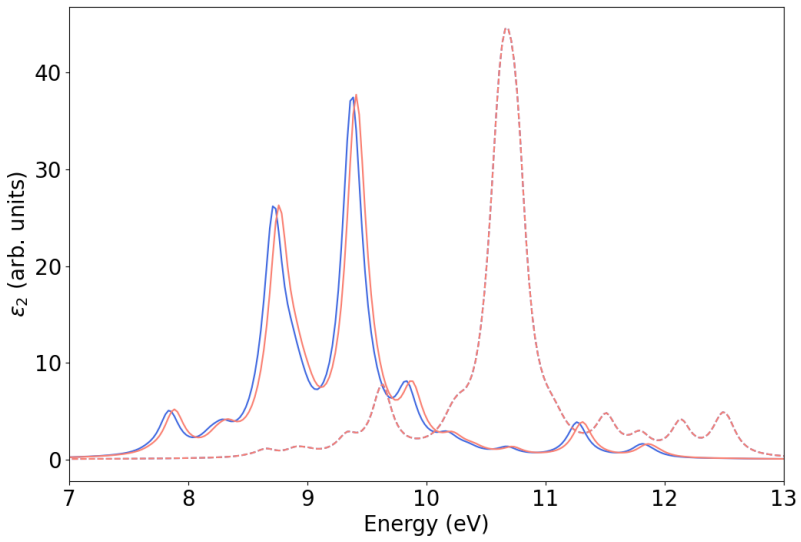

Figure 2.11. – Absorbance spectrum obtained using BSE on top of DFT using the remapped static screening (blue solid line) and the screening computed directly on the supercell (orange solid line). Also the independent particle spectra for the two cases are reported (dashed lines).

Note that Fig. 2.11 also reports in dashed lines the two independent particle spectra. As expected, since in this case the BSE is solved without taking into account the screening, the two spectra perfectly match and they overlap, so that only one of the two colours is showed.

2.6. Conclusions

In this Chapter we moved from the DFT formalism introduced in Chap. 1 and we introduced the Many-Body Perturbation Theory (MBPT) formalism. The necessity of such formalism has been related to the failure of DFT in describing several spectroscopy experiments such as ARPES, inverse ARPES and absorption. In the MBPT context the many-electron problem is rewritten in terms of the quasiparticle picture, where the screening effects are explicitly taken into account. We then established a logical and quantitative connection between such screening effects and the linear response of the material in the presence of an external perturbation (like in a spectroscopy experiment). We mathematically developed these ideas in the form of a set of five integro-differential equations to be solved self-consistently (Hedin's equations) using a formalism based on the Green's function. The exact solution of this set of equations turns out to be impractical unless we make several assumptions and approximations which constitute the *GW* method. We further developed the methodology to include in the problem the neutral excitations due to an external electromagnetic probe. Such neutral excitations lead to the formation of electron-hole pairs that eventually can be bounded in a hydrogen-like system called exciton which determines the optics of the material. A sound treatment of the excitons requires the derivation of an equation of motion for the two-particle correlation functions which is the Bethe-Salpeter equation (BSE). The approximated solution of the BSE allows to obtain the dielectric function of the material in an *ab initio* fashion and in principle it can be carried out on top of the *GW* method (thus including the quasiparticle corrections to the energies) as well as the DFT Kohn-Sham states. The introduction of defects in the crystal adds complexities to the workflow that we have just outlined because of the difficulty of applying the *GW* method in the supercell approach. We gave two ways to study the optics of defects. In the ΔSCF approach one calculates in an approximated way the excited states of a defective system by constraining the occupancies of the Kohn-Sham levels computed using a hybrid exchange-correlation potential, so that we can construct a Franck-Condon Configuration Coordinate Diagram (CCD) and simulate the ground and excited state potential energy surfaces in a harmonic approximation. The CCD allows to find the emission, absorption, Zero-Phonon line and Stokes and Antistokes energies. An alternative way to study the defect optics is by using the BSE on top of a DFT calculation and skipping the *GW* step. The quasiparticle correction can be mimicked using a hybrid functional. The static screening of the defective material which is an ingredient required by the BSE and which is also difficult to calculate in the supercell approach can be approximated by the pure material static screening which is easier to compute. A remapping procedure has been described in order to expand such primitive cell static screening onto the supercell and then compute the BSE.

3. Study of pristine *w*BN

To investigate the potential of *w*BN as a host for defects, it is essential first to understand the characteristics of the ideal crystal, which, unlike the real material, lacks point defects. Therefore in the following sections, we report the results of our *ab initio* study on the ground and excited state properties of pristine *w*BN , illustrating how the theoretical tools introduced in Chaps. 1 and 2 were used in our analysis. The investigation of the defect-host ensemble will be addressed in Ch. 4.

As we will see, the *w*BN structure is formed from *h*BN in a pressure range of 100 to 130 kPa. Consequently, throughout this chapter, we emphasize the dependence of the studied properties on the pressure range where this phase transition occurs. This chapter is organised as follows. In Sec. 3.1 we provide a brief review of the current literature on *w*BN , giving details on its crystal structure and ways of production, its relation with other BN polymorphs and discussing the complex issue of its stability. Secs. 3.2 and 3.3 describe the results of our convergence tests and structural optimization. In Sec. 3.4 we present the vibrational properties obtained by mean of DFPT, illustrating the phonon modes. In Sec. 3.5 we use the *GW* technique on top of DFT to provide the quasiparticle correction of the band structure and compare the band gaps at DFT and *GW* levels. In Secs. 3.6 and 3.7 the optical properties (absorption and phonon-assisted luminescence) of *w*BN are obtained by solving the Bethe-Salpeter equation. The results presented in this chapter have also been included in Ref. [86].

3.1. A review of wurtzite Boron Nitride

Here we describe the general and fundamental features of the *w*BN structure by referring them to the literature. We discuss separately the structure itself, the crucial issue of the thermodynamic stability of *w*BN with respect to other BN phases and we provide the current understanding of its optical properties. The Bravais lattice of *w*BN is an hexagonal cell with a C_{6v} point group and the space group is the $P6_3mc$ (#186) which is nonsymmorphic[87]. The primitive cell (pictured in Fig. 3.1) counts 4 atoms, tetrahedrally coordinated in sp^3 bondings. We indicate with a and c the two lattice parameters of the hexagonal Bravais lattice. The primitive vectors $\boldsymbol{a}_1$ and $\boldsymbol{a}_2$ have length a and they form an angle of 120°. The lattice parameter c parametrizes with respect to a the length of the $\boldsymbol{c}$ vector which is taken parallel to the z-axis (we adopt the notation $\boldsymbol{c}$ instead of $\boldsymbol{a}_3$ to avoid confusion with the vector $\boldsymbol{a}_3$ that will be introduced for the 4-indices Miller-Bravais notation). In accordance with Fig. 3.1, the atomic positions are reported in Tab. 3.1 (in crystal coordinates $n_1\boldsymbol{a}_1 + n_2\boldsymbol{a}_2 + n_3\boldsymbol{c}$) where z is a free parameter. The *w*BN is also closely related to the other BN polymorphs like e.g.

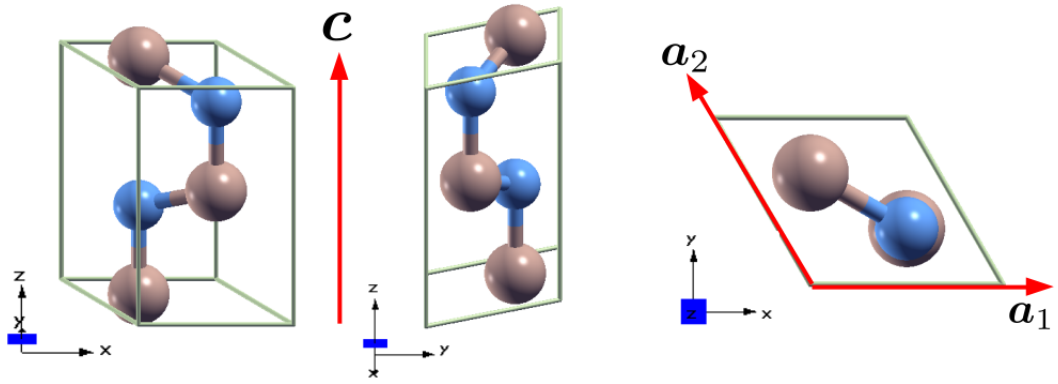

Figure 3.1. – Prospects of wurzite primitive cell in three different orientations : the reader's eye sight line is perpendicular to the x-axis (left panel), the y-axis (central panel) and parallel to the z-axis (right panel). Blue atoms represent nitrogen while brown atoms represent boron. The red arrows are the crystal primitive lattice vectors $\boldsymbol{a}_1$, $\boldsymbol{a}_2$ and $\boldsymbol{c}$.

Atom	n_1	n_2	n_3
B # 1	1/3	2/3	0
N # 1	1/3	2/3	1/2
B # 2	2/3	1/3	z
N # 2	2/3	1/3	$z+1/2$

Table 3.1. – Atomic positions for the Wurtzite structure in crystal coordinates.

the cubic phase (cBN also defined zincblende boron nitride zBN, space group $F\bar{4}3m$, with sp^3 hybridization), the hexagonal phase (hBN , also defined in the literature graphite-like BN or gBN, with space group $P6_3mmc$) and the rhombohedral phase (rBN , space group $R3m$). hBN and rBN are layered materials with sp^2 hybridization, in AA' and ABC stacking sequences respectively, where the layers are linked by Van der Waals bondings [1]. Instead of the usual Miller 3-indices notation, in the literature it is quite common for the hexagonal crystal lattices to use the Miller-Bravais 4-indices notation, which is based on the introduction of another vector $\boldsymbol{a}_3$ (which is not, by any mean, a primitive vector) illustrated in Fig. 3.2. With this notation the 4 indices identify a plane or a direction normal to it. Each index gives the intersection of the plane with the $\boldsymbol{a}_1$, $\boldsymbol{a}_2$, $\boldsymbol{a}_3$ and $\boldsymbol{c}$ axes (0 means no intersection). So, if we refer to Fig. 3.2, the $(10\bar{1}0)$ direction will be perpendicular to the $(10\bar{1}0)$ plane which is the one that intersects $\boldsymbol{a}_1$ in 1, it is parallel to $\boldsymbol{a}_2$, intersects $\boldsymbol{a}_3$ in -1 and is parallel to $\boldsymbol{c}$. In the same way the (0001) direction is the c-axis which is perpendicular to the plane parallel to the xy plane and intersects $\boldsymbol{c}$ in 1.
The problem of thermodynamic stability of wBN has been puzzling researchers for a long time. The reason resides in the difficulties encountered in the attempts to pro-

1. The mentioned forms do not constitute a complete list of all BN polymorphs. For more BN polytypes see the introduction of this thesis.

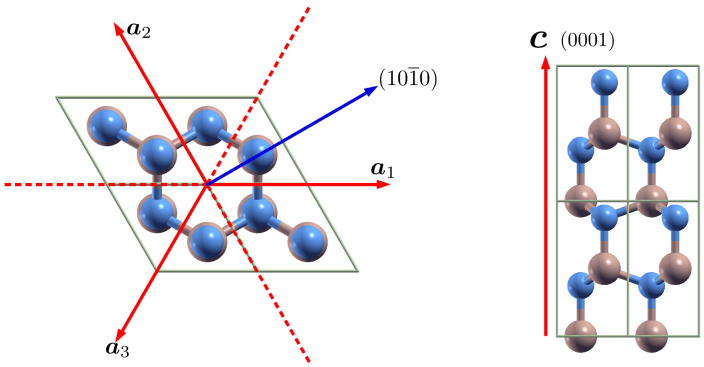

Figure 3.2. – Vectors used in the Miller-Bravais 4-indices notation for hexagonal cells. The $(10\bar{1}0)$ is the blue arrow in the left panel.

duce and analyse *w*BN samples, which is the reason why for a long time its stability at ambient conditions has been questioned, resulting in a lukewarm interest towards the potential applications of this particular polymorph when compared to *h*BN and *c*BN . Until recently, *w*BN has been always manufactured in the form of small crystallites (below μm) produced from *h*BN powder under high pressure. The first reported synthesis of *w*BN powder dates back to the early 1960s by Bundy and Wentorf [88] who were able to obtain *w*BN grains large enough to allow an identification of the polymorph by x-ray diffraction. They established that *h*BN transforms into the bulk phases (*w*BN and *c*BN) between 110 and 130 kBar and that *w*BN is preferred at lower temperature while *c*BN is favoured at higher temperatures[88, 89]. In this first study some of the applied pressures were defined "static", with times of application on *h*BN of the order of minutes. Another option that has been used is shock compression but the purity of the wurtzite phase in the powder obtained in this way can be disputed. Shock compression was used by Soma *et al.* who claimed to have produced *w*BN powder without *c*BN impurities, whereas Tani *et al.* obtained an admixture of phases [90] and Kurdyumov *et al.* [91] considered the crystallites highly defective. The stability at ambient pressure is somehow given for granted by Tani *et al.* [90] but Solozhenko *et al.* showed that *w*BN is metastable in all regions of the PT phase-diagram of BN [92] explaining why this material is so difficult to produce.

A reversion of *w*BN to *h*BN occurs with heating. An apparent impossibility to produce crystallites that are more than 80 % *w*BN was indeed explained by Will [93] with the adiabatic heating during shock compression, but it was argued that annealing of defects in *w*BN powder may increase the temperature necessary to the back transition [91]. Metastability does not mean impossibility to produce stable *w*BN samples. Although *c*BN has a total energy slightly lower than *w*BN and the kinetic barrier between *c*BN and *w*BN can be low [94], stable samples have been produced. We can in fact see *w*BN as an intermediary in the hexagonal-to-cubic phase transition at high pressure if we consider four of the BN polytypes mentioned above and their stacking sequences. *h*BN and *w*BN have the same AA' stacking sequence. When transforming into wurtzite, the layers of the hexagonal phase become "buckled"

and split into two sublayers or bilayers, one made of boron atoms, the other made of nitrogen. The interlayer Van der Waals bonds in *h*BN are replaced by covalent bonds along the (0001) direction. *r*BN and *c*BN share the same relation as the one between *h*BN and *w*BN , with the difference that in this case the stacking sequence is ABC along the 111 direction [95]. In this picture, Refs. [95, 63, 94] argued that the hexagonal-to-cubic phase transition at high pressure may be a two-steps process and not a direct conversion. Under high pressure the *h*BN layers can either retain the same stacking and buckle into *w*BN or they can slide one on each other to assume the ABC stacking sequence. Then *w*BN can rearrange its atoms to make *c*BN while *r*BN can simply replace its Van der Waals bonds with covalent bonds. This perspective gives to *w*BN and *r*BN an active role in the *h*BN to *c*BN phase transition and it also explains why small domains of *w*BN and *r*BN are always present in *c*BN samples [95, 96]. More recently, almost single crystals of *h*BN have been grown and used to produce *w*BN instead of the *h*BN powder. As a result, macroscopic (width $\approx$ 2 mm) samples of *w*BN have been successfully manufactured [33, 63, 97]. The *w*BN is recognized as a superhard material [28], almost hard as *c*BN . Although it is stated in Ref. [97] that a spontaneous reverse transition to *h*BN occurs at ambient pressure, Segura *et al.* proved by IR/visible reflectance and transmittance experiments that it is not the case. They showed that *h*BN transforms into *w*BN between 118 and 130 kBar and the wurtzite form is retained after the release of the pressure. This contradiction in the literature may be explained with the fact that the statement in Ref. [97] is partly based on the Ref. [98] where it is explained that the wurtzite boron nitride obtained in different ways might differ in the stability. Nonetheless, the macroscopic sample presented in Ref. [97] is claimed to be stabilized thanks to a mechanism due to a network of planar faults. Since macroscopic samples of *w*BN could be produced only since 2019, there have not been many experimental studies on the optical properties of *w*BN , while some *ab initio* studies were instead carried out. In the present thesis the electronic and optical properties of *w*BN are computed again using the advanced *GW* method. For completeness, we therefore refer the reader to the past works by e.g. Xu and Ching[94], Christensen and Gorczyca [99], Karch and Bechstedt [100], Ohba *et al.* [101] who used DFT-based methods to compute the electronic properties of *w*BN , together with a number of other compounds. Such references will be recalled later in this chapter if needed. To the best of our knowledge, the sole experimental study on *w*BN optical absorption is the one by Yixi *et al.* [102] who provided an optical band gap of 8.7 eV and an absorption spectrum for a *w*BN sample. This experimental study will be used later for comparison. Segura *et al.* [63] provided an experimental value for the static dielectric constant of $\epsilon_0 = 6.65 \pm 0.03$ and an optical dielectric constant $\epsilon_\infty = 4.50 \pm 0.05$, that will be used in Chap. 4.

3.2. Preliminary study and convergence tests

To start an *ab initio* study we need first a good guess for the atomic positions. In order to perform the convergence tests described in Chap. 1 and required by a DFT

context we used the experimental lattice parameters $a = 2.55$ Å and $c = 4.22$ Å as reported in Refs. [103] and [87]. As explained in Chap. 1, it is necessary to converge the total energy of an SCF calculation with respect to the number of $\boldsymbol{k}$-points in the $\boldsymbol{k}$-grid and the number of $\boldsymbol{G}$ vectors that enters Eq. 1.33, i.e. converge the total energy with respect to the cut-off energy Eq. 1.34. To carry out the convergence we decide to work with the norm conserving semi-local PBEsol functional [104] downloaded from the DOJO online database [105]. In practice we carried out a series of simple SCF calculations for increasing cut-off energy and number of $\boldsymbol{k}$-points. The convergence is reached when the energy per valence electron in the primitive cell E_{tot}/N_{val} is less than 4 meV. Fig. 3.3 reports the total energy per valence electron obtained from our simulations as a function of the cut-off energy and the $\boldsymbol{k}$-point mesh. We found that the convergence is reached for $E_{cut} = 64$ Ry and a $6 \times 6 \times 4$ $\boldsymbol{k}$-grid.

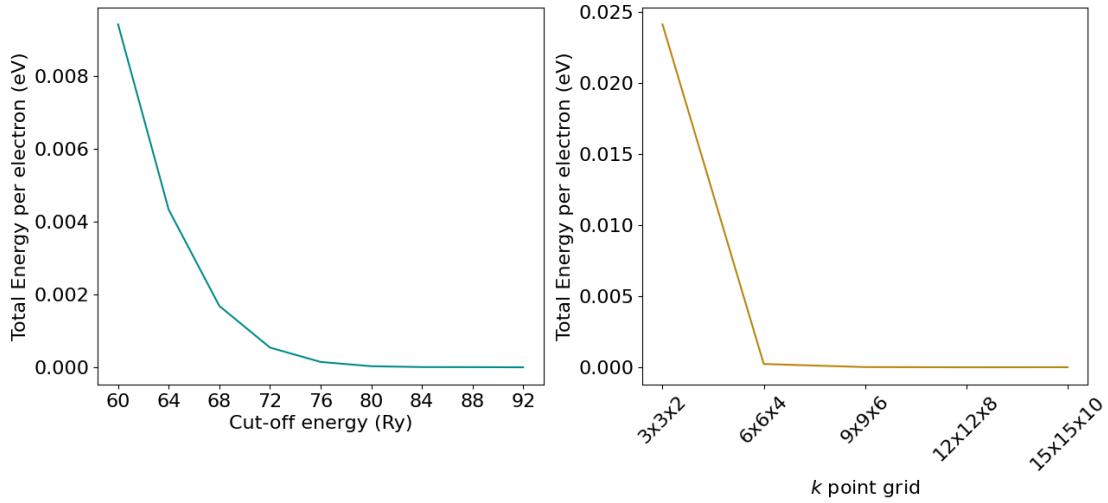

Figure 3.3. – Convergence of the total energy per electron with respect to the cut-off energy (left) and the $\boldsymbol{k}$-point grid used (right). The 0 is set to the minimum value in order to highlight the energy differences between the calculations

3.3. Optimization of the geometry

Now that we found the minimal cut-off energy and $\boldsymbol{k}$-grid necessary to carry out sound and consistent calculations we can optimize the geometry of the crystal. We run a series of relaxations of the primitive cell volume and the atomic positions. Since our aim is to explore the properties of wBN in the range of pressures where it is produced from hBN , we carry out the variable-cell relaxation for 0, 50, 100, 150 and 200 kBar, bearing in mind that according to Ref. [63, 97, 33] the phase transition occurs between 100 and 130 kBar. These relaxations are run with E_{cut} equal to 70 Ry and $\boldsymbol{k}$-grid equal to $12 \times 12 \times 8$, which are slightly above the convergence values. The initial guess for the primitive cell parameters is the same as the one used in the convergence tests

described in Sec. 3.2, while the initial guess for the atomic positions is the one of the perfect ideal wurtzite structure, i.e. the one listed in Tab. 3.1 with the coordinate z set to 3/8. The optimized cell and atomic positions are obtained by minimizing the forces acting on the atoms and the stress tensor. Since in the wurtzite structure the BN bond lenght in the (0001) direction is a free parameter, we let the forces act only on the z coordinate of atoms. In Fig. 3.4 we report the cell parameters obtained from the variable cell relaxations for the pressures explored. Our lattice parameters are in good agreement (difference below 0.6 %) with the experimental a and c parameters measured by Solozhenko *et al.* [92] through x-ray powder diffraction.

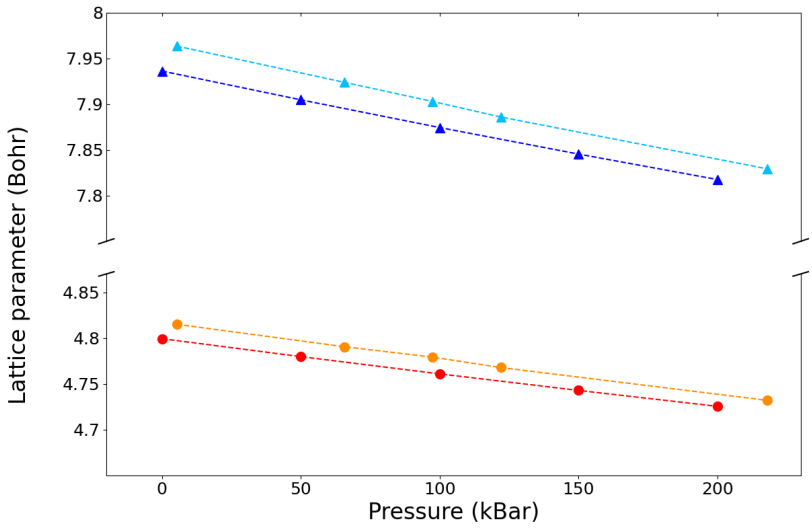

Figure 3.4. – Cell parameters as functions of pressures. a (red circles) is the basal plane lattice parameter of the hexagonal primitive cell, while c (blue triangles) is the lattice parameter in the (0001) direction. Our theoretical values are compared with the experimental a (orange circles) and c (deepskyblue triangles) parameters taken from Ref. [92].

3.4. Vibrational properties

The point group symmetry of wBN is C_{6v}[87]. The character map of C_{6v} group is reported in Tab. 3.2 [106]. Since there are 4 atoms in the wurtzite unit cell we should expect 4×3 = 12 phonon branches in total. Three modes are acoustic and the remaing 9 are optical. According to group theory for phonons (see Chapts. 8 and 11 of Ref. [106] for example), one has to consider the decomposition into irreducible representations of the direct product

$$\Gamma_{ph} = \Gamma_{eq} \otimes \Gamma_{vec} \tag{3.1}$$

where Γ_{ph}, Γ_{eq} and Γ_{vec} are the irreducible representations of the lattice vibrations (i.e. the phonon modes), the equivalent atomic positions and a radial vector (which

C_{6v}	E	C_2	$2C_3$	$2C_6$	$3\sigma_d$	$3\sigma_v$
A_1	1	1	1	1	1	1
A_2	1	1	1	1	-1	-1
B_1	1	-1	1	-1	-1	1
B_2	1	-1	1	-1	1	-1
E_1	2	-2	-1	1	0	0
E_2	2	2	-1	-1	0	0

Table 3.2. – Character table for C_{6v} symmetry group

transforms either as x, y or z), respectively. Such direct product can be done explicitly by calculating the character arrays of Γ_{eq} and Γ_{vec} and doing the arithmetic product of the two in each of the symmetry operation classes. The result is the character table of Γ_{ph} which can be then decomposed in the direct sum

$$\Gamma_{ph} = \bigoplus_{\Gamma_{irr} \in C_{6v}} g(\Gamma_{irr})\, \Gamma_{irr} \tag{3.2}$$

where the direct sum runs over all the irreducible representations Γ_{irr} of the transformations in C_{6v}, i.e A_1, A_2, etc. and $g(\Gamma_{irr})$ are the coefficients of the Γ_{irr}. By following this procedure one finds that the phonons modes for wBN are

$$\Gamma_{ph} = 2A_1 \oplus 2B_1 \oplus 2E_1 \oplus 2E_2 \tag{3.3}$$

for a total of 12 modes (E modes are doubly degenerate). The optical modes are [107]

$$\Gamma_{opt} = A_1 \oplus E_1 \oplus 2E_2 \oplus 2B_1 \tag{3.4}$$

while the acoustic modes are $\Gamma_{ac} = A_1 \oplus E_1$. The scheme of atom displacements in the optical phonons modes are given in Fig. 3.5.

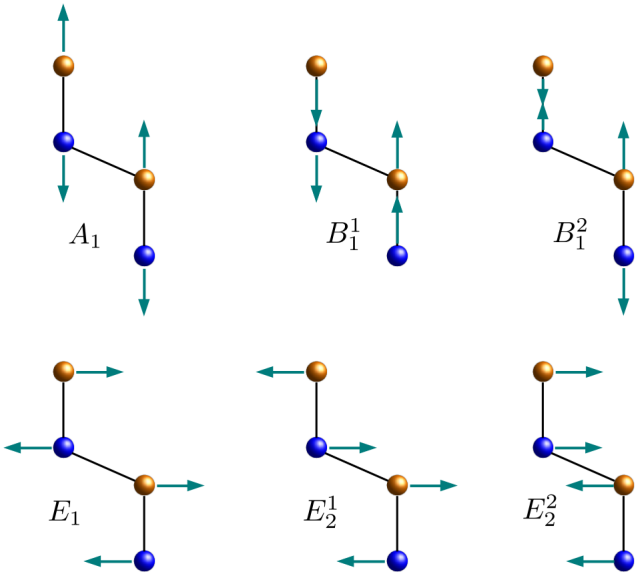

Figure 3.5. – The nine optical phonon modes for the C_{6v} point group. Note that E modes are doubly degenerate.

We compute the phonon dispersion at different pressures using the relaxed structure obtained through structural relaxation. Finding the phonon dispersion means solving for the phonon frequencies Eq. 1.41. The phonon frequencies are found using the program `ph.x` of the Quantum Espresso package, for each pressure, on a uniform $9\times9\times6$ $\boldsymbol{q}$-grid in momentum space. The program `q2r.x` performs a Fourier transform to the real space and computes the interatomic force constants (IFC). It also enforces the acoustic sum rule to avoid negative frequencies at the Γ point for the acoustic modes which are supposed to be identically 0. Finally the program `matdyn.x` carries out a new Fourier transform on the IFCs back to the momentum space, this time on a chosen set of $\boldsymbol{q}$-points in the Brillouin zone, namely a chosen high symmetry path in order to get a smooth phonon dispersion. The entire calculation relies on the Kohn-Sham states obtained using a $\boldsymbol{k}$-grid denser than the one imposed as minimal standard by convergence tests, therefore as we have already done for the structural optimization, we used a $12\times12\times8$ $\boldsymbol{k}$-grid. Since BN is a polar material, to account for the macroscopic electric field at $\boldsymbol{q}=0$, the LO-TO splitting has been computed by imposing to the IFCs the non-analytical correction using the Born effective charges $Z^\star$ while running `ph.x` and `matdyn.x`. In Fig. 3.6 we show the phonon dispersion at pressure 0 kBar including the LO-TO splitting, together with an illustration of the high symmetry points in the Brillouin zone connected by the segments of the path in $\boldsymbol{k}$-space where we interpolate the bands. This path will be also used later to show the electronic band structures of wBN . At the Γ point, all the irreducible representations of the crystal symmetries are reflected in the phonon modes, thus it is possible to associate at each representation the corresponding energy and study its behaviour as a function of the pressure. The phonon energies at Γ are depicted in the left panel of Fig. 3.7 and they are in agreement with the modes found in Refs. [100]

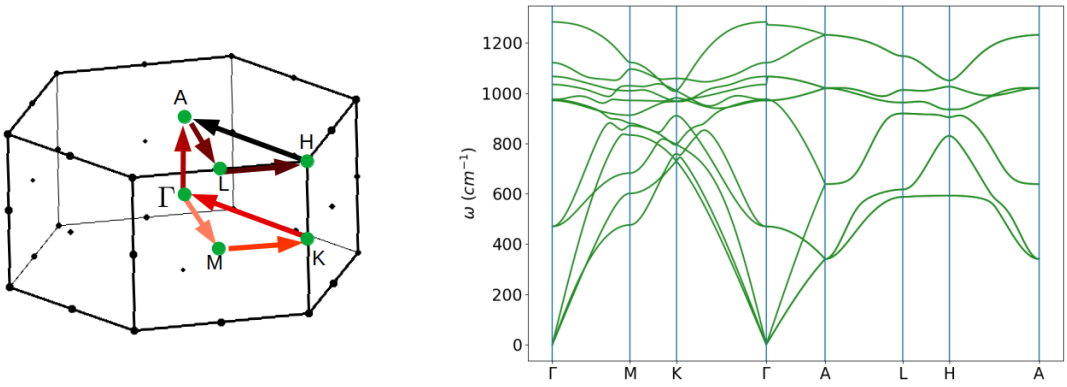

Figure 3.6. – Left panel : path covering the high symmetry points in the 1BZ; right panel : computed phonon dispersion at 0 kBar, note the three acoustic modes with 0 frequency at Γ. The highest level is made of two almost degenerate bands obtained by applying the LO-TO splitting.

.

and [63] (a comparison is presented in Tab. 3.3). We see that for increasing pressure

Mode	IR	Raman	Energy (cm $^{-1}$)	Energy (cm $^{-1}$) (Ref. [63])	Energy (cm $^{-1}$) (Ref. [100])
E_2^1	no	no	469.96	475.1	
E_2^2	no	no	971.08	978.3	
B_1^1	no	no	976.17	981.3	
$A_1(TO)$	no	yes	1034.7	1043.4	1006
$E_1(TO)$	yes	yes	1066.4	1075.9	1053
B_1^2	no	no	1121.3	1131.3	
$A_1(LO)$	yes	yes	1271.8	1278.9	1258
$E_1(LO)$	yes	yes	1283.6	1291.5	1281

Table 3.3. – Phonon modes at Γ and comparison with data from the literature. IR and Raman activity is also given.

almost all the optical modes increase their energies at Γ accordingly. This behaviour is not surprising as for increasing pressures the interatomic distances decrease and in harmonic approximation this brings to an increasing oscillator frequency. This fact is also in agreement with the overall shift to higher energies of the phonon density of states computed on a very dense $\boldsymbol{q}$-grid ($30 \times 30 \times 20$ using the utility `phdos.x`) shown on the right panel of Fig. 3.7. Our calculation at 0 kBar is in agreement with the experimental phonon DOS obtained by inelastic x-ray scattering presented in Ref. [108]. The identification of the phonon modes at Γ is returned by Quantum Espresso and it is confirmed by comparing Fig. 3.5 with the direct visualization of the associated displacements using the utilities xcrysden[109] and Materials Cloud[110].

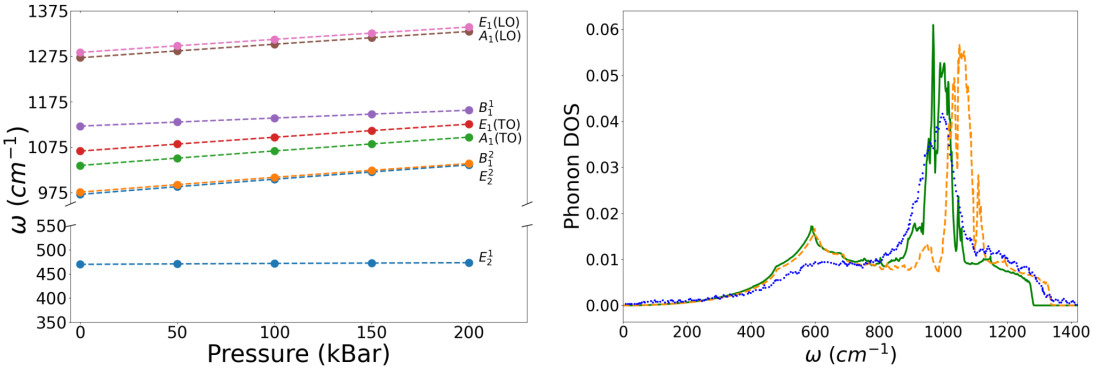

Figure 3.7. – Left panel : energies and identification of the optical phonon modes at Γ as a function of pressure; right panel : phonon density of state computed at 0 kBar (green solid line), 200 kBar (yellow dashed line). The computed phonon DOS is compareed with the experimental one (blue dotted line) taken from Ref. [108].

Again, it is possible to see how all the modes increase their energy at increased pressure, except for the doubly degenerate E_2^1 mode at 470 cm^{-1} which remains constant. This particular behaviour can be explained with the fact that it is a mode associated to the wurtzite-to-cubic phase transition as it is the result of the folding at Γ of the transverse acoustic mode in *c*BN . This mode is also linked to the phonon replica at around 56 meV observed in cathodoluminescence experiments [34] on *c*BN and it may signals the presence of *w*BN domains as imperfection in *c*BN samples. In Tab. 3.4 we report

Pressure (kBar)	E_1(LO)-E_1(TO) (cm^{-1})	A_1(LO)-A_1(TO) (cm^{-1})	E_1(LO)-A_1(LO) (cm^{-1})
0	217.2	237.1	11.7
50	216.2	235.9	11.2
100	215.4	234.8	10.7
150	214.5	233.7	10.2
200	213.7	232.6	9.7

Table 3.4. – LO-TO splittings computed in our phonon calculations.

in detail the values for the LO-TO splittings while the Born effective charges Z^B and the corresponding components of the dielectric tensor

$$\epsilon_\infty = \begin{pmatrix} \epsilon_\infty^\perp & 0 & 0 \\ 0 & \epsilon_\infty^\perp & 0 \\ 0 & 0 & \epsilon_\infty^\parallel \end{pmatrix} = \begin{pmatrix} \epsilon_\infty^{xx} & 0 & 0 \\ 0 & \epsilon_\infty^{yy} & 0 \\ 0 & 0 & \epsilon_\infty^{zz} \end{pmatrix} \tag{3.5}$$

are reported in Tab. 3.5. As the pressure increases the Born effective charges, dielectric functions and therefore the LO-TO splitting itself decrease. This decrease occurs at a pace higher than the variation of the splitting between longitudinal modes E_1 and A_1 (last column of Tab. 3.4), showing that the long-range electrostatic forces dominate

Pressure (kBar)	$\epsilon_\infty^\perp$	$\epsilon_\infty^\parallel$	ϵ_∞	$\Delta\epsilon_\infty$	$Z_\perp^B$	$Z_\parallel^B$	Z^B	$Z^\star$
0	4.52	4.677	4.57	0.033	1.832	1.928	1.864	0.871
50	4.51	4.664	4.56	0.033	1.827	1.922	1.859	0.870
100	4.50	4.652	4.55	0.033	1.821	1.917	1.853	0.869
150	4.49	4.641	4.54	0.033	1.816	1.911	1.848	0.867
200	4.48	4.631	4.53	0.033	1.811	1.906	1.842	0.865

Table 3.5. – Born effective charges and their resulting macroscopic dielectric tensors in their diagonal form. ϵ_∞ is defined as the average of the diagonal elements of the dielectric tensor Eq. 3.5 while $\Delta\epsilon_\infty$ is defined as $(\epsilon_\infty^\parallel - \epsilon_\infty^\perp)/\epsilon_\infty$. Z^B is the average on the diagonal of the Born effective charges tensor and $Z^\star$ is the screened effective charge.

over the short-range interatomic forces that are strongly anisotropic, in analogy to wurtzite AlN and GaN [107].

3.5. Electronic properties

The electronic properties of *w*BN are studied as a function of pressure by mean of MBPT with the *GW* method introduced in Chap. 2 on top of the different unit cell geometries obtained. The quantities which we are mainly interested in, are the electronic band structure and the direct and indirect band gaps. For the band dispersion the energy levels are computed on the same high symmetry path already used for phonons and pictured in the left panel of Fig. 3.6. In order to work with sound results we need to converge the band gap computed via *GW* with respect to the number of $\boldsymbol{G}$ vectors considered (which we call the blocksize) and the number of unoccupied bands.

Pressure (kBar)	$E_{ind}^{qp} - E_{ind}^{dft}$ (eV)	$E_{dir}^{qp} - E_{dir}^{dft}$ (eV)
0	1.406	1.726
50	1.417	1.747
100	1.426	1.768
150	1.436	1.788
200	1.444	1.807

Table 3.6. – Difference between the band gaps computed with and without the quasiparticle correction.

The set of Kohn-Sham states computed so far by `pw.x` with E_{cut} = 70 Ry and $12 \times 12 \times 8$ $\boldsymbol{k}$-grid is now used to reconstruct the Kohn-Sham Hamiltonian. The new Hamiltonian is then re-diagonalized considering many more unoccupied states for a total of 150 bands (this operation is carried out by `pw.x` in a so-called non-self consistent calculation). We converged at 0 kBar the value of the direct gap with respect to the number of bands (while keeping, as initial guess for the number of $\boldsymbol{G}$-vectors

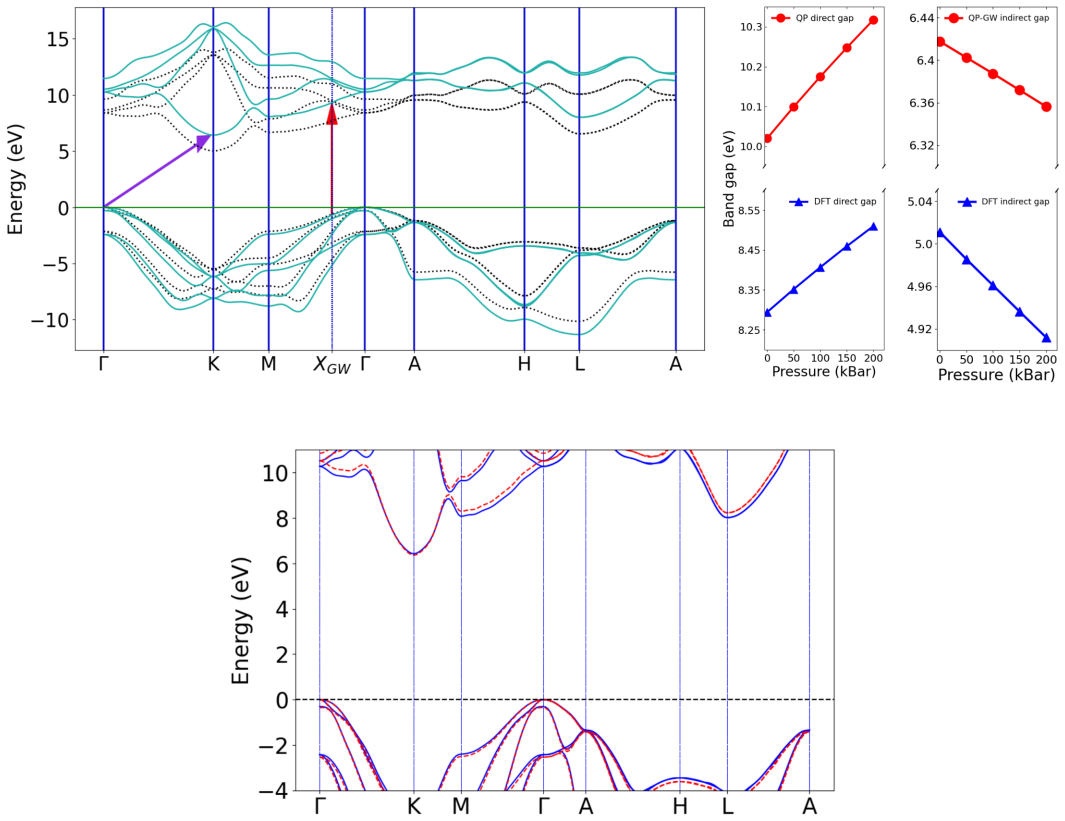

Figure 3.8. – Top left panel : band structure for 0 kBar pressure at DFT (black dotted) and quasiparticle level (light green solid line). The indirect (purple) and direct (red) transition are highlighted with two arrows; top right panel : evolution of the direct and indirect gap at different pressures at both DFT and quasiparticle level; bottom panel : a comparison of the quasiparticle band structure computed at 0 (blue) and 200 (red) kBar.

considered, a reasonable 2 Ry cutoff) and then with respect to the blocksize itself. We found that our calculation can be performed with a 6000 mRy blocksize and 75 bands. Because of several computational difficulties the number of bands used will be reduced to 50. These parameters will be adopted also for the other pressures considered. The plasmon pole approximation[76] introduced in Chap. 2 is adopted with the plasmon position above 27 eV. We thus compute for all the pressures the quasiparticle-corrected band structure, the direct and indirect gaps. These quasiparticle-corrected quantities are then compared with those computed directly from DFT. In the left panel of Fig. 3.8 we can see both the band structures at 0 kBar computed with DFT and including the quasiparticle correction. The evolution of the direct and indirect band gaps as function of all the pressures applied is shown in the right panels.

As expected, the effect of the quasiparticle correction is to open the gap with respect to the one computed with DFT. The indirect transition occurs between the Γ and the K point, independently of the method used, while the $\boldsymbol{k}$ point where we have the

direct transition is shifted in the reciprocal space from the point $X_{DFT} = (0, 1/12, 0)$ at DFT level to the point $X_{GW} = (0, 1/6, 0)$ in crystal coordinates. This shift in $\boldsymbol{k}$ space is the same for all the pressures considered. We also noticed that in the MΓ direction in reciprocal space, in proximity of the direct transition point X_{GW} even though the highest valence band does not change a lot, the conduction band increases its energy with pressure whereas it does the opposite in the K point (see bottom panel of Fig. 3.8). As a consequence the direct and the indirect band gaps present an opposite dependence on the pressure, as shown in the right panels of Fig. 3.8. If we look at the difference between the band gaps computed with DFT and those with the quasiparticle correction (see Tab. 3.6) we can see that the trends shown in the right panels of Fig. 3.8 hardly depend on the method used, as the differences vary by less than a tenth of an eV.

The opposite dependence on pressure of the gaps can be ascribed to the different character of the bands in the points involved in the transitions (Γ and K for the indirect, X_{GW} for the direct one). Fig. 3.9 can help us understanding this feature. We plot the band structure at DFT level at 0 kBar. We project each Kohn-Sham state on the atomic orbitals and a colour describes whether it takes the most contribution from the $2s$ and $2p$ states of boron or from the $2s$ and $2p$ states of nitrogen. We see that the

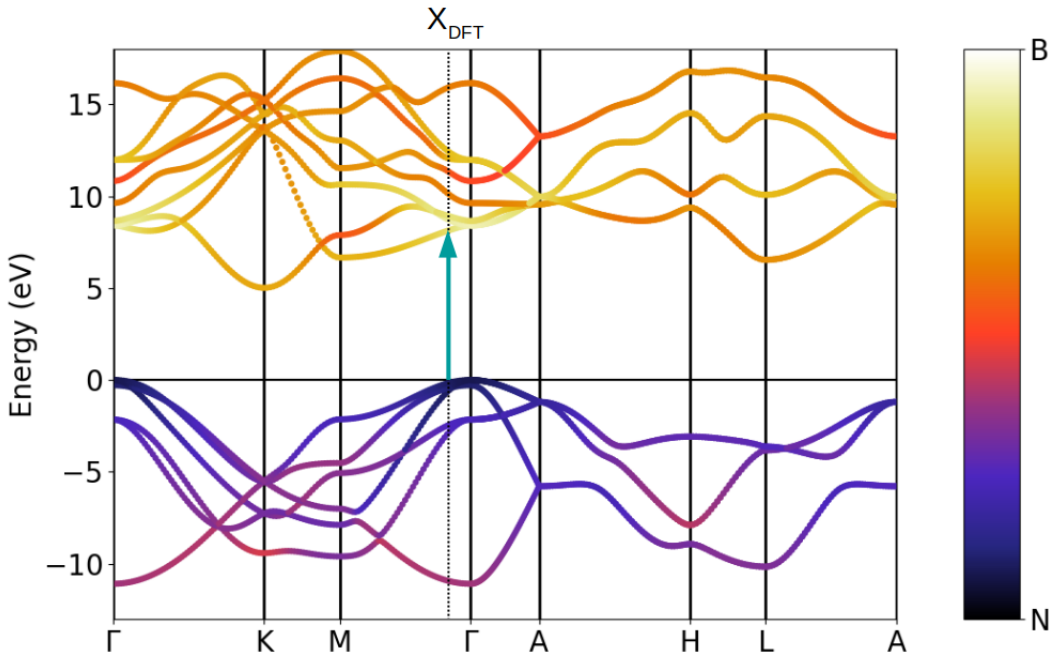

Figure 3.9. – DFT band structure at 0 kBar with wavefunctions projected on the atomic orbitals of B and N. A colormap associates each color to different weights of contribution from one atom and the other.

boron states contribute the most to the conduction band while the nitrogen orbitals contribute mostly to the valence band, as we would expect considering the difference in electronegativity of the two atoms. At the Γ and X_{DFT} points the highest valence

bands take their contributions mostly from the nitrogen states. At X_{DFT} the lowest conduction bands are dominated by the boron states, whereas at the K point they take contributions from both boron and nitrogen atomic states. Thus the indirect transition involves the conduction band in a point where it has a more mixed character than at the X_{DFT} point. The different weight of the contributions at K and X_{DFT} for the indirect and direct transitions, respectively, can explain the opposite behaviour of the direct and the indirect gaps for increasing pressure.

The increase of the direct gap is opposite to the behaviour predicted for hBN where the direct gap decreases with pressure [111]. The difference resides in the different hybridization in wBN and hBN .

3.6. Optical properties

The optical properties have been computed in the studied pressure range by solving the Bethe-Salpeter equation Eq. 2.71 on top of the quasiparticle calculation in GW approximation. The number of bands computed in the DFT non-self consistent calculations sets the maximum number of polarisation bands that we can consider at the GW level. We probe the effects on the BSE-computed dielectric function of different combinations of $\boldsymbol{k}$-grids in the non-self consistent cycle and number of polarisation bands used to expand the screened potential W and the Green's function G. The resulting band gaps at 0 kBar are reported in Tab. 3.7.

$\boldsymbol{k}$-grid	pol. bands	DFT band gap (eV)	GW band gap (eV)
$9\times9\times6$	50	8.278481	10.02118
$9\times9\times6$	100	8.278491	9.973264
$12\times12\times8$	50	8.294258	10.02006
$12\times12\times8$	100	8.294258	9.973027
$15\times15\times10$	50	8.278825	10.02135
$15\times15\times10$	100	8.278825	9.974085

Table 3.7. – Band gaps at 0 kBar obtained for different $\boldsymbol{k}$-grids and number of polarization bands.

The BSE spectra resulting from simulations with some of these set of parameters are reported in Fig. 3.10 where we can see that for different $\boldsymbol{k}$-grids the spectra present the same structures but with slightly different renormalizations (enhancements of some peaks instead of others). By keeping constant the $\boldsymbol{k}$-grid and increasing the number of polarisation bands a slight shift towards lower energies is observed. However the gain in accuracy is not significant enough to justify the computational cost. We decide therefore to perform our calculations using 50 polarisation bands and a $12\times12\times8$ $\boldsymbol{k}$-grid.

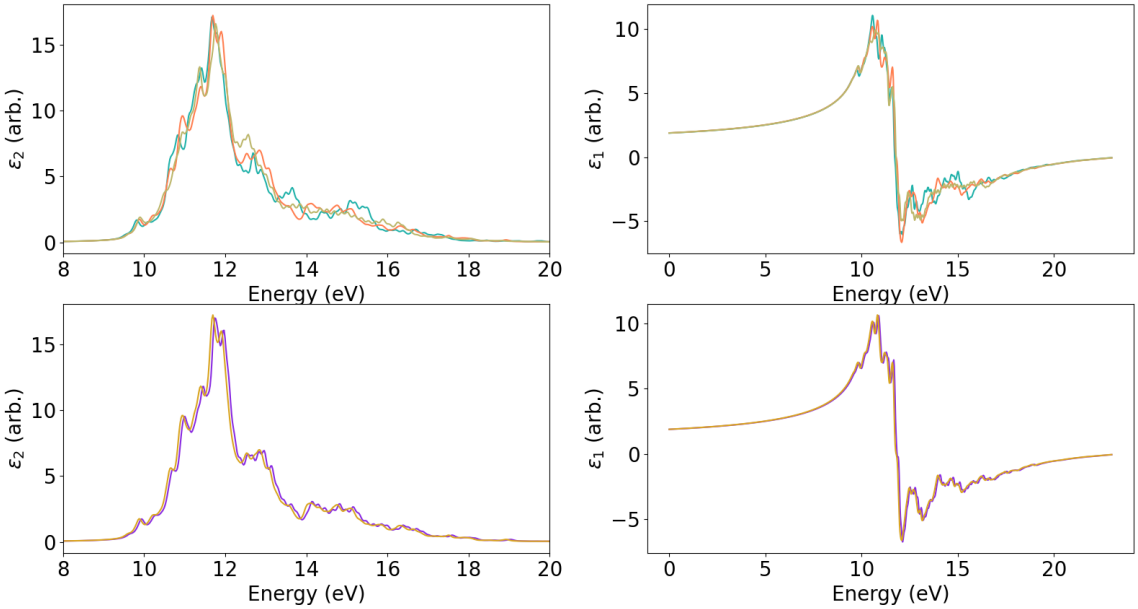

Figure 3.10. – BSE spectra obtained for different numbers of polarisation bands and $\boldsymbol{k}$-grids. Top panels : imaginary (left) and real (right) part of the dielectric functions obtained with 100 polarization bands using a $9 \times 9 \times 6$ (light green), a $12 \times 12 \times 8$ (coral orange) and a $15 \times 15 \times 10$ (dark khaki) $\boldsymbol{k}$-grid; bottom panels : imaginary (left) and real (right) parts of the BSE dielectric functions obtained with a $12 \times 12 \times 8$ $\boldsymbol{k}$-grid using 50 (blue violet) and 100 (goldenrod) polarization bands.

Next, we assess the number of valence and conduction bands that should be included in our BSE calculation. After having compared several spectra computed using different combinations of bands (see Fig. 3.11), we decide to operate with three conduction bands and three valence bands as there are not many features added to the spectra if we used more unoccupied states. We compute the screening in RPA approximation to build the kernel for the BSE pseudo-Hamiltonian. The Hamiltonian is then fully diagonalized to obtain the eigenvalues, the excitonic eigenstates and both the real and imaginary parts of the dielectric function. The resulting spectra are reported in Fig. 3.12 where we see that the structures tend to move towards higher energies for increasing pressure. This effect can be explained by observing that the exciton is constrained to increase its energy following the increased band gap. Since the screening is included in calculating the *GW* gap and in computing the exciton levels, the two effects almost cancel out. The excitons are delocalized, therefore a slight change in the geometry does not change too much the screening and the interaction of the electron with the hole.

We now focus on the case at 0 kBar. In Fig. 3.13 we report the BSE spectrum for the imaginary dielectric function ϵ_2 together with the spectrum obtained in DFT-RPA approximation and in the *GW* independent quasiparticle approximation (i.e. obtained by solving the BSE on top of *GW* without including the screened potential in the kernel). These results are then compared with the experimental spectrum found

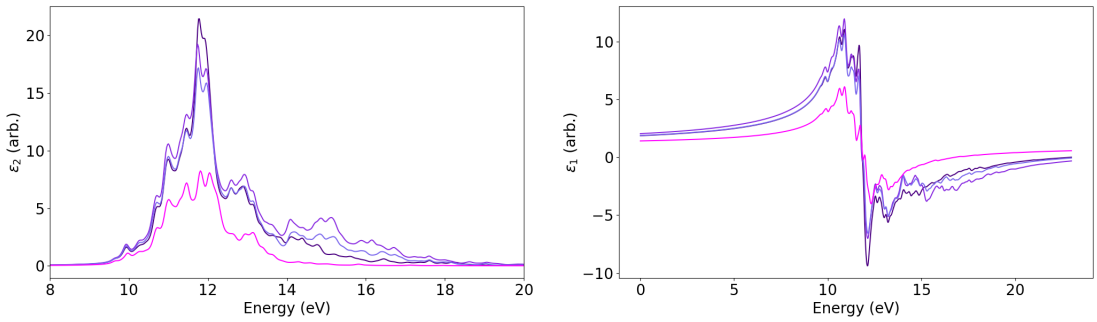

Figure 3.11. – Different BSE spectra at 0 kBar obtained considering different intervals of valence and conduction bands in the computation. Indigo : four valence bands and 2 conduction bands; blueviolet : three valence bands and 4 conduction bands; mediumslateblue : 3 valence bands and three conduction bands; fuchsia : two valence bands and two conduction bands. For all the calculations 50 polarization bands with a $12 \times 12 \times 8$ $\boldsymbol{k}$-grid have been used.

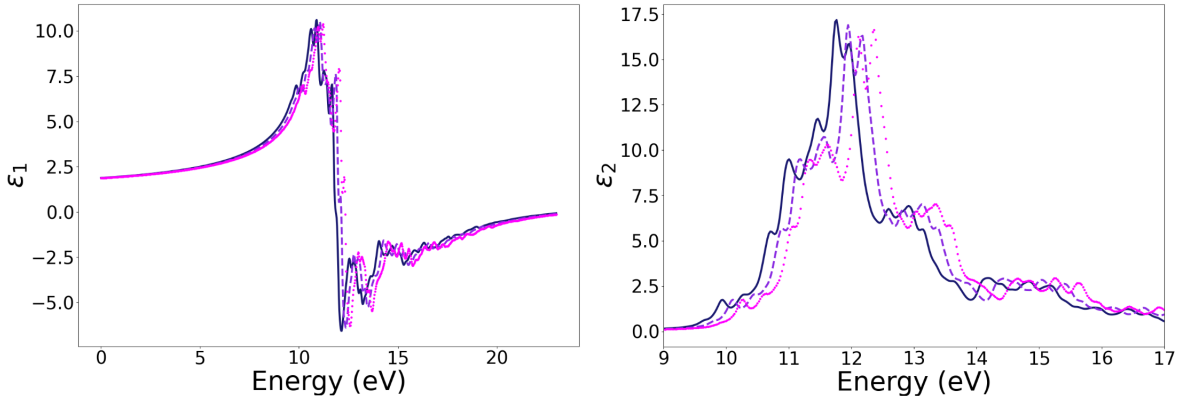

Figure 3.12. – Real (left panel) and imaginary (right panel) parts of the dielectric spectra obtained using the BSE at 0 (solid navy blue), 100 (dashed purple) and 200 kBar (dotted fuchsia).

in Ref. [102] obtained by absorption experiment on annealed solids of nanometer *w*BN powder. To the best of our knowledge, Ref. [102] is the sole experimental study of the absorbance spectrum in the UV region for *w*BN specifically. As expected, the BSE absorbance spectrum presents its main structures at energies which are lower than the RPA and *GW* independent particle spectra, with some features below the *GW* band gap. The structures are also renormalized and redistributed due to the electron-hole interaction. The post-processing allows us to analize the excitons individually, such analysis will then help us to interpret the mismatch between our BSE spectrum and the experimental data. The optical gap is determined by the first bright exciton. The first exciton found in our analysis is dark non-degenerate, the second and the third are dark and degenerate. The first bright excitons are degenerate and they are the fourth and the fifth respectively. In Tab. 3.8 we report in the left table the energy of the first

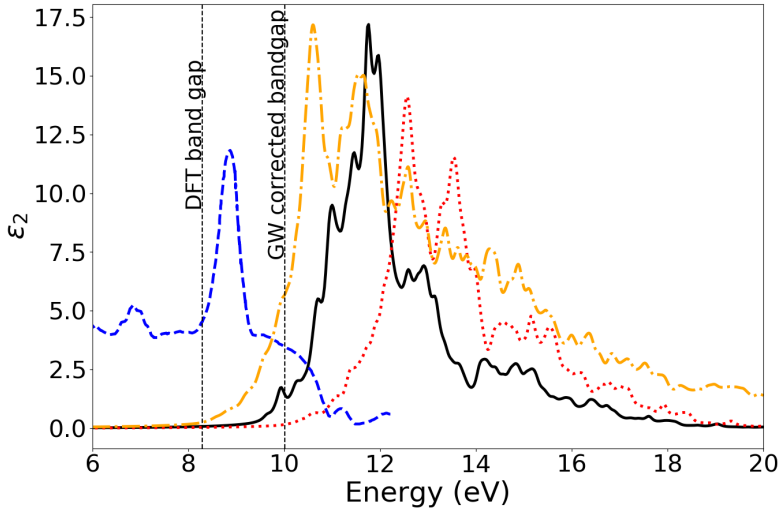

Figure 3.13. – Imaginary part of the dielectric function computed at 0 kBar using the BSE (black solid line), in RPA independent particle approximation (yellow dashed dotted line) and in independent *GW* quasiparticle approximation (red dotted line). The blue dashed line is the measured dielectric function presented in Ref. [102].

exciton as a function of pressure while in the figure on the right we put in relation these energies to the direct band gap in order to evaluate also the binding energy. We can see that the binding energy remains constant at a value of 0.38 eV for rising pressure, confirming that the effects of the variation of the screening on the excitons and the band gap cancel out as explained before. In Fig. 3.14 we plot the excitonic wavefunction of the first 5 excitons while keeping the hole position at the center of the supercell for a pictorial representation (the hole is slightly displaced from a N atoms along the *c*-axis). We finally try to give an explanation to the mismatch between the high peak standing out from the background of the experimental spectrum in Fig. 3.13. The position of the calculated lowest bright exciton at 0 kBar is partially compatible with the claimed experimental optical gap at 8.7 ± 0.5 eV found in Ref [102]. Two effects that have not been included so far in our theory might also explain this inconsistency. Firstly, as it is clear from the literature, production of pure *w*BN is extremely difficult and many impurities like point defects, extended faults and inclusion of domains of other BN polymorphs due to an imperfect phase transition might be the origin of the peak observed. In the next chapter we will try to shine a light on the role of defects in the luminescence of *w*BN; secondly, electron-phonon coupling might induce a broadening of the spectral features so that the optical gap provided by the theory enters the range of energies involved in the experimental peak.

Pressure (kBar)	First bright exciton (eV)
0	9.64393806
50	9.72157669
100	9.79571438
150	9.8669548
200	9.93547344

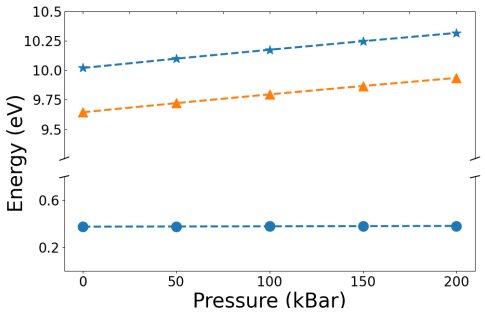

Table 3.8. – Energies of the first bright excitons at different pressures and their binding energy. The values are also reported in the figure in the right panel where we report direct gap (star points), the exciton energies (triangles) and their difference, i.e. the binding energy (circles)

3.7. Phonon-assisted luminescence

Since wBN is an indirect band gap material, with the lowest indirect gap occurring between points Γ and K, we know that the luminescence is possible only if it is assisted by phonon modes. Thus it is essential to consider the exciton-phonon coupling when analysing luminescence, i.e. an indirect exciton of finite $\boldsymbol{q}$ recombining thanks to a phonon of momentum $\boldsymbol{q} = K - \Gamma = K = (1/3, 1/3, 0)$. The symmetry at K is however lower than in Γ and the irreducible representations are different. Therefore we identify the phonon modes at K by using only a number, from 1 to 12. The phonon energies and their dispersion with respect to the hydrostatic pressure are given in Fig. 3.15.

In order to study the phonon-assisted luminescence we applied the following strategy. First a BSE calculation, including the quasi-particle corrections, is carried out for a $\boldsymbol{q} = K$ corresponding to the reciprocal space displacement we are interested in. We then repeated the calculation by discarding the quasi-particle corrections. In this way we estimate a scissor correction that exactly reproduces the position of the exciton at K. We found that the lowest energy exciton computed on top of DFT at $\boldsymbol{q}$ = K is at 4.73 eV while if we include the quasiparticles it is at 6.14 eV. Their difference gives the scissor correction of 1.41 eV. Our choice is motivated by the fact that the quasiparticle correction shift to higher energies the conduction bands computed via DFT by an amount that is independent from the $\boldsymbol{k}$-point considered (see Fig. 3.8). Therefore the same band structure could be equally well-approximated by retaining the DFT bands and applying a rigid shift to the conduction band.

Then we build the supercell in Fig. 3.16 to refold the K point at Γ and we calculated the dielectric constant that enters in BSE with the parameters of the primitive cell (polarization function number of bands) rescaled to the supercell size. Then we solved the BSE on the supercell at transferred momentum $\boldsymbol{q}$ =0, applying the scissor operator estimated above. The excitons found using the remapping supercell are of two types, those which are also direct when the BSE calculation is carried out in the primitive cell, and those which are indirect if the primitive cell is used, which appear now direct

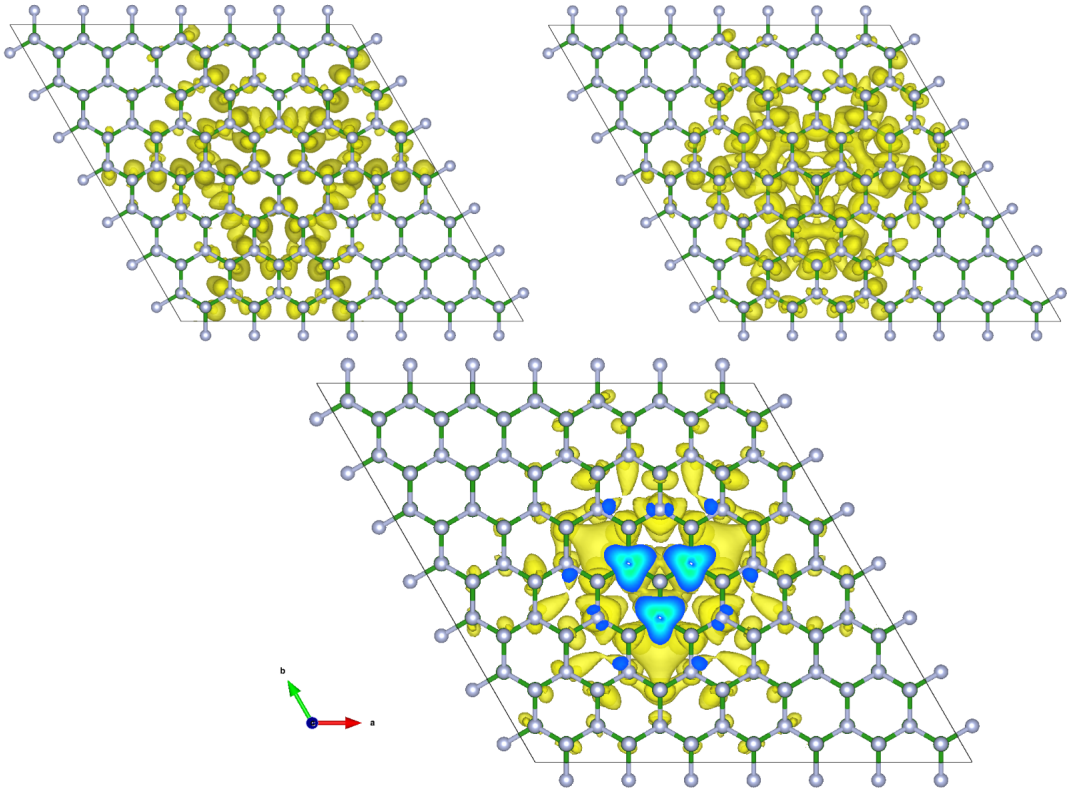

Figure 3.14. – Excitonic wavefunction for the first five excitons at 0 kBar. Top left panel : first non degenerate dark state ; top right panel : second and third degenerate dark excitons ; bottom center : fourth and fifth degenerate bright excitons. Since the exciton is rather delocalised it has been represented on an expanded $7 \times 7 \times 3$ supercell. The reader's eyesight is parallel to the (0001) direction of the crystal.

as the K point is remapped into Γ. These indirect excitons are dark and they need the coupling with a phonon bringing a momentum $\boldsymbol{q} = \Gamma K$ in order to radiatively recombine and participate to the optics of the material.

In a third step we built 12 supercells, one for each phonon mode, with atoms dispaced along the phonon eigenmodes times 0.1 bohr radii. For each displaced supercell we diagonalized the BSE, on top of DFT to make the calculations faster and the quasiparticle effects are approximated by applying the scissor operator. Each one of the 12 BSE diagonalizations has to be performed three times, each one considering a different orientation of the electric field. This is a necessary consideration since the electric field affects the dipole of the exciton. The three directions will allow us to make a spatial average. Moreover, in the displaced supercells we do not recalculate the dielectric constant but we use the equilibrium one. This approximation allows us to speed up calculation and it has been shown not to produce any visible error in the final luminescence spectrum [112].

In order to get a phonon-assisted luminescence spectrum we need to use the Roosbroeck-Shockley formula Eq. 2.81. Therefore we need the second derivative

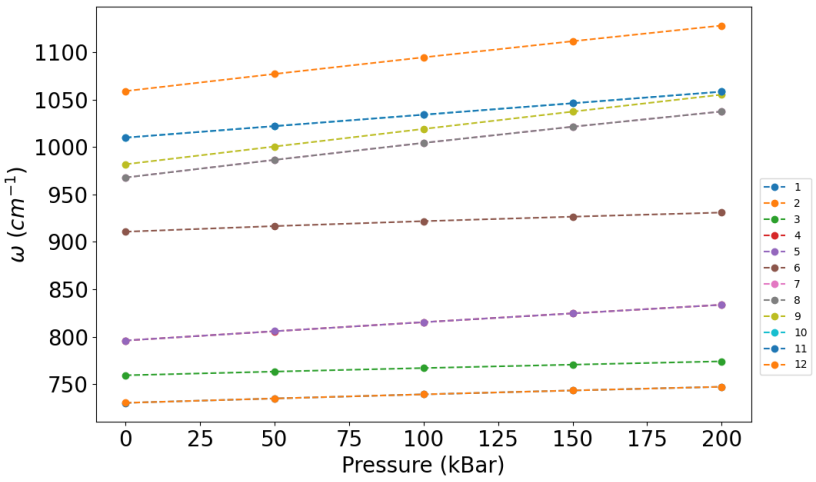

Figure 3.15. – Phonon energies at K point as functions of the pressure.

of the dipole matrix elements that appear at the numerator of the expression for the macroscopic dielectric function in exciton basis Eq. 2.79. Such derivative can be calculated by finite differences. The result is shown in Fig. 3.17 where we discriminated the contributions coming from the polarisations parallel to the xy plane and to the z axis. We note from panel b) of Fig. 3.17 that the coupling mainly occurs with the phonons 12 and 11 which have the highest energies and with the phonons 1 and 2 which are the lowest in energy. When the light is instead polarised along the (0001) direction the main contribution comes from mode 7 and 8. Now, if we want to qualitatively predict the behaviour of such peaks for varying pressure, we must take into account two antagonist tendencies in the crystal. On one hand the phonon modes increase their energies for increasing pressure (see Fig. 3.15), on the other hand at the $\Gamma \rightarrow K$ transition the band gap decreases. As a consequence we can reasonably expect the phonon-assisted luminescence peaks to shift slightly to lower energies with the peak at 6.02 eV shifting more compared to that one at 6.05. As a final remark we should point out that although we displaced the atoms in twelve different ways we did not recompute the static screening each time and we used the one related to the equilibrium relaxed structure (with no phonons). This approximation has already been proved to affect the result only imperceptibly as shown in the case of hBN in [112].

3.8. Conclusions

In this chapter we studied the vibrational, electronic and optical properties of pure wBN using the methodologies introduced in Chaps. 1 and 2. First we presented a short review of the literature on wBN where we tried to clarify the history of the research on this boron nitride polytype with an emphasis on the problem concerning its stability. DFPT has been used to study the energies of the vibrational normal modes while the

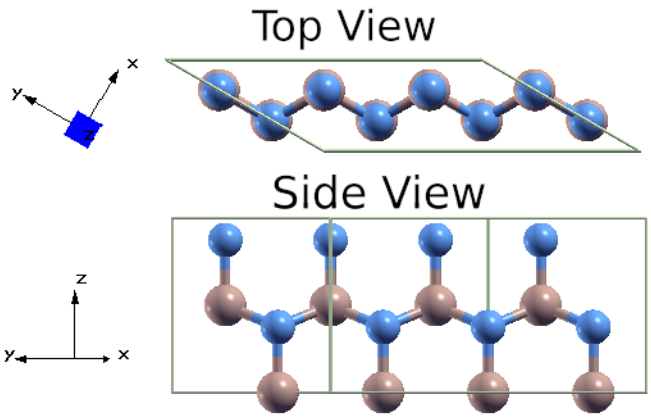

Figure 3.16. – *w*BN supercell used to refold the K point into Γ to study he phonon-assisted luminescence.

electronic properties and the optics have been assessed by mean of the *GW* method and the BSE. The phonon modes, band gaps and the optical spectra have been studied in a range of pressures relevant for the hexagonal to wurtzite phase transition. Finally, we calculated the phonon-assisted luminescence by constructing the Roosbroeck-Shockley formula for the exciton-phonon optical recombination, where we considered the indirect excitons between Γ and *K* points of the Brillouin zone. We observed that all the phonon modes increase their energies as we increase the pressure except for the mode E_2^1 which is related to the folding of the TA mode in *c*BN . Its constant energy is close to a phonon replica observed in *c*BN cathodoluminescence experiments, suggesting that *w*BN inclusions are always present in *c*BN samples. The computed large band gaps confirms that *w*BN is actually an insulator (or a "wide-band-gap semiconductor") and we also observed that for the same range of pressures the direct band gap increases whereas the indirect gap decreases at both DFT and *GW* level. This is due to the different contributions of the boron and nitrogen atomic states to the Bloch's states involved in the direct and indirect transitions. In the same way the BSE optical spectrum moves its features to higher energies as we increase the pressure as well as the first bright excitons. This is due to the fact the direct excitons mainly take their contributions from the direct transition and their excitation energies evolve accordingly. Furthermore, comparison of the BSE optical spectrum with the *GW*-RPA and the DFT optical spectra shows that excitonic effects are important. Interestingly, there is a mismatch between our BSE offset and the experimental optical gap of *w*BN , suggesting that the sample studied in [102] may be rich in defects and that electron-phonon coupling might be necessary in an *ab initio* study. Lastly, the phonon-assisted luminescence spectrum (computed only at ambient pressure) shows several features which originate from two groups of phonon modes. By considering the pressure dependence of the indirect band gap and the phonon energies at the *K* point of the Brillouin zone, we can predict that the two main features in the luminescence spectrum will distance one from each other as we increase the pressure.

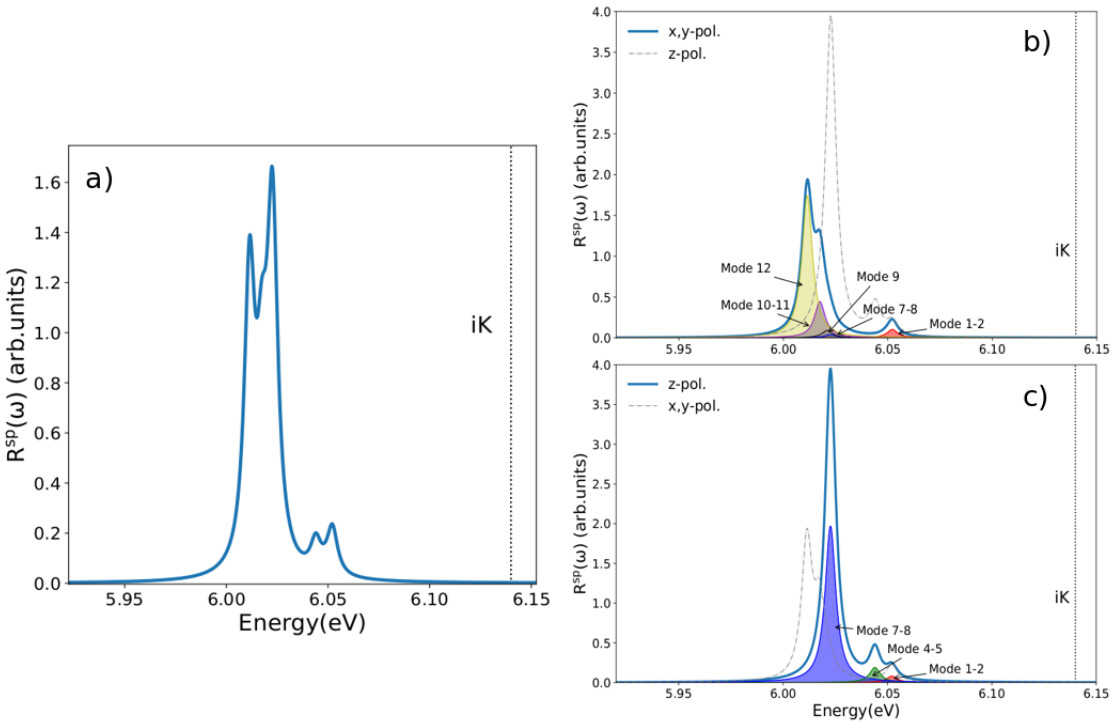

Figure 3.17. – Luminescence spectra obtained by use of the Roosbroeck-Shockley formula. Panel a) : average over the three directions ; panel b) : contributions with xy polarisation ; panel c) : contributions with z polarisation

4. Thermodynamics and optical properties of defects in *w*BN

In this chapter we depart from the ideal model of the pure *w*BN studied in Chap. 3 and we move our focus to a system that is closer to the real material which includes defects. The theoretical methodologies needed to study defective systems have been already outlined in Chaps. 1 and 2 and they will be used now on a set of simple defects. By "simple" we mean that we will chiefly discuss monomers (only one atomic site is involved), which correspond to the very definition of *point* defects. With the sole exception of the carbon dimer, we will not consider the so-called complexes, which are defects originated from the migration and joining of two or more monomers, like it is done for example in Ref. [48] for *h*BN . Also interstitial insertions will not be discussed. This chapter is made of three sections. In Sec. 4.1 we discuss the methodologies used to study the thermodynamics of the defects and their formation energies, describing in detail the procedures followed to compute these properties. Sec. 4.2 will present the results obtained for each defect studied individually and we discuss their electronic features. In Sec. 4.3 instead we will study their optical properties where possible, using the ΔSCF Franck-Condon approach and the remapping procedure and the diagonalization of the BSE presented in Chap. 2. The results presented in this chapter will be incorporated in an upcoming paper which is in preparation at present.

4.1. Computation of the formation energies

In this section we put into practice the theories introduced in Chaps. 1 and 2 to study the thermodynamics for a set of simple point defects. Our aim is to compute their formation energy diagram in the Zhang and Northrup formalism [54]. We thus proceed in three steps which roughly coincide with the three parts that make up the formation energy formula Eq. 1.55, that is, the total energies for the supercells with and without the defect under study, the chemical potential terms and finally the dilute limit correction.

4.1.1. Structural relaxation and total energy

In the present subsection we discuss the total energy calculations needed to calculate the formation energies. In the formation energy expression Eq. 1.55 there are two total energy terms, one referring to the defective system and the other one referring to the pristine crystal. Both have to be computed on supercells of the same size, but

since the total energy of the pristine supercell is the same for the formation energies of all the defects studied it needs to be computed only once. Therefore here we focus only on the calculation of the total energy of the defective system.

As already mentioned in Chap. 1 the supercell needs to be as large as possible to maximize the distance between a defect and its periodic image, bearing in mind that any supercell that we can compute in a HPC will be too small for this purpose, forcing us to correct at least the spurious electrostatic interaction between the defect and its periodic images in an approximated way. The size of *w*BN supercells used in this work is $6 \times 6 \times 4$, meaning that it was built from a unit cell repeated 6 times on the $\boldsymbol{a}_1$ direction, 6 times in the $\boldsymbol{a}_2$ direction and 4 times in the $\boldsymbol{c}$ direction. The total number of atoms in the supercell is given by 4 atoms for each primitive cell times $6 \times 6 \times 4$ for a total of 576 atoms. Attempts to use supercells counting more than 576 atoms resulted in memory failures of the HPCs used to carry-out the calculations presented in this work. As explained in Sec. 2.5, when going from a primitive to a supercell the 1BZ shrinks and the bands fold accordingly. Therefore when applying the supercell approach to defects, instead of a dense $\boldsymbol{k}$-grid we will use only the Γ point. Once the supercell for the pristine crystal is constructed from the primitive cell, we can introduce the defect.

The point defects studied in this work are the boron vacancy V_B, the nitrogen vacancy V_N, the monomer carbon substitutionals C_B and C_N, the antisites B_N and N_B and the carbon dimer $C_BC_N = C_2$ which is a complex formed by the C_N next to a C_B. The boron and nitrogen vacancies reduce the total number of atoms in the supercell from 576 to 575. Since the carbon dimer implicitly defines a direction along the C-C bond, it could in principle either be aligned along the (0001) direction or be composed by two carbon monomers belonging to the same buckled bilayer lying on the (0001) plane. Since *w*BN can be produced from *h*BN under a pressure cycle we assume that any defect likely to be present in the wurtzite crystal was already in the *h*BN sample (in one of its layers) undergoing the phase transition and that in the resulting *w*BN it lies on the same bilayer. The presence of such defects in *h*BN has already been proved by photoluminescence spectroscopy, for example the carbon dimer is a common defect in *h*BN that has been associated to the 4.1 eV emission line [24], moreover, several experiments on the implementation of the boron vacancy for quantum sensing purposes are currently going on,[113]. Once the defective supercell is built we carry out a relaxation of the atomic positions using the PBE semilocal exchange-correlation functional. The fully relaxed structure is then used as a starting point to calculate the total energy using the hybrid Gau-PBE functional. The Gau-PBE functional can not be used for the relaxation, since the computational time would be prohibitive. Although in several studies the hybrid functional has been used also for structural optimization [114], it has also been showed for the case of MoS_2 that the lattice parameters are already well reproduced by semilocal exchange-correlation functionals [23]. This two steps procedure (relaxation followed by total energy calculation with hybrid-DFT) sometimes is not sufficient to obtain an accurate description of the properties - both geometrical and electronic - of the defective material. If the ground state electronic configuration of the system is degenerate then

the Jahn-Teller [115] effect occurs. In the following we describe the procedure we used in this case.

Jahn-Teller effect Sometimes a relaxation calculation in DFT finds a set of atomic positions such that the system possesses a degenerate ground state, i.e. a degree of symmetry higher compared to that one of the real system. In our context of solid state physics, the degeneracy of the ground state means that we have found a HOMO with degeneracy higher than 1 and not completely filled. For example, if the HOMO resulting from a DFT relaxation calculation is a doubly degenerate e state but the number of electrons in the system is sufficient only to fill up one of the two, then we have two degenerate ground states. In one configuration the last electron is accommodated in the e_x degenerate sublevel, in the second one the electron occupies the e_y state. This configuration occurs as the system is lying on an unstable critical point of the potential energy surface. In this case the degeneracy of the electronic configuration will be lifted by distorting the lattice and lowering the total energy and degree of symmetry. This is the Jahn-Teller effect. (See Refs. [115] and [116]). Unfortunately the Quantum Espresso code does not detect the Jahn-Teller effect automatically. A DFT relaxation will however converge to a configuration that minimizes the forces acting on the atoms and it is up to the user to manually verify *a posteriori* that the ground state found is not degenerate. This operation is quite simple as all we need to do is to check the HOMO occupancy returned by the DFT calculation. If the occupation is non-integer, then the Jahn-Teller effect is present and we know that the relaxed structure found is not the real minimum energy configuration. In order to find the real minimum, all we have to do is to restart the structural relaxation by slightly distorting the initial atomic coordinates. In this work, whenever the Jahn-Teller effect has been detected, a slight random change of the initial atomic position of the defect first neighbours (of the order of less than one tenth of Å from the pristine crystal position) has been usually sufficient to restart a relaxation calculation resulting in an optimized structure where the suspicious non-integer occupation is absent and the original degeneracy has been lifted. Of course, we always verified that the total energy is lower in the newly found low symmetry configuration than in the high symmetry configuration. To have an idea of the consequences of the Jahn-Teller effect, in Fig. 4.1 we illustrate the Jahn-Teller distortion of the first neighbours in the case of a negatively charged boron vacancy V_B^-. In Subs. 4.2.1, 4.2.2, 4.2.3 and 4.2.4 dedicated to each type of defects studied we will partially describe the structural distortions due to the Jahn-Teller effect when present.

To conclude, we sum up the procedure we have followed to calculate the total energy of the point defect configurations. We first construct a supercell and introduce the defect. We carry out a structural relaxation using the PBE functional and we check the occupations of the Kohn-Sham states. If the occupations are all integer then the structure is fully relaxed and we use the obtained atomic positions to run a SCF calculation using the Gau-PBE hybrid functional. If after the structural relaxation there are non-integer occupations on a degenerate one-electron state and they do not disappear when a smaller smearing is applied it means that the obtained structure is not at the real minimum of the potential energy surface and that a symmetry needs to

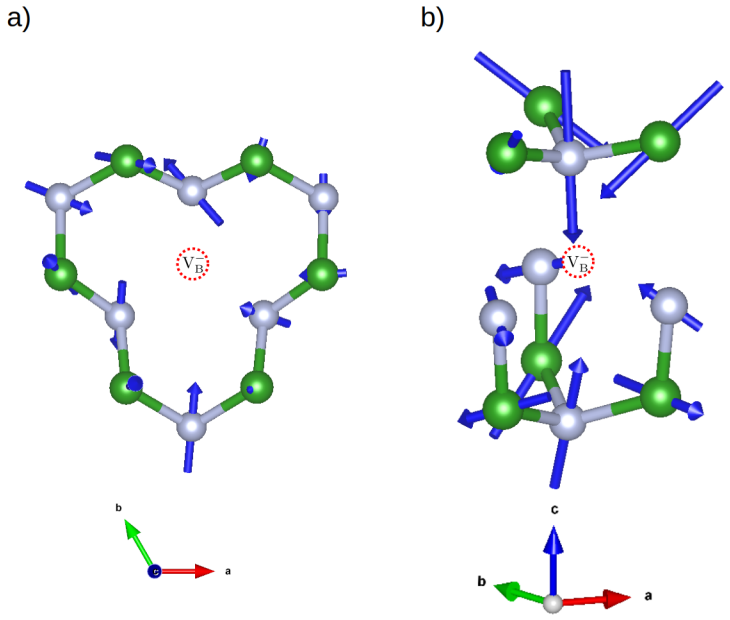

Figure 4.1. – Depiction of the static Jahn-Teller distortion for the first neighbours of the vacancy V_B^- on the (0001) bilayer (panel a)) and from a random point of view (panel b)). The atomic displacement from the unstable high symmetry configuration are depicted as blue arrows.

be lifted. In this case we restart the relaxation by slightly varying the initial coordinates of the atoms. The newly obtained atomic positions are then used in the Gau-PBE calculation to get a more accurate description of the electronic properties and the wavefunctions.

Finally the total energies computed via the Gau-PBE functional are used to calculate the formation energy and the CTLs. This "recipe" is summarised in Fig. 4.2. The main results that we will present in the present chapter are obtained using the Gau-PBE functional.

4.1.2. Chemical potential

In the present section we compute the chemical potential term of the formation energy introduced in Sub. 1.5.1. Since in this work we are discussing vacancies, anti-sites and carbon-related defects, we are concerned by the calculation of the chemical potentials of boron, nitrogen and carbon. The chemical potential μ_i^{ref} for the species i is defined as the total energy per elementary unit of the reservoir of the element i (Eq. 1.57). This definition poses immediately the problem of choosing the right reservoir since for the same element there are usually more than one polymorph that may be chosen, and as already discussed in Sub. 1.5.1 the choice should be made bearing in mind the condition at which the defect can be created. For the carbon reservoir we used the diamond structure (Fig. 4.3, panel c), following e.g. Refs. [24]

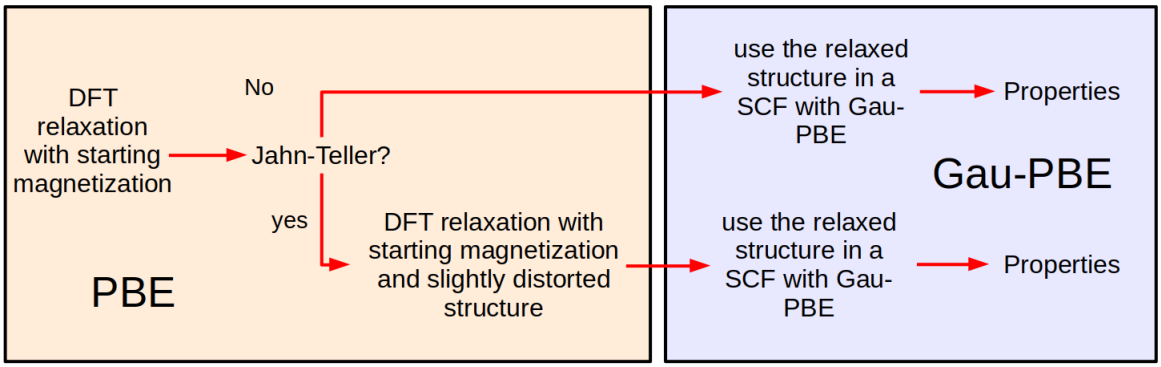

Figure 4.2. – Workflow followed to compute the relaxed structures and the total energies.

and [117]. For nitrogen we opted for the molecular N_2 (Fig. 4.3, panel b) in its gas form as it is common practice in the literature concerning point defects in *h*BN (see e.g. [118, 48]) *w*GaN and *w*AlN [119, 120, 121] and *c*BN [122]. The choice for the boron reservoir is more tricky as this element can assume several polymorphic forms [123]. We followed Refs. [124, 122] and we chose to work with the α-rhombohedral form (Fig. 4.3 panel a). Nonetheless, we should mention alternative options that could be considered. For example in Ref. [124] the chosen nitrogen reservoir is the FCC $\alpha - N_2$ solid nitrogen and not the gaseous form, moreover in Ref. [122] the chosen carbon reservoir is graphene and not diamond.

We now describe in detail the procedure followed to compute the chemical potentials. Since we are in a DFT plane-wave context and we need to keep the consistency of the computational assumptions made for the calculations on different materials, defects etc. , we use DFT with plane waves to compute also the energy of the N_2 gas. This task is performed by simulating an isolated N_2 molecule in a simple cubic primitive cell where we add vacuum to avoid the interaction with its periodic images. We start thus with a good guess for the interatomic distance (1.10 Å [125]). Using the PBE semilocal functional, we converged the total energy with respect to the cell parameter down to a convergence threshold of 10^{-4} eV/electron and we found that 20 bohr radii are sufficient to correctly simulate the vacuum. Then we converged the total energy with respect to the cut-off energy and the $\boldsymbol{k}$-grid. We found converged values for $E_{cut} = 80$ Ry and a $2\times2\times2$ $\boldsymbol{k}$-point mesh. Finally we relax the atomic positions and we found an optimal interatomic distance of 1.1018 Å. These converged values have then been used in a series of SCF calculations using the Gau-PBE hybrid functional to provide the total energy accurately converged with respect to the $\boldsymbol{q}$-grid ($1\times1\times1$)

We followed a similar procedure for α-boron. The primitive cell of the α - rhombohedral boron counts 12 atoms. Convergence of total energy with respect to the cut-off energy and the $\boldsymbol{k}$-point mesh resulted in a $E_{cut} = 60$ Ry and a $4\times4\times4$ $\boldsymbol{k}$-grid. We relaxed the atomic positions and the volume of the unit cell. The optimized structure is used with the Gau-PBE hybrid functional to converge the total energy with respect to the $\boldsymbol{q}$-grid in a series of SCF calculations. We found that the total energy per electron

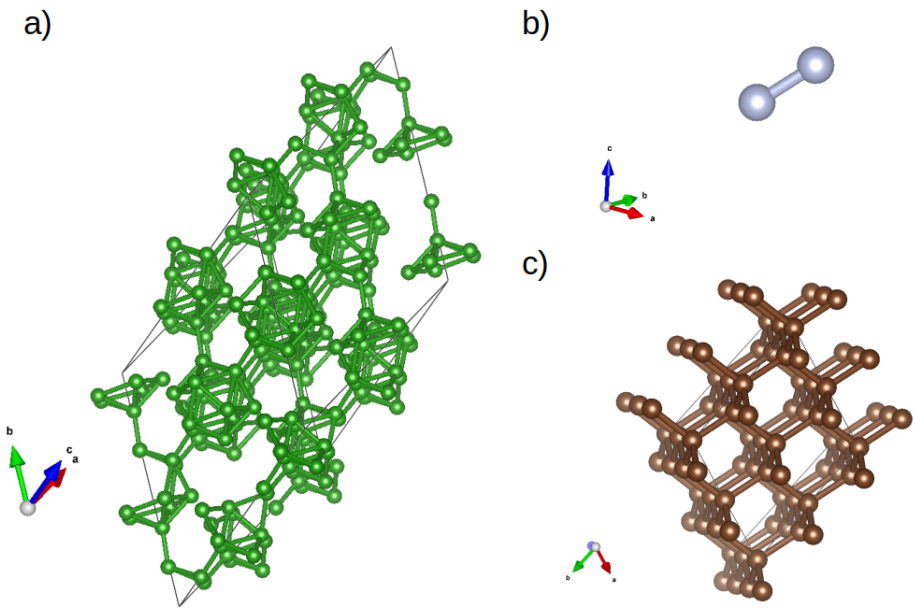

Figure 4.3. – Pristine phases for the atoms involved in the formation of the defect studied. Panel a) : α-rhombohedral boron ; panel b) : nitrogen molecule N_2 ; panel c) : diamond.

converges for a $4\times4\times4$ $\boldsymbol{q}$-grid.

Lastly, we repeated the same steps for diamond to compute the carbon reservoir chemical potential. Convergence is reached at PBE level for a $E_{cut} = 70$ Ry and a $6\times6\times6$ $\boldsymbol{k}$-grid. At the Gau-PBE level, convergence with respect to the $\boldsymbol{q}$-grid showed that a finer $\boldsymbol{k}$-grid was needed. In the end the convergence with the Gau-PBE functional is reached with a $7\times7\times7$ $\boldsymbol{k}$-grid and a $5\times5\times5$ $\boldsymbol{q}$-grid.

We can now finally compute at both PBE and Gau-PBE level the limiting values of the chemical potentials of boron and nitrogen given in Eqs. 1.65. For the pristine boron, carbon and nitrogen the number of elementary units corresponds to the number of atoms in the respective supercells, while for wBN it is equal to the number of BN atomic pairs. By using Eq.1.57 we have

$$\mu_{\mathrm{B}}^{ref} = \frac{E_{tot}^{\mathrm{B}}}{N_{\mathrm{B}}} = \frac{E_{tot}^{\mathrm{B}}}{12} \tag{4.1a}$$

$$\mu_{\mathrm{N}}^{ref} = \frac{E_{tot}^{\mathrm{N}}}{N_{\mathrm{N}}} = \frac{E_{tot}^{\mathrm{N}}}{2} \tag{4.1b}$$

$$\mu_{\mathrm{C}}^{ref} = \frac{E_{tot}^{\mathrm{C}}}{N_{\mathrm{C}}} = \frac{E_{tot}^{\mathrm{C}}}{2} \tag{4.1c}$$

$$\mu_{w\mathrm{BN}} = \frac{E_{tot}^{w\mathrm{BN}}}{N_{w\mathrm{BN}}} = \frac{E_{tot}^{w\mathrm{BN}}}{576/2} = \frac{E_{tot}^{w\mathrm{BN}}}{288} \tag{4.1d}$$

The reference chemical potentials and the enthalpies are given in Tab. 4.1 while the limiting values in Tab. 4.2. The formation enthalpy of *w*BN is equal to -2.43 eV and it can be compared with the value found for *h*BN of -2.89 eV found by Maciaszek *et al.* [48].

Functional	element	μ^{ref}	
PBE	B	-77.167	
	N	-270.805	
	C	-155.015	
	*w*BN	-175.148	
	enthalpy		-2.323
Gau-PBE	B	-77.278	
	N	-271.257	
	C	-155.290	
	*w*BN	-175.484	
	enthalpy		-2.433

Table 4.1. – Reference chemical potentials and enthalpies for the pure phases considered in formation energy calculation at both PBE and Gau-PBE level (eV).

	μ_{B} (eV)	μ_{N} (eV)
B-rich limit (PBE)	-77.17	-273.13
N-rich limit (PBE)	-79.49	-270.80
B-rich limit (Gau -PBE)	-77.28	-273.69
N-rich limit (Gau-PBE)	-79.71	-271.26

Table 4.2. – Limiting values for the chemical potentials at Both PBE and Gau-PBE level (eV).

4.1.3. Dilute limit corrections

In this subsection we give the details concerning the computation of the dilute limit correction within the Freysoldt-Neugebauer-Van de Walle scheme [60, 56], as implemented in the program `sxdefectalign`[61]. According to the theory introduced in Sub. 1.5.1, the program needs as input the charge of the system under study, the position of the point defect in the supercell, the cut-off energy used in the DFT calculation, the static dielectric constant and the potential $V_{bare} + V_H$ for the pristine bulk material and the defective supercell. The idea is to use the bulk potential as a reference and to align the potentials to the average potential far from the defect. The calculation can be carried out only if we have the same cell parameters for the pristine

and the defective supercell, and the same sampling grid for the fast Fourier transform used in computing the potentials. The procedure is quite straightforward. We run the

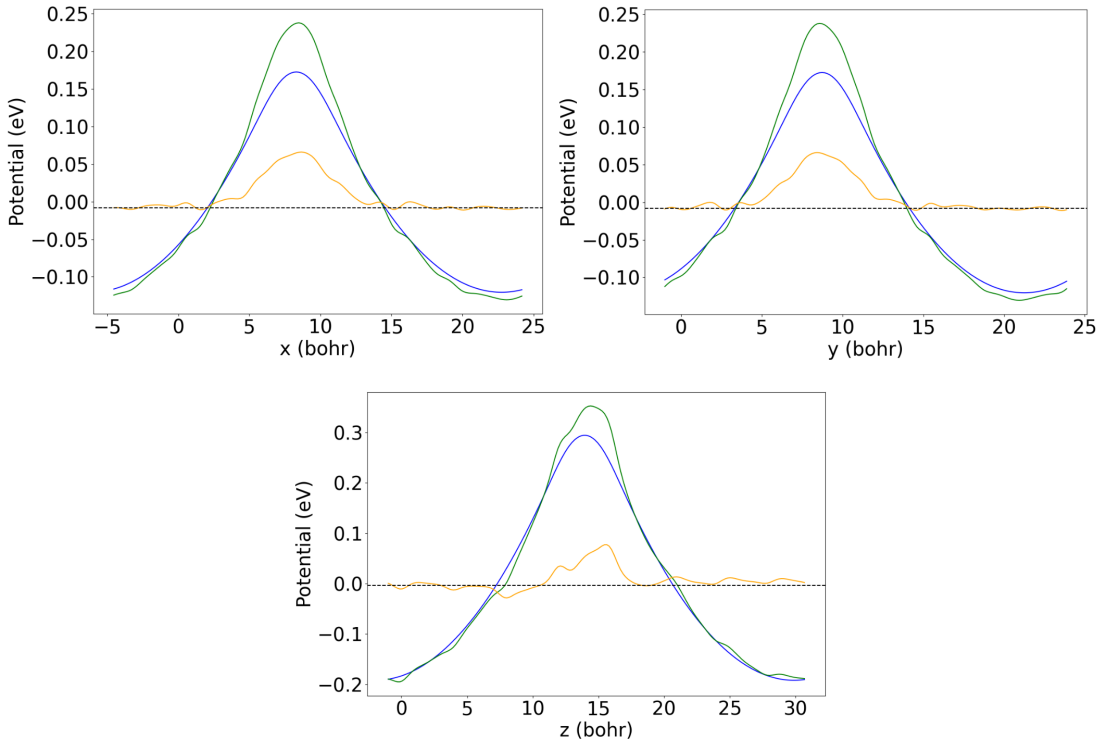

Figure 4.4. – Alignment for the potentials computed by `sxdefectalign` in the three directions for the B_N^{2-}. The green line is the defective supercell potential referenced to the potential of the bulk $V_{def} - V_{bulk}$. The blue line is the long range potential computed using the model charge presented in Eq. 1.85. The yellow line is the difference between the two, determining the alignment (black dashed line) where it reaches a plateau far from the defect.

post-processing (tool `pp.x` available in the Quantum Espresso suite) on the defective supercell and the pristine crystal to get their potentials $V_{bare} + V_H$. We run for a first time the program `sxdefectalign` using the $E_{cut} = 70$ Ry and the experimental static screening for the wBN as taken from Ref. [63]. After the first run it is possible to plot the defective supercell potential referenced to the bulk potential V^q. The quantity V^q is expressed as a function of the ith coordinate which is an average of V^q over the jk plane, where $i = x, y, z$ and j, k obey a cyclic rule. An illustrative example of these plot is reported in Fig. 4.4.

The program also computes the long range component of the potential, V^q_{lr}, using the model charge presented in Eq. 1.85. This first run of the program aims only at finding the alignment C, which ideally should correspond to the plateau of the difference $\tilde{V}^q - \tilde{V}^q_{lr}$. The alignment C defines the short range component of the potential and it

is set manually for the three directions separately (meaning that we decide in a rather arbitrary way where the plateau is, represented as dashed lines in Fig. 4.4). As we are studying an anisotropic system the plot of the potentials in Fig. 4.4 is different in each direction. As explained in Sub. 1.5.1 in this work we define the overall alignment as the average over the three directions. Results for the alignments and their average are reported in Tabs. 4.3 and 4.4 for the two functional used. The average alignment value is then applied in a second run of the program that returns the desired dilute correction limit E^q_{dil} (last column of Tabs 4.3 and 4.4).

It should be mentioned that in the first run of the program it is also possible to apply a spatial average to make the potential plot smoother, so that the search for the plateau is easier. This spatial average dumps the oscillations of the potential graph. In our case we applied a dumping equal to 3.98 Bohr radii, which is roughly the distance along the (0001) direction between two equivalent atoms (belonging to two adjacent bilayers). Lastly, we should remark that, as it is clear from the description, this method is not rigorous especially when the system is such that the function $\tilde{V}^q - \tilde{V}^q_{lr}$ does not reach a plateau. Moreover it is best used in the case of monomers and may fail for complex defects with some axial symmetry like for example the carbon dimer.

defect	align. x (eV)	align. y (eV)	align. z (eV)	average (eV)	E^q_{dil} (eV)
V_B^+	-0.099	-0.1	-0.13	-0.108	0.096
V_B^-	-0.037	-0.036	-0.01	-0.028	0.231
V_B^{2-}	-0.02	-0.02	0.005	-0.012	0.838
V_B^{3-}	-0.011	-0.011	0.018	-0.001	1.837
V_N^+	-0.039	-0.039	-0.048	-0.042	0.162
V_N^-	-0.013	-0.013	-0.016	-0.014	0.217
V_N^{2-}	0.014	0.012	0.028	0.0178	0.779
C_B^+	-0.003	-0.003	-0.01	-0.005	0.199
C_B^-	0.106	0.106	0.16	0.124	0.080
C_N^+	-0.079	-0.078	-0.081	0.079	0.124
C_N^-	0	0	0.005	0.002	0.202
C_2^+	-0.056	-0.055	-0.071	-0.061	0.143
C_2^-	0.061	0.061	0.095	0.072	0.131
B_N^+	-0.03	-0.03	-0.034	-0.031	0.172
B_N^-	-0.007	-0.017	-0.002	-0.009	0.212
B_N^{2-}	-0.003	-0.004	0.01	0.001	0.812
N_B^{2+}	-0.013	-0.013	-0.026	-0.017	0.780
N_B^+	-0.009	-0.009	-0.025	-0.014	0.189

Table 4.3. – Dilute limit correction computed at PBE level. The second, third and fourth columns report the plateaus manually detected in the three directions. The fifth column is the average. Last column reports the computed correction. Corrections for charge states $q = 0$ are identically 0 and do not appear in the table.

defect	align. x (eV)	align. y (eV)	align. z (eV)	average (eV)	E^q_{dil} (eV)
V_B^+	-0.096	-0.095	-0.131	-0.107	0.097
V_B^-	-0.046	-0.038	-0.026	-0.037	0.240
V_B^{2-}	0.022	-0.022	0.01	-0.011	0.837
V_B^{3-}	-0.02	-0.02	0.005	-0.012	1.868
V_N^+	-0.036	-0.035	-0.043	-0.038	0.165
V_N^-	-0.020	-0.021	-0.026	-0.022	0.226
V_N^{2-}	-0.016	-0.016	-0.037	-0.023	0.860
C_B^+	0	0	-0.005	0.002	0.202
C_B^-	0.11	0.11	0.162	0.127	0.076
C_N^+	-0.054	-0.054	-0.046	-0.051	0.152
C_N^-	-0.003	-0.003	0.002	-0.001	0.205
C_2^+	- 0.048	-0.048	-0.055	-0.050	0.153
C_2^-	0.061	0.06	0.094	0.072	0.132
B_N^+	-0.018	-0.018	-0.022	-0.019	0.184
B_N^-	0.014	-0.008	-0.004	0.033	0.236
B_N^{2-}	-0.008	-0.008	-0.004	0.007	0.801
N_B^{2+}	-0.008	-0.008	-0.024	-0.013	0.788
N_B^+	-0.007	-0.007	-0.022	-0.012	0.192

Table 4.4. – Dilute limit correction computed at Gau-PBE level. The meaning of each column is the same as Tab. 4.3.

4.2. Results and discussion

Now that we have all the ingredients, we can finally compute the formation energies which are depicted in Fig. 4.5 using the Gau-PBE functional. For comparison, we also show the same quantities obtained using the PBE semilocal functional.

We recall the fact that according to Eq. 1.55 the formation energy is expressed as a linear function of the electron chemical potential (the Fermi energy) E_F with slope equal to the charge q. In the diagrams given in Fig. 4.5, for each given defect, only the formation energy of the charge state for which it is the lowest is reported. So for example, the horizontal segments correspond to the intervals where the system is more stable in the charge state $q = 0$. Similarly, segments with a positive (negative) slope are those where positive (negative) charge states are more stable. The CTLs are given by the Fermi energies where the formation energy lines at two different charge state intersect and they correspond to the point of contact between the segments. They are showed in Fig. 4.6. For each defect considered we compared its CTLs at PBE and Gau-PBE level by setting their respective vacuum energies to 0 and then aligning them. This procedure is explained in detail in App. A.

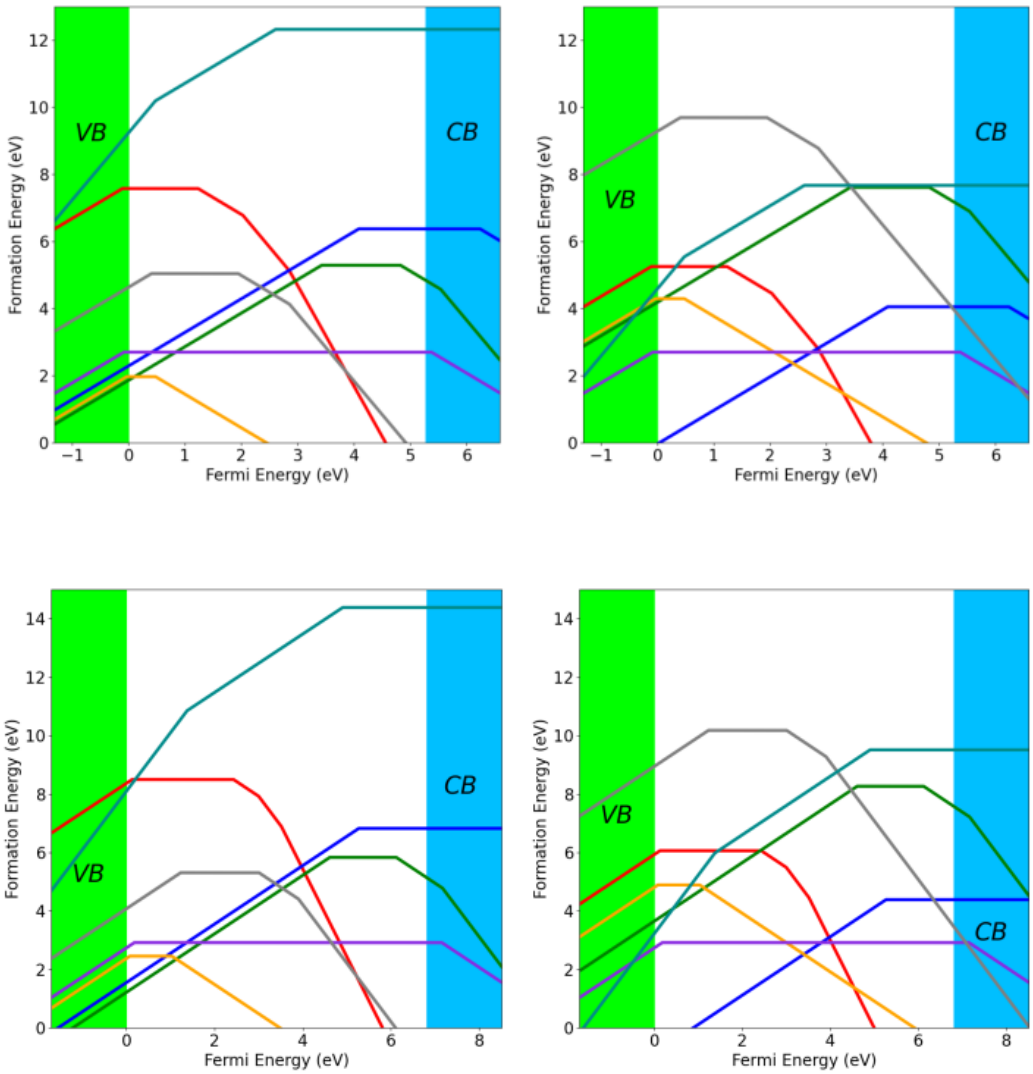

Figure 4.5. – Formation energy diagrams at PBE level (top row) and Gau-PBE level (bottom row) in the Boron (left column) and N-rich limit (right column). Red : V_B ; green : V_N ; blue : C_B ; yellow : C_N ; purple : CC; grey : B_N, dark cyan : N_B. The green and blue bands on the sides correspond to the valence and the conduction band, respectively, of the bulk pristine.

We now take a look at each class of defect individually and we comment the structural relaxation that they have induced and their electronic properties. For each studied defect we will provide a one-electron level scheme obtained using the Gau-PBE functional (see e.g. Fig. 4.9) where the Kohn-Sham energies are represented, separately for the two spin channels, as lines. The valence band, the band gap and the conduction band correspond to the yellow, white and blue areas, respectively. Black dots represent the occupied states while a blank dot is an empty state. Levels without any dot are understood to be filled if they are below a black dotted level, and empty if they are

above a state with the blank dot. The levels are referenced to the bulk valence band edge set to 0. This type of depiction of the one-electron levels does not present any band dispersion as it has been computed only at the Γ point.

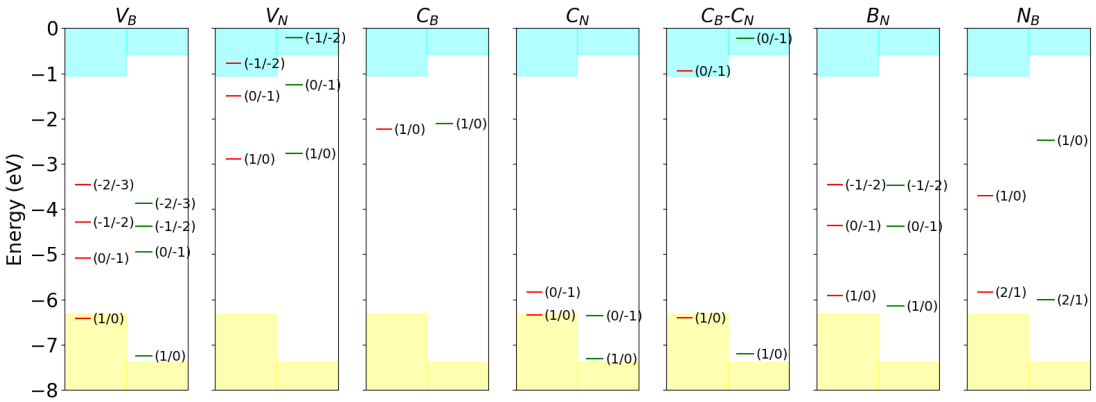

Figure 4.6. – CTLs at PBE (on the left of each plot) and Gau-PBE level (on the right of each plot). The blue area is the conduction band and the yellow area is the valence band of the bulk.

.

4.2.1. Vacancies

We first discuss the relaxed structure when a vacancy (Boron and Nitrogen) is introduced. In order to describe the structural deformation with respect to the pristine material, in Tab. 4.5 we give a list of the interatomic distances between the defect first neighbours forming a tetrahedron around the vacancy, as defined in Fig. 4.7. We should however bear in mind that the deformation involves all the atoms in the supercell and not only the first neighbours.

By creating the vacancy, the bonds of the first neighbours are left unfilled and thus called "dangling bonds". These dangling bonds will rearrange and hybridize among themselves. For example, in the model presented in Refs. [79] and [126] the dangling bonds are used as a basis to build the monoelectronic levels, which are those provided by a DFT calculation. The magnetisation of the vacancies at a given charge state is determined using a filling scheme like the ones in Figs. 4.8 and 4.12 and applying the Hund's rule. We represent the $2s$ and the $2p$ dangling orbitals as squares filled with spin up (upward arrows) and spin down (downward arrows) electrons.

For the pristine material the orbitals are completely filled forming an octet. When a vacancy is created at $q = 0$ the valence electrons of the missing atoms are removed and the left electrons are rearranged in the orbitals by filling, in order, the $2s$ spin up orbital, the $2s$ spin down orbital, the $2p$ spin up suborbitals and finally the $2p$ spin down suborbitals. The difference between the spin up and spin down electrons gives the magnetisation of the defect. Once the configuration at $q = 0$ is determined, we can add or remove more electrons to find the magnetisation of the other charge states. Even though the vacancy has four nearest neighbours we can consider a resonance

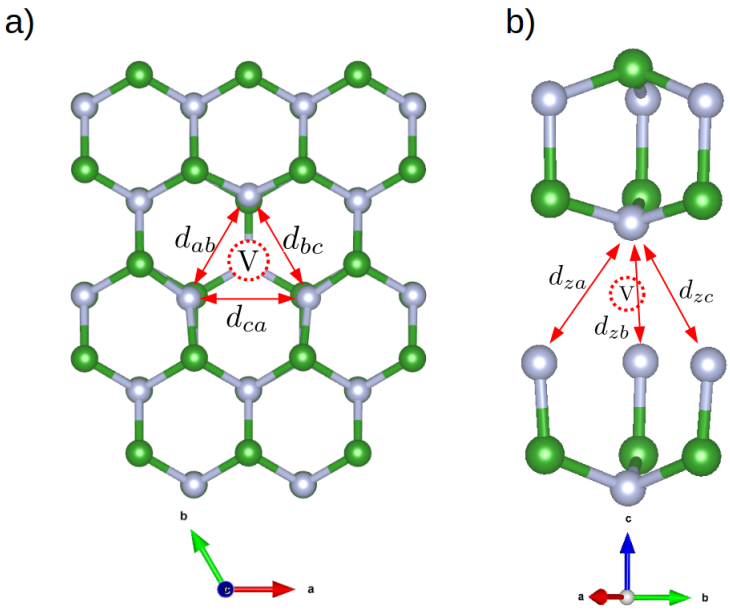

Figure 4.7. – Interatomic distances between the first neighbours of the generic vacancy V forming a tetrahedron around the defect with edges lying on the (0001) plane (panel a)) and out of the (0001) plane (panel b)).

between them, so that this filling procedure needs to be done only for one dangling bond.

Boron vacancy In the V_B defect a boron atom is removed. By comparing its nitrogen first neighbours interatomic distances with those of the bulk using Tab. 4.5, we notice that they move away from the original vacancy coordinates and the covalent bonds with the surrounding atoms get shorter.

A Jahn-Teller effect is observed for the charge states $q = 1$, $q = -1$ and $q = -2$ and therefore the shape of the tetrahedron surrounding the vacancy is distorted. The magnetisations for each charge state are determined in Fig. 4.8 and we can compare that filling scheme with the one-electron level structure reported in Fig. 4.9. At $q = 0$ the supercell will have 3 valence electrons less with respect to the bulk and we are left with three uncoupled spin-up electrons giving a magnetisation $m = 3$. On the contrary, at $q = -3$ the original octet is restored and the magnetisation is $m = 0$. The fact that at $q = -3$ the dangling bonds are filled makes this charge state particular so that it possesses a high degree of symmetry. As expected, in the last panel of Fig. 4.9 the spin up and spin down channels are identical, in accordance with Fig. 4.8. The highest occupied states is for both channels a doubly degenerate e state and a non-degenerate state slightly below. This "number" symmetry is disrupted when we go from the $q = -3$ to the $q = -2$ charge states. As we remove an electron the doubly degenerate e state is not fully occupied anymore, inducing a Jahn-Teller instability so that the crystal is distorted (see Tab. 4.5). A similar situation occurs when we go from

Defect	$d_{ab}=d_{bc}$ $=d_{ca}$	$d_{za}=d_{zb}$ $=d_{zc}$	d_{ab}^{JT}	d_{bc}^{JT}	d_{ca}^{JT}	d_{za}^{JT}	d_{zb}^{JT}	d_{zc}^{JT}
V_B^+	2.783	2.802	2.783	2.787	2.788	2.802	2.801	2.805
V_B^0	2.785	2.801	-	-	-	-	-	-
V_B^-	2.786	2.800	2.789	2.772	2.790	2.766	2.813	2.814
V_B^{2-}	2.799	2.807	2.818	2.787	2.787	2.796	2.796	2.824
V_B^{3-}	2.8179	2.8178	-	-	-	-	-	-
V_N^+	2.688	2.722	-	-	-	-	-	-
V_N^0	2.495	2.687	-	-	-	-	-	-
V_N^-	2.437	2.612	-	-	-	-	-	-
V_N^{2-}	2.347	2.551	-	-	-	-	-	-
bulk	2.549	2.5706	-	-	-	-	-	-

Table 4.5. – Structural data for the boron and nitrogen vacancies after relaxation, in Å . The interatomic distances are defined in Fig. 4.7. When the Jahn-Teller distortion is present, we report also the same quantities after the degeneracy removal (with the superscript JT).

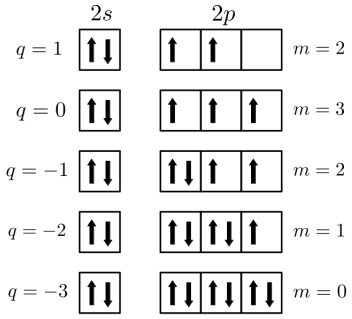

Figure 4.8. – V_B orbitals filling scheme to predicts the magnetisation m for the different charge states in Bohr magneton units.

$q=0$ to $q=-1$ and $q=+1$. In both cases we are adding and removing an electron from a doubly degenerate e state which will be then half-filled, inducing again a Jahn-Teller instability. The Jahn-Teller distortion can also be inferred from the evolution of the plot of the isosurface of the $|\psi|^2$ function for the non-degenerate state in the gap, represented in Fig. 4.10, where we can roughly see that the overall shape does not change as we remove the electrons, except for one of the vertices.

At $q=0$ the symmetry that we had for $q=-3$ is partially restored (we can see new doubly degenerate states) with the difference that we are left with the spin down levels in the gap completely empty. As we removed the electrons in the spin down channel the spin up levels in the gap have been pushed down in energy until the point where they hybridize with the bulk. The fact that at $q=0$ we have an excess of three spin-up electrons on the valence band edge can be seen by comparing the $|\psi|^2$ for the states with spin up channel occupied by these three electrons with the spin polarization

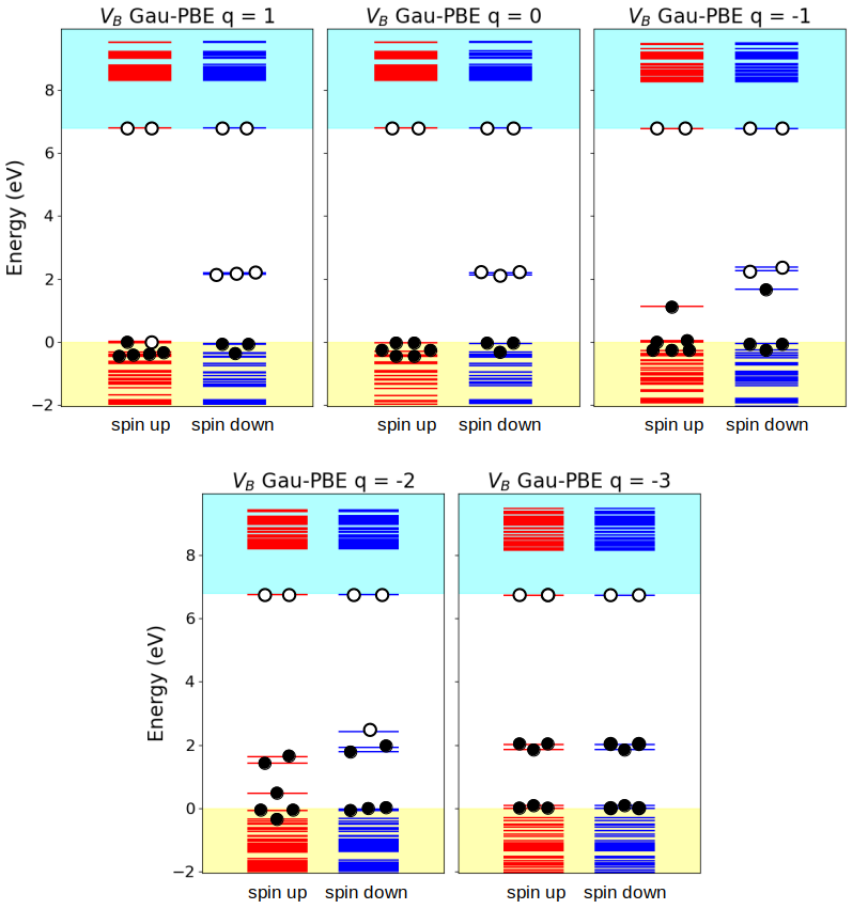

Figure 4.9. – V_B one-electron levels at Gau-PBE level at different charge states. A black dot represents an occupied state while a blank dot represents an empty state.

defined as

$$n_{pol} = n_\uparrow - n_\downarrow = \sum_{occ.} |\psi_\uparrow|^2 - \sum_{occ.} |\psi_\downarrow|^2 \tag{4.2}$$

where the sums run over all occupied states and $n_{\uparrow/\downarrow}$ is the spin up/down electron density. This comparison is reported in Fig. 4.11 where only one of the states on the valence edge occupied by one of the three excess electrons is pictured, as a similar behaviour occurs for the other two. Even though the state is highly delocalized, its spin polarization can account for the moderate hybridization with the defect.

Nitrogen vacancy The same model based on the dangling bonds used as a basis to construct the one-electron states can be used for the nitrogen vacancy. In this case for the charge states explored no Jahn-Teller effect has been observed and the interatomic distances between the vacancy first neighbours (this time boron atoms) are not distorted (see Tab. 4.5). We observe for the positive charge state an outward expansion of the tetrahedral cage surrounding the defect. Conversely, an inward contraction occurs for the neutral and the negative charge states so that the neighbouring atoms

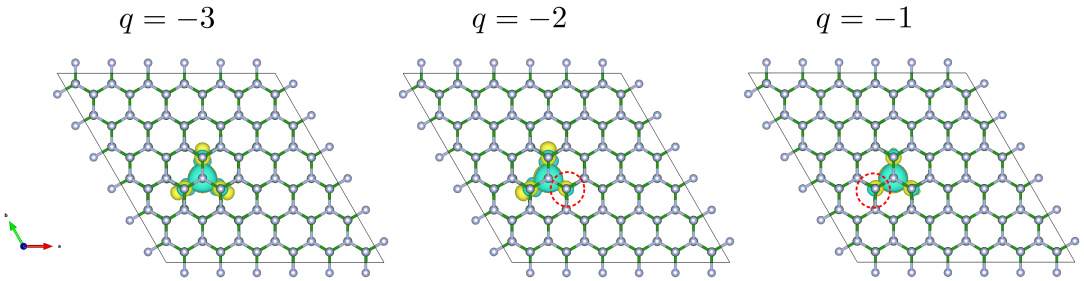

Figure 4.10. – z-axis prospect of the a state in charge states $q = -3$, $q = -2$ and $q = -1$ of V_B, the asymmetry of the isosurface can be clearly noticed (circled in red).

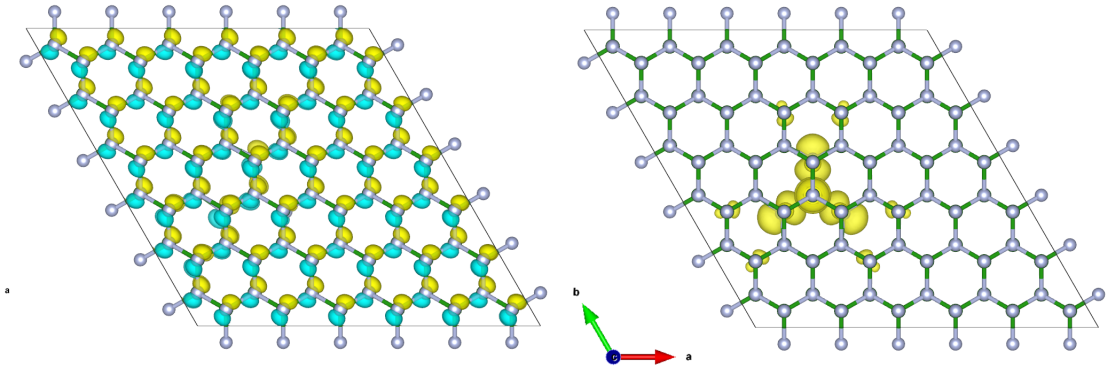

Figure 4.11. – Left panel : $|\psi|^2$ of the state with spin up occupied by one of the excess electrons in V_B^0. The other two states present the same degree of delocalization ; right panel : spin polarization for the charge states $q = 0$.

on the basal plane (0001) get closer to each other with respect to the bulk, indicating an overlap of their $2p$ states as more electrons are added. Also the distances d_{za}, d_{zb} and d_{zc} decrease for increasing number of electrons. This is in agreement with the behaviour observed for the oxygen vacancy in ZnO [22] and the nitrogen vacancy in GaN [121].

Removing a nitrogen atom means that in the $q = 0$ charge state there are 5 valence electrons less with respect to the bulk. Application of the Hund's rule on the dangling bonds reads the magnetisations listed in Fig. 4.12. This filling order is also confirmed by the computed level scheme in Fig. 4.13. At charge state $q = 1$ the $2p$ state is empty, all the electrons are paired, and the levels are the same in the two spin channels. When we pass to the charge state $q = 0$, the added electron determines the magnetisation $m = 1$ and it is found by our DFT calculations to occupy a well localized, non-degenerate state inside the gap at around 4 eV above the VBM. The degeneracy of the e states at 6 eV and at the CBM in both spin channels is not disrupted.

The $|\psi|^2$ isosurfaces of these levels are pictured in Fig. 4.14 where a resemblance to the a and e states reported for the NV^- defect in diamond in Ref. [127] can be remarked. All the other electrons are paired with respect to the spin and they are

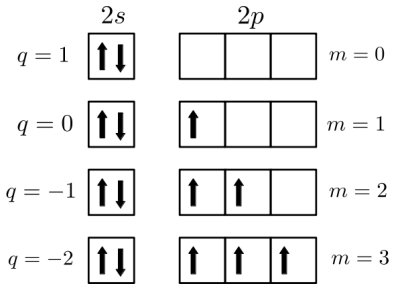

Figure 4.12. – V_N filled dangling bond orbitals and their respective magnetisation m, for the different charge states, in Bohr magneton units

strongly hybridized with the bulk.

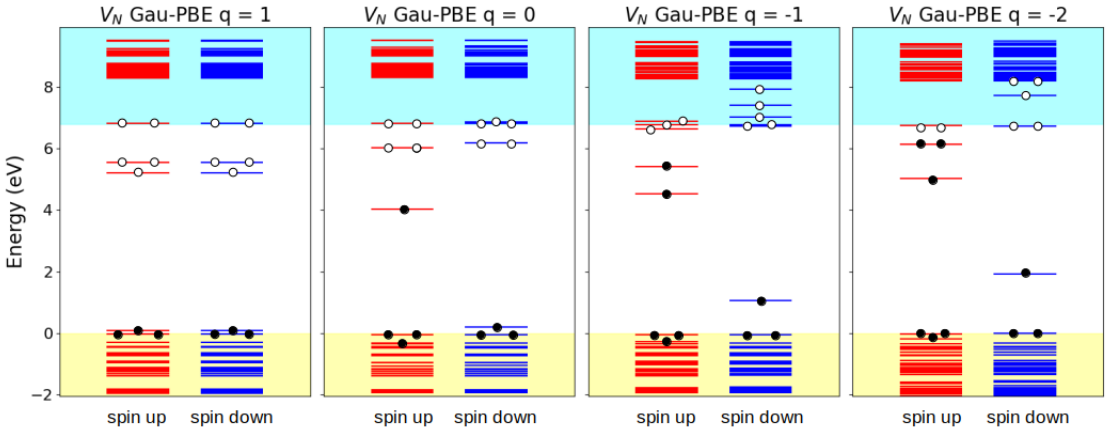

Figure 4.13. – V_N one-electron level scheme obtained from hybrid functional theory. Yellow and blue areas are the valence and the conduction bands respectively. Red and blue lines correspond to the spin up and spin down channels respectively. Black dots are the occupied states. Empty dots are the empty states.

This stuation will change at charge state $q = -1$. The e symmetry of the states described above is lowered to singly degenerate state and the added electron will occupy one of them. In the spin down channel these non-degenerate states are shifted to higher energies above the CBM. This shift to higher energies can be partially explained with the fact that antiparallel spins configurations have higher energies compared to parallel spin configurations, in analogy with the low symmetry case V_B^{2-} where the unpaired spin up electron filling the defect state around 0.5 eV has a lower energy than the unoccupied singly degenerate spin down state around 2.5 eV. Finally in V_N^{2-} a symmetry is partially restored and the non-degenerate states rearrange themselves to form new e levels in both spin up and down channels.

Interestingly, several attempts of convergence of DFT structure relaxation for the charge state $q = +2$ failed, letting us suppose that the structure in this charge state is heavily rearranged. The same problem arised when we relaxed the structure V_N^{3-}.

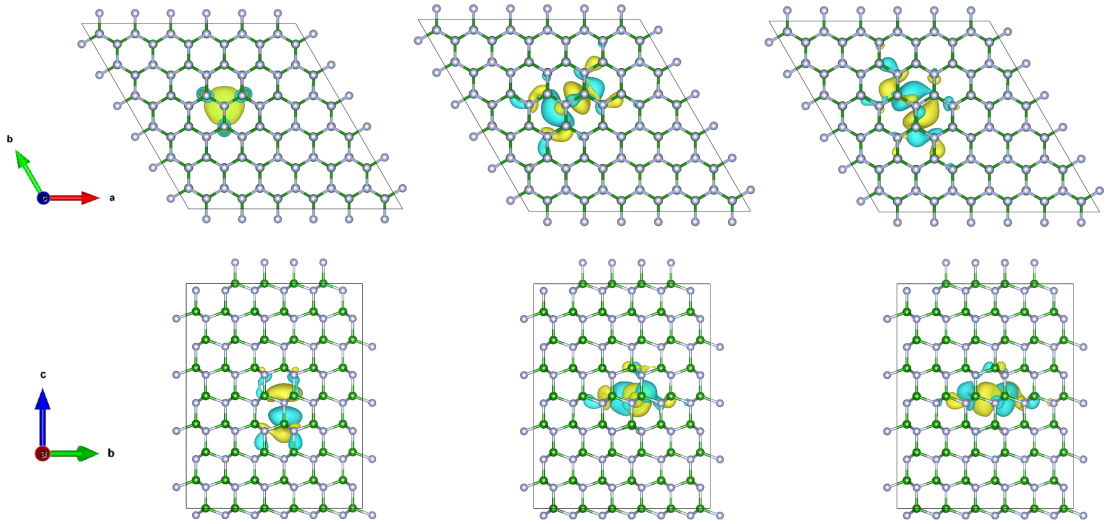

Figure 4.14. – $|\psi|^2$ of the in-gap states for V_N^0, projected on the xy plane (top row) and on the plane perpendicular to the $\boldsymbol{a}_1$ direction (bottom row). Left column shows refers to the singly-degenerate state, center and right columns to the e_x and e_y states. The overall shapes do not change significantly in other negative charge states.

Indeed, we were able to complete a DFT relaxation of the charge state $q = -3$ with many difficulties. Once relaxed, the resulting structure was completely different from the V_N defect. By inspecting the structures resulting from the intermediary steps in the relaxation calculation (i.e. the structures where the forces acting on the atoms are still not converged), we could observe a migration of the vacancy to a nearby B site while the boron atom migrated from its original site to the vacancy position. As a result, in the converged relaxed structure the boron atom and the vacancy swapped their positions and the resulting defect resembles more the complex V_BB_N. This is the reason why this result was dropped and it has not been reported in the formation energy diagrams. In all cases, the prevalently donor character of the V_N defect can be ascribed to higher symmetry of the level structure of charge states $q = 1$ and $q = 0$.

4.2.2. Carbon substitutionals

The structural data of the carbon substitutionals C_B and C_N are given in Tab. 4.6, where unlike for the case of the vacancies, the interatomic distances are taken between the carbon atom and its four nearest neighbours. The Jahn-Teller effect has been detected for the C_N^0 and C_B^0 defects.

defect	$d_a = d_b = d_c$	d_z	d_a^{JT}	d_b^{JT}	d_c^{JT}	d_z^{JT}
C_B^+	1.503	1.527	-	-	-	-
C_B^0	1.507	1.520	2.071	1.461	1.461	1.459
C_B^-	1.513	1.510	-	-	-	-
C_N^+	1.588	1.562	-	-	-	-
C_N^0	1.576	1.564	1.621	1.556	1.578	1.564
C_N^-	1.552	1.568	-	-	-	-
bulk	1.564	1.579	-	-	-	-

Table 4.6. – Structural data in Å for the carbon substitutionals, where the distances are defined in Fig. 4.15. Again, the distances distorted due to the Jahn-Teller effect are denoted by the JT superscript.

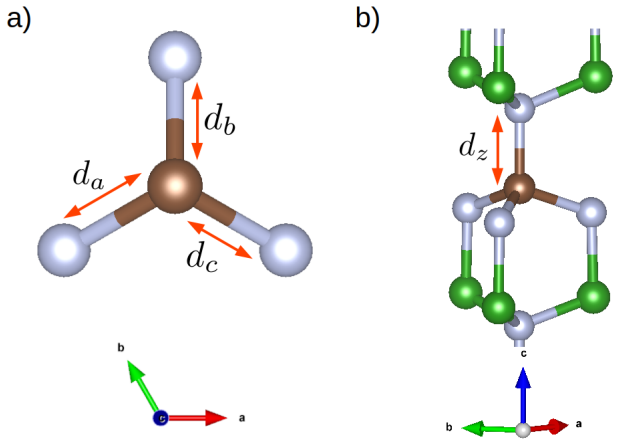

Figure 4.15. – First neighbours tetrahedral cage around a carbon substitutional (brown). The distances used in Tab. 4.6 are also defined.

For the carbon substitutionals we cannot consider anymore the dangling bond introduced above for the case of the vacancies. Here an atom of the original crystal has just been replaced by carbon and the covalent bonds will undergo sp^3 hybridization like in the bulk. To determine the magnetisation for each charge state we apply the Hund's rule on the sp^3 orbital which is formed by considering the orbitals of the C atoms and those of its four first neighbours in resonance. The constructed sp^3 orbitals are illustrated in Fig. 4.16.

We start by discussing the C_B. When forming the defect we remove three B valence electron and add four from the C atom so that C_B^0 has one electron more than the bulk system. The excess electron is not accommodated in the sp^3 orbital as the octet is already complete and it determines a magnetisation $m = 1$. Addition of one more electron gives a $m = 2$ magnetisation for the $q = -1$ charge state. Instead, the charge

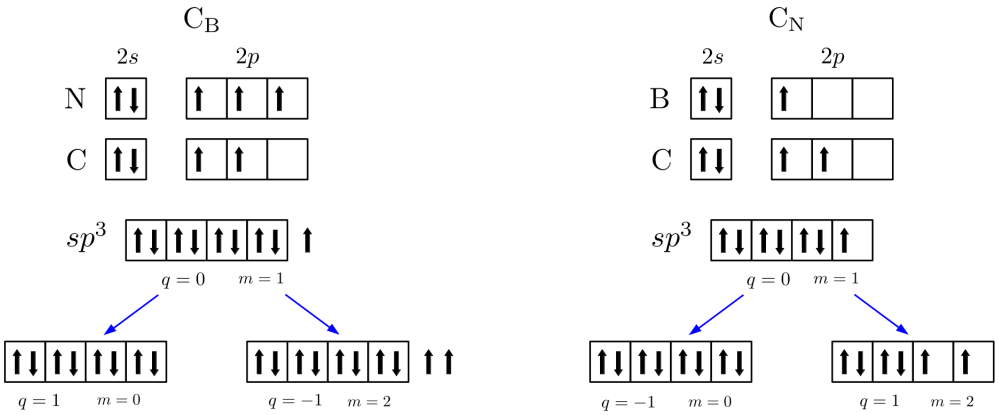

Figure 4.16. – Filling scheme for the sp^3 hybridized orbital for C_B (left) and C_N (right).

state $q = 1$ restores the original number of electrons of the pristine crystal, thus the sp^3 orbital is completely filled with no electron in excess or left unpaired and the magnetisation is $m = 0$, making C_B a donor. By looking at Tab. 4.6 we see that the C_B induces a contraction of the crystal structure towards the carbon atom. This is due to a degree of hybridization between the carbon and nitrogen atoms higher than between the nitrogen and the other B atoms.

In forming the C_N defect, we remove five electrons and we add four. Therefore we end up in the neutrally charged C_N^0 with one electron less than the bulk, making this defect an acceptor. The sp^3 orbital is left with one unpaired electron which gives again a magnetisation $m = 1$ like in the C_B case. The system can acquire one electron from the environment to complete the octet and make a charge transition to the $q = -1$ state which has thus magnetisation $m = 0$. Lastly, the state C_N^+ will instead have two electron less with respect to the original bulk configuration giving a magnetisation $m = 2$ but the CTL $(0/+)$ falls outside the band gap. Therefore we did not consider this case.

The structural deformation with respect to the ideal wurtzite crystal in the case of the C_N is different from the one observed in C_B. In the positively charged C_N^+ the atoms on the basal plane (0001) move away from the carbon atom whereas for $q = -1$ they move towards the substitutional indicating a higher hybridization as observed also for the contraction in C_B. This effect might be due to the larger number of electrons in C_N^- than in C_N^+. On the other hand the parameter d_z is always smaller than in the bulk system, indicating an anisotropy in the hybridization of the orbitals. By looking at the levels schemes in Figs. 4.17 and 4.18 we notice a "specular" behaviour between the C_B^+ and C_N^- since they are isoelectronic systems, with levels at resonance with the band edges. Only for the C_B^0 and C_N^0 some levels sensibly enter the gap.

4.2.3. Carbon dimer

In the carbon dimer C_2 a nitrogen atom and a boron atom, one next to each other, are replaced by carbon atoms. From this point of view the dimer can be understood as

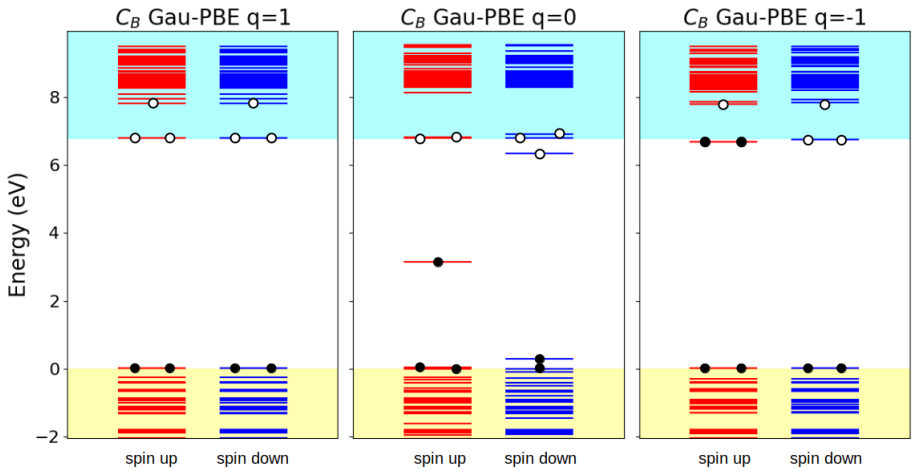

Figure 4.17. – Kohn-Sham one-electron levels for the C_B defect.

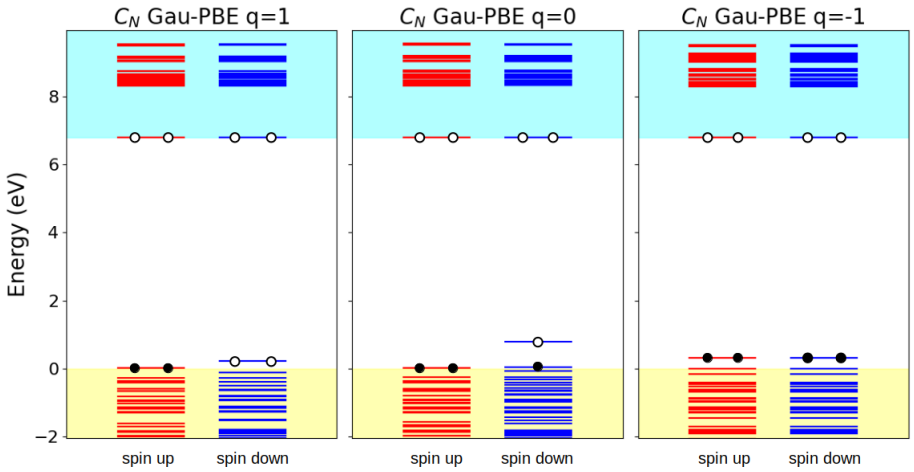

Figure 4.18. – Kohn-Sham one-electron levels for the C_N defect.

a complex of carbon monomers. As already mentioned we studied only the case in which the two carbon atoms belong to the same bilayer lying on the (0001) plane, but in principle we could study also the carbon dimer where the carbon-carbon bonding is parallel to the (0001) axis. We report in Tab. 4.7 the interatomic distances for the three charge states studied (with reference to Fig. 4.19 for the distance definitions).

No Jahn-Teller effect has been detected for the C_2 defect. The main feature that strikes in the carbon dimer is that it is almost electrically inactive. By looking at Fig. 4.6 and comparing the CTL obtained with PBE and Gau-PBE we note that the entire band gap range of energies is dominated by the $q = 0$ charge state which is isoelectronic with the pristine bulk. Only using the Gau-PBE functional the $(-1/0)$ level moves a bit into the gap but it stays almost in resonance with the VBM anyway. In fact, to form the defect we removed 8 electrons (3 valence electrons of the boron atom plus 5 electrons of the nitrogen atom) and we added 8 electrons (4 electron for each carbon atom) and

Charge state	d^z_{cb}	d^z_{cn}	d_{cc}	d^{ab}_{cb}	d^{ab}_{cn}
$C_BC_N^+$	1.594	1.546	1.493	1.592	1.525
$C_BC_N^0$	1.596	1.548	1.492	1.582	1.525
$C_BC_N^-$	1.595	1.544	1.492	1.583	1.528

Table 4.7. – Interatomic distances for the carbon dimer.

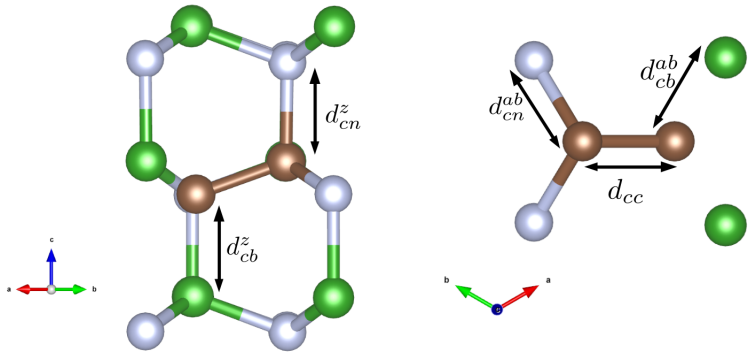

Figure 4.19. – Definitions for the interatomic distances in the C_BC_N.

thus the donor and acceptor characters of the C_B and C_N compensate each other. This picture is also confirmed by the one-electron level scheme in Fig. 4.20, where we can see that there is not any level in the gap.

To understand the nature of the bondings between the carbon atoms and its first neghbours we analyse the charge density distribution. The higher electronegativity of nitrogen explains why the charge density (Fig. 4.21) is concentrated on the nitrogen atoms in the crystal while it seems to be stripped out from the boron atoms. Nonetheless, the difference in electronegativity between the carbon atoms and nitrogen atoms is small enough to distribute the charge not only on the nitrogen first neighbours of the defect but also on the carbon atoms and along the C-C covalent bonding. The weak exchange of charge between the carbon and its boron first neighbour atoms is also in agreement with the carbon-carbon interatomic distance which is shorter than the BN bondings with the same direction in the rest of the crystal.

4.2.4. Antisites

For the boron antisite on a nitrogen site B_N, a nitrogen is replaced by a boron atom bonded with four more boron nearest neighbours. In the nitrogen antisite on the boron site N_B a nitrogen replaces a boron and it is surrounded by a tetrahedral cage with four nitrogen atoms as vertices. In Tab. 4.8 we report the structural data as already done for the other defects. The distances are defined in the same way as for the carbon substitutionals (Fig.4.15). The Jahn-Teller distortion has not been detected for any of the charge states explored.

For the B_N antisite the first neighbours depart from the pristine equilibrium posi-

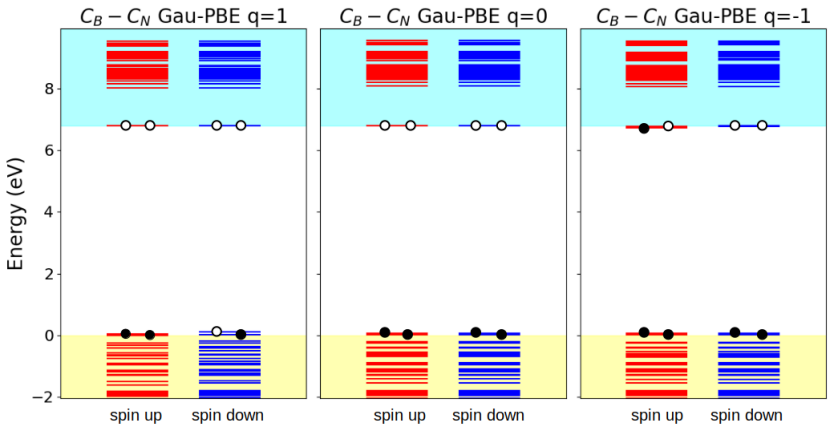

Figure 4.20. – One-electron level scheme for the carbon dimer obtained via DFT with the Gau-PBE functional. Since for different charge states only minor readjustements occur and there is no structure deep in the gap, only 4 states in proximity of the VBM and the CBM are considered.

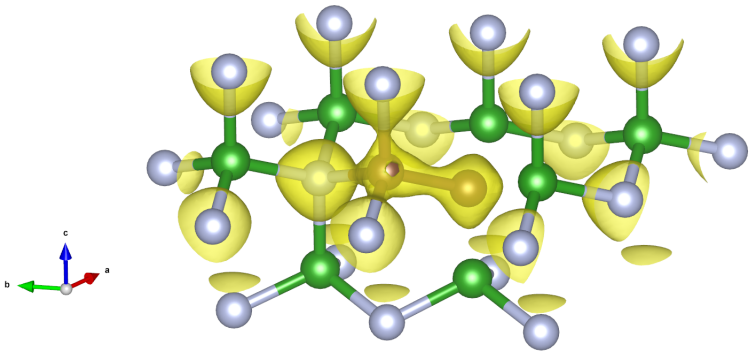

Figure 4.21. – Carbon dimer charge distribution.

tions by moving away from the defect, thus stretching the B-B bonds length. On the other hand in N_B it is more difficult to identify a trend. For the N_B^0 the tetrahedral cage seems to expand with respect to the bulk while in N_B^{2+} it contracts. A strong elongation along the *c*-axis occurs instead for N_B^+, meaning that the electrons from the nitrogen first neighbours on the basal plane hybridize more than the ones from the N-N covalent bond parallel to the *c*-axis.

The magnetization, also confirmed by our DFT calculation, is determined as usual using the Hund's rule on the hybridized sp^3 orbitals. In the B_N five valence nitrogen electrons are removed and three boron valence electrons are added so that the neutral B_N^0 has two electrons less compared to the pristine crystal as shown in the scheme Fig. 4.22. As a consequence, the B_N^{-2} is instead isoelectronic with the pristine crystal and thus its one-electron levels depicted in Fig. 4.23 are the same in the spin up and down channel.

When the (1/0) transition is made we remove an electron from a non-degenerate

defect	d_a	d_z
B_N^+	1.710	1.733
B_N^0	1.702	1.589
B_N^-	1.636	1.596
B_N^{2-}	1.578	1.595
N_B^{2+}	1.510	1.557
N_B^+	1.460	2.029
N_B^0	1.766	1.676
bulk	1.564	1.579

Table 4.8. – Antisite-nearest neighbours interatomic distances in Å.

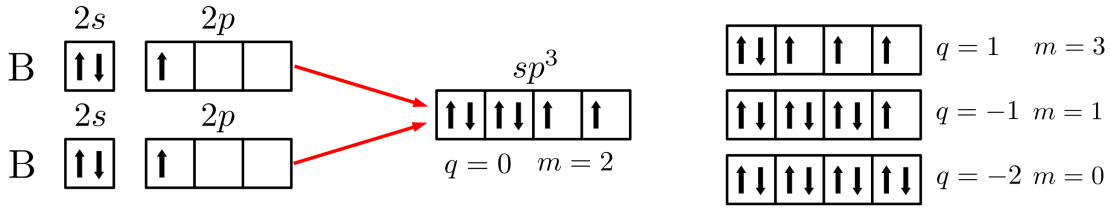

Figure 4.22. – B_N hybridization and filling scheme.

state in B_N^0, the spin down states in the gap are left empty and no *e* degenerate state is split. On the contrary, the charge state B_N^- can be seen either as an addition of an electron to B_N^0 or a removal of an electron from B_N^{2-}. In both cases we are adding or removing an electron from a doubly degenerate *e* state which will be then half-occupied and thus the system rearranges its level structure in a lower symmetry where all levels in the gap are singly degenerate, in analogy to V_N^-, V_B^- and V_B^{2-} (the latter is isoelectronic to B_N^-). Although this rearrangement might recall the Jahn-Teller effect, a distortion of the structure has not been observed.

Since the *e* states are present in all the charge states studied except for the B_N^-, in Fig. 4.24 we compare the shape of the isosurfaces of the three levels in the gap at $q = 0$ with the shape of the same states in the B_N^-. For this comparison the $q = 0$ isosurfaces have been chosen as an example representative also of the $q = 1$ and $q = -2$ charge states, as their overall shape is preserved (with the important note that at $q = 1$ a strong hybridization with the bulk occurs). We notice that since the degeneracy of the *e* state has been lifted in B_N^-, the states in panel e) and f) of Fig. 4.24 are different from the *e* states presented in panel b) and c), whereas the singly degenerate state in panel d) retains the shape of the non-degenerate state in panel a).

It is worth mentioning that the B_N^0 defect is isoelectronic to the NV^- in diamond and they both present in the gap an empty *e* state above a singly degenerate occupied state. This particular level structure suggests that it is possible to induce an optical transition of the electron from the non-degenerate state to one of the *e* states (green arrow in Fig. 4.23), in analogy to the transition studied in the NV^- color center. Therefore this work calls for further studies both theoretical and experimental to asses its utility in

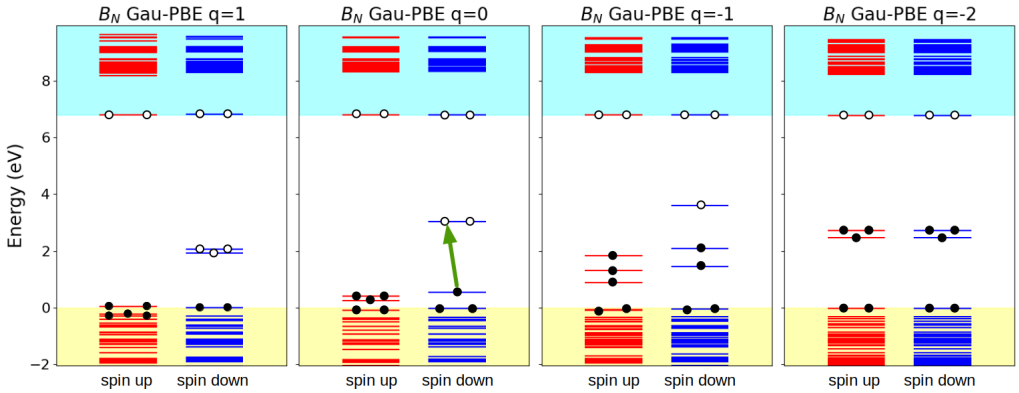

Figure 4.23. – One-electron levels obtained for the B_N defect with the Gau-PBE functional. The green arrow denotes a transition which might be useful in quantum technologies.

quantum technologies, i.e. exploring its potential as a single photon emitter, spin decoherence time and Huang-Rhys factor.

For the N_B^0 three valence electrons of the boron atom have been replaced with five nitrogen valence electrons, hence, there are two electrons in excess with respect to the pristine crystal which are not included in the sp^3 orbital from hybridization of the nitrogen $2p$ state. (see left panel of Fig. 4.25). The charge state $q = -1$ was also explored and a relaxed structure was obtained but the SCF convergence has been difficult at PBE level. Several attempts of calculating the Kohn-Sham states using the Gau-PBE functional on the relaxed structure failed, suggesting that the atomic positions computed at PBE level were unphysical. Another hint that the N_B^- might be unphysical is the fact that the CTL $(0/-)$ computed at PBE level is several eV above the CBM and thus it has not been reported in the formation energy diagram Fig. 4.5.

For all charge states, the one-electron levels in the gap ilustrated in the right panel of Fig. 4.25 present themselves in sets of singly and doubly degenerate states, thus suggesting a high level of symmetry. These levels are retained, although organized in a different order, in the charge states N_B^+ and N_B^{2+}. A possible transition that might be interesting for quantum technologies is the one between the occupied non-degenerate state at 2.4 eV to one of the e states at 5 eV in the N_B^0 (highlighted with a green arrow in Fig. 4.25).

We now compare the charge state N_B^0 with the defect C_B^- which are isoelectronic. Both defects present a completely filled sp^3 orbital with two electrons in excess with respect to the pristine crystal. We try therefore to explain why a N_B^0 has magnetization $m = 0$ whereas C_B^- has magnetization $m = 2$. A possible explanation is that in the case of N_B^0 there is a breathing expansion of the defect region, so that the highest occupied state moves up from the valence band to the gap and it is localized. The two electrons in the gap rearrange thus in a new localized orbital where the Pauli exclusion principle constrains them to occupy a spin up and spin down state. Conversely, for the C_B^- there is a contraction and the electrons in the defect region are more hybridized with the bulk with the highest occupied level at resonance with the conduction band. For this

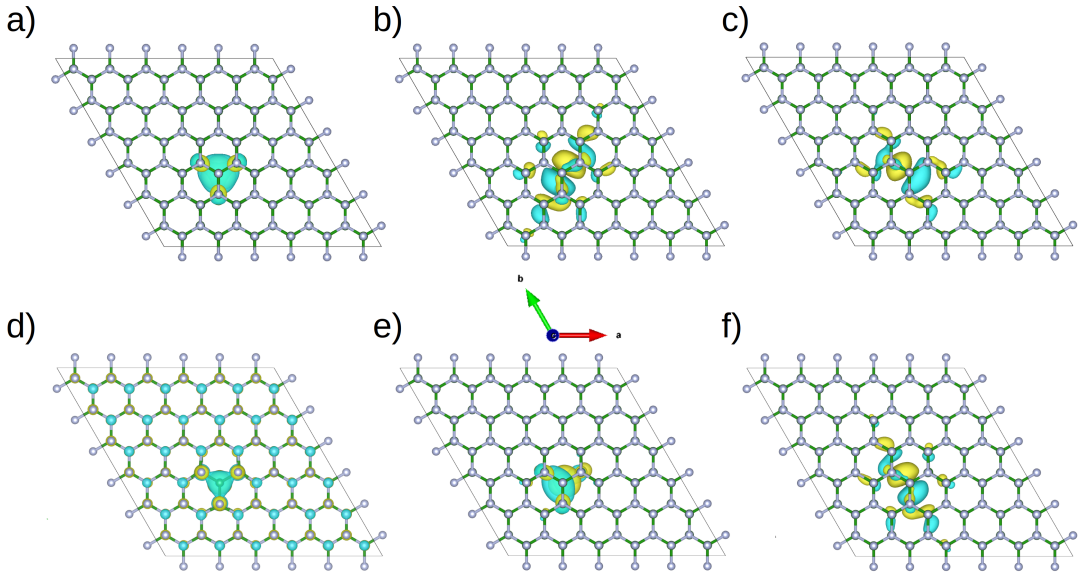

Figure 4.24. – $|\psi|^2$ for the one-electron states in the gap of B_N. Panel a), b) and c) : states at charge state B_N^0. We chose to show the isosurfaces at $q = 0$ by way of illustration, since the same shape is retained for charge states $q = -2$ and $q = 1$; panel d), e) and f) : one-electron states in the gap for $q = -1$.

state the original double degeneracy that it had in C_B^+ is restored and the electrons fill it with a spin-parallel configuration.

4.3. Optical properties of defects

In the present section we will present the results concerning the optical properties of some selected defects. The two methodologies that we have used are those presented in Chap. 2, that is the Franck-Condon model in the ΔSCF approach to the excited states (Sec. 2.4) and the BSE approach using the remapping procedure (see Sec. 2.5). We will see that the latter approach is more versatile.

4.3.1. Optical properties using the ΔSCF approach.

Here we use the method of constrained occupations or ΔSCF to study some particular transitions without departing from a DFT context. The clear advantage of this method is its simplicity, since it is very similar to standard DFT. On the other hand it presents many problems in convergence and its validity is affected by the fundamental problem that its aim is to study excitations using DFT which is, by construction, a ground state theory. Nonetheless, today it is one of the standard approaches to studying the optical properties of defects embedded in supercells.

Our goal is to use the ΔSCF method to build the 1D-Franck-Condon diagrams for the defects under study in order to find the ZPL, absorbance and emission energies

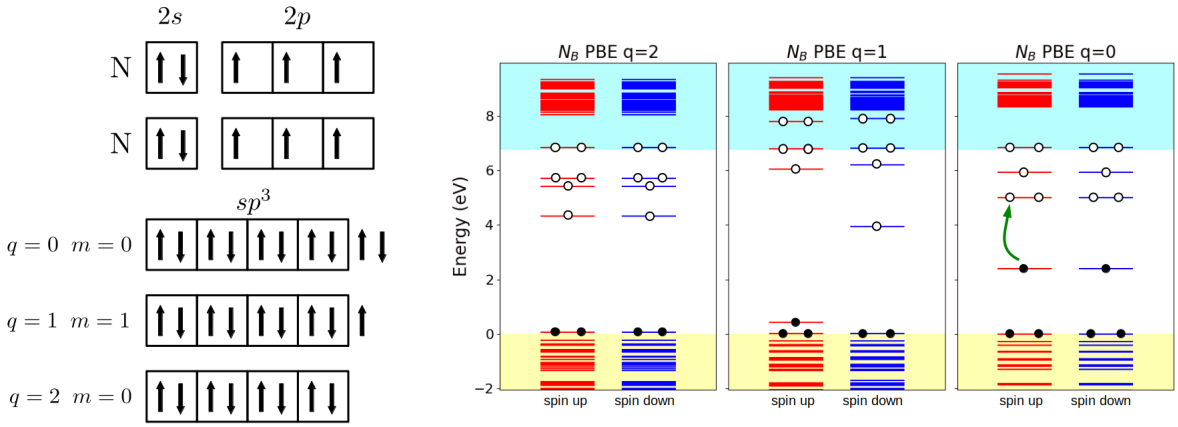

Figure 4.25. – Orbital filling scheme and level structure for the N_B defect.

and the Stokes shifts. Hence, for each defect, we need to find the points A, B, C and D as illustrated in Fig. 2.9, corresponding to four different calculations which we now list in detail.

Point A is obtained by a simple relaxation followed by a SCF calculation using the Gau-PBE functional. This calculations are the same used for the analyses in Sec. 4.2. To find point B we repeat the same Gau-PBE calculation using the relaxed atomic positions used for point A, but we constrain the electrons that we want to excite to occupy an empty level above the HOMO. In this way we simulate an optical absorption assuming that this process is much faster than the relaxation of the structure. After this transition we relax the structure to its equilibrium configuration in the excited state by carrying out a relaxation using PBE while keeping the excited state constrained occupations used for point B. After the excited state equilibrium atomic positions have been found we refine the calculation of the total energy by using the Gau-PBE functional and we find point C. Finally we find point D and simulate the emission by performing a Gau-PBE SCF calculation using the excited state relaxed atomic positions but we drop the constrained occupations. In this way we obtain the parameters defining the 1D model : E_A, E_B, E_C, E_D and the deformation in the configuration coordinate. These parameters can be used to find ZPL and the Stokes shifts for the 1D effective phonon.

To decide which transition we wish to study we look at the formation energy diagram and see which are the defects with the lowest formation energies. We consider the charge transition $C_B^0 \rightarrow C_B^+$, $C_N^- \rightarrow C_N^0$ and $C_2^0 \rightarrow C_2^+$. The choice of the former two transitions are motivated by the fact that they are quite probable to be found in a hypothetical sample of *w*BN , the choice of the latter is motivated by the interest for the carbon dimer in *h*BN [24] and also the fact that this defect dominates in the gap energy range for the Fermi energy.

The transitions are represented as green arrows between levels in Fig. 4.26. For the C_B we consider a singly degenerate state in the gap and we excite it to the CBM. Convergence could be achieved only by using fractional constrained occupations so

that the electron was "split" between the two unoccupied levels (double arrow in left panel of Fig. 4.26). We believe that this problem arises because of the quasi-degeneracy of the unoccupied levels so that the calculation can not converge by occupying one of the two, in analogy to the non-integer occupancies observed in the case of the Jahn-Teller effect. For the same reason in C_N^-, instead of exciting an electron from one of the two degenerate in-gap states to the degenerate states at the CBM, we set the occupancies in the gap state to 0.5 and 0.5 and we do the same with the state at the CBM. As a result the number of electrons promoted is actually one but both the promoted and the leftover electrons are shared in the CBM and the gap states (circled in green in the central panel of Fig. 4.26) respectively. This transition is therefore depicted as an arrow between the two circled degenerate states. This problem does not seem to arise instead for the C_2^0 excitation where a state in the VBM is excited to an empty state in the CBM. Further studies are going on at the moment concerning the internal transitions for the B_N^0 and N_B^0 (marked as green arrows in Figs. 4.23 and 4.25) which might be useful for quantum technology purposes.

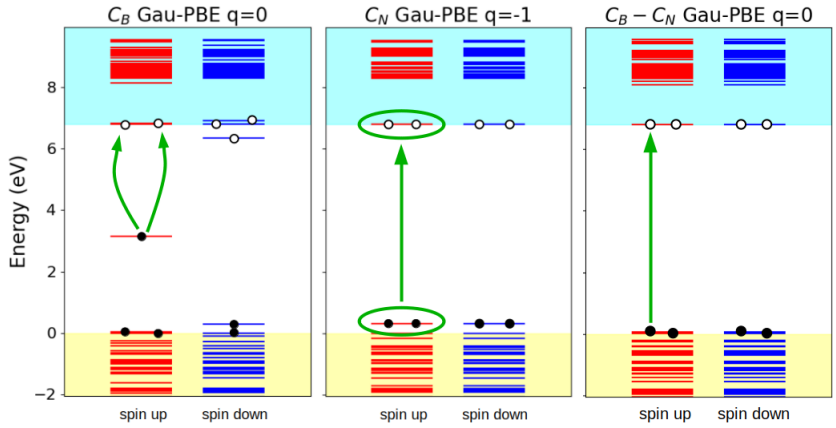

Figure 4.26. – Level schemes for the transitions considered for the ΔSCF approach to luminescence. The green arrows highlight the states where we constrain the occupation.

The results obtained with this method are reported in Tab. 4.9. By looking at theese results we notice the large Stokes and Antistokes shifts that make the results for the $C_B^0 \rightarrow C_B^+$ transition suspicious since a large (Anti)Stokes shifts is symptom of a very large difference in the atomic configuration. This problem might be related to the already mentioned issue of working with non-integer occupations, which means that the found relaxed structure is not the true minimum. Moreover, as already mentioned, the ΔSCF method presents many convergence problems and it is aimed at simulating excited states using a ground state theory. Finally, we have to consider that we are studying one transition at a time which we do not know a priori if dipole-allowed or prohibited. In the next section we introduce a methodology that might help in understanding the entity of the optical transitions due to defects and we try to validate or invalidate the ΔSCF technique.

Charge transition	$C_B^0 \rightarrow C_B^+$	$C_N^- \rightarrow C_N^0$	$C_2^0 \rightarrow C_2^+$
HO level (eV)	3.1425	0.3153 0.3153	0.063
LU level (eV)	6.812, 6.829	6.801, 6.801	6.808
$E(A)$ (Ry)	-7434.4044	-7419.4857	-7425.9850
$E(D)$ (Ry)	-7434.2895	-7419.4768	-7425.9811
Antistokes shift (eV)	1.5629	0.1220	0.0530
$E(B)$ (Ry)	-7434.1348	-7419.0014	-7425.4916
$E(C)$ (Ry)	-7434.2646	-7419.0086	-7425.4933
Stokes shift (eV)	1.7666	0.0970	0.0295
ZPL (eV)	1.901	6.4924	6.690

Table 4.9. – Results for the transitions studied using the ΔSCF approach. HO and LU labels denote the highest and the lowest unoccupied levels, respectively.

4.3.2. Remapped screening BSE approach

We now use the remapping approach outlined in Sec. 2.5 to study the optics on a defective supercell by using the BSE. The remapping procedure allows us to skip the calculation of the static screening on the defective supercell and to use the one calculated on the pristine crystal primitive cell instead. Moreover in this strategy the *GW* calculation is avoided by plugging the Kohn-Sham states from hybrid DFT directly in the BSE. This assumption is justified by comparing the band gap of the crystal computed using *GW* and DFT with Gau-PBE (6.42 and 6.81 eV respectively). The drawback of this approach compared with the ΔSCF approach is that we consider the excitations to compute the spectra without taking into account any structural modification, which would follow the optical excitation.

We first validate the correspondence between the bands used to diagonalize the BSE in a primitive cell with the folded levels when we pass to the supercell. The static screening in the primitive cell has been calculated using 50 polarisation bands. Once refolded it is equivalent to $50 \times 6 \times 6 \times 4 = 7200$ polarisation band. By applying the rules seen in Sec. 2.5 we see that each band is refolded into 144 levels. For example a primitive cell BSE calculation that made use of 3 valence and 2 conduction bands should be in principle equivalent to a our supercell BSE diagonalization using $3 \times 6 \times 6 \times 4$ valence bands and $2 \times 6 \times 6 \times 4$ conduction bands. We can show that this correspondence is not perfect. In Fig. 4.27 we show the absorption spectra for pristine *w*BN obtained from primitive cell calculations using 1) one valence band and one conduction band; 2) two valence bands and one conduction band. These spectra are then compared with 3) the supercell spectrum obtained using the remapped screening with 144 conduction bands and 144 valence bands. If the 1 :144 correspondence due to folding was perfect then the supercell spectrum would have been equivalent to the primitive cell spectrum using only one conduction band and one valence band. Instead we see that, at least up to 11 eV the supercell absorbance spectrum presents structures that resemble more the primitive cell calculation carried out using 2 valence bands. On the other hand, over 11 eV the supercell features become more similar to

those obtained from the primitive cell using one conduction and one valence.

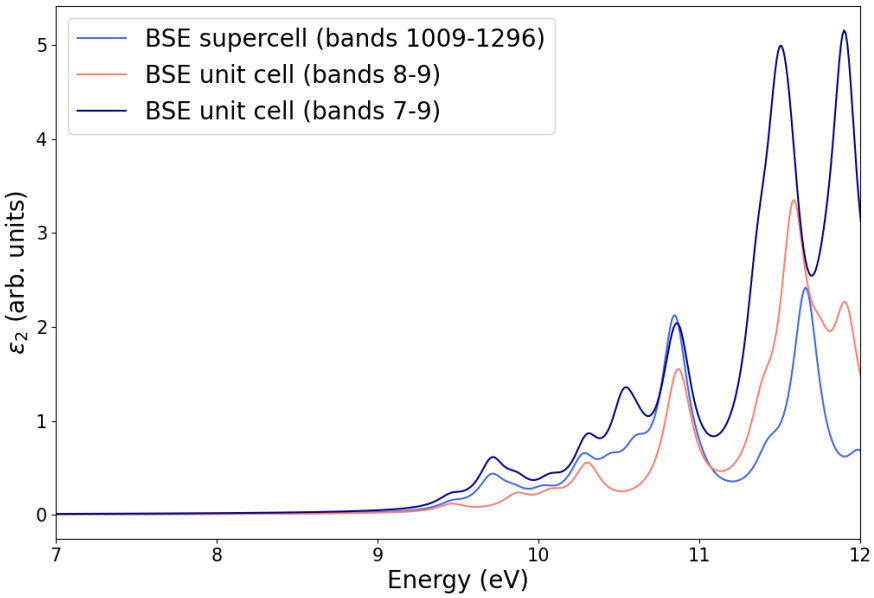

Figure 4.27. – Comparison between the absorbance spectra obtained via BSE on a primitive cell using one conduction and one valence band (orange), on a primitive cell using one conduction and two valence band (navy blue) and on a supercell using a remapped screening using 144 valence and 144 conduction bands (clear blue).

This mismatch may be due to a "migration" of bands initially not considered in the primitive cell calculation that instead enters in the interval of bands included in the supercell calculation thanks to refolding. This effect may be beneficial for our purposes since it opens to the possibility of obtaining sound results using less bands than initially expected. In Fig. 4.28 we illustrate this migration phenomenon. On the right we have the primitive cell bands identified by a colour (red and blue). The solid line is a band that has been included in the BSE calculation of the spectrum while the dashed line band is not included. Let us suppose that when we pass to a supercell, each band should refold into eight levels. We thus compute the BSE on the supercell including eight bands. What we obtain is that not all the levels included (solid lines on the right) have originated from the red band on the left. Some levels are originated from the blue band which was not considered in the primitive cell calculation. On the other hand some of the red levels are not included in the supercell BSE and are therefore marked as dashed lines on the right. As a consequence the spectra obtained using a primitive and a supercell are different, even though the number of bands was correct.

This migration phenomenon forces us however to study the evolution of the spectra for varying intervals of bands. We first consider the C_2^0 dimer. We look at Fig. 4.29 where we further validate our approach. We compare the spectra obtained for the carbon

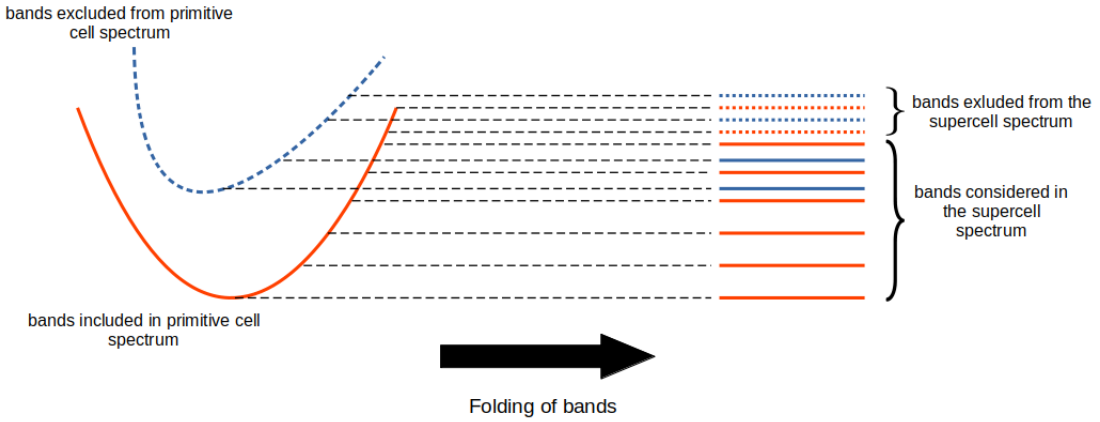

Figure 4.28. – Migration process of bands during refolding. On the left the bands included in BSE in the primitive cell and on the right the corresponding folded levels in the supercell. In both panels the colours are used to distinguish the bands and the corresponding levels from which they have origin. Solid and dashed lines denote bands and levels included and not included in the BSE, respectively.

dimer by using the remapped static screening and the static screening calculated directly on the supercell. In both cases we used 100 bands in BSE diagonalization (from the 100th to the 200th). We recall the fact that using the remapped screening means including in the supercell a screening computed on 7200 folded bands. The screening computed from scratch from the supercell counts instead 1585 polarisation bands since this was the limit of the available computational capabilities. We see that both absorbance spectra show similar features where the peaks are almost rigidly shifted to higher energies and their intensities renormalised as expected since the screening calculated from scratch on the supercell included less bands. As already seen in Sec. 2.5, the two independent spectra when no screening is included coincide perfectly.

Now that the method is validated we explore what happens when we increase the number of bands included in BSE diagonalization from the 100 already used in Fig. 4.29.

In Fig. 4.30 we can see how adding only 10 conduction bands and 10 valence band already heavily affects the spectrum. A big peak centred at 9.8 eV that was not present in Fig. 4.29 appears. An even more important change occur when we add many more conduction bands. In Fig. 4.31 we compared the same spectra showed in Fig. 4.30 with those obtained by including 144 valence levels (equivalent to only one valence band in the primitive cell) and 144 conduction levels (equivalent to just one conduction band in the primitive cell). Much more intense peaks appear at energies above 10 eV and we realize that the features included in the spectra obtained using 100, 110 and 120 bands had a small intensity if compared to those at higher energy. Indeed, in Fig. 4.31 they needed to be multiplied by 50 times in order to make them visible in the plot. Most of these small structures are above the indirect gap energy and are not expected to be visible in photoluminescence. Nonetheless, they show some small features also

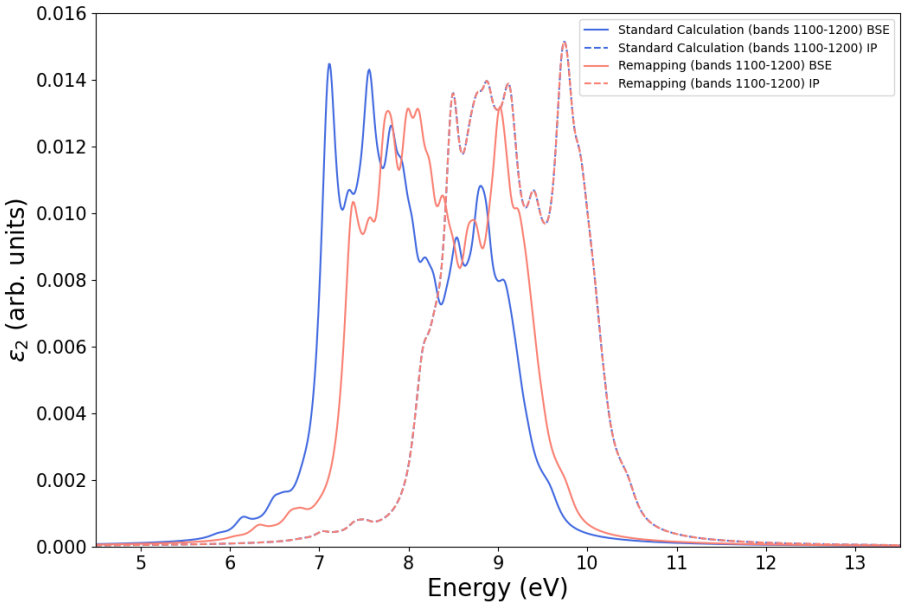

Figure 4.29. – Absorption spectra for the C_2^0 defect using 100 bands for BSE diagonalization. The static screening used has been remapped (orange) and calculated directly on the supercell using 1585 polarisation bands (clear blue). Dashed lines are the independent particle spectra obtained from BSE without including the screening (colours are overlapped).

below the indirect gap. They are originated by some indirect transitions engendered by the breaking of the symmetry due to the defect and they disappear when we use 288 bands (blue line in Fig. 4.31). By comparing the 288 band spectrum with the absorbance of the pristine material (computed using the remapped screening as well) we see that the two almost coincide except for the onset between 7.5 and 8 eV and we can deduce that they are related to the defect. Moreover, they roughly correspond to the low intensity structures already observed in the 100, 110 and 120 bands spectra. We thus make an analysis of the excitons in this energy range. These excitons are represented as the vertical red peaks in Fig. 4.30 computed using the SLEPC algorithm used in the `yambo` code and the most intense ones have been summarized in Tab. 4.10, together with the numerical identifier of the states involved in their transitions. The analysis of these excitons shows that they are related to the defect as they are made of transitions between states of which at least one is rather defect-induced. Their localization can be inferred by looking at the band structure, where we highlighted the flat lines corresponding to the localized states and the plot of the $|\psi|^2$ of one of those states (both in Fig.4.32).

A similar analysis has been also made for the C_N^-. Like for the carbon dimer, the choice of this defect is justified by its low formation energy compared to the other defects. Our analysis showed that the transitions taken into consideration in Sub. 4.3.1

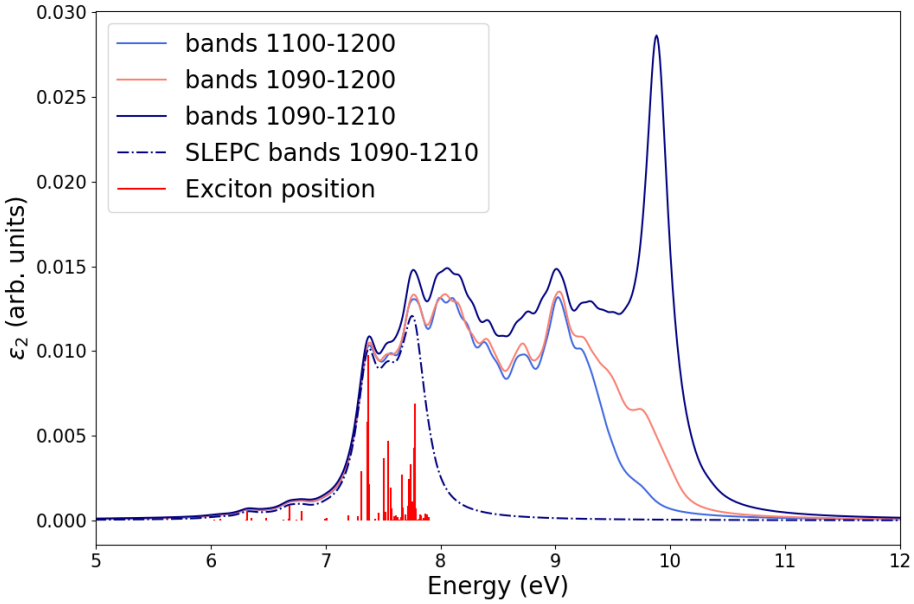

Figure 4.30. – C_2^0 absorption spectra using different number of bands in the BSE hamiltonian. Solid lines report the spectra obtained using 100 (clear blue), 110 (orange), 120 (dark blue). Exciton positions were obtained using the SLEPC algorithm (spectrum in dashed lines) and are represented as red vertical lines.

have small dipoles and they do not contribute much to the spectrum. Instead we focus on the three most intense excitons summarized in Tab. 4.11 and showed as red vertical lines in Fig. 4.33 together with the spectra obtained by varying the number of bands used in BSE diagonalization. We notice a behaviour somehow opposite to that of the carbon dimer. Here for increasing number of bands used the structures at lower energies are enhanced and not suppressed. Their origin from transitions involving defect-induced levels partially hybridized with the bulk can be seen in Fig. 4.34.

To conclude, we used the remapping procedure to make feasible a BSE calculation on a defective supercell by reducing the computational effort and, more importantly, the memory requirements. We applied this approach to overcome the drawbacks of the ΔSCF method in two defects C_2^0 and C_N^-. Since we have validated this technique and we have proven its reliability, it will bee soon applied to other defects.

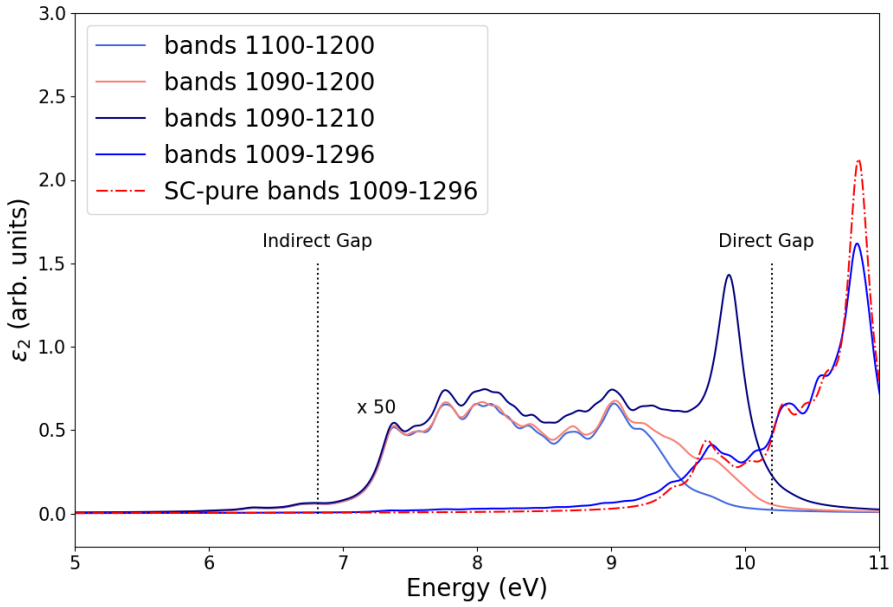

Figure 4.31. – C_2^0 absorption spectra obtained using in the BSE 100 (clear blue), 110 (solid orange), 120 (solid dark blue) and 288 bands (solid blue). Intensities for 100, 110 and 120 bands have been enhanced by 50 times. Also a comparison with the pristine material absorption computed using the remapped screening (dashed red) is reported.

4.4. Conclusions

In this last chapter we finally introduced defects in wBN . The studied defects are the simplest possible, the boron and nitrogen vacancies, boron and nitrogen antisites, carbon substitutionals on a boron or a nitrogen site, the carbon dimer. For these defects we calculated the formation energy diagrams and the charge transition levels using both the semilocal and the hybrid exchange correlation functionals. We can reasonably suppose that the formation energy diagrams are strongly affected by 1) the assumptions made on the choice for the reservoirs of boron, nitrogen and carbon used to compute the chemical potential terms; 2) a partial arbitrariness in the choice for average potential far from the defect in the calculation of the dilute limit correction. For each defect, we presented a comparison between the CTLs computed using the hybrid functional and those calculated using the semilocal functional, using a common absolute scale where the vacuum is set to a common zero. The vacuum level for both the semilocal and the hybrid functional calculation has been calculated using the method described in the App. A. Then we examined in detail the electronic and structural properties of each defect. For the boron and nitrogen vacancy we predicted the magnetization for every charge state by considering the dangling bonds of the first neighbours and applying a spin filling scheme based on the Hund's rule. These

Exc energy (eV)	Band v	Band c	Transition Energy (eV)
6.03	1152	1153	6.74
6.31	1150	1154	7.03
6.68	1144	1154	7.40
6.79	1139	1153-1154	7.51
7.33	1152	1156	8.15
7.49	1150	1155	8.33
7.53	1151	1157	8.28
7.65	1151	1173	8.40
7.72	1151	1178-1179	8.47
	1150	1157	8.51
7.75	1150	1157	8.51
	1152	1187	8.50
7.78	1152	1185-1188-1189-1190	8.50
	1146	1155	

Table 4.10. – C_2^0 exciton analysis with numerical identifier of the one-particle states defining the corresponding electron-hole pairs.

Exc energy (eV)	Band v	Band c	Transition Energy (eV)
6.09	1150	1153-1154	6.80
6.54	1145	1153-1154	7.26
7.63	1150	1161-1162	8.36

Table 4.11. – C_N^{-1} exciton data and their composition in electron-hole pairs.

predictions were also confirmed by the hybrid DFT calculations. The level structures for several charge states of the boron vacancy showed the Jahn-Teller distortion while it was not observed for the nitrogen vacancy. For the carbon substitutionals we did not considered a dangling bond model but we applied the Hund's rule on a sp^3 hybridized orbital between the carbon impurity and the first neighbours. We observed an acceptor and donor level for the C_N and C_B respectively, in their respective two isolectronic charge states. When they complex into a carbon dimer those characters compensate each other, as it can be seen from the formation energy diagram where the charge state 0 dominates. For the boron and nitrogen antisite we constructed again the sp^3 orbitals. The boron antisite presented an interesting level configuration in charge state 0 similar to the negatively charged nitrogen-vacancy complex in diamond. For the nitrogen antisite we compared the level structure of the charge state 0 with its isoelectronic carbon substitutional on a boron site in charge state -1. Both present two electrons in excess with respect to the completely filled octet of the hybridized orbital but they have a different spin configuration which is antiparallel for N_B^0 (giving a 0 magnetization) and parallel for the C_B^- (giving magnetization 2). This different behaviour has been explained by making some assumptions on the symmetry and level degeneracy in the two cases. We then used the ΔSCF approach to study the optics

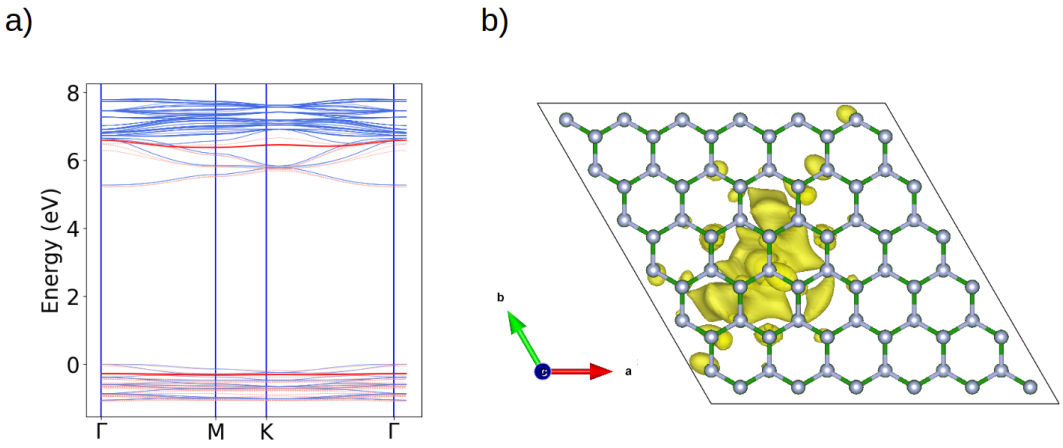

Figure 4.32. – Panel a) : band structure of the dimer (dashed line) and the pristine crystal (solid lines), computed at PBE level. Red flat lines correspond to defect states involved in the transitions discussed; panel b) : $|\psi|^2$ of the state #1155.

for three particular transitions and we constructed the CCD diagrams providing the ZPL, emission, absorption, emission and Stokes and Antistokes energies. Since this approach presented many problems in convergence we also studied the optics using a more traditional approach based on the BSE using the remapping procedure described in Chap. 2. After a validation of this methodology, we focused on the carbon dimer and the C_N^- defects and we observed the excitons due to the defects. Interestingly, by increasing the number of transitions considered in the BSE diagonalization, in the case of the carbon dimer the defect features in the optical spectra were suppressed, while in the case of C_N^- they were enhanced. The remapping procedure allowed to sensibly speed up the calculation of the spectra avoiding the computational effort of computing the static screening on a supercell of hundreds of atoms.

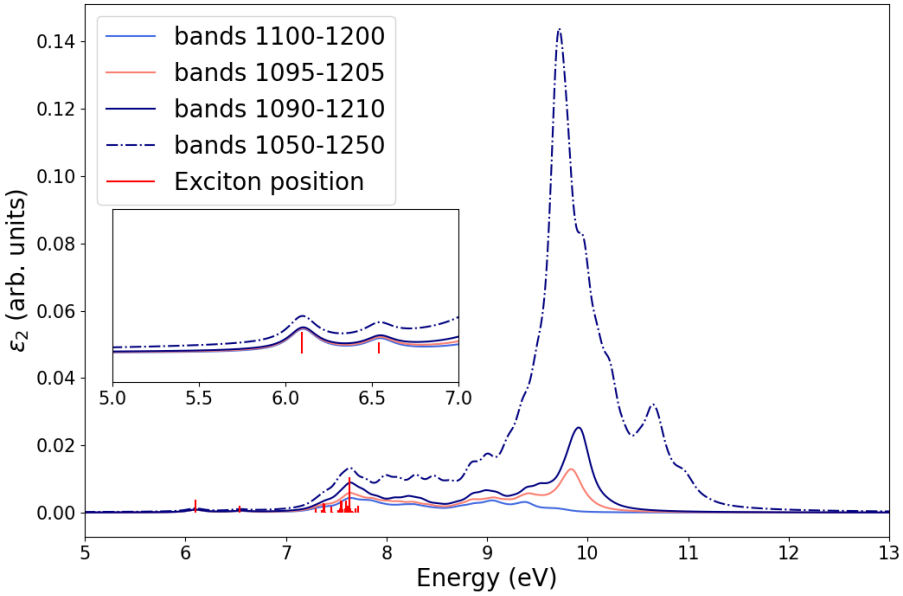

Figure 4.33. – Optical spectra obtained using the remapped static screening and different ranges of bands for the C_N^{-1} defect. By increasing the number of bands the intensity of the structures at lower energies are enhanced. In the inset the same behaviour is showed in detail for the low energy excitons.

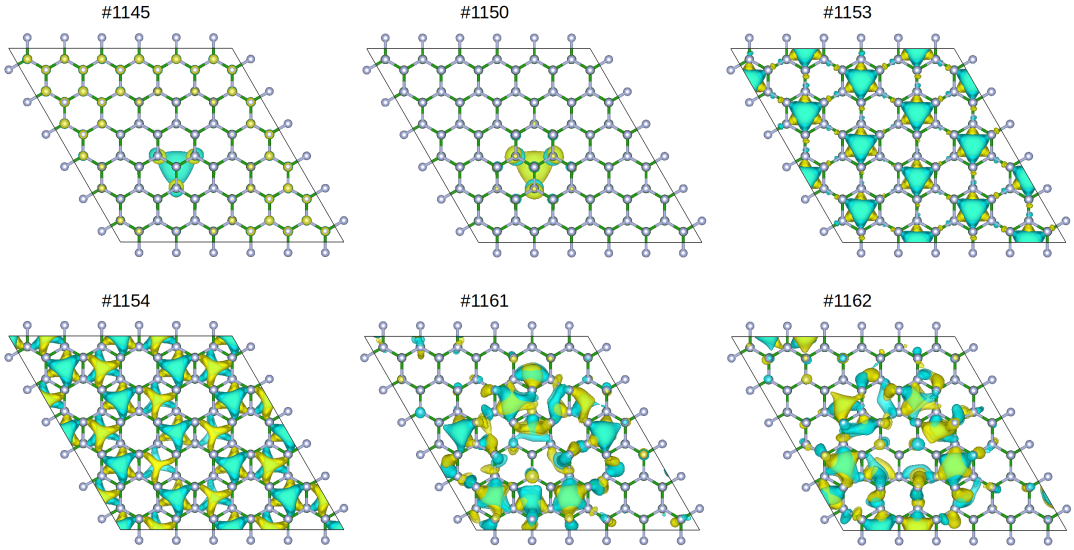

Figure 4.34. – $|\psi|^2$ of the states involved in the excitons listed in Tab. 4.11 with the reader's eye sight line parallel to the (0001) direction.

Conclusion

In the present thesis we wanted to establish the foundations for a characterization of the wurtzite polymorph of boron nitride as an intrinsic semiconductor as well as a host for point defects. The research on this material is still at its infancy since all studies so far focused more on the properties of the BN polytypes that are conventionally considered stable - hexagonal and cubic phases - and tended to see *w*BN almost as an exotic high pressure polymorph or to overlook completely its potentialities as a stand-alone semiconductor. Our research must be understood as an exploratory study aimed at assessing the opportunities offered by this material in the context of optical devices and for this reason it relied on the predictive power of *ab initio* methods.

We proceeded in two steps, first we studied the properties of *w*BN in its pristine phase, then we introduced the defects, we studied their stability and how they affect the structure and the electronic properties. In both cases, our study has made use of methodologies that are well established like DFT and BSE. For the study on the pristine material these techniques have been combined with the *GW* method to include the quasiparticle corrections to the electronic properties and then we studied the phonon assisted luminescence. The optics of the defective system has been studied using two different approaches, one based on the ΔSCF method and one which combined hybrid DFT with BSE. For the latter, direct BSE diagonalization was made possible by using a remapping procedure for the static screening from the primitive cell to the supercell.

Our analysis of the pristine material showed that *w*BN is a wide band gap semiconductor with an absorption spectrum that apparently does not match with the only experimental study on absorption found in the literature. However, in our study we did not include the electron-phonon coupling. It is possible that such coupling would provide a broadening of the spectral features and the optical gap might enter the range of the experimental peak.

A large mismatch between the independent particle and the BSE absorption spectrum proofs that the excitonic effects are important and cannot be neglected. Moreover we showed that the wurtzite domains might be at the origin of the 56 meV phonon replica observed in cathodoluminescence spectra in *c*BN .

The introduction of defects heavily affects he structure of the host and introduces several in-gap levels. For some of the structural changes the symmetry was lowered by distortions due to the Jahn-Teller effects. The formation energy diagrams have been computed along with the CTLs showing that for most of the Fermi energy range, carbon substitutionals and dimer are the most probable defects. We also found that N_B^- and B_N^0 present an electronic level structure similar to that one of the nitrogen-vacancy in diamond, opening for a possible implementation in quantum technologies. The

optical spectra obtained for the C_N^- and C_2^0 showed that those defects have a minimal role in determining the absorbance spectrum.

Future developements

This first non-exhaustive study paves the way to further developments in many directions aimed at answering several questions concerning the reliability of the *w*BN as a useful material in the near future.

This study considered *w*BN as an autonomous crystal, but as already said it is however present in small domains in *c*BN . The relationship between the optical properties of *c*BN and *w*BN should be addressed by *ab initio* studies on *w*BN supercells embedded in a *c*BN crystal. Several structural configurations are possible but electronic microscopy images of those domains are already available and they can be used as a hint to model a realistic *w*BN domain for an *ab initio* study.

At the level of *w*BN as a defect host, the most urgent necessity is a thorough symmetry analysis of each one-electron defect level studied, in order to asses the role of the crystal field on level splitting and the exact process of symmetry lowering. Such analysis should help in analysing the capability of the B_N^0 defect as quantum technology platform. Then a study of the coherence of the photoemission of this defect should be made.

The remapping procedure implemented in this work allowed to make the computation of the optical properties of defective *w*BN very efficient and it will be soon applied to more defects. Further studies and ameliorations of the code are already going on at the moment in order to provide a standard procedure capable of computing the optical properties of defects in few hours.

Finally, we point out that we studied only the most simple point defects. A better model for a defective *w*BN should also consider complexes different from the dimer. We believe that the defect that should have the priority should be the carbon vacancies complexes C_NV_B and C_BV_N and the trimers C_2C_N and C_2C_B. The first two are suggested by the possibility of manipulating the symmetry and the number of electrons to give to the vacancy. The interest for the trimers is motivated by the proved origin of the 1.63 eV line from the carbon trimers in *h*BN .

A. Calculation of the vacuum level

In order to make a comparison between the CTLs calculated at the PBE level and those computed using the hybrid functional it is useful to align them to a common absolute energy, i.e. the vacuum level. Since the CTLs and the Kohn-Sham states for all the defects considered are usually referenced to the HOMO of the bulk material, once the HOMO position with respect to the vacuum is known also the absolute values of the CTLs and the electronic states are determined.

Here we describe the slab-vacuum procedure based on Refs. [128], [129] and [130] that we followed to locate the vacuum. We need to identify a non-polar plane in the material. The idea is to consider a supercell of *w*BN and to simulate a non-polar surface in contact with the vacuum by truncating the atomic structure along the direction perpendicular to it. The region occupied by the atoms will be referred to as the slab, in contrast with the vacuum region. The non-polarity is necessary to avoid divergences of the macroscopic dipole moment in the normal direction when the thickness of the slab tends to infinity (known as polar instability in literature [131, 132, 133]). We identify this non-polar surface with the one circled in blue in Fig. A.1, i.e. the

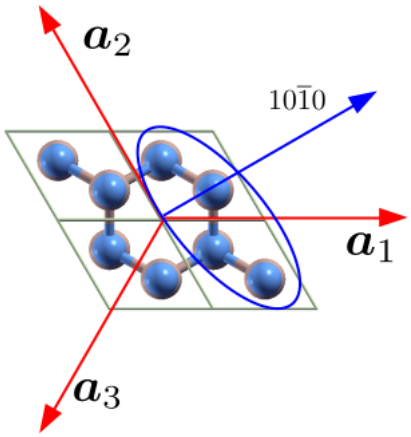

Figure A.1. – The $(10\bar{1}0)$ direction (blue arrow) in the wurtzite structure. The reader's sightline is along the (0001) direction.

$(10\bar{1}0)$ plane, which can be seen as a bilayer with a zig-zag structure. The direction perpendicular to it is denoted by the blue arrow. At this point we need to work with a unit cell that correctly reproduces the wurtzite structure when repeated along the $(10\bar{1}0)$ direction and such that we can add a vacuum region. If we continued to use the usual primitive cell, it would be impossible to simulate the chosen non-polar surface, because it would reproduce the wirtzite structure along the (0001) direction.

Following Ref. [128], we choose to work with an orthorhombic Bravais lattice (a =4.82 bohr, b=7.97 bohr, c = 8.34 bohr, where a, b and c are defined in the last step of Fig. A.2). The cost that we pay is that in this new unit cell we now have eight atoms instead of four. The lattice parameters have been chosen considering the wurtzite atomic positions and distances between the $(10\bar{1}0)$ planes. The simple transposition of the Cartesian atomic positions from the wurtzite primitive cell to the new lattice results in the atoms being out of the orthorhombic cell (first panel of Fig. A.2). Therefore we performed a series of translations and rotations (implemented in a simple python script and showed in Fig. A.2) to correctly arrange those atoms in the orthorhombic lattice. With reference to the steps illustrated in Fig. A.2, we applied, in sequence, a 90° rotation along the y axis, a 30° rotation along the x axis, a 90° rotation along the z axis and finally a translation along the b direction to arrange all the atoms in the cell. In

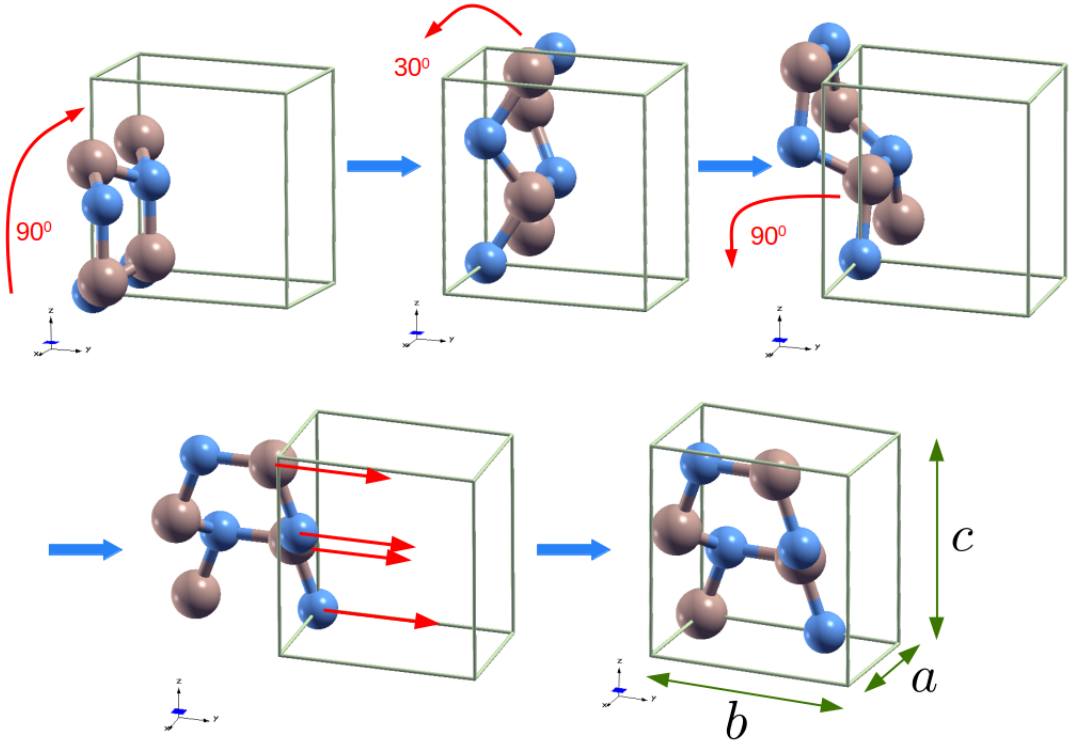

Figure A.2. – Series of transformations made to correctly arrange the wurtzite atoms in the orthohrombic primitive cell. a. b and c cell parameters are also visualized.

the last step we can see that the bilayers perpendicular to the $(10\bar{1}0)$ direction are now perpendicular to the orthorhombic cell c-axis. Next we carry-out three steps. First, we construct a supercell by repeating the orthorhombic unit cell along its new c-axis. Then we add the vacuum by modifying the orthorhombic cell parameter c. Finally we notice that after the previous two steps the non-polar surface is not correctly reproduced yet since it is still made of only half bilayer. The third and last step consists thus in

moving the two atoms that make the incomplete bilayer from one end of the supercell to the equivalent sites at the opposite side. This three steps procedure to build the supercell is pictured in Fig. A.3. The procedure outlined so far correctly reproduced

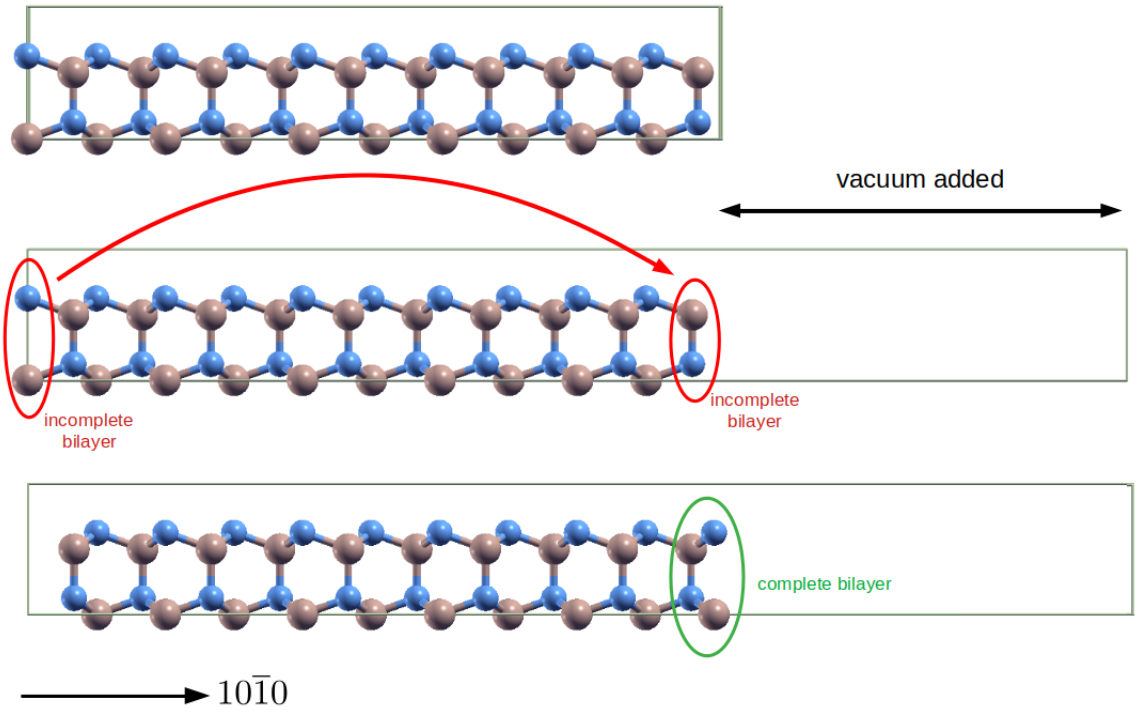

Figure A.3. – Three-steps procedure (from top to bottom) to build the supercell by adding the vacuum and reconstructing the non-polar surfaces. For reasons of space and clarity only 40 atoms are represented instead of 64.

the non-polar surface along the $(10\bar{1}0)$ direction. Now few questions arise :

— How much vacuum should we include in the supercell, and consequently, how long should the orthorhombic supercell be?
— How thick should the slab be and how many atoms should it contain?
— How many $\boldsymbol{k}$-points are needed to simulate the 1BZ of this supercell? What is the cut-off energy needed?

To answer these question we studied the convergence of the total energy of the supercell with respect to the amount of vacuum, the number of atoms, the DFT $\boldsymbol{k}$-grid and the cut-off energy E_{cut}. The total energy per atom in the supercell is converged at a vacuum of 40 Bohr radii, independently from the number of atoms used, and with 64 atoms (for the latter see Fig. A.4). The results of these convergence studies are reported in Tab. A.1.

In the same way we converged the $\boldsymbol{k}$-grid and the cut-off energy down to a threshold of ΔE_{tot}/number of electrons < 4 meV. We found that we need a $6\times6\times1$ $\boldsymbol{k}$-grid with an $E_{cut} = 80$ Ry.

Now we proceed to relax both the orthorhombic supercell volume and the surface atomic positions. In particular we relax the atoms belonging to the two bilayers closest

Number of atoms	Vacuum (bohr)	Total energy per atom (eV)	difference with smaller vacuum
40	40	-175.017796	none
40	50	-175.017719	7.64×10^{-5}
40	60	-175.017783	-6.4×10^{-5}
40	70	-175.017782	8.98×10^{-7}
48	40	-175.039586	none
48	50	-175.039585	7.23×10^{-7}
48	60	-175.039517	6.8×10^{-5}
48	70	-175.039593	-7.58×10^{-5}
56	40	-175.055157	none
56	50	-175.055149	7.95×10^{-6}
56	60	-175.055145	3.73×10^{-6}
56	70	-175.055154	-8.27×10^{-6}

Table A.1. – Convergence test with respect to the number of atoms and the thickness of the vacuum region. The last column reports the difference between the total energy per atom and the same quantity in the previous row, for a constant number of atoms.

to the vacuum, on both side of the slab (sixteen atoms in total) while keeping frozen the rest (as it is done in Ref. [26]). The fully relaxed structure has cell parameters $a = 4.82$ bohr, $b = 7.98$ bohr and $c = 104.62$ bohr. At this point we compute the electrostatic potential $V_{bare} + V_H + V_{xc}$ for the orthorhombic supercell and for the wurtzite bulk supercell (thanks to the post-processing utility in Quantum Espresso `pp.x` using the option `plotnum = 1`, then the utility `average.x` readily gives the plot of such potential). The electrostatic potential is formulated in terms of an average on the xy plane, and thus expressed as a function of the coordinate z. We denote with $V_{bulk}(z)$ the electrostatic potential for the wurtzite bulk supercell and $V_{orth}(z)$ the electrostatic potential for the orthorhombic supercell constructed (we should remind here that for the wurtzite bulk supercell the z direction corresponds to the (0001) direction of the wurtzite structure, in the orthorhombic supercell it corresponds to the $(10\bar{1}0)$ direction). We included the V_{xc} contribution which is supposed to be zero in the vacuum region. Interaction between the slab and its periodic image might introduce in the calculation a non-physical exchange-correlation contribution, nonetheless, we verified that this interaction was not significant. The plots of the electrostatic potential for the bulk and orthorhombic supercells are reported in Figs. A.5 and A.6, respectively, at both PBE and Gau-PBE level. We average $V_{bulk}(z)$ over a space window to obtain the macroscopic value $\overline{V}_{bulk}$ for the potential (dashed lines in Fig. A.5). The average of $V_{orth}(z)$ gives instead the macroscopic value for the potential in the slab $\overline{V}_{slab}$ (red and blue-violet dashed lines in Fig. A.6) and the macroscopic value for the potential in the vacuum $\overline{V}_{vac}$ (brown and navy blue dashed lines in Fig. A.6). For both supercells, the averages have been carried out over a large space window (28 bohr radii) to completely flatten any oscillation. The values $\overline{V}_{bulk}$, $\overline{V}_{slab}$ and $\overline{V}_{vac}$ are not

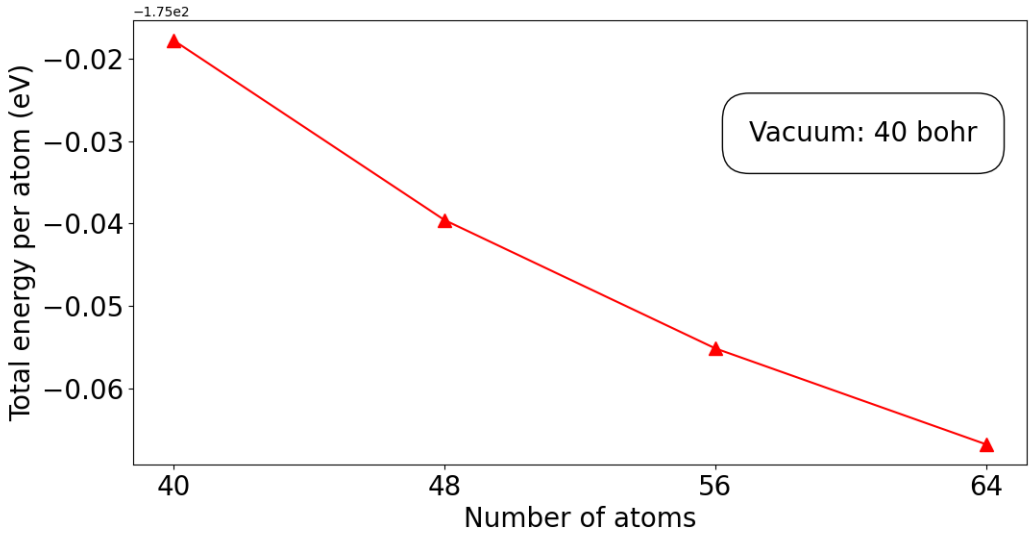

Figure A.4. – Convergence of total energy per atom in the orthorhombic supercell with respect to the number of atoms. Vacuum distance is kept constant at 40 bohr.

aligned and their numerical value has no physical meaning as it is.

The alignment consists of two impositions. In the absolute scale the vacuum level is set to 0 and the macroscopic potentials computed in the slab and in the bulk supercell must have the same value. Once the alignement is done, it is straightforward to get the absolute values of the HOMO and LUMO of the bulk supercell. The absolute value of the potential in the slab with respect to the vacuum is

$$\phi_{slab} = \overline{V}_{slab} - \overline{V}_{vac} \tag{A.1}$$

We align the value $\overline{V}_{bulk}$ to the slab potential by setting $\phi_{bulk} = \phi_{slab}$ where ϕ_{bulk} is the value of $\overline{V}_{bulk}$ in the absolute scale. The absolute value of the bulk HOMO is determined by its difference with respect to $\overline{V}_{bulk}$. Therefore its absolute position E^{abs}_{VBM} is given by

$$E^{abs}_{VBM} = (E_{VBM} - \overline{V}_{bulk}) + (\overline{V}_{slab} - \overline{V}_{vac}) \tag{A.2}$$

Where E_{VBM} is the HOMO level returned by a DFT calculation on the pristine wBN . This procedure has been followed to find the alignment using both the PBE and Gau-PBE functional. In the case of the Gau-PBE functional we converged the total energy with respect to the $\boldsymbol{q}$-grid used in the calculations on the orthorhombic supercell to accurately describe the electron density. We found that with a $\boldsymbol{q}$-grid 3×3×1 the total energy is converged (Convergence data are contained in Tab. A.2). The values found in the alignment procedure are reported in Tab. A.3.

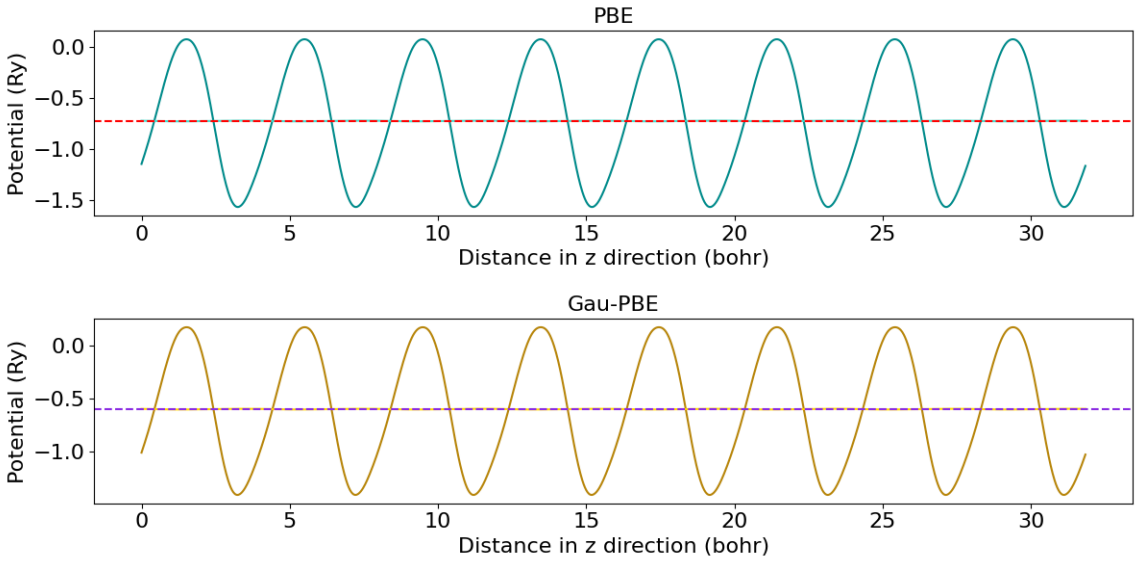

Figure A.5. – Plot of the potential $V_{bulk}(z)$ at PBE (top panel) and Gau-PBE level for the bulk wBN supercell used as reference for the formation energies.

$\boldsymbol{q}$-grid	Total energy (Ry)	Total energy per electron (eV)	Difference
1×1×1	-831.279	-44.18	-
2×2×1	-825.325	-43.863	0.316
3×3×1	-825.282	-43.861	0.002
4×4×1	-825.282	-43.861	5×10^{-10}

Table A.2. – Convergence data for the Gau-PBE calculation on the orthorhombic supercell.

Functional	$\overline{V}_{bulk}$	E_{VBM}	E_{CBM}	$\overline{V}_{slab}$	$\overline{V}_{vac}$	E^{abs}_{VBM}	E^{abs}_{CBM}
PBE	-9.9601	11.2334	16.5026	-16.3698	11.1392	-6.3153	-1.0463
Gau-PBE	-8.1951	10.0489	16.8606	-14.5677	11.0607	-7.3841	-0.5726

Table A.3. – Energies in eV (with both functionals) for the averaged potentials $\overline{V}_{bulk}$, $\overline{V}_{slab}$ and $\overline{V}_{vac}$, the HOMO and LUMO E_{VBM} and E_{CBM} and their absolute values E^{abs}_{VBM} and E^{abs}_{CBM}

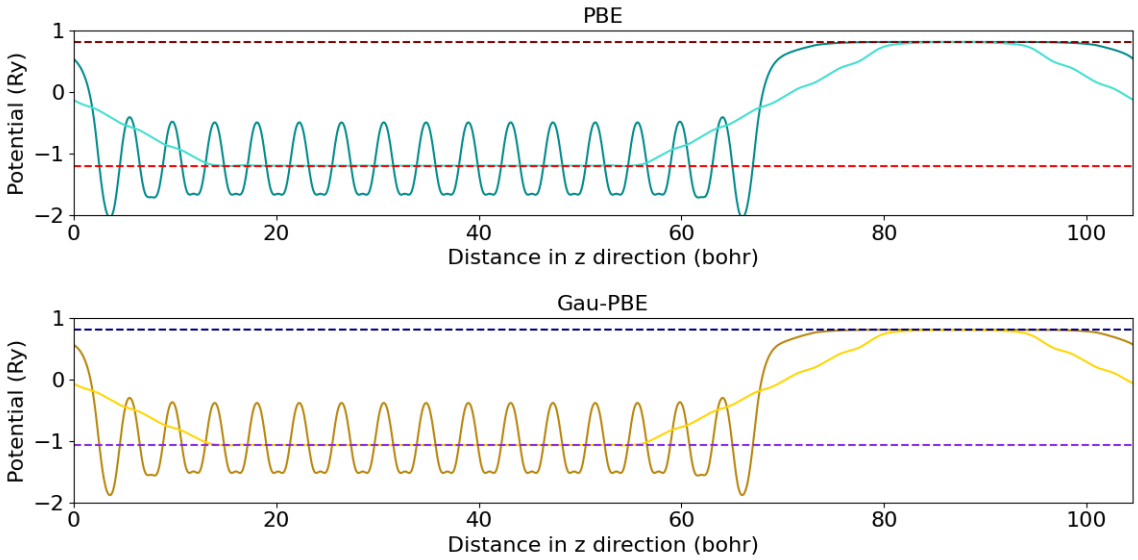

Figure A.6. – Plot of the potential $V_{orth}(z)$ at PBE (top panel) and Gau-PBE level for the orthorhombic supercell. The dashed lines indicate $\overline{V}_{vac}$ (brown and navy blue) and $\overline{V}_{slab}$ (red and blue-violet)

Bibliographie

[1] Joel B. Varley, Bo Shen et Masataka Higashiwaki. « Wide bandgap semiconductor materials and devices ». In : *Journal of Applied Physics* 131.23 (juin 2022), p. 230401. issn : 0021-8979. doi : 10.1063/5.0100601. eprint : https://pubs.aip.org/aip/jap/article-pdf/doi/10.1063/5.0100601/16507797/230401_1_online.pdf. url : https://doi.org/10.1063/5.0100601 (cf. p. 30).

[2] Yuan Liu et al. « Van der Waals heterostructures and devices ». In : *Nature Reviews Materials* 1.9 (2016), p. 16042. issn : 2058-8437. doi : 10.1038/natrevmats.2016.42. url : https://doi.org/10.1038/natrevmats.2016.42 (cf. p. 30).

[3] Audrius Alkauskas, Matthew D. McCluskey et Chris G. Van de Walle. « Tutorial : Defects in semiconductors—Combining experiment and theory ». In : *Journal of Applied Physics* 119.18 (mai 2016), p. 181101. issn : 0021-8979. doi : 10.1063/1.4948245. eprint : https://pubs.aip.org/aip/jap/article-pdf/doi/10.1063/1.4948245/19940133/181101_1_1.4948245.pdf. url : https://doi.org/10.1063/1.4948245 (cf. p. 30, 79, 81, 82).

[4] Audrius Alkauskas, Qimin Yan et Chris G. Van de Walle. « First-principles theory of nonradiative carrier capture via multiphonon emission ». In : *Phys. Rev. B* 90 (7 2014), p. 075202. doi : 10.1103/PhysRevB.90.075202. url : https://link.aps.org/doi/10.1103/PhysRevB.90.075202 (cf. p. 30).

[5] Xie Zhang et al. « First-principles calculations of defects and electron–phonon interactions : Seminal contributions of Audrius Alkauskas to the understanding of recombination processes ». In : *Journal of Applied Physics* 135.15 (avr. 2024), p. 150901. issn : 0021-8979. doi : 10.1063/5.0205525. eprint : https://pubs.aip.org/aip/jap/article-pdf/doi/10.1063/5.0205525/19886023/150901_1_5.0205525.pdf. url : https://doi.org/10.1063/5.0205525 (cf. p. 30).

[6] Gary Wolfowicz et al. « Quantum guidelines for solid-state spin defects ». In : *Nature Reviews Materials* 6.10 (2021), p. 906-925. issn : 2058-8437. doi : 10.1038/s41578-021-00306-y. url : https://doi.org/10.1038/s41578-021-00306-y (cf. p. 31).

[7] Gang Zhang et al. « Material platforms for defect qubits and single-photon emitters ». In : *Applied Physics Reviews* 7.3 (sept. 2020), p. 031308. issn : 1931-9401. doi : 10.1063/5.0006075. eprint : https://pubs.aip.org/aip/apr/article-pdf/doi/10.1063/5.0006075/19742082/031308_1_online.pdf. url : https://doi.org/10.1063/5.0006075 (cf. p. 31).

[8] Luke Gordon et al. « Quantum computing with defects ». In : *MRS Bulletin* 38.10 (2013), p. 802-807. issn : 1938-1425. doi : 10.1557/mrs.2013.206. url : https://doi.org/10.1557/mrs.2013.206 (cf. p. 31).

[9] J. R. Weber et al. « Quantum computing with defects ». In : *Proceedings of the National Academy of Sciences* 107.19 (2010), p. 8513-8518. doi : 10.1073/pnas.1003052107. eprint : https://www.pnas.org/doi/pdf/10.1073/pnas.1003052107. url : https://www.pnas.org/doi/abs/10.1073/pnas.1003052107 (cf. p. 31).

[10] C. L. Degen, F. Reinhard et P. Cappellaro. « Quantum sensing ». In : *Rev. Mod. Phys.* 89 (3 2017), p. 035002. doi : 10.1103/RevModPhys.89.035002. url : https://link.aps.org/doi/10.1103/RevModPhys.89.035002 (cf. p. 31).

[11] L. Gordon, A. Janotti et C. G. Van de Walle. « Defects as qubits in 3C− and 4H−SiC ». In : *Phys. Rev. B* 92 (4 2015), p. 045208. doi : 10.1103/PhysRevB.92.045208. url : https://link.aps.org/doi/10.1103/PhysRevB.92.045208 (cf. p. 31).

[12] Meysam Mohseni et al. « Positively charged carbon vacancy defect as a near-infrared emitter in 4H-SiC ». In : *Phys. Rev. Mater.* 7 (9 2023), p. 096202. doi : 10.1103/PhysRevMaterials.7.096202. url : https://link.aps.org/doi/10.1103/PhysRevMaterials.7.096202 (cf. p. 31).

[13] Hosung Seo et al. « Designing defect-based qubit candidates in wide-gap binary semiconductors for solid-state quantum technologies ». In : *Phys. Rev. Mater.* 1 (7 2017), p. 075002. doi : 10.1103/PhysRevMaterials.1.075002. url : https://link.aps.org/doi/10.1103/PhysRevMaterials.1.075002 (cf. p. 31).

[14] Guodong Bian et al. « Neutral oxygen-vacancy defect in cubic boron nitride : A plausible qubit candidate ». In : *Applied Physics Letters* 114.10 (mar. 2019), p. 102105. issn : 0003-6951. doi : 10.1063/1.5083076. eprint : https://pubs.aip.org/aip/apl/article-pdf/doi/10.1063/1.5083076/13584158/102105_1_online.pdf. url : https://doi.org/10.1063/1.5083076 (cf. p. 31).

[15] Tesfaye A. Abtew et al. « Theory of Oxygen-Boron Vacancy Defect in Cubic Boron Nitride : A Diamond NV^- Isoelectronic Center ». In : *Phys. Rev. Lett.* 113 (13 2014), p. 136401. doi : 10.1103/PhysRevLett.113.136401. url : https://link.aps.org/doi/10.1103/PhysRevLett.113.136401 (cf. p. 31, 81).

[16] J. B. Varley, A. Janotti et C. G. Van de Walle. « Defects in AlN as candidates for solid-state qubits ». In : *Phys. Rev. B* 93 (16 2016), p. 161201. doi : 10.1103/PhysRevB.93.161201. url : https://link.aps.org/doi/10.1103/PhysRevB.93.161201 (cf. p. 31).

[17] Ádám Gali. « Ab initio theory of the nitrogen-vacancy center in diamond ». In : *Nanophotonics* 8.11 (2019), p. 1907-1943. doi : doi:10.1515/nanoph-2019-0154. url : https://doi.org/10.1515/nanoph-2019-0154 (cf. p. 31).

[18] Adam Gali et al. « Theory of Spin-Conserving Excitation of the $N-V^-$ Center in Diamond ». In : *Phys. Rev. Lett.* 103 (18 2009), p. 186404. doi : 10.1103/PhysRevLett.103.186404. url : https://link.aps.org/doi/10.1103/PhysRevLett.103.186404 (cf. p. 31, 81).

[19] Fumiyasu Oba et Yu Kumagai. « Design and exploration of semiconductors from first principles : A review of recent advances ». In : *Applied Physics Express* 11.6 (2018), p. 060101. doi : 10.7567/APEX.11.060101. url : https://dx.doi.org/10.7567/APEX.11.060101 (cf. p. 31).

[20] Daniel Barragan-Yani, Jonathan M. Polfus et Ludger Wirtz. « Native defects in monolayer GaS and GaSe : Electrical properties and thermodynamic stability ». In : *Phys. Rev. Mater.* 6 (11 2022), p. 114002. doi : 10.1103/PhysRevMaterials.6.114002. url : https://link.aps.org/doi/10.1103/PhysRevMaterials.6.114002 (cf. p. 31, 46, 50, 54).

[21] J. L. Lyons, A. Janotti et C. G. Van de Walle. « Role of Si and Ge as impurities in ZnO ». In : *Phys. Rev. B* 80 (20 2009), p. 205113. doi : 10.1103/PhysRevB.80.205113. url : https://link.aps.org/doi/10.1103/PhysRevB.80.205113 (cf. p. 31).

[22] Anderson Janotti et Chris G. Van de Walle. « Native point defects in ZnO ». In : *Phys. Rev. B* 76 (16 2007), p. 165202. doi : 10.1103/PhysRevB.76.165202. url : https://link.aps.org/doi/10.1103/PhysRevB.76.165202 (cf. p. 31, 124).

[23] Hannu-Pekka Komsa et Arkady V. Krasheninnikov. « Native defects in bulk and monolayer MoS_2 from first principles ». In : *Phys. Rev. B* 91 (12 2015), p. 125304. doi : 10.1103/PhysRevB.91.125304. url : https://link.aps.org/doi/10.1103/PhysRevB.91.125304 (cf. p. 31, 50, 110).

[24] M. Mackoit-Sinkevičienė et al. « Carbon dimer defect as a source of the 4.1 eV luminescence in hexagonal boron nitride ». In : *Applied Physics Letters* 115.21 (nov. 2019), p. 212101. issn : 0003-6951. doi : 10.1063/1.5124153. eprint : https://pubs.aip.org/aip/apl/article-pdf/doi/10.1063/1.5124153/13286483/212101_1_online.pdf. url : https://doi.org/10.1063/1.5124153 (cf. p. 31, 110, 112, 135).

[25] M. G. Ganchenkova et R. M. Nieminen. « Nitrogen Vacancies as Major Point Defects in Gallium Nitride ». In : *Phys. Rev. Lett.* 96 (19 2006), p. 196402. doi : 10.1103/PhysRevLett.96.196402. url : https://link.aps.org/doi/10.1103/PhysRevLett.96.196402 (cf. p. 31).

[26] John L. Lyons et Chris G. Van de Walle. « Computationally predicted energies and properties of defects in GaN ». In : *npj Computational Materials* 3.1 (mar. 2017). issn : 2057-3960. doi : 10.1038/s41524-017-0014-2. url : http://dx.doi.org/10.1038/s41524-017-0014-2 (cf. p. 31, 46, 50, 151).

[27] Isamu Akasaki et al. « The nobel prize in physics 2014 ». In : *The Royal Swedish Academy of Science* (2014). url : https://s3.eu-de.cloud-object-storage.appdomain.cloud/kva-image-pdf/2017/05/nobelposterphysics2014_high.pdf (cf. p. 31).

[28] Yinjuan Liu et al. « Hardness of Polycrystalline Wurtzite Boron Nitride (wBN) Compacts ». In : *Scientific Reports* 9.1 (2019), p. 10215. issn : 2045-2322. doi : 10.1038/s41598-019-46709-4. url : https://doi.org/10.1038/s41598-019-46709-4 (cf. p. 31, 90).

[29] Léonard Schué et al. « Bright Luminescence from Indirect and Strongly Bound Excitons in h-BN ». In : *Phys. Rev. Lett.* 122 (6 2019), p. 067401. doi : 10.1103/PhysRevLett.122.067401. url : https://link.aps.org/doi/10.1103/PhysRevLett.122.067401 (cf. p. 31).

[30] Kenji Watanabe, Takashi Taniguchi et Hisao Kanda. « Direct-bandgap properties and evidence for ultraviolet lasing of hexagonal boron nitride single crystal ». In : *Nature Materials* 3.6 (2004), p. 404-409. issn : 1476-4660. doi : 10.1038/nmat1134. url : https://doi.org/10.1038/nmat1134 (cf. p. 31).

[31] G. Cassabois, P. Valvin et B. Gil. « Hexagonal boron nitride is an indirect bandgap semiconductor ». In : *Nature Photonics* 10.4 (2016), p. 262-266. issn : 1749-4893. doi : 10.1038/nphoton.2015.277. url : https://doi.org/10.1038/nphoton.2015.277 (cf. p. 31).

[32] E. Cannuccia, B. Monserrat et C. Attaccalite. « Theory of phonon-assisted luminescence in solids : Application to hexagonal boron nitride ». In : *Phys. Rev. B* 99 (8 2019), p. 081109. doi : 10.1103/PhysRevB.99.081109. url : https://link.aps.org/doi/10.1103/PhysRevB.99.081109 (cf. p. 31).

[33] Momoko Deura et al. « Nanoindentation measurements of a highly oriented wurtzite-type boron nitride bulk crystal ». In : *Japanese Journal of Applied Physics* 56.3 (2017), p. 030301. doi : 10.7567/JJAP.56.030301. url : https://dx.doi.org/10.7567/JJAP.56.030301 (cf. p. 31, 90, 91).

[34] Anna Tararan et al. « Optical gap and optically active intragap defects in cubic BN ». In : *Phys. Rev. B* 98 (9 2018), p. 094106. doi : 10.1103/PhysRevB.98.094106. url : https://link.aps.org/doi/10.1103/PhysRevB.98.094106 (cf. p. 32, 96).

[35] P Giannozzi et al. « Advanced capabilities for materials modelling with Quantum ESPRESSO ». In : *Journal of Physics : Condensed Matter* 29.46 (2017), p. 465901. doi : 10.1088/1361-648X/aa8f79. url : https://dx.doi.org/10.1088/1361-648X/aa8f79 (cf. p. 34, 41).

[36] Paolo Giannozzi et al. « QUANTUM ESPRESSO : a modular and open-source software project for quantum simulations of materials ». In : *Journal of Physics : Condensed Matter* 21.39 (2009), p. 395502. doi : 10.1088/0953-8984/21/39/395502. url : https://dx.doi.org/10.1088/0953-8984/21/39/395502 (cf. p. 34, 41).

[37] Stefano Baroni et al. « Phonons and related crystal properties from density-functional perturbation theory ». In : *Rev. Mod. Phys.* 73 (2 2001), p. 515-562. doi : 10.1103/RevModPhys.73.515. url : https://link.aps.org/doi/10.1103/RevModPhys.73.515 (cf. p. 35, 46).

[38] M. Born et R. Oppenheimer. « Zur Quantentheorie der Molekeln ». In : *Ann. Phys.* 84 (1927). (Leipzig), p. 457 (cf. p. 35).

[39] B. H. Bransden et C. J. Joachain. *Physics of atoms and molecules*. Longman Scientific & Technicals, 1983 (cf. p. 36).

[40] P. Hohenberg et W. Kohn. « Inhomogeneous Electron Gas ». In : *Phys. Rev.* 136 (3B 1964), B864-B871. doi : 10.1103/PhysRev.136.B864. url : https://link.aps.org/doi/10.1103/PhysRev.136.B864 (cf. p. 37).

[41] R. M. Martin. *Electronic Structure - Basic Theory and Practical Methods*. Cambridge University Press, 2004 (cf. p. 37, 38).

[42] W. Kohn et L. J. Sham. « Self-Consistent Equations Including Exchange and Correlation Effects ». In : *Phys. Rev.* 140 (4A 1965), A1133-A1138. doi : 10.1103/PhysRev.140.A1133. url : https://link.aps.org/doi/10.1103/PhysRev.140.A1133 (cf. p. 38, 44).

[43] J. F. Janak. « Proof that $\frac{\partial E}{\partial n_i} = \epsilon$ in density-functional theory ». In : *Phys. Rev. B* 18 (12 1978), p. 7165-7168. doi : 10.1103/PhysRevB.18.7165. url : https://link.aps.org/doi/10.1103/PhysRevB.18.7165 (cf. p. 40).

[44] Christian Carbogno et al. « Numerical quality control for DFT-based materials databases ». In : *npj Computational Materials* 8.1 (2022), p. 69. issn : 2057-3960. doi : 10.1038/s41524-022-00744-4. url : https://doi.org/10.1038/s41524-022-00744-4 (cf. p. 43).

[45] D. R. Hamann, M. Schlüter et C. Chiang. « Norm-Conserving Pseudopotentials ». In : *Phys. Rev. Lett.* 43 (20 1979), p. 1494-1497. doi : 10.1103/PhysRevLett.43.1494. url : https://link.aps.org/doi/10.1103/PhysRevLett.43.1494 (cf. p. 44, 45).

[46] John P. Perdew, Kieron Burke et Yue Wang. « Generalized gradient approximation for the exchange-correlation hole of a many-electron system ». In : *Phys. Rev. B* 54 (23 1996), p. 16533-16539. doi : 10.1103/PhysRevB.54.16533. url : https://link.aps.org/doi/10.1103/PhysRevB.54.16533 (cf. p. 45).

[47] John P. Perdew. « Density functional theory and the band gap problem ». In : *International Journal of Quantum Chemistry* 28.S19 (1985), p. 497-523. doi : https://doi.org/10.1002/qua.560280846. eprint : https://onlinelibrary.wiley.com/doi/pdf/10.1002/qua.560280846. url : https://onlinelibrary.wiley.com/doi/abs/10.1002/qua.560280846 (cf. p. 45).

[48] Marek Maciaszek, Lukas Razinkovas et Audrius Alkauskas. « Thermodynamics of carbon point defects in hexagonal boron nitride ». In : *Phys. Rev. Mater.* 6 (1 2022), p. 014005. doi : 10.1103/PhysRevMaterials.6.014005. url : https://link.aps.org/doi/10.1103/PhysRevMaterials.6.014005 (cf. p. 46, 50, 53, 109, 113, 115).

[49] Jong-Won Song, Koichi Yamashita et Kimihiko Hirao. « Communication : A new hybrid exchange correlation functional for band-gap calculations using a short-range Gaussian attenuation (Gaussian-Perdue–Burke–Ernzerhof) ». In : *The Journal of Chemical Physics* 135.7 (août 2011), p. 071103. issn : 0021-9606. doi : 10.1063/1.3628522. eprint : https://pubs.aip.org/aip/jcp/article-pdf/doi/10.1063/1.3628522/15439309/071103_1_online.pdf. url : https://doi.org/10.1063/1.3628522 (cf. p. 46).

[50] Jong-Won Song et al. « Communication : Singularity-free hybrid functional with a Gaussian-attenuating exact exchange in a plane-wave basis ». In : *The Journal of Chemical Physics* 138.24 (juin 2013), p. 241101. issn : 0021-9606. doi : 10.1063/1.4811775. eprint : https://pubs.aip.org/aip/jcp/article-pdf/doi/10.1063/1.4811775/15460905/241101_1_online.pdf. url : https://doi.org/10.1063/1.4811775 (cf. p. 46).

[51] Xavier Gonze et Changyol Lee. « Dynamical matrices, Born effective charges, dielectric permittivity tensors, and interatomic force constants from density-functional perturbation theory ». In : *Phys. Rev. B* 55 (16 1997), p. 10355-10368. doi : 10.1103/PhysRevB.55.10355. url : https://link.aps.org/doi/10.1103/PhysRevB.55.10355 (cf. p. 48).

[52] Christoph Freysoldt et al. « First-principles calculations for point defects in solids ». In : *Rev. Mod. Phys.* 86 (1 2014), p. 253-305. doi : 10.1103/RevModPhys.86.253. url : https://link.aps.org/doi/10.1103/RevModPhys.86.253 (cf. p. 50, 51).

[53] G. A. Baraff et M. Schlüter. « Calculation of the total energy of charged point defects using the Green's-function technique ». In : *Phys. Rev. B* 30 (4 1984), p. 1853-1866. doi : 10.1103/PhysRevB.30.1853. url : https://link.aps.org/doi/10.1103/PhysRevB.30.1853 (cf. p. 50).

[54] S. B. Zhang et John E. Northrup. « Chemical potential dependence of defect formation energies in GaAs : Application to Ga self-diffusion ». In : *Phys. Rev. Lett.* 67 (17 1991), p. 2339-2342. doi : 10.1103/PhysRevLett.67.2339. url : https://link.aps.org/doi/10.1103/PhysRevLett.67.2339 (cf. p. 51, 109).

[55] G. A. Baraff et M. Schlüter. « Electronic Structure, Total Energies, and Abundances of the Elementary Point Defects in GaAs ». In : *Phys. Rev. Lett.* 55 (12 1985), p. 1327-1330. doi : 10.1103/PhysRevLett.55.1327. url : https://link.aps.org/doi/10.1103/PhysRevLett.55.1327 (cf. p. 51).

[56] Christoph Freysoldt, Jörg Neugebauer et Chris G. Van de Walle. « Electrostatic interactions between charged defects in supercells ». In : *physica status solidi (b)* 248.5 (2011), p. 1067-1076. doi : https://doi.org/10.1002/pssb.201046289. eprint : https://onlinelibrary.wiley.com/doi/pdf/10.1002/pssb.201046289. url : https://onlinelibrary.wiley.com/doi/abs/10.1002/pssb.201046289 (cf. p. 54, 57, 115).

[57] M Leslie et N J Gillan. « The energy and elastic dipole tensor of defects in ionic crystals calculated by the supercell method ». In : *Journal of Physics C : Solid State Physics* 18.5 (1985), p. 973. doi : 10.1088/0022-3719/18/5/005. url : https://dx.doi.org/10.1088/0022-3719/18/5/005 (cf. p. 54).

[58] G. Makov et M. C. Payne. « Periodic boundary conditions in ab initio calculations ». In : *Phys. Rev. B* 51 (7 1995), p. 4014-4022. doi : 10.1103/PhysRevB.51.4014. url : https://link.aps.org/doi/10.1103/PhysRevB.51.4014 (cf. p. 54).

[59] C. W. M. Castleton, A. Höglund et S. Mirbt. « Managing the supercell approximation for charged defects in semiconductors : Finite-size scaling, charge correction factors, the band-gap problem, and the ab initio dielectric constant ». In : *Phys. Rev. B* 73 (3 2006), p. 035215. doi : 10.1103/PhysRevB.73.035215. url : https://link.aps.org/doi/10.1103/PhysRevB.73.035215 (cf. p. 54).

[60] Christoph Freysoldt, Jörg Neugebauer et Chris G. Van de Walle. « Fully Ab Initio Finite-Size Corrections for Charged-Defect Supercell Calculations ». In : *Phys. Rev. Lett.* 102 (1 2009), p. 016402. doi : 10.1103/PhysRevLett.102.016402. url : https://link.aps.org/doi/10.1103/PhysRevLett.102.016402 (cf. p. 54, 57, 115).

[61] Christoph Freysoldt, Jörg Neugebauer et Chris G. Van de Walle. *Sphynx Add-ons*. https://sxrepo.mpie.de/projects/sphinx-add-ons/files. Accessed : 19/10/2023 (cf. p. 57, 115).

[62] Yu Kumagai et Fumiyasu Oba. « Electrostatics-based finite-size corrections for first-principles point defect calculations ». In : *Phys. Rev. B* 89 (19 2014), p. 195205. doi : 10.1103/PhysRevB.89.195205. url : https://link.aps.org/doi/10.1103/PhysRevB.89.195205 (cf. p. 57).

[63] A. Segura et al. « Nonreversible Transition from the Hexagonal to Wurtzite Phase of Boron Nitride under High Pressure : Optical Properties of the Wurtzite Phase ». In : *The Journal of Physical Chemistry C* 123.33 (2019), p. 20167-20173. doi : 10.1021/acs.jpcc.9b06163. eprint : https://doi.org/10.1021/acs.jpcc.9b06163. url : https://doi.org/10.1021/acs.jpcc.9b06163 (cf. p. 57, 90, 91, 95, 116).

[64] A. Fetter et J. Walecka. *Quantum Theory of Many-Particle Systems*. McGraw Hill, 1971 (cf. p. 61, 63, 64).

[65] R. Martin, L. Reining et D. Ceperley. *Interacting Electrons*. Cambridge University Press, 2016 (cf. p. 61, 67, 73).

[66] G Strinati. « Application of the Green's functions method to the study of the optical properties of semiconductors ». In : *La Rivista del Nuovo Cimento (1978-1999)* 11.12 (déc. 1988), p. 1-86 (cf. p. 61).

[67] Giovanni Bussi . « Effects of the Electron–Hole Interaction on the Optical Properties of Materials : the Bethe–Salpeter Equation ». In : *Physica Scripta* 2004.T109 (2004), p. 141. doi : 10.1238/Physica.Topical.109a00141. url : https://dx.doi.org/10.1238/Physica.Topical.109a00141 (cf. p. 61).

[68] F Aryasetiawan et O Gunnarsson. « The GW method ». In : *Reports on Progress in Physics* 61.3 (1998), p. 237. doi : 10.1088/0034-4885/61/3/002. url : https://dx.doi.org/10.1088/0034-4885/61/3/002 (cf. p. 61, 73, 75).

[69] Viktor Mikhailovich Galitskii et Arkadii Beinusovich Migdal. « Application of quantum field theory methods to the many body problem ». In : *Sov. Phys. JETP* 7.96 (1958), p. 18 (cf. p. 64).

[70] Mark S. Hybertsen et Steven G. Louie. « Electron correlation in semiconductors and insulators : Band gaps and quasiparticle energies ». In : *Phys. Rev. B* 34 (8 1986), p. 5390-5413. doi : 10.1103/PhysRevB.34.5390. url : https://link.aps.org/doi/10.1103/PhysRevB.34.5390 (cf. p. 64).

[71] Lars Hedin et Stig Lundqvist. « Effects of Electron-Electron and Electron-Phonon Interactions on the One-Electron States of Solids ». In : sous la dir. de Frederick Seitz, David Turnbull et Henry Ehrenreich. T. 23. Solid State Physics. Academic Press, 1970, p. 1-181. doi : https://doi.org/10.1016/S0081-1947(08)60615-3. url : https://www.sciencedirect.com/science/article/pii/S0081194708606153 (cf. p. 64).

[72] Lars Hedin. « New Method for Calculating the One-Particle Green's Function with Application to the Electron-Gas Problem ». In : *Phys. Rev.* 139 (3A 1965), A796-A823. doi : 10.1103/PhysRev.139.A796. url : https://link.aps.org/doi/10.1103/PhysRev.139.A796 (cf. p. 71).

[73] Giovanni Onida, Lucia Reining et Angel Rubio. « Electronic excitations : density-functional versus many-body Green's-function approaches ». In : *Rev. Mod. Phys.* 74 (2 2002), p. 601-659. doi : 10.1103/RevModPhys.74.601. url : https://link.aps.org/doi/10.1103/RevModPhys.74.601 (cf. p. 73, 76).

[74] Andrea Marini et al. « yambo : An ab initio tool for excited state calculations ». In : *Computer Physics Communications* 180.8 (2009), p. 1392-1403. issn : 0010-4655. doi : https://doi.org/10.1016/j.cpc.2009.02.003. url : https://www.sciencedirect.com/science/article/pii/S0010465509000472 (cf. p. 74, 75).

[75] D Sangalli et al. « Many-body perturbation theory calculations using the yambo code ». In : *Journal of Physics : Condensed Matter* 31.32 (2019), p. 325902. doi : 10.1088/1361-648X/ab15d0. url : https://dx.doi.org/10.1088/1361-648X/ab15d0 (cf. p. 74).

[76] R. W. Godby et R. J. Needs. « Metal-insulator transition in Kohn-Sham theory and quasiparticle theory ». In : *Phys. Rev. Lett.* 62 (10 1989), p. 1169-1172. doi : 10.1103/PhysRevLett.62.1169. url : https://link.aps.org/doi/10.1103/PhysRevLett.62.1169 (cf. p. 75, 98).

[77] W. van Roosbroeck et W. Shockley. « Photon-Radiative Recombination of Electrons and Holes in Germanium ». In : *Phys. Rev.* 94 (6 1954), p. 1558-1560. doi : 10.1103/PhysRev.94.1558. url : https://link.aps.org/doi/10.1103/PhysRev.94.1558 (cf. p. 78).

[78] Fulvio Paleari et al. « Exciton-Phonon Coupling in the Ultraviolet Absorption and Emission Spectra of Bulk Hexagonal Boron Nitride ». In : *Phys. Rev. Lett.* 122 (18 2019), p. 187401. doi : 10.1103/PhysRevLett.122.187401. url : https://link.aps.org/doi/10.1103/PhysRevLett.122.187401 (cf. p. 78).

[79] A. Lenef et S. C. Rand. « Electronic structure of the N-V center in diamond : Theory ». In : *Phys. Rev. B* 53 (20 1996), p. 13441-13455. doi : 10.1103/PhysRevB.53.13441. url : https://link.aps.org/doi/10.1103/PhysRevB.53.13441 (cf. p. 78, 120).

[80] Lukas Razinkovas et al. « Vibrational and vibronic structure of isolated point defects : The nitrogen-vacancy center in diamond ». In : *Phys. Rev. B* 104 (4 2021), p. 045303. doi : 10.1103/PhysRevB.104.045303. url : https://link.aps.org/doi/10.1103/PhysRevB.104.045303 (cf. p. 78, 82).

[81] Cyrus E. Dreyer et al. « Radiative capture rates at deep defects from electronic structure calculations ». In : *Phys. Rev. B* 102 (8 2020), p. 085305. doi : 10.1103/PhysRevB.102.085305. url : https://link.aps.org/doi/10.1103/PhysRevB.102.085305 (cf. p. 81, 82).

[82] Audrius Alkauskas et al. « First-principles theory of the luminescence lineshape for the triplet transition in diamond NV centres ». In : *New Journal of Physics* 16.7 (2014), p. 073026. doi : 10.1088/1367-2630/16/7/073026. url : https://dx.doi.org/10.1088/1367-2630/16/7/073026 (cf. p. 81, 82).

[83] Yu Jin et al. « Photoluminescence spectra of point defects in semiconductors : Validation of first-principles calculations ». In : *Phys. Rev. Mater.* 5 (8 2021), p. 084603. doi : 10.1103/PhysRevMaterials.5.084603. url : https://link.aps.org/doi/10.1103/PhysRevMaterials.5.084603 (cf. p. 81, 82).

[84] Audrius Alkauskas et al. « First-Principles Calculations of Luminescence Spectrum Line Shapes for Defects in Semiconductors : The Example of GaN and ZnO ». In : *Phys. Rev. Lett.* 109 (26 2012), p. 267401. doi : 10.1103/PhysRevLett.109.267401. url : https://link.aps.org/doi/10.1103/PhysRevLett.109.267401 (cf. p. 82).

[85] Fulvio Paleari. « First-principles approaches to the description of indirect absorption and luminescence spectroscopy : exciton-phonon coupling in hexagonal boron nitride ». Available at https://orbilu.uni.lu/handle/10993/41058. PhD thesis. Luxembourg : Université du Luxembourg, 2019 (cf. p. 83, 84).

[86] Martino Silvetti, Claudio Attaccalite et Elena Cannuccia. « Pressure dependence of electronic, vibrational and optical properties of wurtzite-boron nitride ». In : *Phys. Rev. Mater.* 7 (5 2023), p. 055201. doi : 10.1103/PhysRevMaterials.7.055201. url : https://link.aps.org/doi/10.1103/PhysRevMaterials.7.055201 (cf. p. 87).

[87] Natalia Izyumskaya et al. « Recent Development of Boron Nitride towards Electronic Applications ». In : *Advanced Electronic Materials* 3.5 (2017), p. 1600485. doi : https://doi.org/10.1002/aelm.201600485. eprint : https://onlinelibrary.wiley.com/doi/pdf/10.1002/aelm.201600485. url : https://onlinelibrary.wiley.com/doi/abs/10.1002/aelm.201600485 (cf. p. 87, 91, 92).

[88] F. P. Bundy et Jr. Wentorf R. H. « Direct Transformation of Hexagonal Boron Nitride to Denser Forms ». In : *The Journal of Chemical Physics* 38.5 (mar. 1963), p. 1144-1149. issn : 0021-9606. doi : 10.1063/1.1733815. eprint : https://pubs.aip.org/aip/jcp/article-pdf/38/5/1144/18828961/1144_1_online.pdf. url : https://doi.org/10.1063/1.1733815 (cf. p. 89).

[89] Masao Wakatsuki, Kaoru J. Takano et Goroh Fujita. « Topotaxial and some other characters of the transformation from hexagonal to wurtzitic BN ». In : *Physica B+C* 139-140 (1986), p. 256-258. issn : 0378-4363. doi : https://doi.org/10.1016/0378-4363(86)90571-1. url : https://www.sciencedirect.com/science/article/pii/0378436386905711 (cf. p. 89).

[90] Eiji Tani et al. « A Stability of Wurtzite Type Boron Nitride under High Pressure ». In : *Japanese Journal of Applied Physics* 14.10 (1975), p. 1605. doi : 10.1143/JJAP.14.1605. url : https://dx.doi.org/10.1143/JJAP.14.1605 (cf. p. 89).

[91] A.V. Kurdyumov et al. « The structural aspect of wurtzite boron nitride phase stabilization ». In : *Journal of Physics and Chemistry of Solids* 54.9 (1993), p. 1051-1053. issn : 0022-3697. doi : https://doi.org/10.1016/0022-3697(93)90012-G. url : https://www.sciencedirect.com/science/article/pii/002236979390012G (cf. p. 89).

[92] Vladimir L. Solozhenko et al. « Equation of state of wurtzitic boron nitride to 66 GPa ». In : *Applied Physics Letters* 72.14 (avr. 1998), p. 1691-1693. issn : 0003-6951. doi : 10.1063/1.121186. eprint : https://pubs.aip.org/aip/apl/article-pdf/72/14/1691/18533061/1691_1_online.pdf. url : https://doi.org/10.1063/1.121186 (cf. p. 89, 92).

[93] R.R Wills. « Wurtzitic boron nitride—a review ». In : *International Journal of High Technology Ceramics* 1.2 (1985), p. 139-153. issn : 0267-3762. doi : https://doi.org/10.1016/0267-3762(85)90005-0. url : https://www.sciencedirect.com/science/article/pii/0267376285900050 (cf. p. 89).

[94] Yong-Nian Xu et W. Y. Ching. « Calculation of ground-state and optical properties of boron nitrides in the hexagonal, cubic, and wurtzite structures ». In : *Phys. Rev. B* 44 (15 1991), p. 7787-7798. doi : 10.1103/PhysRevB.44.7787. url : https://link.aps.org/doi/10.1103/PhysRevB.44.7787 (cf. p. 89, 90).

[95] L. C. Nistor, G. Van Tendeloo et G. Dinca. « Crystallographic aspects related to the high pressure–high temperature phase transformation of boron nitride ». In : *Philosophical Magazine* 85.11 (2005), p. 1145-1158. doi : 10.1080/14786430412331325058. eprint : https://doi.org/10.1080/14786430412331325058. url : https://doi.org/10.1080/14786430412331325058 (cf. p. 90).

[96] Shigeo Horiuchi et al. « Monoclinic phase of boron nitride appearing during the hexagonal cubic phase transition at high pressure and high temperature ». In : *Applied Physics Letters* 68.2 (jan. 1996), p. 182-184. issn : 0003-6951. doi : 10.1063/1.116453. eprint : https://pubs.aip.org/aip/apl/article-pdf/68/2/182/18516306/182_1_online.pdf. url : https://doi.org/10.1063/1.116453 (cf. p. 90).

[97] Chunlin Chen et al. « Stabilizing the metastable superhard material wurtzite boron nitride by three-dimensional networks of planar defects ». In : *Proceedings of the National Academy of Sciences* 116.23 (2019), p. 11181-11186. doi : 10.1073/pnas.1902820116. url : https://www.pnas.org/doi/abs/10.1073/pnas.1902820116 (cf. p. 90, 91).

[98] T. Taniguchi et al. « Effect of nonhydrostaticity on the pressure induced phase transformation of rhombohedral boron nitride ». In : *Applied Physics Letters* 70.18 (mai 1997), p. 2392-2394. issn : 0003-6951. doi : 10.1063/1.118882. eprint : https://pubs.aip.org/aip/apl/article-pdf/70/18/2392/18526642/2392_1_online.pdf. url : https://doi.org/10.1063/1.118882 (cf. p. 90).

[99] N. E. Christensen et I. Gorczyca. « Optical and structural properties of III-V nitrides under pressure ». In : *Phys. Rev. B* 50 (7 1994), p. 4397-4415. doi : 10.1103/PhysRevB.50.4397. url : https://link.aps.org/doi/10.1103/PhysRevB.50.4397 (cf. p. 90).

[100] Krystian Karch et Friedhelm Bechstedt. « Ab initio lattice dynamics of BN and AlN : Covalent versus ionic forces ». In : *Phys. Rev. B* 56 (12 1997), p. 7404-7415. doi : 10.1103/PhysRevB.56.7404. url : https://link.aps.org/doi/10.1103/PhysRevB.56.7404 (cf. p. 90, 94, 95).

[101] Nobuko Ohba et al. « First-principles study on structural, dielectric, and dynamical properties for three BN polytypes ». In : *Phys. Rev. B* 63 (11 2001), p. 115207. doi : 10.1103/PhysRevB.63.115207. url : https://link.aps.org/doi/10.1103/PhysRevB.63.115207 (cf. p. 90).

[102] Su Yixi et al. « Vacuum-ultraviolet reflectance spectra and optical properties of nanoscale wurtzite boron nitride ». In : *Phys. Rev. B* 50 (24 1994), p. 18637-18639. doi : 10.1103/PhysRevB.50.18637. url : https://link.aps.org/doi/10.1103/PhysRevB.50.18637 (cf. p. 90, 102, 103, 107).

[103] A. Nagakubo et al. « Elastic constants of cubic and wurtzite boron nitrides ». In : *Applied Physics Letters* 102.24 (juin 2013), p. 241909. issn : 0003-6951. doi : 10.1063/1.4811789. eprint : https://pubs.aip.org/aip/apl/article-pdf/doi/10.1063/1.4811789/14019390/241909_1_online.pdf. url : https://doi.org/10.1063/1.4811789 (cf. p. 91).

[104] John P. Perdew et al. « Restoring the Density-Gradient Expansion for Exchange in Solids and Surfaces ». In : *Phys. Rev. Lett.* 100 (13 2008), p. 136406. doi : 10.1103/PhysRevLett.100.136406. url : https://link.aps.org/doi/10.1103/PhysRevLett.100.136406 (cf. p. 91).

[105] M.J. van Setten et al. « The PseudoDojo : Training and grading a 85 element optimized norm-conserving pseudopotential table ». In : *Computer Physics Communications* 226 (2018), p. 39-54. issn : 0010-4655. doi : https://doi.org/10.1016/j.cpc.2018.01.012. url : https://www.sciencedirect.com/science/article/pii/S0010465518300250 (cf. p. 91).

[106] M. S. Dresselhaus, G. Dresselhaus et A. Jorio. *Group Theory - Application to the Physics of Condensed Matter*. Springer, 2008 (cf. p. 92).

[107] I. Gorczyca et al. « Optical phonon modes in GaN and AlN ». In : *Phys. Rev. B* 51 (17 1995), p. 11936-11939. doi : 10.1103/PhysRevB.51.11936. url : https://link.aps.org/doi/10.1103/PhysRevB.51.11936 (cf. p. 93, 97).

[108] Alexey Bosak et Michael Krisch. « Lattice dynamics of tetrahedrally bonded boron nitride probed by inelastic X-ray scattering ». In : *Radiation Physics and Chemistry* 75.11 (2006). Proceedings of the 20th International Conference on X-ray and Inner-Shell Processes, p. 1661-1665. issn : 0969-806X. doi : https://doi.org/10.1016/j.radphyschem.2005.07.024. url : https://www.sciencedirect.com/science/article/pii/S0969806X06002362 (cf. p. 95, 96).

[109] Anton Kokalj. « XCrySDen—a new program for displaying crystalline structures and electron densities ». In : *Journal of Molecular Graphics and Modelling* 17.3 (1999), p. 176-179. issn : 1093-3263. doi : https://doi.org/10.1016/S1093-3263(99)00028-5. url : https://www.sciencedirect.com/science/article/pii/S1093326399000285 (cf. p. 95).

[110] Leopold Talirz et al. « Materials Cloud, a platform for open computational science ». In : *Scientific Data* 7.1 (2020), p. 299. issn : 2052-4463. doi : 10.1038/s41597-020-00637-5. url : https://doi.org/10.1038/s41597-020-00637-5 (cf. p. 95).

[111] Alfredo Segura et al. « Tuning the Direct and Indirect Excitonic Transitions of h-BN by Hydrostatic Pressure ». In : *The Journal of Physical Chemistry C* 125.23 (2021), p. 12880-12885. issn : 1932-7447. doi : 10.1021/acs.jpcc.1c02082. url : https://doi.org/10.1021/acs.jpcc.1c02082 (cf. p. 100).

[112] Pierre Lechifflart, Fulvio Paleari et Claudio Attaccalite. « Excitons under strain : light absorption and emission in strained hexagonal boron nitride ». In : *SciPost Physics* 12.5 (2022), p. 145. doi : 10.21468/SciPostPhys.12.5.145. url : https://scipost.org/10.21468/SciPostPhys.12.5.145 (cf. p. 105, 106).

[113] Roberto Rizzato et al. « Extending the coherence of spin defects in hBN enables advanced qubit control and quantum sensing ». In : *Nature Communications* 14.1 (2023), p. 5089. issn : 2041-1723. doi : 10.1038/s41467-023-40473-w. url : https://doi.org/10.1038/s41467-023-40473-w (cf. p. 110).

[114] Cesar Jara et al. « First-Principles Identification of Single Photon Emitters Based on Carbon Clusters in Hexagonal Boron Nitride ». In : *The Journal of Physical Chemistry A* 125.6 (2021), p. 1325-1335. issn : 1089-5639. doi : 10.1021/acs.jpca.0c07339. url : https://doi.org/10.1021/acs.jpca.0c07339 (cf. p. 110).

[115] G. Gross et G. P. Parravicini. *Solid State Physics*. Academic Press, 2014 (cf. p. 111).

[116] M. Stoneham. *Theory of Defects in Solids*. Oxford University Press, 1975 (cf. p. 111).

[117] L. Weston et al. « Native point defects and impurities in hexagonal boron nitride ». In : *Phys. Rev. B* 97 (21 2018), p. 214104. doi : 10.1103/PhysRevB.97.214104. url : https://link.aps.org/doi/10.1103/PhysRevB.97.214104 (cf. p. 113).

[118] Mehdi Abdi et al. « Color Centers in Hexagonal Boron Nitride Monolayers : A Group Theory and Ab Initio Analysis ». In : *ACS Photonics* 5.5 (2018), p. 1967-1976. doi : 10.1021/acsphotonics.7b01442. eprint : https://doi.org/10.1021/acsphotonics.7b01442. url : https://doi.org/10.1021/acsphotonics.7b01442 (cf. p. 113).

[119] Jörg Neugebauer et Chris G. Van de Walle. « Atomic geometry and electronic structure of native defects in GaN ». In : *Phys. Rev. B* 50 (11 1994), p. 8067-8070. doi : 10.1103/PhysRevB.50.8067. url : https://link.aps.org/doi/10.1103/PhysRevB.50.8067 (cf. p. 113).

[120] Andrew Hung et al. « An ab initio study of structural properties and single vacancy defects in Wurtzite AlN ». In : *The Journal of Chemical Physics* 120.10 (mar. 2004), p. 4890-4896. issn : 0021-9606. doi : 10.1063/1.1645790. eprint : https://pubs.aip.org/aip/jcp/article-pdf/120/10/4890/19069792/4890_1_online.pdf. url : https://doi.org/10.1063/1.1645790 (cf. p. 113).

[121] K Laaksonen, M G Ganchenkova et R M Nieminen. « Vacancies in wurtzite GaN and AlN ». In : *Journal of Physics : Condensed Matter* 21.1 (2008), p. 015803. doi : 10.1088/0953-8984/21/1/015803. url : https://dx.doi.org/10.1088/0953-8984/21/1/015803 (cf. p. 113, 124).

[122] Sharmila N. Shirodkar, Cyrille Armel Sayou Ngomsi et Pratibha Dev. « Small Electron Polaron in Carbon-Doped Cubic Boron Nitride ». In : *ACS Applied Electronic Materials* 5.3 (2023), p. 1707-1714. doi : 10.1021/acsaelm.2c01743. eprint : https://doi.org/10.1021/acsaelm.2c01743. url : https://doi.org/10.1021/acsaelm.2c01743 (cf. p. 113).

[123] Xu Sun et al. « Two-Dimensional Boron Crystals : Structural Stability, Tunable Properties, Fabrications and Applications ». In : *Advanced Functional Materials* 27.19 (2017), p. 1603300. doi : https://doi.org/10.1002/adfm.201603300. eprint : https://onlinelibrary.wiley.com/doi/pdf/10.1002/adfm.201603300. url : https://onlinelibrary.wiley.com/doi/abs/10.1002/adfm.201603300 (cf. p. 113).

[124] W. Orellana et H. Chacham. « Atomic geometry and energetics of vacancies and antisites in cubic boron nitride ». In : *Applied Physics Letters* 74.20 (mai 1999), p. 2984-2986. issn : 0003-6951. doi : 10.1063/1.123987. eprint : https://pubs.aip.org/aip/apl/article-pdf/74/20/2984/18541576/2984_1_online.pdf. url : https://doi.org/10.1063/1.123987 (cf. p. 113).

[125] James E. House. *Descriptive Inorganic Chemistry (Third Edition)*. Academic Press, 2020 (cf. p. 113).

[126] J R Maze et al. « Properties of nitrogen-vacancy centers in diamond : the group theoretic approach ». In : *New Journal of Physics* 13.2 (2011), p. 025025. doi : 10.1088/1367-2630/13/2/025025. url : https://dx.doi.org/10.1088/1367-2630/13/2/025025 (cf. p. 120).

[127] Adam Gali, Maria Fyta et Efthimios Kaxiras. « Ab initio supercell calculations on nitrogen-vacancy center in diamond : Electronic structure and hyperfine tensors ». In : *Phys. Rev. B* 77 (15 2008), p. 155206. doi : 10.1103/PhysRevB.77.155206. url : https://link.aps.org/doi/10.1103/PhysRevB.77.155206 (cf. p. 124).

[128] Tapio T. Rantala et al. « Surface relaxation of the (1010) face of wurtzite CdS ». In : *Surface Science* 352-354 (1996). Proceedings of the 15th European Conference on Surface Science, p. 77-82. issn : 0039-6028. doi : https://doi.org/10.

1016/0039-6028(95)01094-7. url : https://www.sciencedirect.com/science/article/pii/0039602895010947 (cf. p. 148, 149).

[129] Mo-Rigen He, Rong Yu et Jing Zhu. « Reversible wurtzite-tetragonal reconstruction in ZnO(1010) surfaces ». In : *Angewandte Chemie (International ed. in English)* 51.31 (2012), 7744—7747. issn : 1433-7851. doi : 10.1002/anie.201202598. url : https://doi.org/10.1002/anie.201202598 (cf. p. 148).

[130] Mo-Rigen He, Rong Yu et Jing Zhu. « Supporting information - Reversible wurtzite-tetragonal reconstruction in ZnO(1010) surfaces ». In : *Angewandte Chemie (International ed. in English)* 51.31 (2012), 7744—7747. issn : 1433-7851. doi : 10.1002/anie.201202598. url : https://doi.org/10.1002/anie.201202598 (cf. p. 148).

[131] Yoyo Hinuma et al. « Categorization of surface polarity from a crystallographic approach ». In : *Computational Materials Science* 113 (2016), p. 221-230. issn : 0927-0256. doi : https://doi.org/10.1016/j.commatsci.2015.11.042. url : https://www.sciencedirect.com/science/article/pii/S0927025615007612 (cf. p. 148).

[132] Claudine Noguera. « Polar oxide surfaces ». In : *Journal of Physics : Condensed Matter* 12.31 (2000), R367. doi : 10.1088/0953-8984/12/31/201. url : https://dx.doi.org/10.1088/0953-8984/12/31/201 (cf. p. 148).

[133] Jacek Goniakowski, Fabio Finocchi et Claudine Noguera. « Polarity of oxide surfaces and nanostructures ». In : *Reports on Progress in Physics* 71.1 (2007), p. 016501. doi : 10.1088/0034-4885/71/1/016501. url : https://dx.doi.org/10.1088/0034-4885/71/1/016501 (cf. p. 148).